

# **Aerosol Jet Printed Electronic Devices and Systems**

Zur Erlangung des akademischen Grades eines  
DOKTOR-INGENIEURS

an der Fakultät für Elektrotechnik  
und Informationstechnik  
des Karlsruher Instituts für Technologie (KIT)

genehmigte  
DISSERTATION

von

**Dipl.-Ing. Ralph Eckstein**

geb. in Karlsruhe

Datum der mündlichen Prüfung: 27.10.2016  
Referent: Prof. Dr. Uli Lemmer  
Korreferent: Prof. Dr. Wolfgang Kowalsky



This document is licensed under the Creative Commons Attribution – Share Alike 3.0 DE License (CC BY-SA 3.0 DE): <http://creativecommons.org/licenses/by-sa/3.0/de/>





*With pride and affection to my father, Herbert, and my mother, Gabriele.*

*And to my beloved wife Claudia, for her endless support and for being the perfect mother to our lovely and very sparkly daughter Emilia.*



# Abstract

The field of printed electronics provides enormous innovative capabilities to establish new markets in the field of flexible, conformable, imperceptible or customized devices and systems for novel applications, as well as new design concepts. Also in light of the trillion sensors movement, which was founded to accelerate and coordinate the development of sensing devices to meet predicted demand in the near future, the importance of the research area of printed electronic and optoelectronic devices and systems cannot be underestimated.

The present work relates to the digital aerosol jet printing of electronic components. Firstly, transparent conductors as top anodes for solar cells based on conductive polymers and aerosol jet printed metal grids were fabricated, characterized optically, electrically, and mechanically, as well as validated by additional device simulations. Secondly, this work deals with the fabrication of semi-transparent and flexible organic photodiodes with spectral responsivities (SR) of 0.2 A/W, specific detectivities ( $D^*$ ) up to  $2 \cdot 10^{11}$  cm Hz<sup>0.5</sup>/W, and bandwidths (BW) of  $\sim 300$  kHz. The devices were fabricated exclusively by aerosol jet printing with a focus on the printing of homogeneous active layers by evaluating the influence of process parameters, such as velocity, material flow, and multi-pass printing. Thirdly, the fabrication of self-organizing metallic micro-structures using digitally printed dewetting patterns was developed and investigated throughout this thesis. Therefore, the wetting morphology of the underlying dewetting process was investigated, which included the correlation between prevalent surface energies and tensions of different substrate materials and fluids, as well as the limitation of the maximum fluid volume depending on the feature size. Furthermore, application examples of printed electronic systems were demonstrated. This included the fabrication of Ag source-drain contact layers for 3-stage ring oscillators, which revealed an oscillation frequency of up to 400 Hz. In addition, passive matrix photodiode arrays with 256 pixels were successfully aerosol jet printed, showing state-of-the-art performances with SR of 0.3 A/W,  $D^*$  of  $8 \cdot 10^{11}$  cm Hz<sup>0.5</sup>/W, and BW of 220 kHz and showed a very uniform performance over the entire array.



# Kurzfassung

Die *gedruckte Elektronik* eröffnet durch innovative technische und neue gestalterische Aspekte ein enormes Potenzial für viele Branchen, wie beispielsweise der Automobil-, Verpackungs- und Display-Industrie. Eigenschaften, wie Flexibilität, Transparenz, ein sehr geringes Gewicht, oder neuartige Design-Konzepte bei elektronischen Bauteilen und Systemen stehen hierbei an vorderster Stelle. Das Forschungsgebiet der gedruckten Elektronik erstreckt sich hierbei von der Materialsynthese und Herstellung geeigneter funktionaler Tinten, über die Prozesstechnik, bis hin zur Bauteil-Physik und Schaltungsdesign und bildet hierbei eine Wertschöpfungskette von der Chemie, über den Maschinenbau, bis hin zur Elektrotechnik.

Die vorliegende Arbeit beschäftigt sich mit dem Herstellen elektronischer Komponenten, Bauteile und Systeme mit dem Aerosol Jet Druckverfahren. Bei diesem Druckverfahren handelt es sich um ein hoch-präzises, kontaktloses und digitales Verfahren, welches speziell für den Einsatz in der gedruckten Elektronik entwickelt wurde. Es lassen sich damit eine große Vielfalt an leitenden, halbleitenden und isolierenden Materialien für die Herstellung elektronischer Bauteile, wie beispielsweise Metalle, Polymere, kleine Moleküle und Metalloxide mit Strukturauflösungen von wenigen Mikrometern Linienbreite drucken. Der erste Teil dieser Arbeit beschäftigt sich mit dem Drucken von hybriden Elektrodensystemen für den Einsatz als transparente Frontelektroden in organische Solarzellen. Die hybriden Elektrodensysteme bestehend aus einem flächigen leitfähigen Polymer (PEDOT:PSS) und gedruckten Gitterstrukturen aus Silber wurden dabei optisch, elektrisch und mechanisch untersucht, als auch zusätzlich durch Bauteil-Simulationen validiert und optimiert. Der zweite Teil der Arbeit befasst sich mit der Herstellung von Multischichtsystemen in Form von organischen Fotodioden. Im Fokus standen dabei das Drucken homogener funktionaler Schichten, unter Berücksichtigung verschiedener Prozess-Parameter, wie Druckgeschwindigkeit, Materialzufuhr und Variation der Druckdurchgänge zur Einstellung der Aktivschichtdicke und Schichthomogenität. Es konnten so vollständig Aerosol gedruckten semi-transparenten Fotodioden mit spektralen Responsivitäten (SR) von  $0.2 \text{ A/W}$ , spezifischen Detektivitäten von  $2 \cdot 10^{11} \text{ cm Hz}^{0.5}/\text{W}$ , und Bandbreiten (BW) von  $300 \text{ kHz}$  hergestellt werden. Im letzten Teil dieser Arbeit wird ein Verfahren zur reproduzierbaren Strukturierung von flüssig-prozessierten Metallkontakten im Mikrometer-Bereich vorgestellt, welches auf Aerosol gedruckten Entnetzungsstrukturen basiert. Es wurden hierbei die Zusammenhänge zwischen Oberflächenspannungen und -energien von verschiedenen Substraten und Fluiden, sowie Einschränkungen des maximalen Fluidvolumens in Bezug auf die Strukturweiten untersucht. Das Verfahren wurde anschließend für die Herstellung von Source-Drain-Kontakten in organischen Ringoszillatoren mit Oszillator-Frequenzen von bis zu  $400 \text{ Hz}$ , als auch für die Herstellung von passiv angesteuerten Fotodioden-Matrizen mit  $256 \text{ Pixeln}$  mit spektralen Responsivitäten

von  $0.3 \text{ A/W}$ , spezifischen Detektivitäten von  $8 \cdot 10^{11} \text{ cm Hz}^{0.5}/\text{W}$  und Bandbreiten bis zu  $220 \text{ kHz}$ , verwendet.

# Publications

## Peer-Reviewed Publications

1. Y. Zakharko, M. Held, A. Graf, T. Rödlmeier, **R. Eckstein**, G. Hernandez-Sosa, B. Hähnlein, J. Pezoldt, and J. Zaumseil, 2017, submitted
2. N. Bolse, **R. Eckstein**, M. Schend, A. Habermehl, C. Eschenbaum, G. Hernandez-Sosa, and U. Lemmer, 2017, submitted
3. Y. Zakharko, M. Held, A. Graf, T. Rödlmeier, **R. Eckstein**, G. Hernandez-Sosa, B. Hähnlein, J. Pezoldt, J. Zaumseil, *ACS Photonics* 2016, 3, 2225, DOI: 10.1021/ac-photonics.6b00491
4. S. Stolz, M. Petzoldt, N. Kotadiya, T. Rödlmeier, **R. Eckstein**, J. Freudenberg, U. H. F. Bunz, U. Lemmer, E. Mankel, M. Hamburger, *J. Mater. Chem. C* 2016, 4, 11150, DOI: 10.1039/C6TC04417D
5. **R. Eckstein**, M. Alt, T. Rödlmeier, P. Scharfer, U. Lemmer, G. Hernandez-Sosa, *Adv. Mater.* 2016, 28, 7708, DOI: 10.1002/adma.201602082
6. **R. Eckstein**, T. Rödlmeier, T. Glaser, S. Valouch, R. Mauer, U. Lemmer, G. Hernandez-Sosa, *Adv. Electron. Mater.* 2015, 1, 1500101, DOI: 10.1002/aelm.201500101
7. J. Maibach, T. Adermann, T. Glaser, **R. Eckstein**, E. Mankel, A. Pucci, K. Müllen, U. Lemmer, M. Hamburger, T. Mayer, W. Jaegermann, *J. Mater. Chem. C* 2014, 2, 7934, DOI: 10.1039/C4TC00769G
8. G. Hernandez-Sosa, S. Tekoglu, S. Stolz, **R. Eckstein**, C. Teusch, J. Trapp, U. Lemmer, M. Hamburger, N. Mechau, *Adv. Mater.* 2014, 26, 3235, DOI: 10.1002/adma.201305541
9. **R. Eckstein**, G. Hernandez-Sosa, U. Lemmer, N. Mechau, *Org. Electron.* 2014, 15, 2135, DOI: 10.1016/j.orgel.2014.05.031
10. M. Reinhard, **R. Eckstein**, P. Sonntag, L. Burkert, B. Dimmler, U. Lemmer, A. Colsmann, *Conf. Rec. IEEE Photovolt. Spec. Conf.* 2013, 3226, DOI: 10.1109/PVSC.2013.6745139
11. G. Hernandez-Sosa, **R. Eckstein**, S. Tekoglu, T. Becker, F. Mathies, U. Lemmer, N. Mechau, *Org. Electron.* 2013, 14, 2223, DOI: 10.1016/j.orgel.2013.05.040
12. M. Reinhard, P. Sonntag, **R. Eckstein**, L. Bürkert, A. Bauer, B. Dimmler, U. Lemmer, A. Colsmann, *Appl. Phys. Lett.* 2013, 103, DOI: 10.1063/1.4824017.

13. M. Reinhard, **R. Eckstein**, A. Slobodskyy, U. Lemmer, A. Colsmann, *Org. Electron.* 2013, 14, 273, DOI: 10.1016/j.orgel.2012.10.039

### **Conference Presentations**

- Society of Photographic Instrumentation Engineers (SPIE) Optics + Photonics, San Diego, USA, 2016 (oral)
- Materials Research Society (MRS) Meeting, Fall, Boston, USA, 2015 (oral)
- Society of Photographic Instrumentation Engineers (SPIE) Optics + Photonics, San Diego, USA, 2015 (oral)
- Karlsruhe Days of Optics and Photonics (KDOP), KSOP, Karlsruhe, Germany, 2015 (poster)
- e-Print, Basel, Swiss, 2014 (poster)
- Karlsruhe Days of Optics and Photonics (KDOP), KSOP, Karlsruhe, Germany, 2013 (poster)
- Materials Research Society (MRS) Meeting, Spring, San Francisco, USA, 2013 (poster)
- International Optomec User Meeting, Liège, Belgium, 2012 (oral)

# Contents

<b>Contents</b>	<b>IX</b>
<b>1. Introduction</b>	<b>1</b>
1.1. Motivation . . . . .	1
1.2. Scope of this Work . . . . .	3
1.3. Structure of the Thesis . . . . .	3
<b>2. Fundamentals of Organic Semiconductors</b>	<b>5</b>
2.1. Organic Semiconductors . . . . .	6
2.1.1. The Hybridization of Carbon Atoms . . . . .	7
2.1.2. Excitons in Organic Matter . . . . .	8
2.1.3. From Intra- to Inter-Molecular Charge Carrier Transport . . . . .	8
2.2. Organic Optoelectronic Devices . . . . .	9
2.2.1. Ultrafast Charge Transfer Via Bulk-Heterojunctions (BHJ) . . . . .	9
2.2.2. Dominating Recombination Processes in Bulk-Heterojunctions . . . . .	11
2.3. Device Physics . . . . .	11
2.3.1. Equivalent Circuit of Organic Optoelectronic Devices . . . . .	11
2.3.2. Key Parameter of Solar Cells . . . . .	13
2.3.3. Characteristics of Photodiodes . . . . .	15

## CONTENTS

<b>3. Printing and Coating Techniques</b>	<b>21</b>
3.1. Aerosol Jet Printing . . . . .	21
3.1.1. Working Principle . . . . .	22
3.1.2. Printing Parameters . . . . .	23
3.2. Inkjet Printing . . . . .	26
3.3. Spin Coating . . . . .	27
3.4. Device Encapsulation . . . . .	27
<b>4. Characterization Methods</b>	<b>33</b>
4.1. Fluid and Substrate Characterization . . . . .	33
4.1.1. Contact Angles, Surface Energies and Surface Tensions . . . . .	33
4.1.2. Determination of Polar and Dispersive Surface Tensions . . . . .	34
4.2. Thin-Film Characterization . . . . .	35
4.2.1. Optical Characterization . . . . .	35
4.2.2. Surface Topography . . . . .	35
4.2.3. Electrical Conductivity Measurements . . . . .	36
4.3. Device Characterization . . . . .	37
4.3.1. Current Density - Voltage Measurements . . . . .	37
4.3.2. Light Beam Induced Current Measurements (LBIC) . . . . .	37
4.3.3. Steady State and Dynamic Photodiode Characterization . . . . .	38
4.4. Modeling of Hybrid Electrodes with COMSOL . . . . .	40
4.4.1. Finite Element Method . . . . .	40

<b>5. AJ Printed Grid Electrodes for Organic Solar Cells</b>	<b>43</b>
5.1. Metal-Organic Decomposition Ink . . . . .	43
5.1.1. Specific Conductivity . . . . .	44
5.1.2. Ink Formulation for Aerosol Jet Printing . . . . .	46
5.1.3. Summary . . . . .	49
5.2. Aerosol Jet Printed Metal Grids . . . . .	49
5.2.1. Summary . . . . .	52
5.3. Mechanical Stability . . . . .	52
5.3.1. Bending Fatigue in Hybrid Electrodes . . . . .	53
5.3.2. Strain Fatigue in Hybrid Electrodes . . . . .	54
5.3.3. Summary . . . . .	55
5.4. Solar Cells Comprising AJ Printed Hybrid Transparent Conductors . . . . .	56
5.4.1. Device Preparation . . . . .	56
5.4.2. Device Characterization and Discussion . . . . .	57
5.4.3. Summary . . . . .	60
5.5. Electrode and Device Modeling . . . . .	61
5.5.1. Physical Model . . . . .	61
5.5.2. Grid Geometries . . . . .	63
5.5.3. Boundary Conditions . . . . .	65
5.5.4. Effective Sheet Resistance and PEDOT:PSS Conductivity . . . . .	67
5.5.5. Current Densities . . . . .	69
5.5.6. Summary . . . . .	69

<b>6. Fully AJ Printed Organic Photodiodes</b>	<b>71</b>
6.1. Optimization of AJ Printing Parameters for Smooth Functional Layers . . .	71
6.1.1. Impact of Printing Speed and Multi-Pass Printing . . . . .	72
6.1.2. Impact of Material Flow Rate . . . . .	73
6.1.3. Impact of Ultrasonic Atomization on Functional Polymeric Matter	74
6.1.4. Summary . . . . .	75
6.2. ITO comprising Photodetectors . . . . .	75
6.2.1. Device Preparation . . . . .	75
6.2.2. Characterization of Semi-Transparent ITO comprising OPDs . . .	77
6.2.3. Summary . . . . .	80
6.3. Fully Printed OPDs . . . . .	81
6.3.1. Device Preparation . . . . .	81
6.3.2. Characterization of ITO-free OPDs . . . . .	82
6.3.3. Summary . . . . .	86
<b>7. Digitally Printed Dewetting Patterns for Self-Organizing Microelec- tronics</b>	<b>87</b>
7.1. The Dewetting Process . . . . .	87
7.2. Wetting Morphologies . . . . .	89
7.2.1. Contact Angles and Work of Adhesion . . . . .	89
7.2.2. Correlation between Ink Volume and Normalized <i>Wetting Area</i> . .	90
7.2.3. Interface Energetic Dependencies . . . . .	92
7.3. Application Examples . . . . .	96
7.3.1. Fully Printed Organic Photodetectors . . . . .	96
7.3.2. Fully Printed 256 Pixel Photodetector-Array . . . . .	99
7.3.3. Digitally Patterned Source-Drain Electrodes for Organic Field- Effect Transistors and Circuits . . . . .	104
7.3.4. Summary . . . . .	107
<b>8. Summary and Outlook</b>	<b>109</b>

<b>Appendix</b>	<b>113</b>
<b>A. Appendix: Fully AJ Printed Organic Photodiodes</b>	<b>115</b>
A.1. AJ Printed Active Material: Influence of Tube Temperature on Film Homogeneity . . . . .	115
A.2. Linearity of ITO-free OPDs . . . . .	115
<b>B. Appendix: Digitally Printed Dewetting Patterns for Self-Organizing Microelectronics</b>	<b>117</b>
B.1. Surface Topography of AJ-Printed SU-8 . . . . .	117
B.2. Substrate Variation for Self-Organized Ag Patterns . . . . .	117
B.3. Unipolar Ring Oscillators . . . . .	118
B.3.1. SPICE Model . . . . .	118
<b>List of Abbreviations</b>	<b>121</b>
<b>List of Figures</b>	<b>123</b>
<b>List of Tables</b>	<b>129</b>
<b>Bibliography</b>	<b>131</b>
<b>Acknowledgments</b>	<b>143</b>



# 1. Introduction

## 1.1. Motivation

I want to start with a very convenient excerpt from a 25th anniversary review article about bulk-heterojunction solar cells by Alan J. Heeger in 2013, a pioneer in this field.[1]

"The initial discovery of ultrafast electron transfer occurred in late 1992. It was a discovery based purely on curiosity. [...] During a random discussion in my office, we speculated on what would happen if we mixed these two novel materials. We made several speculative guesses, but decided to do some initial experiments even though the idea was not yet well formed in our minds. We obtained the now famous soluble fullerene derivative, PCBM, from Fred Wudl and the story began to unfold."[1]

Once the ultrafast electron transfer based on bulk-heterojunctions (BHJ) was discovered in 1993 and electron transfer times below 100 *fs* were reached for the first time, the (r)evolution of solution-processable organic solar cells began. [2] *Yu et al.* demonstrated the first organic BHJ based solar cell, comprising MEH-PPV:PCBM sandwiched between ITO and calcium electrodes, in 1995.[3] Here, they first observed a substantial improvement of the device efficiency compared to pure MEH-PPV cells by the introduction of the spontaneous phase-separation, resulting in a bicontinuous donor-acceptor (D-A) network, where the increased interface-area combined with the relatively small domain sizes of the donor and acceptor regions was determined as the underlying cause. The visualization of the phase separation in the active layer was shown by transmission electron microscopy (TEM), clearly validated the previously stated hypothesis.[4] The continuation of solution-processable layers towards multi-layer devices culminated in the fabrication of tandem solar cells comprising six subsequently deposited layers between the ITO and aluminum electrodes.[5] This was possible by following certain fundamental rules, namely the orthogonality of subsequently processed solvents need to be guaranteed to prevent the dissolution of underlying films. Another approach is to make the previously deposited film insoluble by cross-linking or cleaving of solubility responsible side-chains. In the meanwhile, apart from the steady improvement of material properties by the excellent work of chemists, the advances of process engineering, especially towards the printing of functional materials, developed a parallel but interdependent scientific route. Printed electronics evolved into a fusion of microelectronics, chemistry and printing / process engineering, comprising the formulation of functional inks, controlling the thermodynamic effects during and after the printing, and drying mechanisms.

Conductive materials are equally important to the organic semi-conducting compounds

## 1. Introduction

and are necessary for wiring, electrodes or contacts. Nowadays, a large diversity of printable metals in the form of metal-organic decomposition (MOD) inks, nanoparticle, or nanowire dispersions are available, including precious metals like gold, silver, platinum, or the cost-efficient metal copper.[6–8] Beyond that, carbon-based compounds, such as graphene or carbon nanotubes (CNTs) found applications in transparent electrode systems and show outstanding performances.[9–11] Immense progress has been achieved in the past 5 to 10 years, where the sinter conditions (e.g. temperature), of especially silver inks, could be decreased from initially 200 to 300° C to almost room temperature.[12] Also, highly conductive and transparent polymer electrodes have been discovered and studied extensively and depict the only solution-processable transparent and homogeneously conductive electrode material.[13–15] Since then, vast quantities of conductive and semi-conducting materials and inks have been developed to further push the realization of fully printed electronic devices on cost-efficient and flexible substrates, such as PET or paper.[16–18] Novel sinter techniques, including photonic, low pressure argon plasma, microwave, or DC current sintering additionally enhance the degrees of freedom in solution-processable metal inks (Au, Cu, Pt, etc.) on low temperature substrates.[8] However, a crucial, but maybe initially almost subordinated *printing* step turned out to be by far more complex than suggested. Nearly every printing technique and source material requires a tailored formulation, where the boiling point, the visco-elastic properties, as well as thermodynamic effects during printing and drying, have to be considered and in many cases adjusted.[19? , 20]

Recent development and research on printed electronics has led to a vast amount of physical devices, covering temperature, pressure, strain, light and mechanical sensors, and chemical devices, covering biosensors, pH, ions, gas or vapor sensors. Furthermore, the trillion sensors movement was founded to accelerate and coordinate the development to achieve the upcoming sensor demand. The driving fields of interest hereto span, for instance, the Internet of Things, wearables for daily life applications such as personal health care, or industry relevant applications such as local energy harvesting, supervision of grocery transportation, or telecommunications. In many cases, the unique properties of printed electronics, such as flexibility, conformability or transparency can generate new markets, since conventional inorganic devices usually lack these properties. For example, organic solar cells could be fabricated comprising a certain semi-transparency and conformability, which could be beneficial for an implementation into building facades and windows. In addition to that, the use of environmentally friendly solvents, biocompatible materials, and a low energy consumption during the fabrication process and therefore lower fabrication costs could promote the demand for printed devices. These properties and features are reflected in the market forecast for printed sensors (capacitive, piezoresistive, piezoelectric, photodetectors, digital x-ray, temperature, bio and gas) from IDTechEx, which expects a market volume of around > \$ 8 billion by 2025.

By now, fully solution processed solar cells have been successfully demonstrated by *Angmo et al.* at the end of 2012, utilizing roll-to-roll and printing techniques.[21] The first entirely printed photodiodes, however, have been recently published in 2015.[22, 23] Interestingly, both publications were based on only spray coating techniques, which shows the potential of this deposition method and massively motivates the research and development of printed electronics exploiting this underestimated technology compared to other digital deposition techniques, such as inkjet printing.

## 1.2. Scope of this Work

This work relates to the advancement and applicability of the aerosol jet (AJ) printing technique for fabricating organic electronic devices and systems. It should contribute to the identification of possibilities and benefits of using this printing technique for novel applications. The reason for that is, that the AJ printing technique entails unique operational capabilities, such as very small feature sizes ( $\leq 10 \mu\text{m}$ ) and a high substrate clearance ( $\geq 5 \text{ mm}$ ) allowing for a contact-free local deposition of a vast variety of functional materials and inks.

In this work a strong focus was set on the fabrication of optoelectronic devices, such as organic solar cells and organic photodiodes, but also integrated transistor circuits were realized. At first glance, the fabrication, optimization and application of printed metal grids as top electrodes for organic solar cells were investigated both experimentally and by device simulations. Furthermore, the applicability of AJ printing, involving the optimization of functional materials and printing process parameters, was investigated to bring forth the fabrication of fully digitally printed organic photodiodes. Moreover, the conception and development of a dewetting process for fabricating micro-structures by exploiting the self-organization of functional inks caused by digitally printed epoxy resin was presented. The printed patterns enabled an accurate and reproducible fabrication of structures and devices in the micrometer regime, which satisfies remaining issues regarding the uniformity and reproducibility of printed devices in a larger device quantity, and at the same time the down-scaling of the device footprint for higher integrated and more complex electronic circuits and arrays. Its successful application was therefore demonstrated in fully printed photodiode arrays and integrated transistor circuits comprising digitally printed source-drain layers showing state-of-the-art performances.

## 1.3. Structure of the Thesis

This thesis is organized into 8 chapters, beginning with the motivation of this work in **chapter 1** and a brief background of organic electronic's history. The **2nd chapter** introduces fundamentals of organic materials and working principles in opto-electronics. **Chapter 3** elucidates the fabrication processes and fundamental application analysis of Aerosol and Inkjet printing. The following, **chapter 4**, describes the primarily used characterization methods and also introduces the physical finite element model (FEM) used for the grid and device simulations from **chapter 5**. Here, the experimental and simulative work is presented on digitally printed metal grids as transparent top electrodes in organic solar cells. **Chapter 6** deals with the fabrication and characterization of entirely AJ printed photodetectors, while **chapter 7** then focuses on a novel digital structuring process for functional materials, such as silver electrodes, by exploiting established dewetting mechanisms to fabricate highly accurate and reproducible devices. **Chapter 8** will summarize the results and give a brief outlook, consisting of main issues to be faced and a personal opinion for the future of printed electronics.



## 2. Fundamentals of Organic Semiconductors

*This chapter describes the fundamental framework in physics and chemistry of organic semiconductors (SC) and the prevalent electronic processes relevant for this thesis. Additionally, the device physics and key parameters of organic solar cells and photo diodes are described.*

According to Albert Einstein and Leopold Infeld from 1938, "*But what is light really? Is it a wave or a shower of photons? There seems no likelihood for forming a consistent description of the phenomena of light by a choice of only one of the two languages. It seems as though we must use sometimes the one theory and sometimes the other, while at times we may use either. We are faced with a new kind of difficulty. We have two contradictory pictures of reality; separately neither of them fully explains the phenomena of light, but together they do.*" [24]

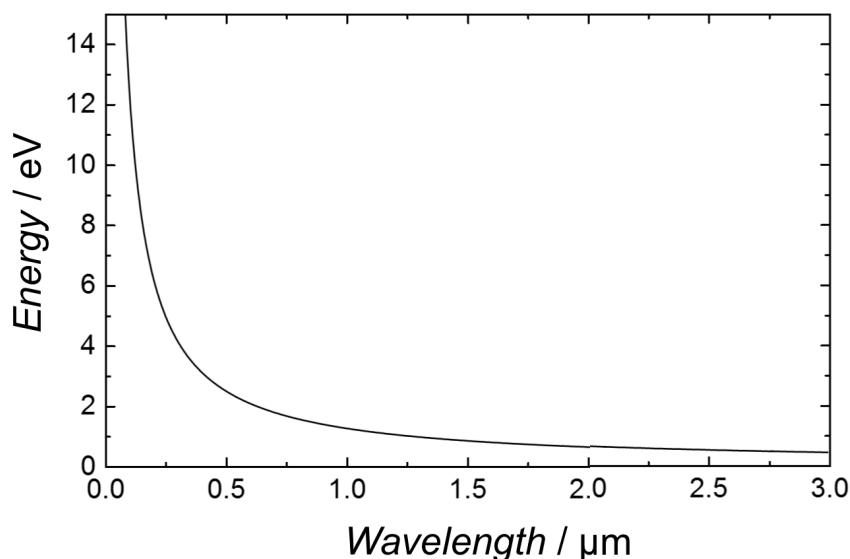


Figure 2.1.: The photon energy as a function of wavelength.

A. Einstein already speculated over 100 years ago that photons combine both properties of particles and waves, the so-called *wave-particle duality*, where the energy of electromagnetic waves (*photons* or *quanta of light energy*) are directly related to the frequency  $f$  via the Planck-Einstein relation:[25]

## 2. Fundamentals of Organic Semiconductors

$$E_{ph} = hf = \frac{hc}{\lambda} [eV] \quad (2.1)$$

where  $h$  is the Planck constant; and  $c$  the speed of light. The energy as a function of wavelength is illustrated in **Figure 2.1**.

The effect of harvesting the photon energy by a conversion into electrical energy, the so-called photovoltaic effect, first observed by Alexandre Edmond Becquerel in 1839[26], is almost 200 years later still of exceptional interest and depicts the basis of the far-reaching investigations of photovoltaic materials and application. Not only classic inorganic materials, such as Si or GaAs, but also organic materials take an important role in the large variety of photosensitive matter.

### 2.1. Organic Semiconductors

One thing all organic materials have in common is that they are based on carbon atoms. Albeit, diamond, which also consists of an arrangement of carbon atoms, appertains to inorganics. All the way back to the polymeric organic materials, which usually owns insulating properties, Kallmann and Pope extended this level of awareness by first discovering semiconducting properties in anthracene crystals in 1960. From that on, the machinery of organic photovoltaics was set in motion.[27, 28] Organic semiconductors (SC) in contradiction to its traditionally crystalline inorganic counter part show utterly different optical, mechanical and electrical qualities. Especially, organic semiconducting dyes, also called absorber materials, excel very strong absorptions even in very thin films below 100 nm. This property in turn allows for lower charge carrier diffusion lengths compared to inorganic semiconductors.[29] Beyond that, the solution processability of organic materials conditioned by an adequate synthesis and the introduction of relevant side groups to the semi-conducting polymer backbone opens a large prospect in terms of device fabrication. From a mechanical point of view, polymeric matter also vitally distincts from inorganics, where organics are based on prevailing weak intermolecular Van-der-Waals cohesion forces.[30] The very low binding energies from 0,001 to 0,01 eV also cause low dielectric constants around  $\epsilon_r \simeq 3 - 4$ . [31]

#### 2.1.1. The Hybridization of Carbon Atoms

A single carbon atom (C-atom) has four valence electrons in a configuration of  $1s^2 2s^2 2p^2$  in its ground state. For the formations of bonds to adjacent atoms the valence electrons create new orbitals, the so-called hybrid orbitals. The most stable hybridization consists of four tetrahedrally arranged hybrid orbitals, as can be found in diamond, taking us back to the previously mentioned example for inorganic carbon-based materials. Nevertheless, in

organic SCs another arrangement of hybrid orbitals determines the electronic properties. In particular, alternating single and double bonds with an over the molecule delocalized  $\pi$ -electron system is formed by  $sp_2$ -hybridized C-atoms.

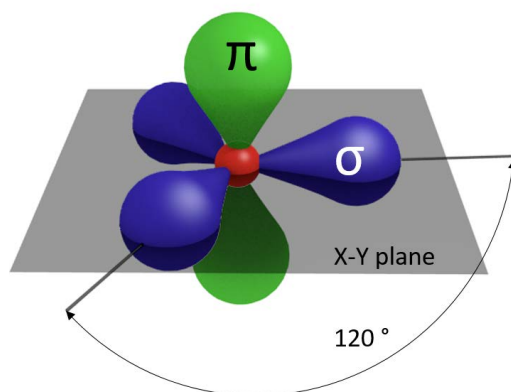


Figure 2.2.: Schematic of  $sp_2$  hybridized C-atom.

This configuration involves three identical  $sp_2$  hybrid orbitals (blue) in the x-y plane with an angular distance of  $120^\circ$ , as presented in Figure 2.2. These  $sp_2$ -orbitals can then covalently bound to other atoms in so-called  $\sigma$ -bonds, which consist of localized electrons, as shown in the example of ethene in **Figure 2.3(a)**. The leftover unhybridized  $2p_z$ -orbitals, perpendicular to the x-y plane, can form weak  $\pi$ -bonds with other  $2p_z$ -orbitals from adjacent  $sp_2$ -hybridized atoms. The overlap of  $2p_z$ -orbitals over the whole molecule leads to a delocalization of the  $\pi$ -electrons and defines its electrical properties.

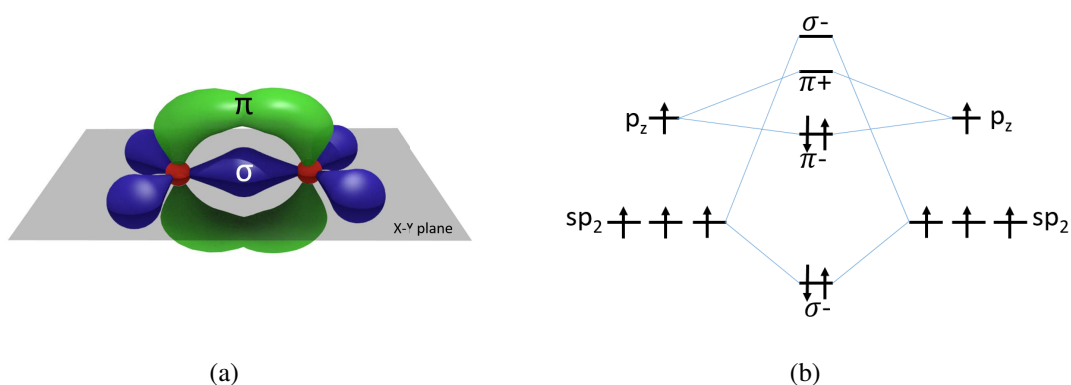


Figure 2.3.: a) Schematic illustration of electronic configuration of an ethene molecule with covalently bound strong  $\sigma$ - and weak  $\pi$  bonds. b) Energy levels of ethene.

The large overlap of the  $sp_2$ -orbitals leads to a strong separation into an unoccupied binding  $\sigma^-$  and an occupied anti-binding  $\sigma^+$  orbital with a very large energy gap, as shown in Figure 2.3(b). The weak overlapping  $p_z$  orbitals, instead, split up in binding  $\pi^-$  and

## 2. Fundamentals of Organic Semiconductors

anti-binding  $\pi^+$  orbitals with a much smaller energy gap than the  $\sigma$  orbitals. Therefore, they define the highest occupied molecular orbital (HOMO) and the lowest unoccupied molecular orbital (LUMO) with typical band gaps of 1.5 to 3 eV.[32]

### 2.1.2. Excitons in Organic Matter

Incident photons with the energy  $h\nu$  can be absorbed in the organic SC and excite an electron into the LUMO of the material forming bound electron-hole-pairs. These electron-hole pairs, named *Frenkel excitons*, are electrically neutral and store potential energy. Excitons are strongly bound by Coulomb interactions (0.2 – 0.5 eV)[33], which on the one hand, is caused by the the low dielectric constant of organic matter. The high Coulombic attraction of an electron ( $e$ ) and hole ( $h$ ) leads to a broader Coulomb potential well than in inorganic SCs. Furthermore, the  $e$ - $h$ -pair binding energy leads to a strong localization of the exciton, which can expand over an entire molecule length. On the other hand, the weak inter-molecular bonds cause that the electron's wave functions are spatially confined.[34] The exciton diffusion length  $L$  in an isotropic organic SC is typically 5 – 10 nm and can be described by the diffusion equation as follows:

$$L = \sqrt{\tau_0 D} \quad (2.2)$$

where  $\tau_0$  is the exciton life time; and  $D$  the diffusion coefficient.[35]

### 2.1.3. From Intra- to Inter-Molecular Charge Carrier Transport

The separation of excitons is possible, when its Coulombic binding energy is overcome. This can be achieved for instance with high electric fields ( $> 10^6 \text{ V cm}^{-1}$ ). The charge carrier transport in organic materials derogates strongly from the well-known band transport in crystalline inorganic SCs. Whereas the intra-molecular electrical conduction is defined by the delocalized  $\pi$ -electrons, an inter-molecular conduction is based on a thermally activated hopping transport of charge carriers between overlapping  $\pi$ -orbitals of adjacent molecules.[30, 32] In comparison to the band model with valence and conduction band in inorganic SCs, the charge transport in organics can be described by a hopping model. It assumes an energetic density of states based on a Gaussian distribution, where the mobility of charge carriers is dependent on the electric field strength and the temperature.[36] Therefore, organic SCs depict much lower charge carrier mobilities ( $\sim 1 \text{ cm}^2 \text{ Vs}^{-1}$ ) than their inorganic counter parts. An exception arises from highly ordered organic single-crystals, where mobilities up to  $40 \text{ cm}^2 \text{ Vs}^{-1}$  have been demonstrated.[37]

## 2.2. Organic Optoelectronic Devices

### 2.2.1. Ultrafast Charge Transfer Via Bulk-Heterojunctions (BHJ)

In section (2.1), we discussed the generation of Frenkel-excitons, their high Coulombic attraction, and by that their short diffusion length of around 10 nm in these disordered materials. The electronic limitations due to the strong exciton binding energies and the low charge carrier mobilities compared to inorganic SCs changed drastically due to the invention of the buckminster fullerene  $C_{60}$ , which bestowed Smalley, Curl, and Kroto the Nobel Prize in chemistry in 1996.[1, 38]

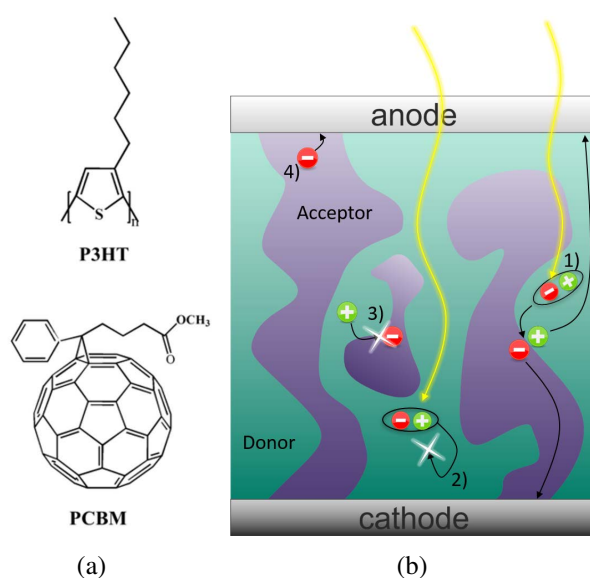


Figure 2.4.: a) Typical representative for a polymer donor with P3HT (Poly(3-hexylthiophene-2,5-diyl)) and an acceptor fullerene with PCBM ([6,6]-Phenyl  $C_{60}$  butyric acid methyl ester). b) Schematic drawing of a bulk-heterojunction solar cell, showing (1) the generation of the exciton and its subsequent charge separation at the donor-acceptor interface, (2) a geminate recombination process, and non-geminate recombination processes with (3) and (4).

With the synthesis of the soluble fullerene derivative, PCBM, as shown in **Figure 2.4(a)**, by Wudl *et al.* the first solution processed organic BHJ solar cell was published by Yu *et al.* in 1995, where a large improvement of the photo current was observed for devices comprising MEH-PPV:PCBM compared to pure MEH-PPV devices.[3] The BHJ consists of a blend of acceptor and donor material, which typically forms in the deposited layer acceptor-rich and donor-rich domains. The interpenetrating phase-separated donor-acceptor network significantly enhances the exciton dissociation by a considerably increased interfacial area in conjunction with domain sizes within the range of the exciton diffusion length. Though, the domain size and phase separation depends on the drying and

## 2. Fundamentals of Organic Semiconductors

annealing conditions of the blend, or through solvent additives.[39–41] **Figure 2.5** shows the band diagram of a BHJ device. In theory, after generation of an exciton followed by a dissociation into free charge carriers at the acceptor-donor interface, the charges drift via inter-molecular hopping processes to the corresponding metal-organic interface, where they can be extracted and contribute to the photo current.

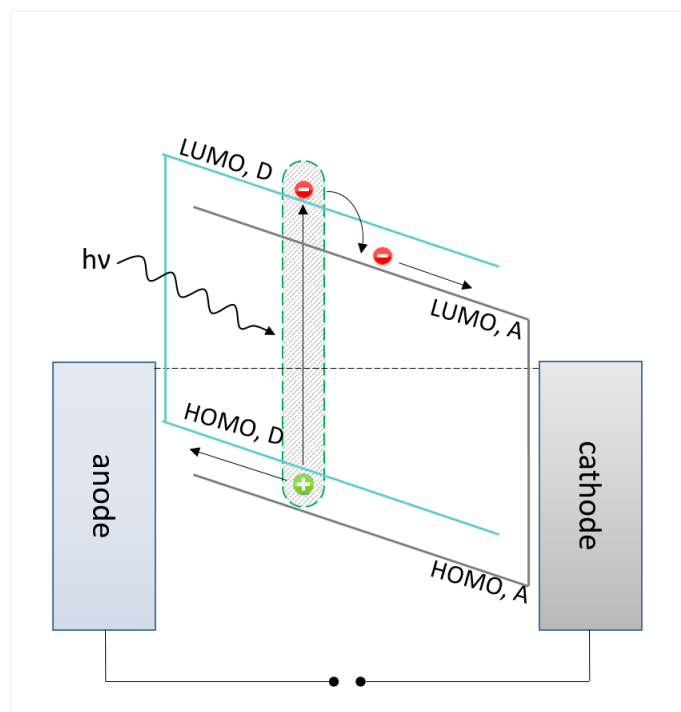


Figure 2.5.: Band diagram of a bulk-heterojunction architecture, where an intermixed donor-acceptor blend provides a highly dispersed network of donor-acceptor interfaces, which allows for an improved charge separation. The absorption of a photon within the donor material excites an electron into the  $LUMO_D$ . The bound exciton then diffuses to a donor-acceptor interface, where the electron is collected by the acceptor  $LUMO_A$ . The separated charge carriers then drift to the corresponding electrodes to be extracted, which leads to a current flow.

### 2.2.2. Dominating Recombination Processes in Bulk-Heterojunctions

Shockley and Queisser postulated a theoretical limit for the efficiency of solar cells back in 1961, the so-called Shockley-Queisser limit, which mainly bases on relaxation processes of excess photon energy to the band edges and on incident photons with energies below the band gap. In their model a perfect solar cell with 100 % absorption and a band gap of  $1.34 \text{ eV}$  under an irradiation of  $1000 \text{ W m}^{-2}$  (AM 1.5 solar spectrum) is predicted to have an efficiency of 33.7 %.[42] However, other processes play a major role in organic SCs and

mainly limit the energy conversion from photonic to electrical energy by recombination of charge carriers. They can be split up in two main contributions:

**Geminate recombination** which arises from diffusion limited motion of Frenkel-excitons, if no donor-acceptor interface is reached within their diffusion length, as shown in (2) in Figure 2.4(b). This involves recombinations either on one molecule or electron-hole pairs located on adjacent molecules. The latter is possible due to the average inter-molecular distances of roughly around  $1\text{ nm}$ , which is less than the Coulomb capture radius  $r_c$  of electrons and holes of around  $20\text{ nm}$ . [36]

**Non-geminate recombination** instead base on electrons and holes from free charge carriers, where in case of *indirect non-geminate* recombination traps or defects due to impurities within the polymeric matter take a significant importance. Figure 2.4(b) illustrates cases of *direct non-geminate* recombination, where (3) an electron from the  $LUMO_A$  recombines with a hole from  $HOMO_D$  and (4) a charge recombines at the opposite electrode. Non-geminate recombination processes increase with light-intensity, what means that the probability of a bimolecular recombination increases with the amount of free charge carriers.

## 2.3. Device Physics

This section will focus on the fundamental physics of solar cells and photodiodes, including the commonalities between solar cells and photodiodes, such as equivalent circuit, the mathematical description of the current-voltage characteristic, as well as the differences between both device types, which accrue from their fundamentally distinct fields of application.

### 2.3.1. Equivalent Circuit of Organic Optoelectronic Devices

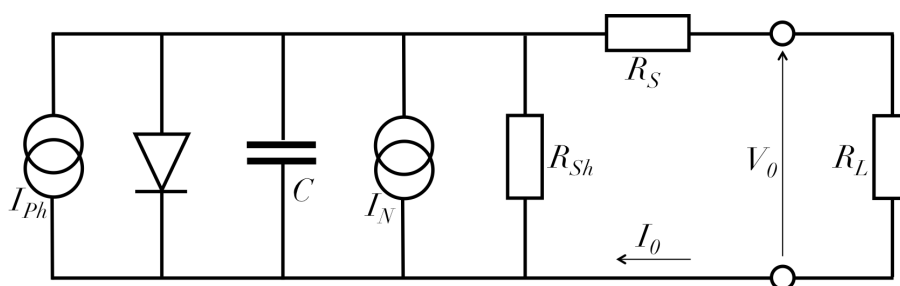


Figure 2.6.: One-diode equivalent circuit for solar cells and photodiodes. [43]

**Figure 2.6** shows a one-diode equivalent circuit, which describes the organic solar cell and photodiode electrically. The diode represents the recombination in the quasi-neutral regions ( $\propto e^{qV/kT}$ ). The photon induced current is conventionalized as a current source parallel to the diode, which causes the typical rectifying diode shape. The noise sources,

## 2. Fundamentals of Organic Semiconductors

such as shot noise, thermal noise and flicker noise are summarized in the current source  $I_N$ .  $R_{Sh}$  gives description about the parallel resistance through the active layer and accounts for leakage currents, or shunts through the semi-conducting matter.  $R_S$  accounts for losses arising from electrode resistances, supply lines and contact resistances. Internal parasitic loss effects can be therefore ascribed in a certain extent to those two characteristic resistances.  $C$  describes the plate capacitor, which is formed between the two electrodes and is of crucial relevance for the speed of organic photodiodes. Neglecting the noise current sources  $I_N$  the implicit equation 2.3 for the photo current over a certain voltage range is derived from Kirchhoff's second law, as followed:

$$I = I_0 \underbrace{\left[ \exp\left(\frac{V + IR_S}{nV_T}\right) - 1 \right]}_{\text{dark current}} - \underbrace{\frac{V + IR_S}{R_{Sh}}}_{\text{shunt resistance}} - \underbrace{I_{ph}}_{\text{photo current}} \quad [A] \quad (2.3)$$

where  $I_0$  is the reverse saturation current of the diode;  $n$  is the ideality factor corresponding to the diode's deviation regarding the Shockley diffusion theory and adjusts the influence of the different recombination processes;  $V_T$  corresponds to the thermal energy of  $0.025 \text{ eV}$  at room temperature, as presented in equation 2.4:

$$V_T = \frac{k_b T}{q} [V] \quad (2.4)$$

where  $q$  depicts the electronic charge;  $k_b$  is the Boltzmann constant; and  $T$  the temperature of the device.

The shunt resistance can be determined from the inverse slope of the I-V characteristic at the origin, as followed:

$$R_{Sh} = \frac{V}{I} [\Omega] \quad (2.5)$$

To quantify the resulting series resistance  $R_s$ , the following Equation 2.6 was utilized:[44]

$$\frac{dV}{dI} = \frac{\frac{nk_b T}{q}}{I_{SC} + I - \frac{V}{R_{sh}}} + R_s \quad (2.6)$$

where  $n$  is the slope of the function; and  $R_s$  can be read out from the intercept with the y-axis.

The capacitance  $C$ , which is present in almost all OSC and OPD architectures, due to the fact that they form a classical plate capacitor can be described by the following equation:

$$C = \frac{\varepsilon_r \varepsilon_0 A}{d} [F] \quad (2.7)$$

where  $\epsilon_r$  is the relative static permittivity;  $\epsilon_0$  accounts for the vacuum permittivity ( $8.854 \cdot 10^{-12} \text{ F m}^{-1}$ );  $A$  and  $d$  define the active area and the distance between the electrodes, respectively.

### 2.3.2. Key Parameter of Solar Cells

The differences in organic solar cells and photodiodes basically only appear in their application relevant key parameters and thus in the way they are characterized. Organic solar cells, apriori, are energy harvesting devices. For that, the *photon-to-electrical* power conversion is foregrounded and the principal aim is to achieve a high output power at a given incident optical power  $P_{opt}$ .

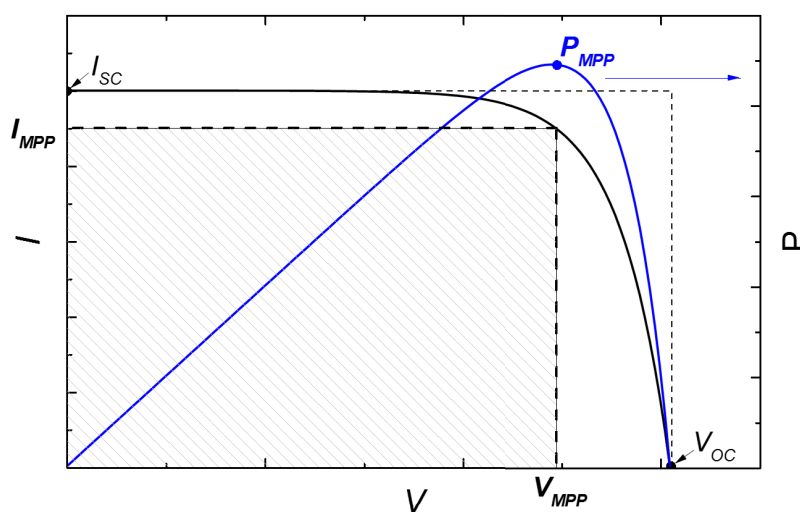


Figure 2.7.: Current-voltage ( $I$ - $V$ ) and power-voltage ( $P$ - $V$ ) characteristic of a solar cell. The hatched area accentuates the maximum extractable electrical power out of the cell.

**Figure 2.7** displays a typical  $I$ - $V$  characteristic and the corresponding power over voltage plot ( $P$ - $V$ ) of a solar cells.  $I_{SC}$  presents the generated photo current for short-cuttet electrodes and refers only to photons, which are absorbed within the diffusion length of the excitons.[29] .  $V_{OC}$  expresses the open circuit voltage and ideally ensues from the difference of  $LUMO_A$  and  $HOMO_D$  of the organic SC, as well as the Schottky-barriers at the metal-organic interfaces. The energy level alignment of the anode and cathode work function is therefore of great importance for the power conversion efficiency (PCE,  $\eta$ ). The PCE is defined by the ratio of generated electrical power  $P_{el}$  to incident optical power  $P_{opt}$ , as presented in Equation 2.8:

$$\eta = \frac{P_{el}}{P_{opt}} = \frac{I_{MPP}V_{MPP}}{P_{opt}} = FF \frac{I_{SC}V_{OC}}{P_{opt}} \quad (2.8)$$

## 2. Fundamentals of Organic Semiconductors

where  $I_{MPP}$  is the current in A and  $V_{MPP}$  the voltage at the maximum extractable power (maximum power point, MPP).  $P_{MPP}$  is also accentuated as the hatched area in Figure 2.7, since the power can be expressed as the product of the current and the voltage; furthermore, the fill factor (FF) relates the hatched area ( $P_{MPP}$ ) to the area under  $I_{SC} \cdot V_{OC}$  and serves as a quality factor for the diode shape.

### 2.3.3. Characteristics of Photodiodes

Photodiodes (PD) rather take over the task of detecting optical signals than harvesting energy from incident light. Nevertheless, the working principle of photon to electrical energy conversion is analogous to that of solar cells.

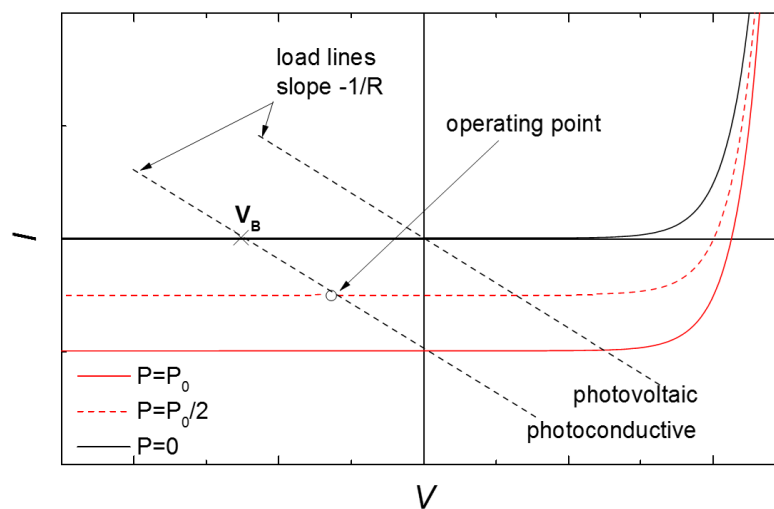


Figure 2.8.:  $I - V$  characteristic of a OPD illuminated with  $P_0$ , half the energy  $P_0/2$ , and in dark.

### Operation Modes

PDs are either operated in the photoconductive or photovoltaic mode, which is defined by a negatively or positively applied bias voltage and the sign of the current:

- **Photoconductive mode:** In this mode the PD is driven in reverse bias. The photo current is negative, as shown in **Figure 2.8** and follows the load line, as indicated for a specific load resistance. Additionally, since the charges are veritably pulled to the corresponding electrodes by the external electric field, an increase in the external quantum efficiency arises. Adversely, the dark current increases with higher reverse bias that entails worse detection limits. The advantage of this mode is an increase in detection speed with an increase in reverse bias.

- **Photovoltaic mode:** For positive bias and negative currents the diode is operated in the photovoltaic mode. This mode is comparable to the point of operation prevalent in solar cells, where power from incident photons can be harvested. A load resistance higher than the diode resistance ( $R_L \gg R_D$ ) causes a voltage across the diode depending on the illumination intensity. For  $R_L \ll R_D$  the leads to a linear increase in the photocurrent as a function of the incident illumination level, which is exemplarily shown in the load line in Fig. 2.8. As a consequence, the operating point can be set to the maximum power point by adjusting the load resistance according to Ohm's law. This operation mode is also prevalent in directly amplified photodiodes without external bias, where the diode is connected between the negative and positive amplifier inputs.

### Steady State Characteristics

As mentioned above, solar cells can be briefly characterized by  $J - V$  characteristics, where  $J$  is the current density in  $A\ cm^{-2}$ , and the power conversion efficiency. But how about the detection of optical signals? When it comes to sensors, one can ascertain quite quickly, that on the one hand the sensitivity is legitimately of high importance. Depending on the application the absorption spectrum is of great interest, which involves a specific spectral response of the device.

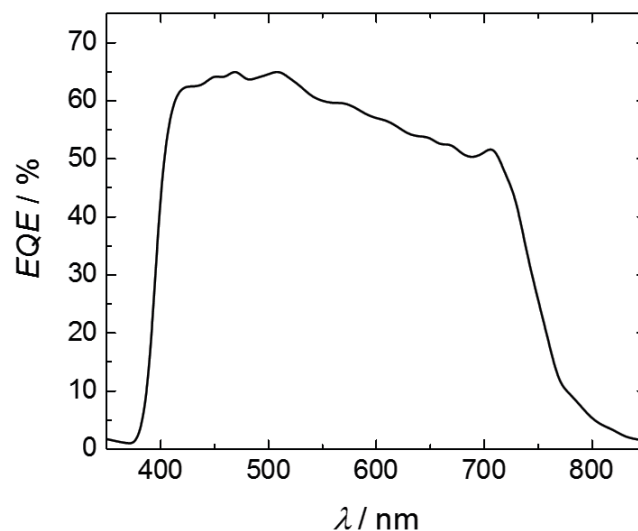


Figure 2.9.: External quantum efficiency (EQE) plot of a polymer:fullerene BHJ device.

**Quantum Efficiency** The quantum efficiency, as shown in **Figure 2.9**, accounts for the ratio of successfully converted incident photons to electrons. It depicts a characterization method widely used for PDs and solar cells, since it allows for wavelength resolved steady state analysis of the device's sensitivity. It has to be distinguished between the

## 2. Fundamentals of Organic Semiconductors

internal (IQE) and external (EQE) quantum efficiency. While the IQE is the ratio between the quantity of collected charge carriers and the quantity of absorbed photons, the EQE is the ratio between the quantity of collected charge carriers and the quantity of incident photons, as shown in Equation 2.9:

$$IQE(\lambda) = \frac{EQE(\lambda)}{(1 - R_\lambda - T_\lambda)} \quad (2.9)$$

The EQE is a function of the measured photo current  $J_{Ph}$  at a known incident optical power  $P_I$  factorized by the photon energy  $hc/\lambda$  and the electron charge  $q$ . The photo current already considers all contributing optical losses (reflectance, transmittance, coupling losses) and electrical losses (recombination processes), as described in section 2.2.2 on page 11, and can be expressed as followed:

$$EQE(\lambda) = \frac{I_{ph} hc}{P_I \lambda q} \quad (2.10)$$

At short circuit conditions the EQE cannot exceed 100%. Nevertheless, in case of a sufficiently high reverse bias voltage the carrier lifetime can exceed the transit time across the device. [45–47].

**Spectral Response** The spectral response  $SR(\lambda)$  describes the ratio of photo current  $I_{ph}(\lambda)$  to incident optical power  $P_I(\lambda)$  (equation 2.11), as shown in **Figure 2.10**. It is the direct relation between the extracted current and the incident optical power measured over the wavelength range of interest. Furthermore,  $SR(\lambda)$  correlates to the EQE, as expressed in Eq. 2.11.

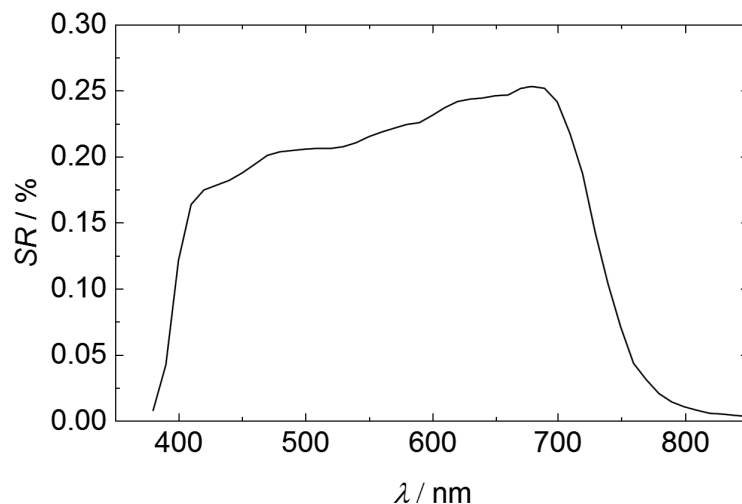


Figure 2.10.: Spectral responsivity ( $SR$ ) plot of a polymer:fullerene BHJ device.

$$SR(\lambda) = \frac{I_{ph}(\lambda)}{P_I(\lambda)} = EQE(\lambda) \frac{q\lambda}{hc} \quad (2.11)$$

## Detector Noise

Noise is and will always be present in photodetectors. The main sources of noise have been described by Rice et al. in 1944 and identified to the following contributions:[48–51]

**Shot Noise** Shot noise (also known as Schottky noise) reckons among the white noise sources, which implies a constant power spectral density (PSD) over the entire frequency range. This noise source is present in almost all semi-conductors and represents one of the major noise contributions.[51] It mainly occurs when discrete charges independently from each other pass an potential barrier. The discreteness of charges at very low current flows therefore leads to a fluctuation in the number of charges. This effect is described by the Poisson statistics of *root mean square (rms)* uncertainties. Its square of the shot noise current can be described by the following equation 2.12:

$$\overline{i_s^2} = 2qI_D\Delta f \quad (2.12)$$

where  $q$  is the electron charge;  $I_D$  is the dark current; and  $\Delta f$  is the bandwidth.

**Thermal Noise** This noise source is also called *Johnson noise* and is also independent of the frequency and therefore constitutes a white noise source. It is caused by thermal fluctuations in conducting and semi-conducting materials and originates either from the collision between charge carriers and with the lattice (originally observed in inorganic crystals) due to thermally induced motions of the carriers, or in organic SCs due to randomly activated charge carriers.[51] Its PSD at 0 K is zero. The square of the thermal noise current  $i_{th}$  can be expressed as followed (Equation 2.13):

$$\overline{i_{th}^2} = \frac{4k_bT}{R}\Delta f \quad (2.13)$$

where  $k_b$  is the Boltzmann constant;  $T$  the temperature in Kelvin; and  $\Delta f$  the bandwidth.

The dominant noise sources in organic PDs, the thermal and shot noise, contribute with a constant spectral noise densities (*white noise*) to the total noise current, and can be described as followed:

$$i_{noise} = \sqrt{\overline{i_s^2} + \overline{i_{th}^2}} \quad (2.14)$$

## 2. Fundamentals of Organic Semiconductors

An individual quantification of the detection limit is described by the noise-equivalent-power (NEP). The NEP in  $W Hz^{0.5}$  is defined as the minimum incident power required to achieve a photo current equal to the total noise current  $i_{noise}$  at a specified frequency.[52]

$$NEP = \frac{i_{noise}}{SR(\lambda)} \frac{1}{\sqrt{\Delta f}} [W Hz^{-0.5}] \quad (2.15)$$

### Specific Detectivity

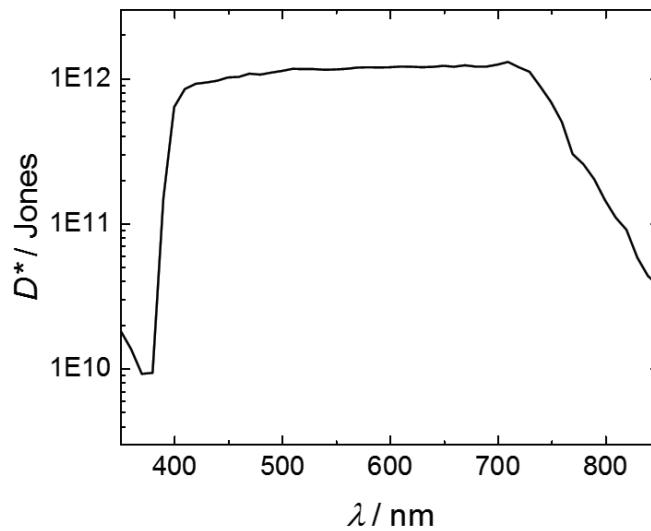


Figure 2.11.: Calculated specific detectivity ( $D^*$ ) plot of a polymer:fullerene BJJ device. (Eq. 2.16)

The NEP reveals a unique device specific measure. The specific detectivity  $D^*$  instead, as shown in **Figure 2.11**, which was introduced by Robert Clark Jones back in 1953, allows for a comprehensive device comparability by implementing the active area  $A$  into the equation.[53] Hence, the  $D^*$  serves as a figure of merit for photodetectors. The unit of  $D^*$  is commonly expressed in *Jones*. The relation between  $D^*$ , the NEP,  $SR(\lambda)$  and the shot noise is represented in Equation 2.16.

$$D^* = \frac{\sqrt{A \cdot \Delta f}}{NEP} \approx \frac{SR(\lambda)}{\sqrt{2qJ_D}} [cm Hz^{0.5} W^{-1}, Jones] \quad (2.16)$$

where the shot noise depicts the dominant noise source at reverse biased photodiodes.[52]

Another figure of merit is given by the linear dynamic range (LDR), which reveals a measure for the linearity of the photosensitivity in the following way:

$$LDR = 20\log(J_{Ph}^*/J_d) [dB] \quad (2.17)$$

where  $J_{Ph}^*$  is the photocurrent; and  $J_d$  is the dark current.

### Dynamic Response

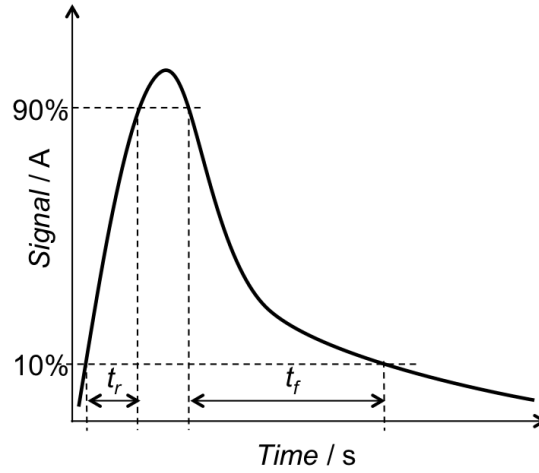


Figure 2.12.: Signal response of a photodiode to an impinging 1 ns short light pulse.

Many applications assigned to PDs bear on a fast response time to incident optical signals, as for instance in optical communication systems.[54] Therefore, the dynamic response of PDs is usually characterized in terms of rise ( $t_r$ ) and fall times ( $t_f$ ), as well as the detector bandwidth ( $BW$ ).  $t_r$  is the measure of the PD response speed to a light pulse, as shown in **Figure 2.12**. It is the time required to increase its output from 10% to 90% of the final value.  $t_f$  relates the same way to the fall time from 90% to 10% of peak current. Mainly responsible for the detection speed is the time constant  $t_{RC} \sim RC$ , as included in the following equations:

$$t_{90-10} = \sqrt{t_{tr}^2 + t_{RC}^2} \quad (2.18)$$

$$I(t) = I_0(1 - e^{-\frac{1}{RC}t}) [A] \quad (2.19)$$

where  $I_0$  is the initial maximum current arising from incident light of wavelength  $\lambda$ ; and  $R = R_L + R_S$ . The capacitance  $C$  depicts a typical plate capacitor, as shown in equation 2.20:

$$C = \varepsilon_0 \varepsilon_r \frac{A}{d} \quad (2.20)$$

## 2. Fundamentals of Organic Semiconductors

where  $A$  is the detector area; and  $d$  the thickness of the active layer;  $\varepsilon_0$  is the vacuum permittivity; and  $\varepsilon_r$  is the relative permittivity. The RC-time constant in an idealized case, under exclusion of recombination effects, can be expressed by the following equation:

$$t_{RC} = 2.2(R_S + R_L)C_D \quad (2.21)$$

where  $R_S$  is the series resistance;  $R_L$  is the load resistance; and  $C_D$  the device capacitance. Furthermore, the transit time for charges through the semi-conductor can be expressed as followed:

$$t_{tr} = \frac{d^2}{\mu(U_{Bias} + U_{bi})} \quad (2.22)$$

where  $U_{Bias}$  is the reverse bias voltage;  $U_{bi}$  is the built-in voltage arising from the difference in workfunction of the anode and cathode electrodes; and  $\mu$  is the charge carrier mobility (assuming  $\mu_n = \mu_p$ ) within the semi-conductor.

### 3. Printing and Coating Techniques



Figure 3.1.: Aerosol Jet Printing System (Optomec, AJ300)

*This chapter attends to the device fabrication methods, such as the printing and coating techniques used in this work. The title of this thesis already alludes that the main focus is set to aerosol jet (AJ) printing. Therefore, I will present in this chapter the general working principle of the AJ printing as well as the influence of the important printing parameters on the printing outcome. Furthermore, I will show fundamental design rules, which in my opinion need to be considered for an appropriate printing result. Additionally, the inkjet printing technique (IJ), which constitutes a primary constituent in additive digital manufacturing techniques, will be briefly described. Finally, spin coating, which presents an versatile deposition technique for laboratory-scale device preparation and is the standard technique for solution processed organic materials and therefore will also be presented.*

## 3.1. Aerosol Jet Printing

The AJ technology is a *digital* and *contact-free* additive manufacturing technology based on spray deposition. It is eminently suitable for fine- and coarse-feature printing. **Figure 3.1** shows an image of the Optomec AJ300, which was used in this work. In comparison to inkjet, aerosol jet printing makes use of an *aerodynamic focusing* of a previously inline atomized ink, the *aerosol*. The aerosol comprises droplets with a mean diameter in the sub-micrometer range. This allows for a precise deposition of a large variety of functional inks from solution or dispersion with a feature accuracy down to  $10\ \mu\text{m}$  depending on the nozzle diameter and the focusing ratio. First of all, we will clarify the terminology of *aerosol* and *aerodynamic focusing*, as well as the widely used buzzwords *digital* and *contact-free*.

**Aerosol** An aerosol is by definition a solid (particle) or liquid (droplet) matter dispensed in a gas phase. In the present case, the suspended matter constitutes of fluids or more specifically of polymer solutions and nanoparticle dispersions.

**Digital printing** The terminology of *digital printing* implies, that the tool path, which contains the printing pattern, is designed digitally on a computer. In this case, the tool path translates a vectorial drawing (drawing interchangeable file format, DXF) into the machine code, which can then be interpreted by the printers software, whereupon the substrate x-y-(z) stage moves according to the desired path.

**Contact-free** A contact-free and local deposition of a material signifies, that no contact occurs between the printer and the substrate surface. This is of great importance when it comes to multi-layer deposition, as used in many electronic devices, where a subsequent deposition of layers in the sub- $100\ \text{nm}$  regime is needed and every slight contact could cause defects or damage the underlying layers.

**Aerodynamic focusing** The aerosol printer utilizes a focusing technique, which makes use of two nitrogen flows. The primary nitrogen stream, or *atomizer gas flow*, carries the aerosol from the atomizer section into the nozzle head. Together with a secondary nitrogen flow, *sheath gas flow*, a coaxial stream is formed at the nozzle orifice. By varying the pressure parameters for both gas flows, the inner material stream can be compressed or relaxed, which results in the *aerodynamic focusing*.

### 3.1.1. Working Principle

**Atomization** Both a pneumatic and an ultrasonic aerosol generator (atomizer) are implemented in the printer. The pneumatic atomizer (PA) is able to atomize liquids with a viscosity up to  $1000\ \text{cP}$ . These would reveal a honey-like appearance. However, a large amount of fluid volume is needed  $\sim 30\ \text{ml}$ , which in some cases raises the costs tremendously depending on the used functional material. In this work, only the ultrasonic atomization was used, therefore the pneumatic atomization process won't be mentioned during the further thesis.

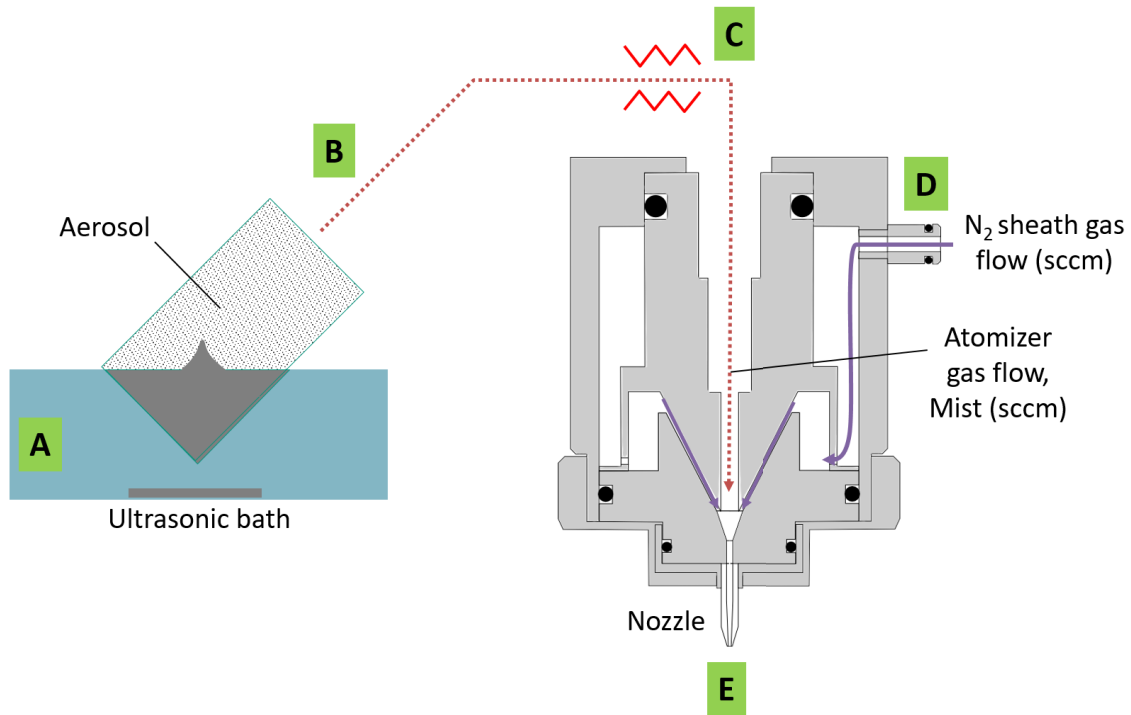


Figure 3.2.: Schematic of AJ printing system with ultrasonic atomizer section.

The ultrasonic atomizer, as shown in **Figure 3.2**, is restricted to inks with a viscosity below 10 cP. A big advantage is the low fluid volume requirements, which can be limited to  $\sim 1$  ml. In case of the UA system the vial with the source material is positioned inside a water filled coupling fluid reservoir. The ultrasonic waves induce a capillary wave in the functional fluid inside the vial, which causes the ink to be atomized. The droplet mean diameter  $D$  can be estimated by the following equation and typically amounts to 2 to 5  $\mu\text{m}$ : [55, 56]

$$D = 0.34 \cdot \left( \frac{8\pi\sigma}{\rho f^2} \right)^{1/3} \quad (3.1)$$

$D$  is merely influenced by the surface tension  $\sigma$ , the fluid density  $\rho$ , and the excitation frequency  $f$  of the transducer. The effective mist density is affected by the ultrasonic power and can be adjusted to fulfill the required material throughput. Furthermore, the vial position needs to be adjusted using the angular and lateral translation rails for an optimal fluid coupling.

**Material Transport, Focusing and Deposition** After the atomization by the ultrasonic inducer (A), the source matter is carried by a nitrogen gas flow (B) through a polyethylene tube into the nozzle head. A tube heater (C), which muffs the carrier gas tube, can be activated to refine the aerosol right in front of the nozzle head (Fig. 3.2). This

### 3. Printing and Coating Techniques

can be utilized, for instance to concentrate the ink droplets by evaporating excess solvent. Within the nozzle head the mist is then aerodynamically focused by the annular sheath gas flow (D), as described above. The collimated co-axial flow of mist and sheath gas is guided through the ceramic nozzle tip, where the focusing occurs at the nozzle orifice (E). Here, the material stream can be constricted down to a tenth of the nozzle diameter. In the present system, nozzles with diameters ranging from  $100\ \mu\text{m}$  to  $300\ \mu\text{m}$  are applicable to the deposition head, where an appropriate choice already defines a certain focus range. For fine-feature printing nozzle diameters between  $100\ \mu\text{m}$  and  $150\ \mu\text{m}$  are recommended. A detailed analytic work on aerosol jet printing and its association with the *Stokes number* for behavior of particles entrained in a flow can be found elsewhere.[57, 58]

An electrically driven shutter arm is mounted below the nozzle orifice, which guarantees that material is deposited only on demand. Thus, excess material e.g. during idle mode or during substrate displacements gets collected by the shutter. The nominal standoff distance of 5 to 10 mm between the nozzle tip and the substrate is used for the placement of the shutter arm, but also allows for precise deposition on non-planar surfaces, such as protruding or dented structures exceeding height variations in the order of several millimeter. The printing patterns are generated using a computer aided design (CAD) software, which is then compiled and executed by the printer's firmware. Printing a pattern is finally accomplished by placing the substrate on the motorized and heatable x-y stage that executes the tool path by moving the substrate at a defined speed and precise lateral displacement with an accuracy of  $\leq 6\ \mu\text{m}$ .

#### 3.1.2. Printing Parameters

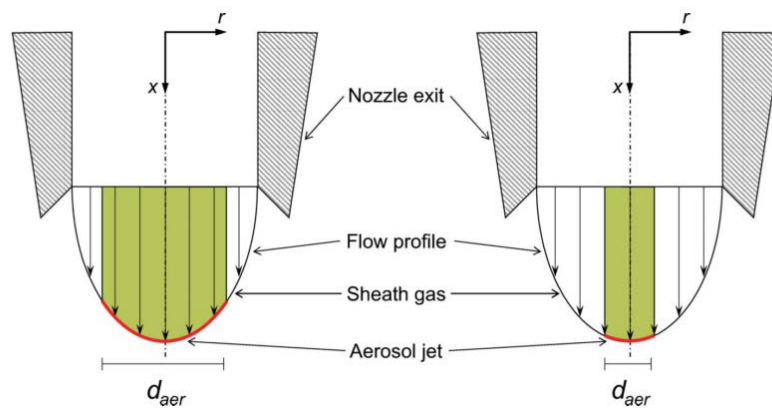


Figure 3.3.: Schematic of the nozzle orifice flow profile with contributions of the sheath and atomizer gas flows. (left) small flow ratio, (right) high flow ratio. (Reprinted from Binder *et al.* [58])

The AJ printer is based on a complex pressure system and is therefore strongly dependent on perfect pressure conditions. That implies in particular the tightness of sealings and high quality standard in terms of cleanliness. Smallest leakages can cause pressure drops and by that could cause insufficient printing results. Moreover, residues in the ceramic

nozzle can provoke turbulences and detrimentally affect the printing outcome. The following paragraphs exemplifies general influences of parameter sets, such as the material flow and focusing possibilities, as well as design rules for proper printing results.

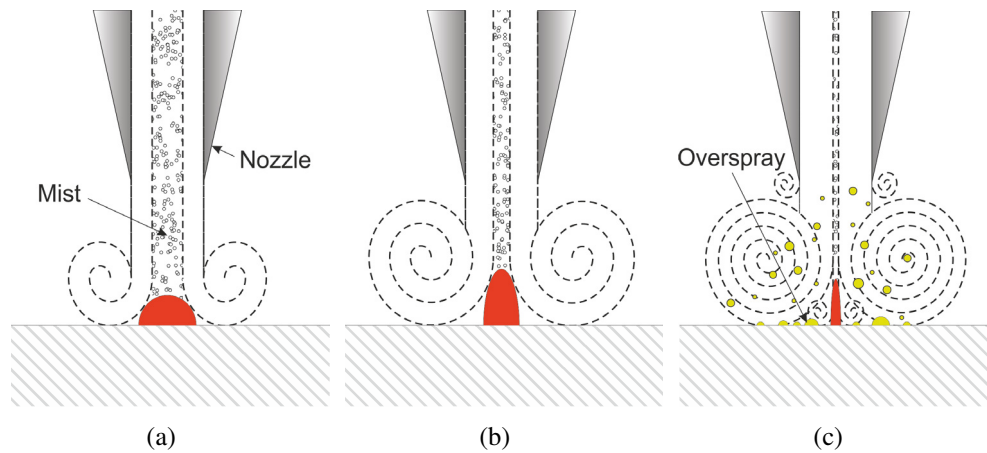


Figure 3.4.: Schematics of different sheath gas flows. a) Low sheath gas flow causing low turbulences at the substrate front. b) High sheath gas flow causing higher aspect ratio, but also increased turbulences. c) Exceeding sheath gas flow causing *overspray* due to turbulences at the orifice front

### Sheath and Atomizer Gas Flow

The focusing of the material takes place inside the nozzle head, where the injected aerosol gets co-axially surrounded by the sheath gas. In this situation both gas flows are drastically accelerated due to the decreased nozzle diameter. This linear and axially symmetrical flow prevents from contact of aerosol particles and the inner wall of the nozzle tip even for very narrow nozzle diameters, as shown in **Figure 3.3** in the left image, showing the flow profile of the aerosol jet at the nozzle orifice.[58] A further increase of the sheath gas flow leads to a reduction of the aerosol stream diameter and thus sets the focus, see right image.

**Figure 3.4** illustrates the impact of different sheath-to-atomizer gas ratios. In theory the aerosol stream diameter only depends on two parameters, which are the nozzle orifice diameter and the focusing ratio. This seems valid up to a certain point, where the sheath gas flow starts to throttle the material stream, or when turbulences at the nozzle orifice disturb the linear flow. Reasons for that can be given by particle or fluid contamination of the inner nozzle wall or just exceedingly high pressures. This effect could nicely be demonstrated in an experiment, where the sheath gas flow was varied in order to influence the printed line width.

**Figure 3.5** illustrates the printing results, performed with a nano-particulate silver ink<sup>1</sup>

<sup>1</sup>(Silverjet DGP-40LT-15C, SigmaAldrich) diluted with 3-heptanone in a ratio of 1:1

### 3. Printing and Coating Techniques

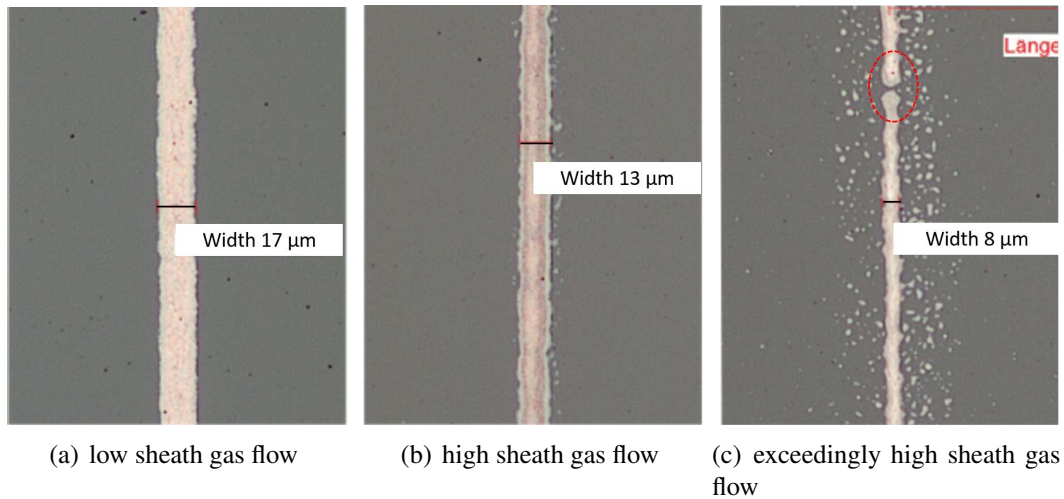


Figure 3.5.: Microscope images of AJ printed nanoparticulate silver ink on glass of an a) moderate, b) high, and c) exceedingly high sheath-to-atomizer flow ratio.

on a cleaned glass substrate. A nozzle diameter of  $100\ \mu\text{m}$  was used and the atomizer gas flow was set to  $20\ \text{sccm}$ . While for lower flow ratios the line width decreases as expected. However, an exaggeration of this ratio causes a deterioration of the print image and the appearance of satellite drops, the so-called *overspray* and also line disruptions due to a pinch off of the material, as marked with a red ellipse in Fig. 3.5(c).

It should be kept in mind, that the printing parameter analysis can be superimposed by the substrate and fluid properties and interactions, which can vary vigorously. One of the main disadvantages present in this particular printer model can be found in the material atomization via the ultrasonic system and the material transport system. It was observed, that fluid volume, vial position and bath temperature strongly influence the aerosol density and quality. Furthermore, the dry nitrogen carrier gas expedites the evaporation of low boiling point solvents and hence a change in ink composition. The latter can partly be compensated by an a priori moistening of the nitrogen and the use of solvents with boiling points superior to  $100\ ^\circ\text{C}$ .

#### Tool Path and Design Rules

Despite the gas flow parameters, also tool path related parameters can strongly influence the resulting print image. **Figure 3.6** shows line profiles of AJ printed epoxy resin (SU-8). For these printing tests all gas flow related parameters were kept constant. Only the printing velocity was varied from  $1\ \text{mm s}^{-1}$  to  $7\ \text{mm s}^{-1}$ . Furthermore, lines were printed with two and three consecutive passes and show that an increase in line height can be achieved by multi-pass printing, while the line width is merely affected. This allows for a change in the aspect ratio of printed structures, where line heights up to  $15\ \mu\text{m}$  were achieved for three consecutive passes.

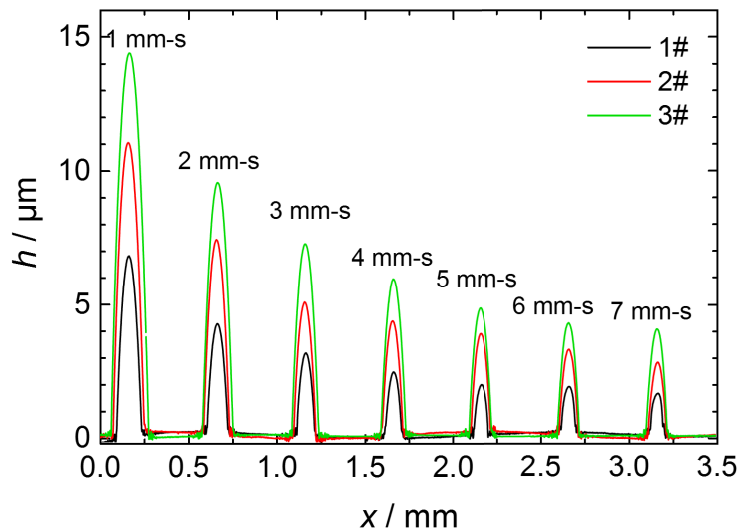


Figure 3.6.: Cross-sectional line profiles as a function of the printing velocity and multi-passes. (Sheath and atomizer gas flow were kept constant during the experiment)

The printing speed provides an additional tuning parameter for the line width, height and shape. Compared to conventional printing techniques, such as gravure or flexo printing, sequential digital printing techniques, like inkjet and aerosol jet, cannot compete in terms of printing speed. Nevertheless, an increasing speed can also negatively affect the print quality, since the pattern is deposited on a substrate using a motorized x-y stage that entails a certain inertia. Abrupt changes of direction at elevated velocities ( $> 5 \text{ mm s}^{-1}$ ) can cause vibrations, which result in a deviation between printed and the initial path vector. **Figure 3.7 a)** shows two test patterns aiming for depositing two narrow lines with a pitch of  $30 \mu\text{m}$ . One containing an abrupt direction change with an angle of  $45^\circ$ , the other one converging by a radiused corner. Already at  $5 \text{ mm s}^{-1}$  the vibration is clearly observable, as presented in **Figure 3.7 b)**, while in **c)** a very smooth approach occurs and line are perfectly separated from each other. Increasing the printing velocity to  $10 \text{ mm s}^{-1}$  furthermore demonstrates the advantage of this tool path modification to fulfill the needs of shorter printing times and high accuracies for features in the micrometer regime.

## 3.2. Inkjet Printing

Inkjet typifies the concept of digital additive manufacturing and represents an indispensable part of printed electronics. The model used in this work is a Dimatix Fujifilm DMP-2831 drop-on-demand (DoD) printer (**Figure 3.8**) developed for prototyping and evaluation of inks, fluids, fluid-substrate interactions, and product development. The Dimatix makes use of disposable 16 nozzle cartridges with 1 pL and 10 pL nominal drop volume

### 3. Printing and Coating Techniques

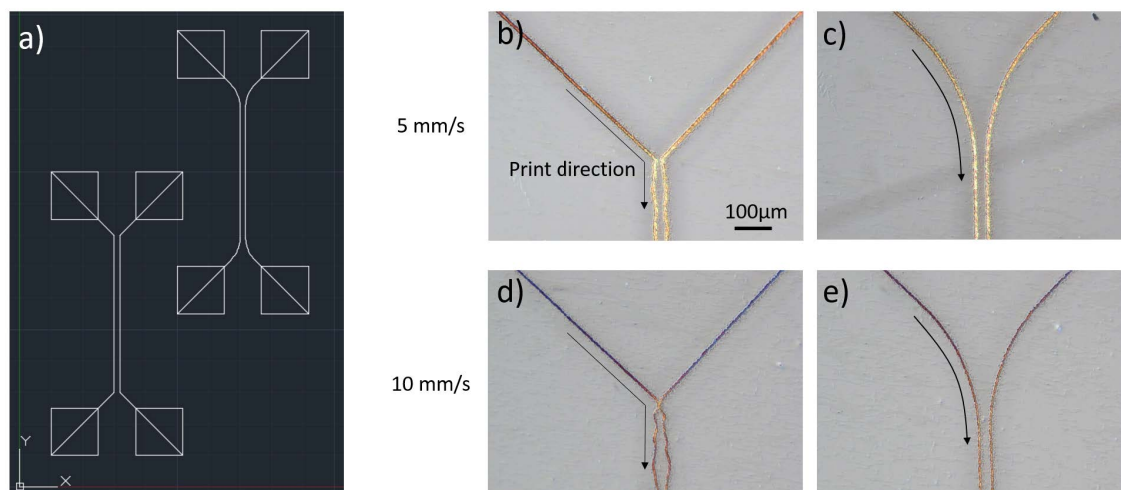


Figure 3.7.: Test pattern with two approaching lines with and without rounded corners printed with nanoparticulate Ag ink on glass. a) Schematic of tool path. Microscope images of printing results with b) sharp corners printed at  $5 \text{ mm s}^{-1}$ , c) b) rounded corners printed at  $5 \text{ mm s}^{-1}$ , d) b) sharp corners printed at  $10 \text{ mm s}^{-1}$ , and e) rounded corners printed at  $10 \text{ mm s}^{-1}$ .



Figure 3.8.: Inkjet printer Dimatix Fujifilm DMP-2831 and cartridge. (Photos reprinted from [www.fujifilmusa.com](http://www.fujifilmusa.com))

are available, where the smaller drop volume applies for high resolution printing as used in fine feature electrode structures.

The voltage pulse (waveform) shown in **Figure 3.9(a)**, comprising a rise, dwell and fall time, as well as an amplitude, forces a piezo transducer to expand or contract in a well-defined manner and thus compresses or relaxes the ink reservoir. Assuming that the ink is a non-compressible fluid, it consequently gets ejected at the nozzle plate and forms a droplet of defined volume and shape, as shown in Figure 3.9(b). In an analogous manner, a *non-jetting* waveform is applied in idle mode, which keeps the fluid in motion without forming a droplet and prevents the fluid from drying at the orifice. Detailed information

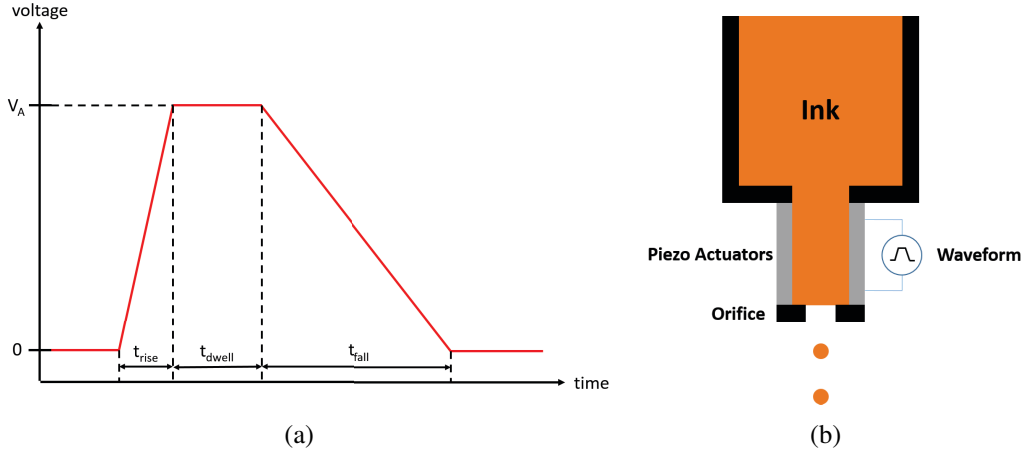


Figure 3.9.: a) Example for a jetting waveform. b) Schematic drawing of a DoD inkjet nozzle comprising an ink reservoir, piezo electric actuators driven by an applied waveform, and an orifice with a defined diameter.

about the influence of jetting frequency, as well as waveform including the rise time  $t_{rise}$ , dwell time  $t_{dwell}$ , and fall time  $t_{fall}$  can be found elsewhere.[59–62]

The ink properties equally contribute to the jettability and printing quality likewise the printer's parameter set. Therefore, ink pre-requisitions for an optimal print window can be described by the dimensionless *Ohnesorge*-number  $Oh$ . [61, 63, 64] *Ohnesorge's* analysis discusses the importance of ink's inertia, viscosity, and surface tension by introducing the Reynolds number  $Re$  and the Weber number  $We$ :

$$Re = \frac{\rho v d}{\eta} \quad (3.2)$$

$$We = \frac{\rho v^2 d}{\sigma} \quad (3.3)$$

where  $\rho$  depicts the fluid's density;  $v$  the drop velocity;  $d$  the orifice diameter (nozzle diameter);  $\eta$  the fluid viscosity;  $\sigma$  the surface tension of the fluid. The *Ohnesorge* number  $Oh$  results as the fraction of the  $Re$  and  $We$  numbers, as followed:

$$Z = \frac{\sqrt{We}}{Re} = \frac{\eta}{\sqrt{\rho \sigma d}} = \frac{1}{Oh} \quad (3.4)$$

where  $Z$  is the inverse of  $Oh$ . **Figure 3.10** illustrates the regime of stable drop formation for DoD printers and thus printability of fluids.[64] As can be discerned from Figure 3.10 the  $Z$ -number for an optimal printability should range between 1 and 10.

For nozzle diameters of  $21 \mu\text{m}$  for the  $10 \text{ pL}$  the fluid viscosity should be between 1 and  $25 \text{ mPa}\cdot\text{s}$ , while the surface tension should be in the range of  $25$  to  $50 \text{ mN}\cdot\text{m}^{-1}$ . In practice, it should be ensured that the ink is filtered using an appropriate  $0.2 \mu\text{m}$  filter prior to loading the cartridge. As a rule of thumb, particles should be 100 times smaller in

### 3. Printing and Coating Techniques

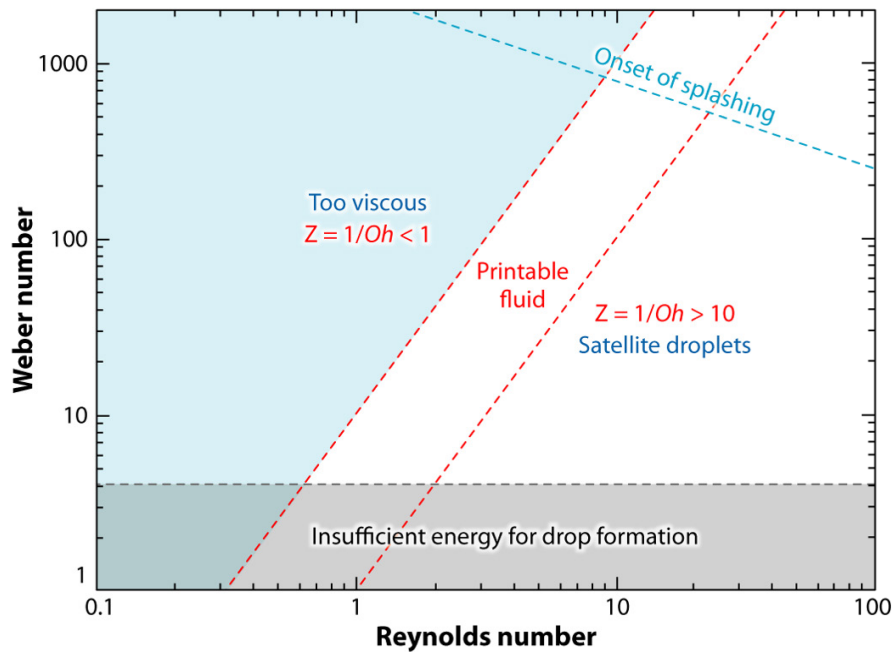


Figure 3.10.: Printability window of fluids and its relationship between the Weber and Reynolds number (reprinted from Derby et al., 2010) [64]

diameter than the nozzle diameter to prevent clogging. Once, the cartridge is loaded with the source material a jetting and non-jetting waveform needs to be defined to eject a droplet and to adjust its shape. The voltage amplitude of the waveform defines the drop velocity, which typically ranges from 7 to 12  $mm\ s^{-1}$ . The operator can visually observe the drop formation and shape via the drop watcher and thus directly see the influence of the adjustments in the waveform, as illustrated in **Figure 3.11**.

The wet film thickness is defined by the ink volume per area, which can be influenced by the drop spacing since the drop volume is fixed for a certain cartridge. Limitations are set by the wetting behavior on the substrate. For a proper printing result a contact angle of around  $45^\circ$  is presumed according to the Dimatix manual. A pattern editor is implemented into the software to draw basic patterns, while more complex layouts can be imported from bitmap files.

### 3.3. Spin Coating

Spin coating is a widely used technique to deposit uniform layers from solution with well defined and reproducible thicknesses. Therefore, the substrate has to be placed on a substrate holder (chuck). The dissolved or dispersed material is then spread on the substrate and subsequently rotated at a specific velocity and for a specific period of time. The excess liquid spins away from the substrate by the centrifugal force, while a film with the desired thickness remains on the substrate. The film thickness depends on the

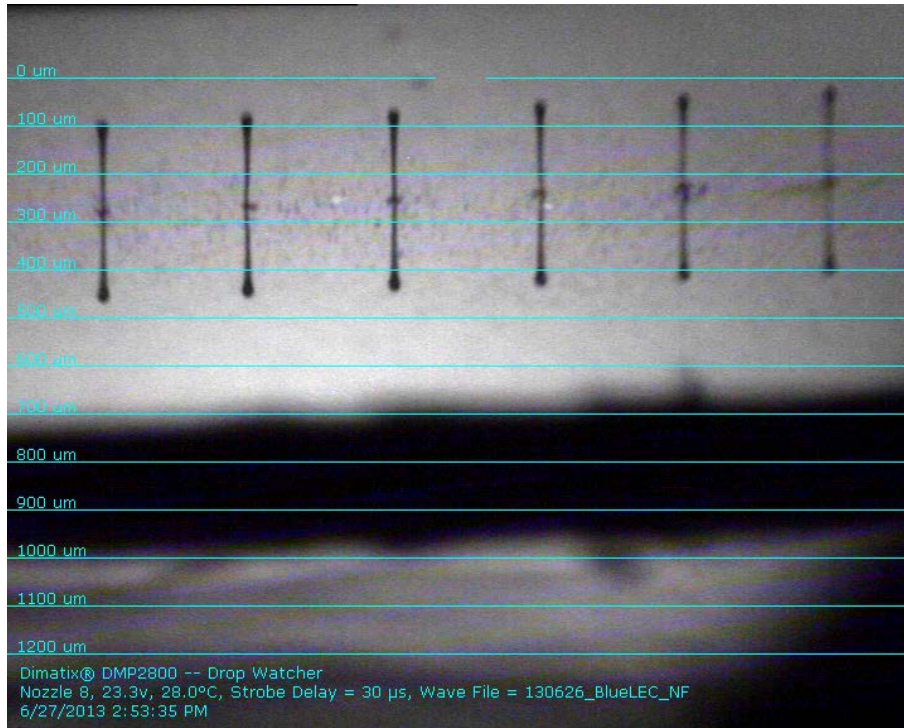


Figure 3.11.: Image of the Dimatix DMP-2800 drop watcher showing the ejection of droplets from the nozzles.

solid concentration, viscosity of the liquid, and the angular velocity, and thus is only suitable for relatively small substrates. The higher the rotation speed, the thinner the resulting thickness. With this procedure, film thicknesses of very few nanometers can be processed.

### 3.4. Device Encapsulation

The encapsulation represents the final but very important step of the device fabrication. It prevents the organic matter from an early degradation before or during the device characterization. Therefore, the samples are transferred into a nitrogen filled glove box, which provides an atmosphere free of humidity and oxygen. Then, a flexible adhesive PET foil containing a humidity and oxygen barrier layer (FTB-3-125, 3M) is affixed on the device, as shown in **Figure 3.12** for the two devices without and with the barrier foil attached. The application of controlled pressure ensures a proper sealing to prevent also lateral infiltration of humidity or oxygen. The barrier foil should exceed the active area by at least 2 to 3 mm.

### 3. Printing and Coating Techniques

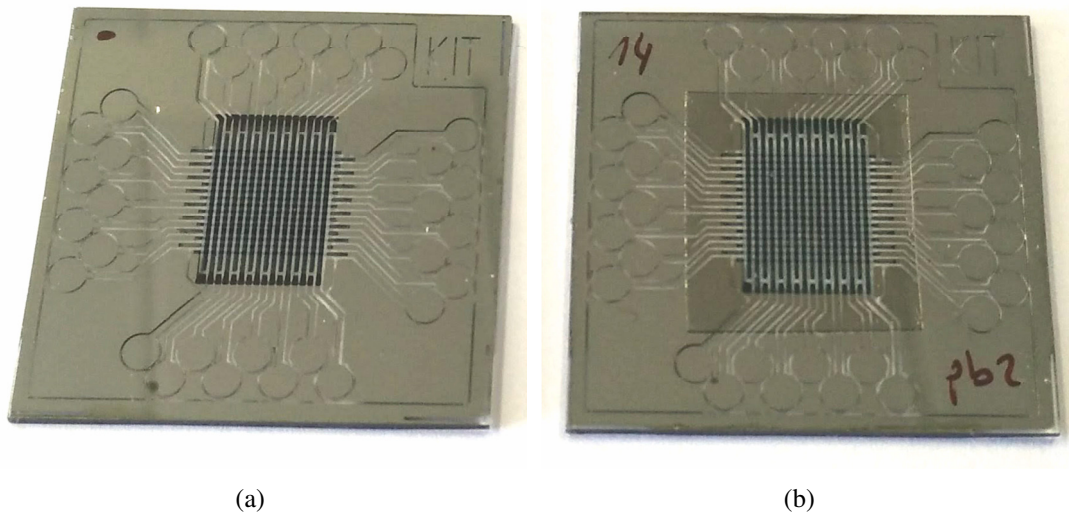


Figure 3.12.: a) Device without encapsulation foil, and b) with encapsulation foil.

## 4. Characterization Methods

*This chapter describes the primarily utilized measurement and characterization methods. Furthermore, it introduces a physical simulation model based on a finite element method, which was used for the physical device simulations in chapter 5.*

### 4.1. Fluid and Substrate Characterization

The *Krüiss* DSA-100 drop shape analyzer is used for the measurements of surface tensions and energies in fluids and solids, respectively. This system provides two main measurement modes, where one has to distinguish between the pendant drop and sessile drop method. The pendant drop analysis is used to measure the total surface tension of a specific fluid. In contrast, the sessile drop is used to determine the surface energies of solids among others.

#### 4.1.1. Contact Angles, Surface Energies and Surface Tensions

Surface free energies of substrates are determined using de-ionized water ( $H_2O$ ), ethylene glycol (*EG*), diiodomethane (*DIM*), and glycerine as reference fluids. According to Young's equation (Eq. 4.1) there is a correlation between the contact angle  $\theta$ , the surface tension of the fluid  $\sigma_{fg}$ , interface tension between fluid and solid  $\sigma_{sf}$ , and the surface tension  $\sigma_{sg}$ . [65] The contact angle is measured from a sessile drop, as illustrated in **Figure 4.1(a)**.

$$\sigma_{sg} = \sigma_{sf} + \sigma_{fg} \cdot \cos \theta \quad (4.1)$$

Intermolecular forces between the solid and liquid phase can be segmented into various interface interactions, such as dispersive forces (*Van-der-Waals*), polar interactions, hydrogen bonds, and acid/base components. In this work, I complied to the model by Owens, Wendt, Rabel and Kaelble (*OWRK*) that confines the complexity of the contributing forces down to the polar  $\sigma^p$  and dispersive part  $\sigma^d$ . [66–68]

$$\sigma^t = \sigma^d + \sigma^p \quad (4.2)$$

where  $\sigma^t$  is the total surface energy/tension.

#### 4. Characterization Methods

The surface tension of a fluid can be measured by the pendant drop analysis, as illustrated in Figure 4.1(b). Thereby, the fluid is hanging in equilibrium from a needle. The resulting shape depends on the surface tension of the fluid, the interfacial tension between the gas and liquid phase and the gravity. The latter deforms the drop shape due to its own mass or density according to the *Young-Laplace* equation.[69]

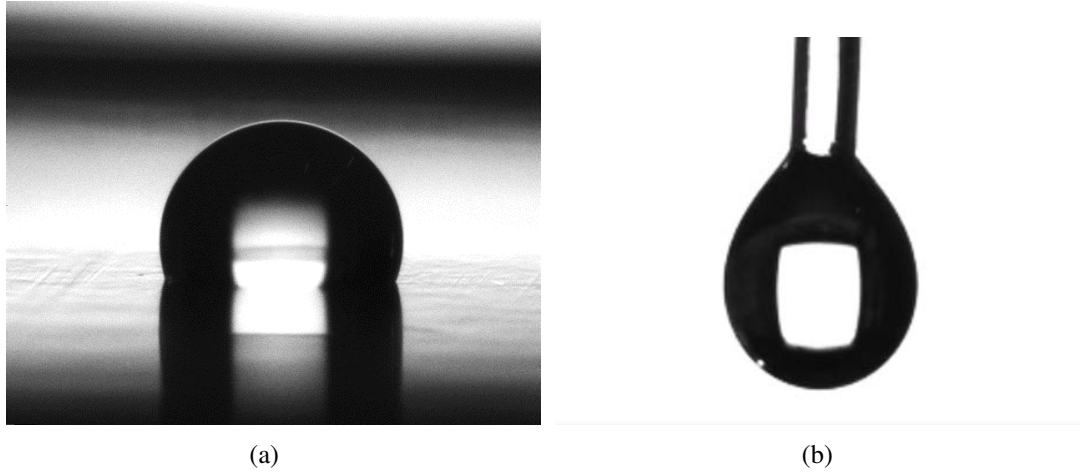


Figure 4.1.: a) Image of a water droplet on Teflon. b) Image of a pendant drop hanging from a needle.

#### 4.1.2. Determination of Polar and Dispersive Surface Tensions

To reveal the polar and dispersive parts of an unknown fluid, the values for total surface tension  $\sigma^t$  of the fluid and the surface energy of a purely disperse surface are needed (e.g. Teflon, poly propylene). From that, the dispersive part of the fluid can be calculated by using equation 4.4 based on the *Young-Dupré* equation for the work of adhesion 4.3:[70]

$$W_{sf} = (1 + \cos\theta) \cdot \sigma_f^t = 2 \left( \sqrt{\sigma_s^p \sigma_f^p} + \sqrt{\sigma_s^d \sigma_f^d} \right) \quad (4.3)$$

where after dividing through  $\sigma_f^d$  the following term arises:

$$\sqrt{\sigma_s^p} \cdot \frac{\sqrt{\sigma_f^p}}{\sqrt{\sigma_f^d}} + \sqrt{\sigma_s^d} = \frac{(1 + \cos\theta) \cdot \sigma_f^t}{2\sqrt{\sigma_f^d}} \quad (4.4)$$

where  $\sigma_s^d$ ,  $\sigma_s^p$ ,  $\sigma_f^d$ , and  $\sigma_f^p$  are the dispersive and polar part of the surface free energy of the solid and the dispersive and polar part of the surface tension of the fluid, respectively. With respect to  $\sigma_s^p = 0$  for Teflon or poly propylene, the equation can be simplified and resolved to the dispersive part of the fluid (equation 4.5):

$$\sigma_f^d = \frac{(1 + \cos\theta)^2 \cdot \sigma_f^{2t}}{4\sigma_f^d} \quad (4.5)$$

## 4.2. Thin-Film Characterization

### 4.2.1. Optical Characterization

#### Optical Microscopy

Optical light microscopic images were performed using a Nikon Eclipse 80i connected to a 5.0-megapixel pixel high definition camera head (DS-Fi1). Images and lateral measurements were recorded with a software (Basic Research, *Nikon*). The microscope provides measurement modes for bright-field (BF) and dark-field (DF), differential interference contrast (DIC), fluorescence, as well as polarization. Therefore, it allows for a profound optical inspection of a large variety of samples.

In this work, the optical microscopy was used to visually observe the quality of AJ printed Ag lines, where the DF and DIC modes were used to examine the inhomogeneities and overspray arising from the printing process. Furthermore, the DIC mode was utilized to observe slight thickness variations in printed layers.

#### UV-Vis Spectroscopy

The UV/Vis-spectrometer (*Avantes*) allows for measuring the absorption and transmittance of thin films or devices in a spectral range of 200 to 1100 nm with a resolution of 0.6 nm. The device under test (DUT) is mounted between two fiber optics, where one is connected to the light source (Avalight-DH-S BAL Deuterium-Halogen Light Sources) and the second fiber optic to the spectrometer (Avaspec-ULS3648).

### 4.2.2. Surface Topography

Profilometers are used to measure film thicknesses, non-uniformities, or profiles of protruding structures with height differences ranging from several micrometer down to a few nanometer. Therefore, three measurement setups were used. The stylus profilometer and optical 3D profilometer are used for larger areas, while the atomic force microscopy has the highest resolution. Surface profilometry constitute very important measurements, since inhomogeneities in printed functional layers attributed to a specific printing technology can strongly influence the layer quality and hence the device performance.

### Stylus Profilometry

The stylus profilometer (Dektak 150, Veeco) uses a needle with a defined tip radius, pressure, and measurement rate (ideally around  $40 \mu\text{m s}^{-1}$ ) that moves over the sample surface. The layer thickness can be revealed by measuring over a step edge, which can be obtained by carefully scratching a groove into the deposited film. Preferably a soft object, such as a plastic tweezers, should be used not to harm the substrate. The height profile over the step edge is then recorded using the manufacturer's software.

### Confocal and White-Light Microscopy

The *Sensofar* Neox provides a 3-dimensional profile measurement technique based on non-contact light interferometry and confocal microscopy. The interferometric profile measurement makes use of different optical path lengths between a reference surface and the surface under test, which results in a spatial interference pattern containing the height information of the sample. The confocal scanning technique utilizes an aperture at the confocal plane of the lens, which allows only *focused* light to pass and being imaged. Thus, 2D or 3D images can be captured by scanning the aperture in the out-of-plane direction.

### Atomic Force Microscopy

An atomic force microscope (DS95 Dualscope, DME) was used for high resolution topography measurements of thin films and printed structures. Therefore, a cantilever with a sharp tip scans line by line over the specimen (max.  $50 \times 50 \mu\text{m}$ ). Height deviations are detected by the force dependent deflection of the cantilever. All measurements were performed using the *tapping mode*, where the cantilever oscillates at a given frequency against the specimens surface. The resolution is mainly limited by the radius of the tip.

### 4.2.3. Electrical Conductivity Measurements

The resistance of conductive lines can be measured by a simple two wire setup, where according to *Ohm's law* the resistance can be calculated from a known applied constant current, while the voltage is measured across the trace. The measurement itself is performed by a multimeter or a source measurement unit (Keithley 2400). Measurement uncertainties are given by the omission of resistance from the wires and contact between the DUT and the measurement probes.

To determine the sheet resistance of conductive thin films, however, this technique comprises further measurement uncertainties, since the DUT would have to be exactly quadratic. An alternative option is a 4-wire electrode array measurement setup that uses separated probes for the application of current and the sensing of the respective voltage according to

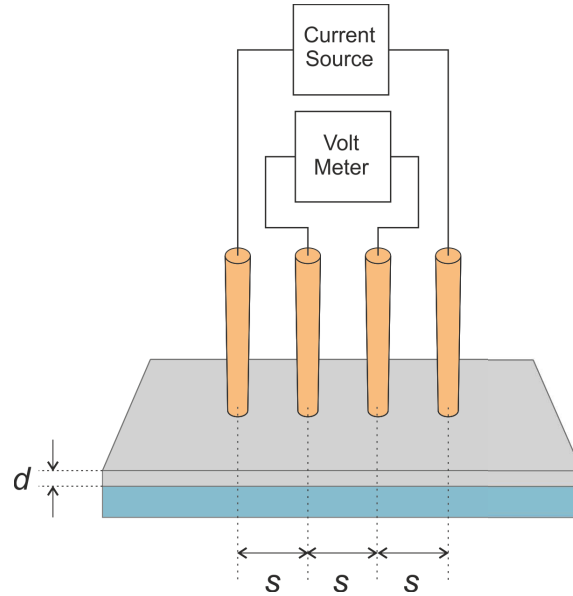


Figure 4.2.: 4-wire electrode array for resistance measurements of thin films with a layer thickness  $d$ . Current is applied at the outer pins and the voltage is measured at the inner pins. The array comprises equidistant pins with a spacing  $s$ .

the resistance of the film. The setup is depicted in **Figure 4.2**. This technique eliminates the resistance from the wires and the contact resistances and can therefore be used to measure precisely low resistance values. The four electrode pins are equally spaced and with the assumption, that the DUT provides a homogeneous resistance over the whole area, the sheet resistance  $R_{sheet}$  can be calculated from the measured resistance  $R_{meas}$  by using the van-der-Pauw method, as followed:

$$R_{sheet} = \frac{\pi}{\ln(2)} * R_{meas} \quad (4.6)$$

## 4.3. Device Characterization

### 4.3.1. Current Density - Voltage Measurements

Current density ( $J$ ) measurements appertains to the standard measurement protocol for solar cells and photodiodes (PD). Under illumination they reveal relevant parameters for solar cells, such as short circuit current density ( $J_{SC}$ ), open circuit voltage ( $V_{OC}$ ), fill factor ( $FF$ ), and the device's efficiency ( $\eta$ ). For PDs, which can be operated either in the photovoltaic or photoconductive mode the dark current density, as well as the photocurrent at different bias voltages can be of great interest.

After a 30 min lamp warming phase, the light source (LOT-Quantum Design 450-1000W Xe Arc Lamp Power Supply LSN555, Solar Simulator System LS0900 Series) can be calibrated with an inorganic silicon reference cell (ReRa Solution, covered with a KG 2 filter)

#### 4. Characterization Methods

to  $1000 \text{ W m}^{-2}$ . Therefore, the reference cell is connected to the source measurement unit (SMU, Keithley 2636 B). The light intensity is adjusted to the targeted photocurrent of the reference cell by changing the current at the lamp's power supply. Afterwards, the DUT is connected to the SMU via clips or a sample holder.

#### 4.3.2. Light Beam Induced Current Measurements (LBIC)

The light beam induced current measurement (LBIC) is used to record the photocurrent of a solar cells or PD spatially resolved over a certain area. This technique is well suited to detect inhomogeneous contributions to the photocurrent generation within a solar cell. Therefore, a laser beam at  $\lambda = 543 \text{ nm}$  (R-30972, Newport) is chopped into an AC signal and directed onto the DUT through an neutral density filter and an achromatic 4x objective. The cell is then laterally displaced by a micrometer precision motorized x-y stage. The spatially induced currents are measured with a *Lock-In*-amplifier (LockIn 250, Anfatec) and mapped with respect to its pixel position.

#### 4.3.3. Steady State and Dynamic Photodiode Characterization

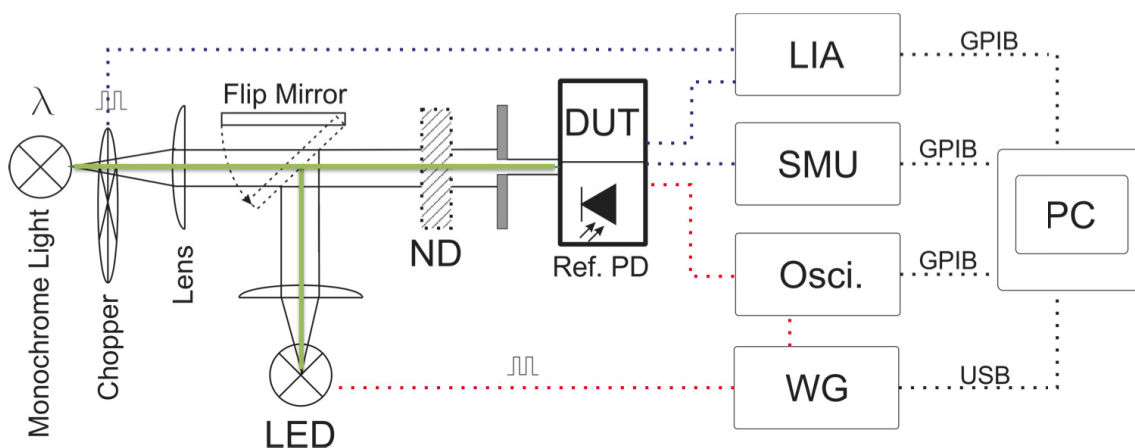


Figure 4.3.: EQE and bandwidth measurement setup.

#### External Quantum Efficiency (EQE)

Within this work, a characterization unit for EQE and bandwidth measurements for steady state and static device characterization was built. The EQE setup, as illustrated in Figure 4.3, uses a xenon arc light source (LOT-Quantum Design 450-1000W Xe Arc Lamp Power Supply LSN558, LSH601 Lamp Housing), which is connected through an infrared (IR) filter and an additional high-pass filter wheel (FA-2448-1, Princeton Instruments) to an Acton SpectraPro monochromator (SP-2150, Princeton Instruments). The cut-off filters are used to avoid higher order contributions from shorter wavelengths in the monochromatic beam. The entrance and outlet slits of the monochromator are adjusted

to reveal a  $\sim 10$  nm full-width-half-maximum (FWHM) wavelength distribution. An optical chopper (MC2000, Thorlabs) with a 10-slot chopper blade suitable for frequencies from 20 to 1 kHz (MC1F10, Thorlabs) chops the steady state light beam into the desired frequency (normally between 175 and 400 Hz) and passes the chopping frequency also as a trigger signal to the *Lock-In*-amplifier (LIA). A lens system collimates the monochromatic beam, which then passes an iris diaphragm placed in front of the DUT to ensure an illumination of solely the desired pixel. The DUT or the Si reference cell (calibrated FDS100, Thorlabs) is connected to a self-built shielded probe station mounted on an x-y-z translation stage, which again provides connections to the LIA (SR-830, Stanford Research Systems), an SMU for applying a bias voltage, and an additional auxiliary input for DUTs with deviating sample layouts. The spectral response (SR) and the EQE are then calculated from equation ?? and ?? using an automated self-built Labview software.

### Dynamic Response

**Bandwidth Determination** The bandwidth (BW) measurement setup, integrated in the EQE/BW setup, used a green high-power LED (Luxeon Rebel, 532nm) modulated by a rectangular wave form with a duty cycle of 50% coming from an Agilent DSA 33522A wave generator (WG). The current signal was then amplified (FEMTO DHPCA-100) and recorded using an oscilloscope (DSO6102A, Agilent). The min and max values of the arising photo response signal was determined software-wise and recorded for a certain frequency range from 20 Hz up to 500k Hz. The decrease in the min-max values was then used to calculate the bandwidth at  $-3$  dB. The LED's BW was determined to  $\sim 3$  MHz, which ensures a reliable measurement within the defined frequency regime.

**Transient Photo-Response to Pulsed Laser Excitation** The bandwidth of printed PDs was determined using transient photocurrent measurement setup comprising a pulsed laser (1Q355-2, CryLas). The DUT is excited by a 1 ns laser pulse ( $\lambda = 532$  nm) with a repetition rate of 200 Hz. The current response from the DUT, which is mounted in an electrically shielded high-frequency probe station and recorded by an oscilloscope (DSO6102A, Agilent). The pulse response is then transformed by a Fast Fourier Transformation (FFT) into the frequency regime, as shown in **Figure 4.4**. The  $-3$  dB cut-off frequency can then directly be read out. However, this measurement concept is limited by the oscilloscope's memory and thus the number of recorded samples, which in this case does not reveal data in the low frequency regime.

## 4.4. Modeling of Hybrid Electrodes with COMSOL

The AJ printing technique allows for a contact-free deposition of digitally designed geometries, which nicely suits for prototyping and to compare empirically the influence of different grid geometries. Nevertheless, in order to support the experimental data and to

#### 4. Characterization Methods

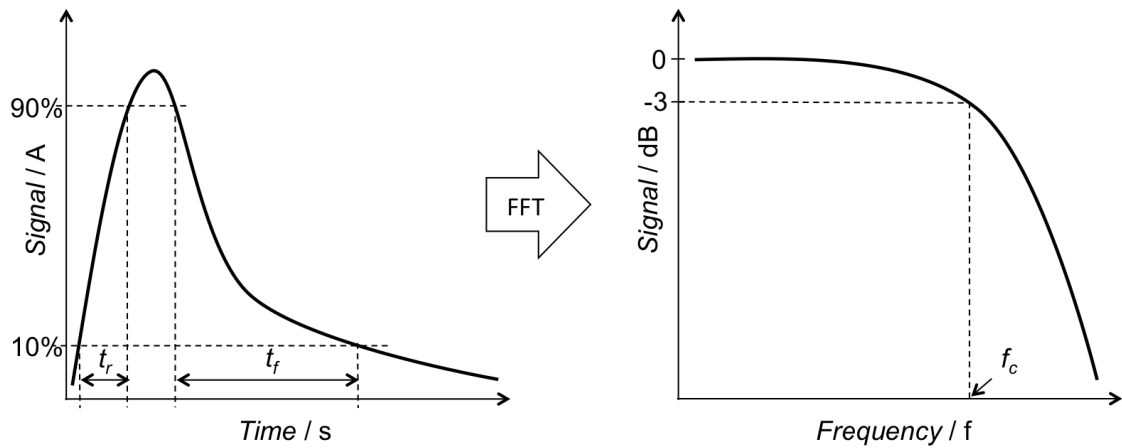


Figure 4.4.: Pulse response of a photodiode with rise ( $t_r$ ) and fall ( $t_f$ ) time. The Fast-Fourier-Transform (FFT) reveals the signal (dB) as a function of frequency ( $f$ ) with the bandwidth  $BW$  defined at  $-3$  dB.

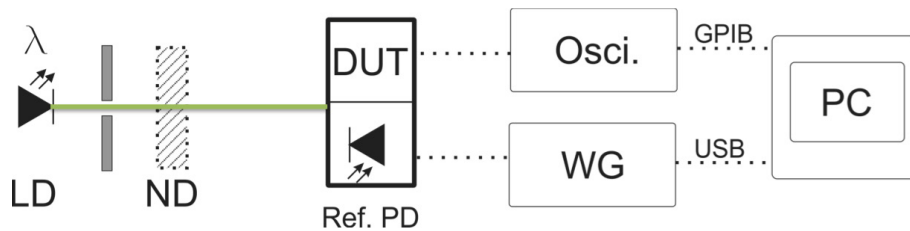


Figure 4.5.: Schematic drawing of transient photocurrent measurement setup using a 1.1 ns excitation laser pulse at 532 nm. The samples are mounted in a shielded probe station. The signal is measured by an oscilloscope. The reverse bias voltage is applied using a wavegenerator.

gain further insight into the spatially resolved physics and electrical processes in a hybrid TC comprising solar cell, a computational tool (*COMSOL Multiphysics*) based on a *finite element method (FEM)* was set up with a strong focus set to the practicality in printed applications.<sup>1</sup> This involves a modeling of realistic conductivities for the conductive components, as well as realistic physical and geometrical values with feature sizes ( $\geq 10 \mu m$ ). The FEM qualifies for the device modeling, since the attention is directed to the hybrid electrode system comprising two materials with completely different optical and electrical properties, which requires a lateral resolved consideration of local physical parameters, such as the potential, resistance and transmittance.

#### 4.4.1. Finite Element Method

**Partial Differential Equations** A partial differential equation 4.7 (PDE) describes an equation containing at least one unknown function  $u$  of the variables  $x_1, x_2, \dots, x_n$  and

<sup>1</sup>A part of this work was carried out in the master thesis of Jan Preinfalk in 2013

its derivatives for at least two variables, which have to fulfill the Dirichlet boundary conditions, saying that the boundaries have to consist of defined values.

$$F(x, u, \nabla u, \nabla^2 u, \dots, \nabla^n u) = 0 \quad (4.7)$$

$$\nabla = \left( \frac{\partial}{\partial x_1}, \frac{\partial}{\partial x_2}, \dots, \frac{\partial}{\partial x_n} \right)^T \quad (4.8)$$

where  $\nabla$  is the nabla operator.

Important for electrical simulations is the *Poisson* equation, which satisfies for electrostatic equations:

$$\Delta u(x) = f(x), \quad x \in \Omega, \quad \Omega \subset \mathbb{R}^d \quad d \geq 1 \quad (4.9)$$

where  $\Delta$  is the Laplace operator, which is the sum of all (local) second partial derivatives;  $f$  is a function (when  $f \equiv 0$  the equation gets a Laplace equation). For electrostatic simulations the continuity equation (Eq. 4.10) depicts the correlation between the current density vector  $\vec{J}$  and the charge density  $\rho$ :

$$\nabla \cdot \vec{J} = -\frac{\partial \rho}{\partial t} = Q \quad (4.10)$$

where  $\rho$  is the charge density; and  $-\frac{\partial \rho}{\partial t}$  its temporal derivative that describes a current source. The electric field vector  $\vec{E}$  relates to the electrostatic potential  $\phi$  in the following way:

$$\vec{E} = -\nabla \cdot \phi \quad (4.11)$$

where  $\vec{E}$  has also a constitutive relation to  $\vec{J}$ :

$$\vec{J} = \sigma \vec{E} \quad (4.12)$$

where  $\sigma$  is the specific electrical conductivity.

These correlations lead to the following PDEs:

$$\nabla \cdot \vec{J} = \nabla \cdot (\sigma \vec{E}) = \nabla \cdot (\sigma (-\nabla \phi)) = -\frac{\partial \rho}{\partial t} \quad (4.13)$$

$$\nabla^2 \cdot \phi = \Delta \cdot \phi = \frac{1}{\sigma} \frac{\partial \rho}{\partial t} \quad (4.14)$$

#### 4. Characterization Methods

**Finite Element Method** Geometrical objects (1D, 2D, or 3D) initially get split up into discrete nodes by applying a (mostly physics-controlled) mesh consisting of triangular and rectangular sub cells, as shown in **Figure 4.6**. The density of nodes can be defined software-wise, where finer meshes lead on the one hand to more precise results. On the other hand, the simulation time rises. The FEM subdivides the unity of *problems* into small "*finite*" portions, which can be solved by differential equations. For each node a starting function is defined, where the PDE is solved by fitting trial functions to minimize the approximation errors.

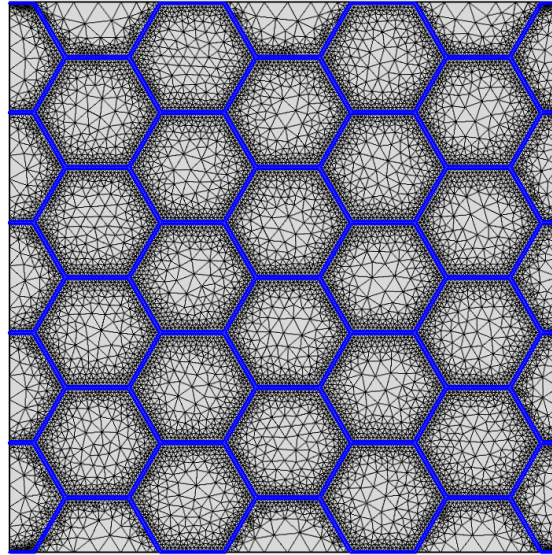


Figure 4.6.: Example of a geometrical layout for simulating a hybrid electrode comprising a hexagonal grid (blue). In each vertex the differential equations are solved according to the boundary conditions using the finite element method.

## 5. AJ Printed Grid Electrodes for Organic Solar Cells



Figure 5.1.: Photograph of a P3HT:PCBM solar cell comprising AJ printed hexagonal Ag grids.

*This chapter addresses the fabrication and simulation of hybrid electrodes as top contacts for organic solar cells. As already introduced in section 4.4, on page 40, these composite electrode systems consist of a homogeneously transparent polymer layer supported by a highly conductive, but opaque metal network, which can consist of Ag nanowire mesh or an Ag grid. These hybrid transparent conductors (TCs) represent very promising systems for a wide field of electronic applications, such as light-emitting devices,[71? –73] or solar cells.[74–79] The latter will be discussed in the following chapter with focus on the fabrication and characterization of AJ printed metal structures and its application as top electrodes for organic solar cells, as illustrated in **Figure 5.1**.*

*In addition to the experimental work on printed metal grids, a computational device simulation tool, introduced in section 4.4 (p.40), was utilized to gain further insight into the different contributions of the vast parameter set. The totality of these sections represent a profound study of grid geometries, material conductivities, and the overall transparency of the hybrid TCs. Furthermore, simulations were conducted on the dependency of the*

current density, which led to an overall re-evaluation of hybrid TC requirements based on the PEDOT:PSS in combination with a printed Ag network.

### 5.1. Metal-Organic Decomposition Ink

In this work, a commercially available metal-organic decomposition (MOD) ink was utilized, which represents a very promising candidate for application in printed organic electronics. As its name implies, a Ag film is formed after the thermal decomposition of a metal-organic complex. In the following, I will present the development of a suitable ink formulation with special focus on the conductivity and printability.

The main focus of the first section is the optimization of digital aerosol jet printed current-collecting grids for transparent hybrid electrodes, towards their application in large area organic optoelectronic devices. This entails the examination of the MOD ink's specific annealing conditions concerning time and temperature. These parameters encompass crucial requisites for the application as top layers on organic functional materials. Furthermore, the ink formulation was optimized for the AJ printing process by adding co-solvents with higher boiling points compared to the main solvent ethanol, as the pristine formulation led to a very poor printing quality at printing speeds  $\geq 5 \text{ mm s}^{-1}$ .

#### 5.1.1. Specific Conductivity

**Figure 5.1** presents the specific conductivity  $\sigma_{Ag}$  of solution processed Ag layers annealed on a hotplate in air at different temperatures ranging from  $80^\circ\text{C}$  to  $200^\circ\text{C}$  and annealing times ranging from 10 s to 1 h. For this experiment, the pristine MOD ink was spin cast on glass slides and annealed directly after coating, since the formation of conductive Ag layers was found to require a wet film. In contrast, already dried or partly dried layers appeared rough and brownish and thermal treatment revealed the lack of a conductive silvery film. Apart from that, it was found that oxygen or humidity is required, since layers fabricated inside a  $N_2$  filled glove box did not reveal similar results. The influence of annealing temperatures and various annealing times was characterized by conductivity measurements done with a 4 wire measurement setup, as described in section 4.2.3 on page 36. The highest conductivity was achievable at  $120^\circ\text{C}$  for 5 – 10 min. Similar results were attained at  $\geq 140^\circ\text{C}$ , but with a drastically reduced annealing time of only  $\sim 10$  s. Since the requirements for organic electronics are very critical in terms of thermal energy input in combination with oxygen devices should be kept as short as possible in the ambient atmosphere.  $140^\circ\text{C}$  for  $\leq 1$  min constitutes a reasonable treatment parameter set, even for ambient processing.

For the sake of completeness, it should be mentioned that, besides the MOD ink also nano-particulate (NP) inks have been considered. However, although they provide higher solid loading, which can be also beneficial for faster printing processes or even to increase the line height to lower the *effective* sheet resistance, at the time these experiments were

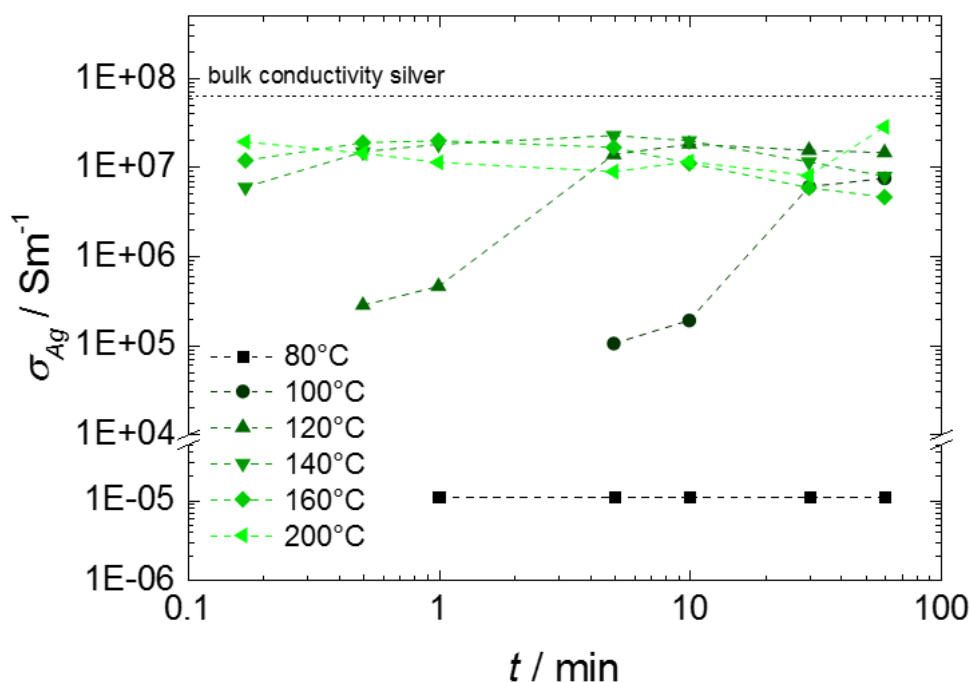


Figure 5.2.: Specific conductivity of spin-coated MOD Ag ink for different annealing temperatures and annealing durations.

performed, no suitable low temperature NP ink was found, which implies that either the specified annealing temperature was too high ( $< 140^{\circ}\text{C}$ ), or the ink viscosity was not in the required range of 1 – 10 cP for usage with the ultrasonic atomizer. To evade the issue with high annealing temperatures, also competitive sintering techniques were considered, such as flash sintering.[21] In light of the fact that the Ag patterns are considered to be printed on top of the organic absorbing material, which implies also a photonic sintering of the organic matter, this idea was rejected.

Thermo-gravimetric analysis (TGA), as shown in **Figure 5.3**, of the MOD ink were measured at  $120^{\circ}\text{C}$  in cooperation with the Institute of Organic Chemistry (OCI, University of Heidelberg) by Torben Adermann. The results were in good agreement with the annealing temperatures and times from Fig. 5.2. The initial mass of 35 mg was reduced due to solvent evaporation and vanishing of organic residues to  $\sim 5$  mg. Hence,  $\sim 14.3$  wt.% solids remained in the crucible, which considering the Ag weight fraction of only  $< 10$  wt.% (see Table 5.1) implies, that in proportion to a Ag content of 10 % one third of the final mass is unknown matter. Due to the fact that the MOD ink is composed to a considerable fraction of organic compounds, it stands to reason that the excess weight can be attributed to organic Ag complexes or partly decomposed organic matter.

The SEM images in **Figure 5.4** show cross-sections produced by FIB<sup>1</sup> cuts to Ag layers

<sup>1</sup>focused ion beam

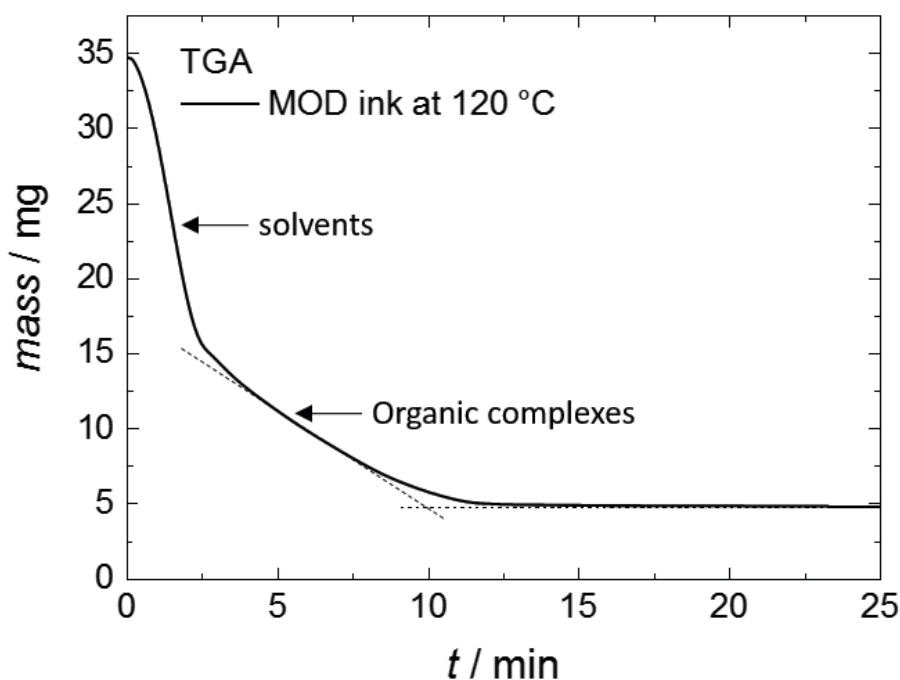
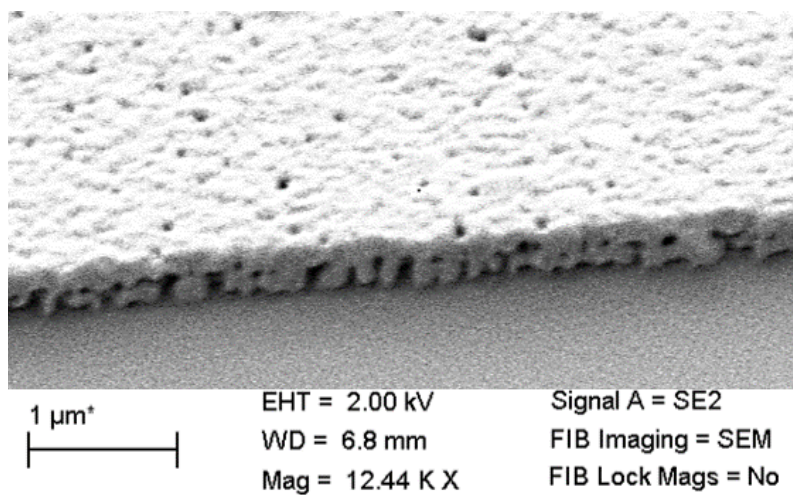


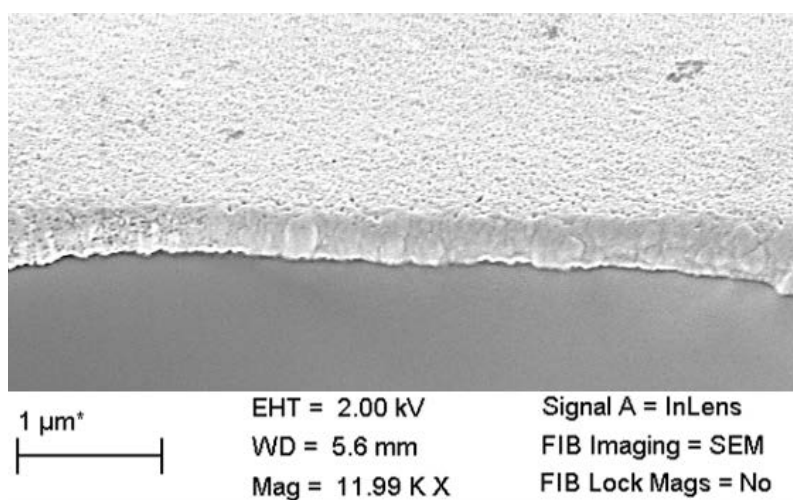
Figure 5.3.: Thermo-gravimetric analysis (TGA) of MOD ink at 120 °C.

printed with aerosol jet from a) the MOD, and b) a nano-particulate (NP) Ag ink (Cabot Ink). The latter was used as a reference fabricated under similar conditions, such as annealing temperature (120 °C) and time (30 min). The NP ink revealed a very densely packed particle layer. Although the annealing temperature of the NP ink specified by the manufacturer to 150 – 200 °C, the images present evident differences in the layer morphology between the inks. The Ag layer from the MOD ink instead revealed a nanoporous interlayer between the Ag and the substrate. This observation supports the findings from the TGA measurements, where an unknown remaining mass besides Ag was detected in the final layer. These measurements were done in cooperation with the Institute of High Frequency Technology (Technical University of Braunschweig) by Christian Müller.

Fabricated layers from the MOD ink exhibit an outstanding specific conductivity of  $\sim 2 \cdot 10^7 \text{ S m}^{-1}$  at the mentioned annealing conditions, as shown in **Figure 5.2**. That corresponds to one third of the bulk Ag conductivity. This leads to two assumptions: First, the dense top layer needs to consist mainly of elementary Ag to reveal the observed conductivity under consideration of the presence of  $\sim 50\%$  residues. Second, it is quite likely that the decomposed organic matter is encapsulated in the cavities between the substrate and a superincumbent dense Ag layer. However, the mesoporous interlayer was not further investigated and gives space for further investigations, if e.g. the cavities are completely filled with organic residues or other decomposition or partly decomposed products. In addition to that, the influence of possible residues at the bottom interface on the work function is not yet investigated.



(a) MOD ink



(b) nano-particulate ink

Figure 5.4.: SEM images of Aerosol Jet printed and subsequently annealed (120 °C) Ag layers on glass a) from the MOD ink, and b) from a nano-particulate Ag ink (Cabot Ink).

### 5.1.2. Ink Formulation for Aerosol Jet Printing

For a proper atomization of the MOD ink using ultra-sonic atomization the pristine ink was diluted with its main solvent ethanol. The atomization clearly improved, meaning the mist density was significantly increased, for a dilution ratio of 1:1. A reason for the poor atomization could partly be ascribed to the viscosity, which is specified to 10 – 300 cP according to the manufacturer (InkTec). Furthermore, the ethanol has a significantly lower surface tension ( $24.6 \text{ mN m}^{-1}$ ) compared to the MOD ink ( $30 - 32 \text{ mN m}^{-1}$ ), which directly correlates to the droplet size according to Eq. 3.1 from section 3.1.1 on page 22. The printing speed emerged to be a crucial parameter for the successful printing of Ag lines and structures. At first glance, an already dried Ag complex ink cannot be annealed

## 5. AJ Printed Grid Electrodes for Organic Solar Cells

Table 5.1.: MOD ink (PR-010, Inktec) ingredients extracted from the MSDS .

Ingredients	% By weight
Silver	< 10 %
Ethanol	< 58 %
2-Amino-1-butanol	2 %

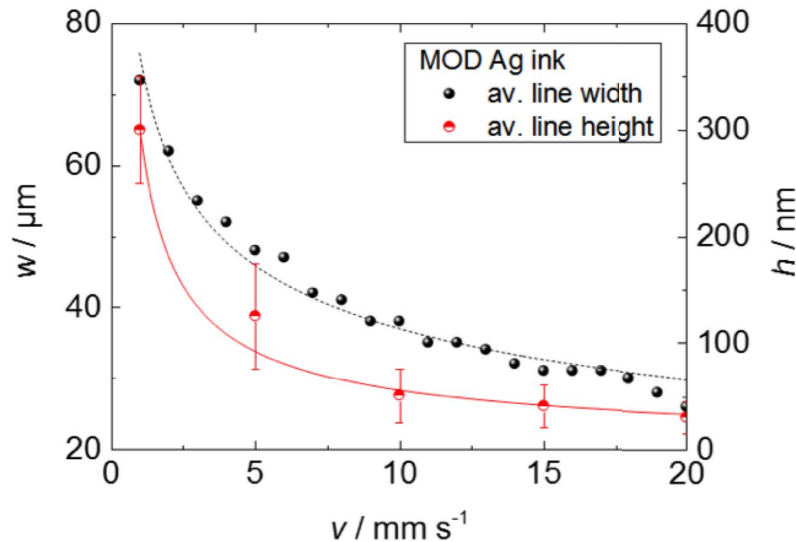


Figure 5.5.: Line width and height of Aerosol Jet printed (AJP) Ag lines from MOD ink on PEDOT:PSS covered glass. The dashed lines are allometric and exponential fits to the line height, as well as an allometric fit to the line width.

anymore. It turns brownish and rough. In addition to that, an increase in printing speed is indispensable to guarantee a wet film after the printer process with its sequential tool path is finished.

Therefore, the sheath and atomizer gas flows were set to constant values (see Table 5.2), while the printing speed  $v$  was varied from  $1 \text{ mms}^{-1}$  to  $20 \text{ mms}^{-1}$ . The qualitative profile analysis is shown in **Figure 5.5**, exhibiting the nominal line width and height plotted as a function of the printing speed. The reduction of ink volume per area due to a faster substrate motion leads to both, a nominal reduction in line width and the line height. However, the widths and heights in the graph depict average values extracted from white light interferometric profile measurements. As illustrated in **Figure 5.6**, the increasing printing speeds leads to an increasing surface roughness culminating in line disruptions, which negatively influence the line conductivity. Underlying causes can be found in the increasing surface-to-volume ratio, which may provoke an instability leading to uncontrolled drying effects. [80–83] Moreover, an intensified influence of the dry  $N_2$  sheath gas flow with respect to the surface-to-volume ratio may affect the drying kinetics. In addition, Figure 5.5 shows fits to the line height and width. In both cases an allometric fit ( $w = A * v^B$ ) was chosen, where  $A$  and  $B$  are not further specified. That is based on the fact that the material volume flow rate is kept constant, while the velocity increases,

which results theoretically in a decrease of volume per line segment. A good agreement was found for both the line height and width.

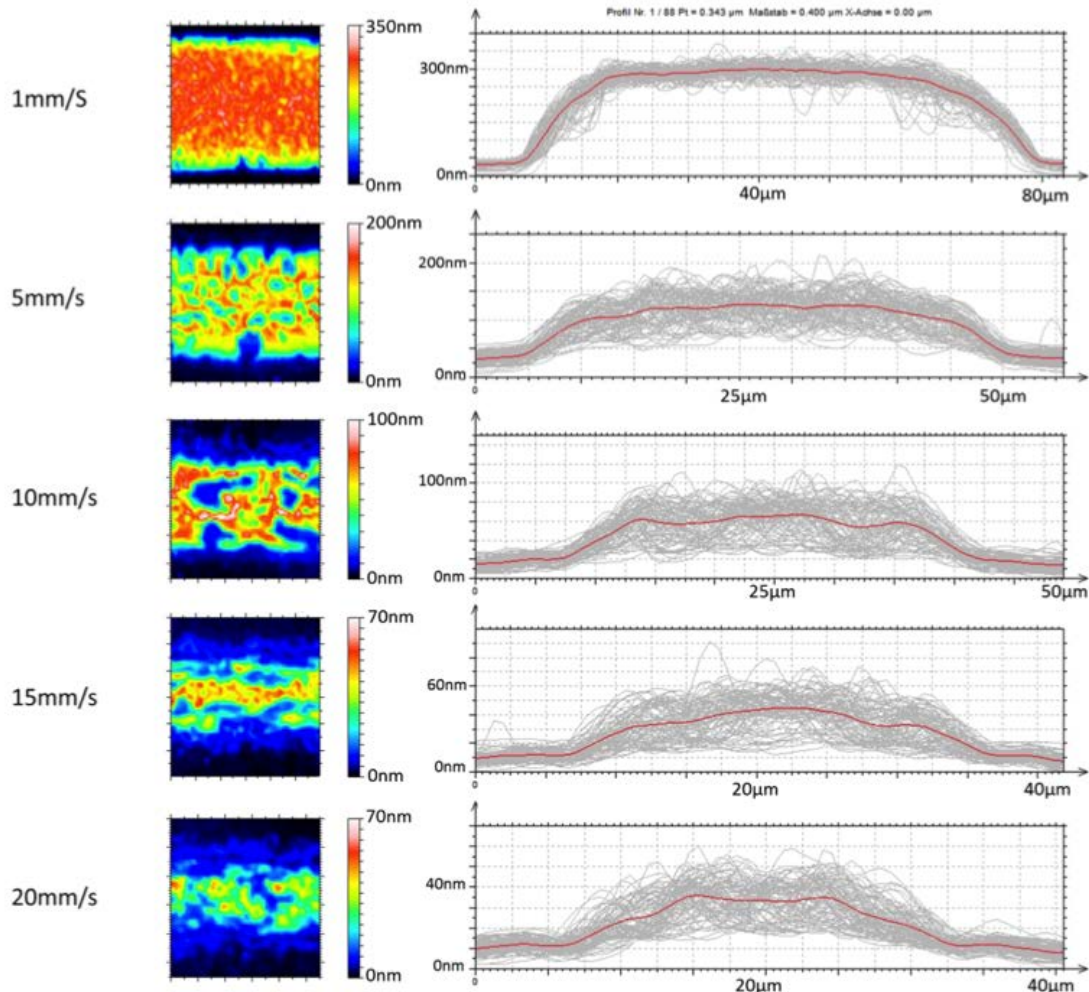


Figure 5.6.: False color topography images of the line heights and cross-sectional profiles of AJP Ag lines at various printing speeds recorded with white light interferometry.

For an application in transparent electrode systems, e.g. in large area organic solar cells, the line shape and its conductivity at faster printing speeds ( $> 5 \text{ mms}^{-1}$ ) are of great importance. The prevalent uncontrolled drying kinetics prevent an increase in printing speed and need to be suppressed. One approach has been described by Fukuda *et al.* in 2013, where the impact of ambient conditions on the drying kinetics and thus the quality of inkjet printed water-based nanoparticle silver inks was investigated.[84] They observed a suppression of the solvent evaporation speed by increasing the ambient humidity, leading to a change in the cross-sectional line shape of the printed structures. Another approach, which is from a practical point of view much more convenient, was chosen to restrain the proceeding drying kinetics, and was published by Kim *et al.* in 2006.[82] They added ethylene glycol (EG) with a boiling point ( $BP$ ) of  $197^\circ\text{C}$  to a water based Ag nanoparticulate ink. EG exhibits a much lower surface tension compared to water and effec-

## 5. AJ Printed Grid Electrodes for Organic Solar Cells

Table 5.2.: AJ printing parameter set for MOD:ethanol ink formulation.

Nozzle Diameter	100 $\mu\text{m}$
Sheath Gas Flow	20 ccm
Atomizer Gas Flow	20 ccm

tively compensates the Marangoni-type outward convection flow with a gradient-induced inward Marangoni flow. At this point, it is important to explicitly state, that the present drying kinetics are not necessarily based on Marangoni type flows. However, a deceleration of the drying is expected. Therefore, the impact of three different solvents (toluene, anisole, and EG) with  $BP$  between 110 °C and 197 °C was investigated as additives for the MOD ink. All of these solvents are very miscible with ethanol, which was an obvious pre-requisite for the preliminary choice. In the following text, the formulations will be coded, as shown in Table 5.3.

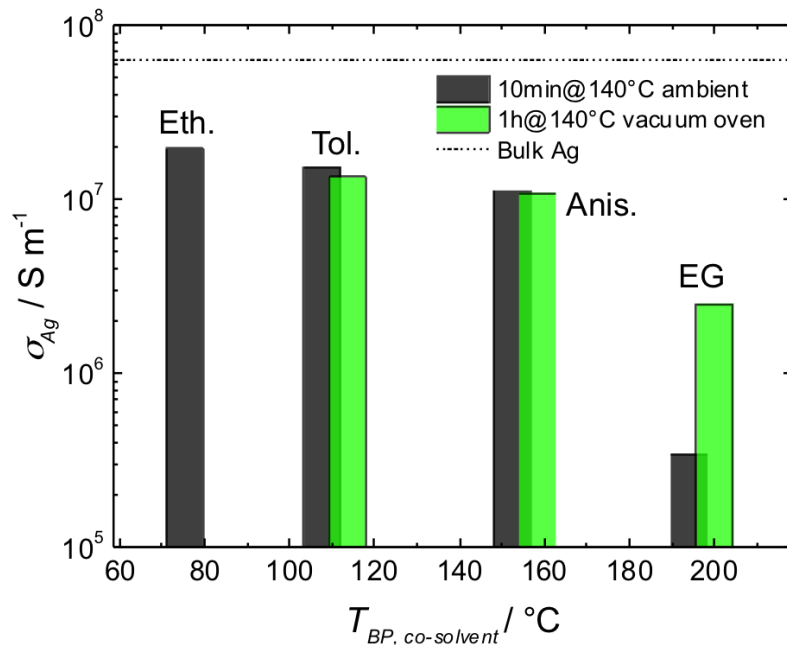


Figure 5.7.: Specific conductivity measurements of the diluted pristine MOD ink and the formulations with 10% additional co-solvent as a function of the additive's boiling point. The annealing temperature was set to 140 °C. The ambient conditions were varied with 10 min in air and 1 h in a vacuum oven.

**Figure 5.7** reveals the impact of the additives, with different boiling points, on the specific conductivity  $\sigma_{Ag}$  of each formulation, as a function of co-solvent boiling point. These data were obtained from 4 wire resistance measurements of spin cast formulations. A marginal decrease in  $\sigma_{Ag}$  can be observed for the formulations with 10% toluene (#2) and 10% anisole (#3). However, a huge drop in  $\sigma_{Ag}$  was measured for the 10% EG (#4) containing formulation. The loss in  $\sigma_{Ag}$  was assumed to be attributed to residual solvent trapped in the layer. Therefore, the influence of annealing conditions under a reduced oxygen atmosphere was investigated by annealing in a vacuum oven (15 mbar)

for 1 h. Thereby, the conductivity of the EG containing ink could be increased to around  $2.5 \cdot 10^6 \text{ S m}^{-1}$ . It was found, that oxygen is needed for the decomposition process and hence for a high specific conductivity.

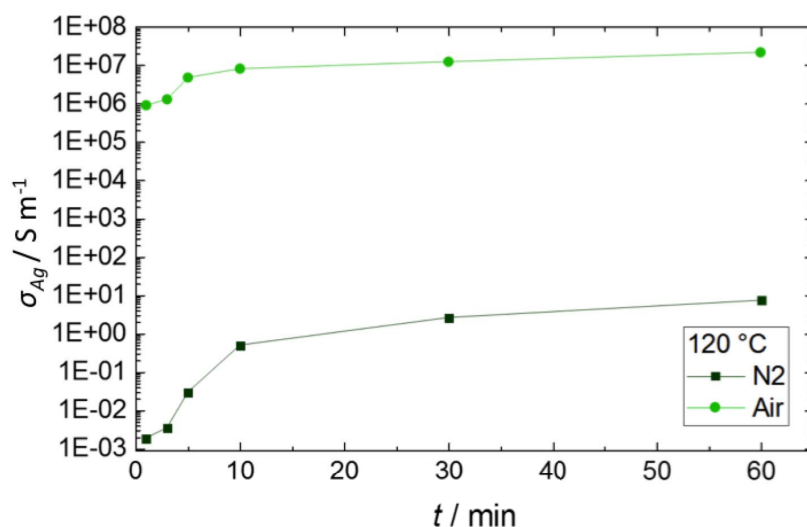


Figure 5.8.: Specific conductivity measurements of the pristine MOD ink, annealed in air and under nitrogen ( $N_2$ ) atmosphere, at  $120^\circ \text{C}$ , as a function of annealing time ( $t$ ). (data obtained with permission from Dr. A. Morfa, LTI, KIT)

The necessity of oxygen during the decomposition process, taking place to form elementary Ag, is shown in **Figure 5.8**. Spin cast MOD layers were annealed on a hotplate either in air or in nitrogen atmosphere inside a glove box. This experiment shows, that under exclusion of oxygen the specific conductivity remained around 7 orders of magnitude lower than annealed under presence of oxygen. In both cases a significant increase in conductivity could be observed for annealing times below 10 min. A further increased time solely marginally improved it. These results are in good conformity to the previous experiment, where the samples were annealed in a vacuum oven at a pressure of  $15 \text{ mbar}$ .

The images of AJ printed Ag lines from **Figure 5.9** show the print quality obtained from the different formulations. For better comparison, the printing parameters were set to achieve  $\sim 40 \mu\text{m}$  line widths and comparable line heights of  $\sim 200 \text{ nm}$ . All lines were printed at  $5 \text{ mm s}^{-1}$  on top of a PEDOT:PSS covered glass substrate and afterwards annealed at  $140^\circ \text{C}$  on a hotplate. The formation of line disruptions, predominantly visible for #1, was significantly reduced with all three other formulations with a clear trend to more homogeneous print qualities towards higher BP additive. #4 gives evidently the smoothest print quality. Nevertheless, recalling the fact that #4 reveals by far the lowest conductivity, it is therefore inappropriate for the purpose of high performance current collecting grids.

The impact of the anisole fraction ( $\chi_{Anisol}$ ) in the MOD ink was further investigated with focus on the specific conductivity. The annealing conditions were set to  $140^\circ \text{C}$  for 1 min.

## 5. AJ Printed Grid Electrodes for Organic Solar Cells

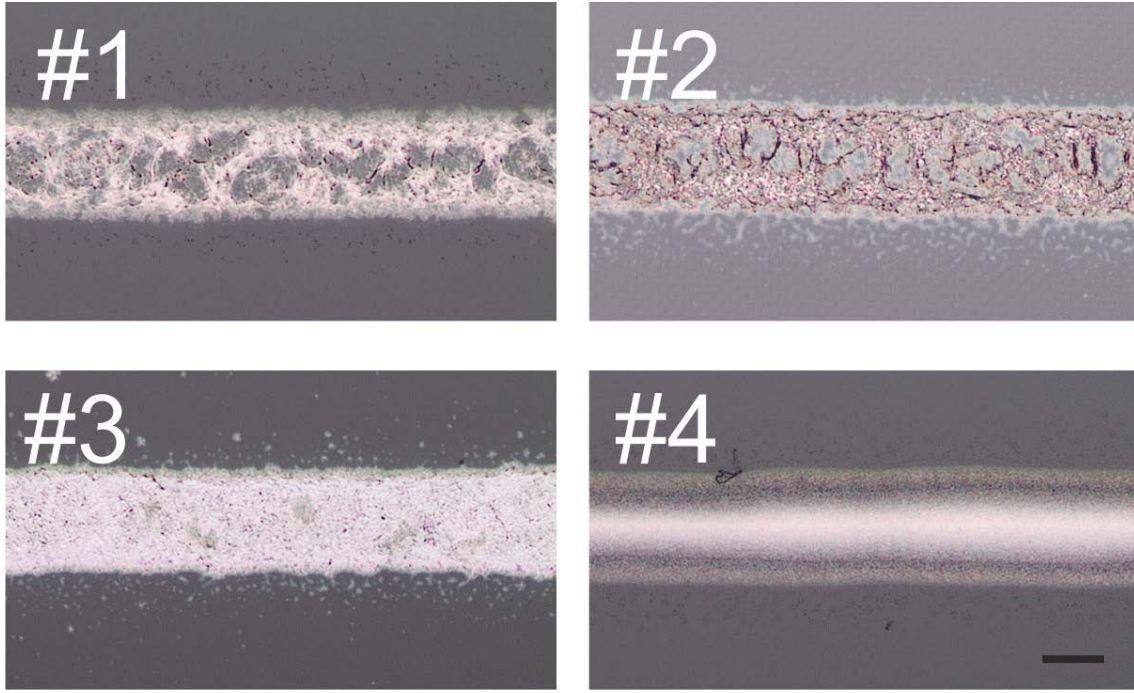


Figure 5.9.: Microscope images of AJ printed Ag lines at  $5 \text{ mm s}^{-1}$ . without co-solvent (#1), with 10% toluene (#2), 10% anisole (#3), and 10% ethylene glycol (EG) (#4). (Scale bar  $20 \mu\text{m}$ )

This parameter set, embodied a thermal exposure still acceptable for organic functional materials and a relatively short annealing time to minimize possible degradation processes occurring in organic materials at ambient conditions.

**Figure 5.10** shows the  $\sigma_{MOD}$  for a diluted MOD formulation with ethanol in a ratio of 1 : 1, and for formulations containing additionally a certain volume fraction of anisole.  $\sigma_{MOD}$  stayed constant or even slightly increased for the lowest anisole fraction of 5%, which could be ascribed to the fabrication and measurement uncertainties. A drop of  $\sim 20\%$  was observed for 10% anisole, which nevertheless still constituted a very good value regarding the annealing conditions. Furthermore, it showed a significant improvement in terms of printability. A further increase of  $\chi_{Anisole}$  led to a dewetting of the MOD formulation on the glass slides, which made characterization of the conductivity impossi-

Table 5.3.: Specific conductivities  $\sigma_{Ag}$  for annealed Ag layers at  $140^\circ\text{C}$  on a hotplate (hp) for 10 min and in a vacuum oven (vac) for 1 h. Surface roughness  $r_{rms}$  of  $20 \times 20 \mu\text{m}^2$  areas of AJ printed Ag lines.

Formulation	Code	$\sigma_{Ag} [S m^{-1}]$ (hotplate)	$\sigma_{Ag} [S m^{-1}]$ (vacuum)
MOD:EtOH (1:1)	(#1)	$1.97 \cdot 10^7$	-
MOD:EtOH:Tol. (1:1:0.1)	(#2)	$1.52 \cdot 10^7$	$1.35 \cdot 10^7$
MOD:EtOH:Anis. (1:1:0.1)	(#3)	$1.12 \cdot 10^7$	$1.07 \cdot 10^7$
MOD:EtOH:EG (1:1:0.1)	(#4)	$3.41 \cdot 10^5$	$2.48 \cdot 10^6$

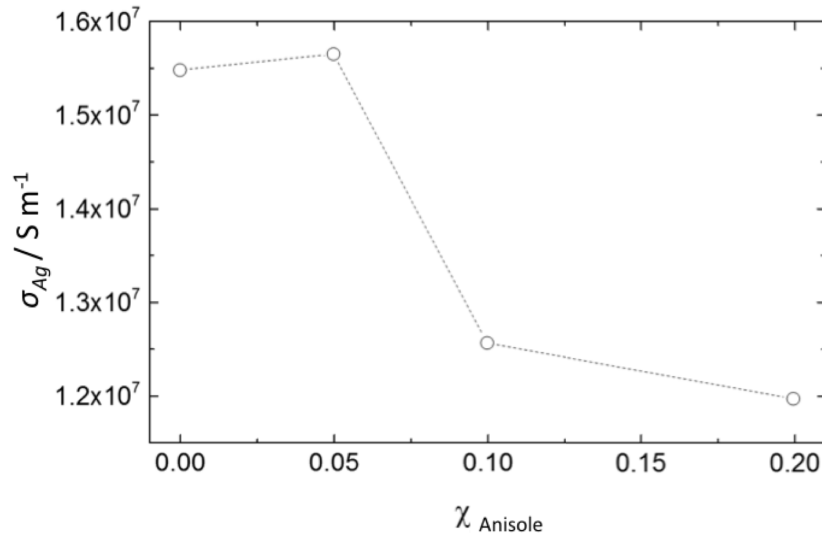


Figure 5.10.: Specific conductivity of MOD ink as a function of anisole fraction.

ble, and furthermore indicates an increase in the surface tension of the formulation.

### 5.1.3. Summary

The suitability of the MOD Ag ink could be confirmed in terms of annealing temperature and time for the use in organic electronics. A post-processing parameter set of  $< 140^\circ \text{C}$  and  $< 1 \text{ min}$  was found to be satisfactory for a conductivity of  $\sim 1 - 2 \cdot 10^7 \text{ S m}^{-2}$ . Although, the nano-porous interface between the Ag and the PEDOT:PSS is not fully investigated, it can be assumed that a certain amount of organic residues is trapped within the cavities. Nevertheless, an Ag / PEDOT:PSS interface is present at the line edges, which is, considering a lateral charge collection from the PEDOT:PSS area hereby assigned. However, to be able to AJ print, the MOD ink was diluted with the main solvent of the pristine formulation. Moreover, the poor print quality at increased printing speed required further ink modifications to reduce unwanted drying kinetics, which was tackled by the addition of higher boiling point additives. A reasonable compromise between print quality and specific conductivity was found with the addition of 10% anisole. Additives with higher boiling points, such as EG, completely negate the advantages of the low temperature and fast annealing process with the MOD ink. Finally, the MOD:anisole formulation revealed a specific conductivity of  $\sim 1.25 \cdot 10^7 \text{ S m}^{-1}$ .

## 5.2. Aerosol Jet Printed Metal Grids

In the section above, a suitable ink formulation was established, which was then used in all following experiments to fabricate hybrid TCs based on AJ printed grids. The main criteria for these electrode systems are in a first place a high lateral conductivity paired

## 5. AJ Printed Grid Electrodes for Organic Solar Cells

with a high optical transparency in the UV-Vis to NIR spectrum. Therefore, spectral transmittance measurements were conducted. The *equivalent* metal sheet resistance  $R_{sheet,M}$ , which is defined as the resistance across a squared grid, was recorded at squared electrode areas by measuring over two opposing contact pads, which releases mainly the contribution of the markedly higher conductive and thus dominant metal mesh. *Equivalent* in this case refers to a sheet resistance corresponding to the one of a homogeneous conductive layer.

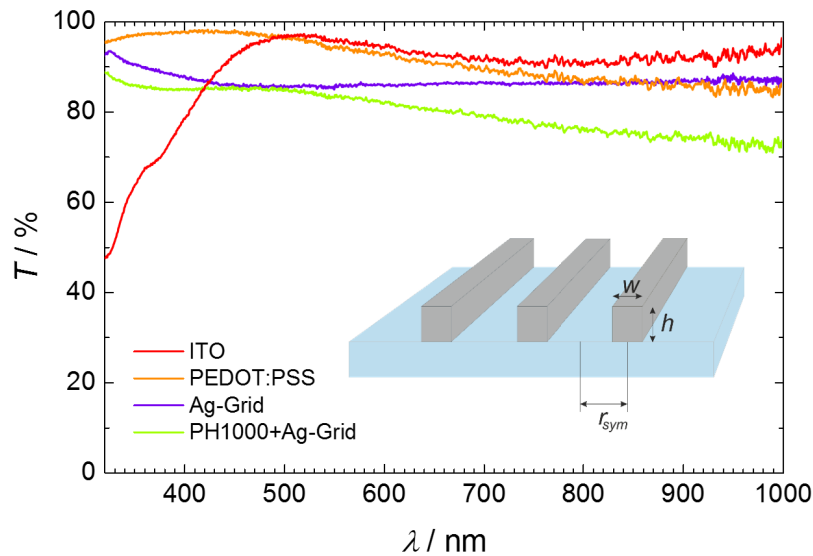


Figure 5.11.: Transmittance spectra of a  $\sim 160$  nm thick PEDOT:PSS TC, a Ag grid with a symmetry radius  $r_{sym}$  of  $200 \mu\text{m}$  and  $\sim 30 \mu\text{m}$  wide lines, and the hybrid electrode with Ag grid and PEDOT:PSS layer.

The presence of metal grids on a TC, such as PEDOT:PSS, significantly reduces the overall TC's sheet resistance.[85] This allows for very thin PEDOT:PSS layers, which conversely increases the TC transparency. The result is a superposition of the transparencies of the laterally conductive PEDOT:PSS and the Ag mesh. **Figure 5.11** illustrates the superposition of a  $\sim 160$  nm thick PEDOT:PSS TC and a 1-dimensional Ag grid with  $r_{sym} = 200 \mu\text{m}$ , which shows markedly the reduced resulting transmittance spectra of the PEDOT:PSS in the near-infrared (NIR). To counteract the high absorption in the NIR the PEDOT:PSS layer thickness can be reduced, since the lateral path lengths are drastically reduced by the grid.

**Figure 5.12** demonstrates the influence of the PEDOT:PSS layer thickness on the transmittance spectra of hybrid TCs comprising a 1-dimensional Ag grid with a symmetry radius  $r_{sym}$  of  $200 \mu\text{m}$  and a line width  $w$  of  $\sim 25 \mu\text{m}$ . The PEDOT:PSS sub-layer was spin cast with various spin speeds of  $4k$ ,  $3.5k$ , and  $2k$  rpm correspond to thicknesses of  $\sim 70$  nm,  $\sim 80$  nm, and  $\sim 120$  nm, respectively. As to be expected, the transmittance of hybrid TCs, increases in the NIR with lower PEDOT:PSS thicknesses. An almost constant transmittance in the visible to near-infrared regime can be achieved for PEDOT:PSS thicknesses  $\leq 100$  nm.

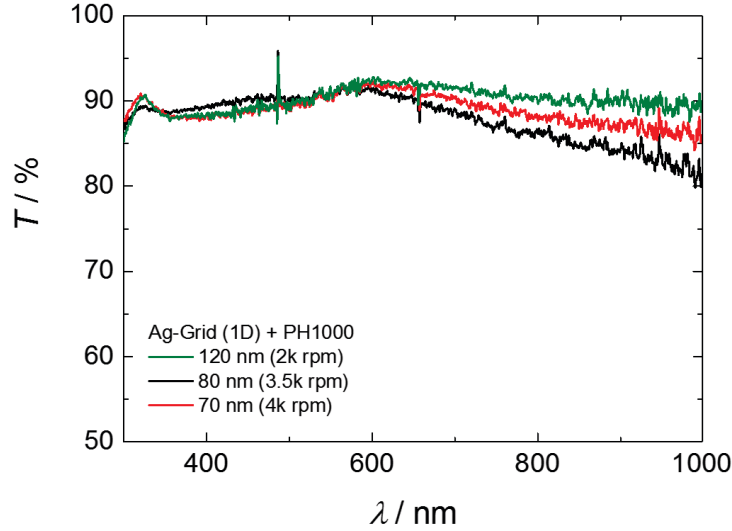


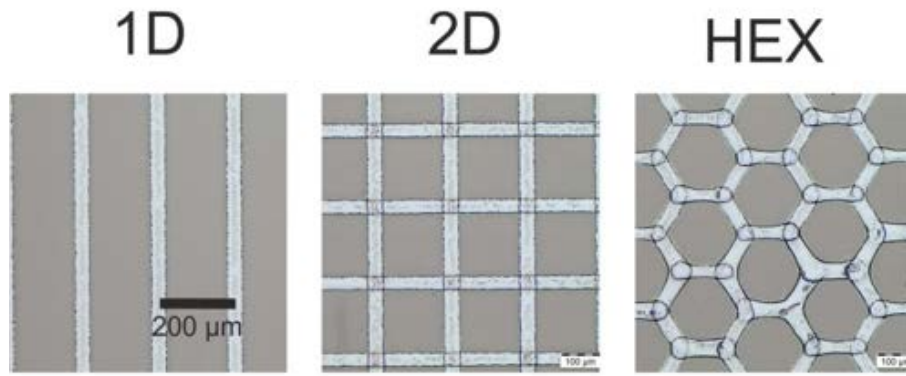
Figure 5.12.: Transmittance spectra of hybrid electrodes with an Ag grid symmetry radius  $r_{sym}$  of  $200 \mu\text{m}$  and line width  $w$  of  $\sim 25 \mu\text{m}$  comprising different PEDOT:PSS layer thicknesses by different spin speeds.

**Figure 5.13** shows the transmittance spectra of 1-dimensional, symmetrically squared, which will be named in the following as *2-dimensional*, and hexagonal grids with  $r_{sym} = 100 \mu\text{m}$ , which were processed on  $100 \text{ nm}$  thick PEDOT:PSS (PH1000, Heraeus) covered glass slides. The PEDOT:PSS covered glass slide ( $1.1 \text{ mm}$  Borofloat33, Schott) was used as the reference spectra. The microscope images in a) present the AJ printed grids having line widths of  $\sim 30 \mu\text{m}$  ( $\pm 5 \mu\text{m}$ ). The 1-dimensional hybrid electrode entails the highest transparency with over  $85 \%$ . The drop in transparency for the 2-dimensional and hexagonal grids arise from the increased shading for equal symmetry radii. The measured values for the transmittances correlate well with calculated values for surface coverage from the equations 5.9 and 5.12 presented on page 63. Nevertheless, the acceleration and deceleration of the x-y stage in short line sections can additionally influence the resulting line width. That can be observed in the image of the hexagonal grid. All geometries however show similar effective sheet resistances  $R_{sheet,M}$  of  $\sim 3 \Omega/\square$ .

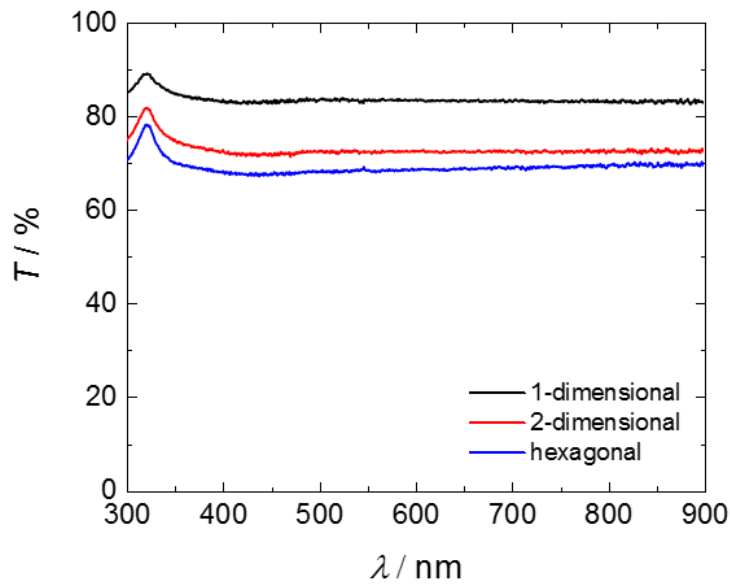
**Figures 5.14** and **5.15** show microscope images and transmission spectra of hybrid electrodes comprising a symmetry radius of  $200 \mu\text{m}$  and  $400 \mu\text{m}$ , respectively. The different geometries with a  $r_{sym} = 200 \mu\text{m}$  still show a perceptible difference in transparency, where the 1-dimensional geometry reaches  $90 \%$ , the 2-dimensional and hexagonal ones present transmittances of  $84$  and  $86 \%$ , respectively. Merely a slight increase in transparency could be observed for  $r_{sym} = 400 \mu\text{m}$ , where all geometries show transparencies between  $90$  to  $92 \%$  with equivalent sheet resistances of  $10 \Omega/\square$ .

The Table 5.4 summarizes the values equivalent sheet resistances  $R_{sheet,M}$  for the presented transmittance data, which accounts for  $2.7 - 3 \Omega/\square$  for  $r_{sym} = 100 \mu\text{m}$ ,  $4.9 - 5 \Omega/\square$  for  $r_{sym} = 200 \mu\text{m}$ , and  $10 - 10.1 \Omega/\square$  for  $r_{sym} = 400 \mu\text{m}$ .

## 5. AJ Printed Grid Electrodes for Organic Solar Cells



(a)  $r_{sym} = 100 \mu m$

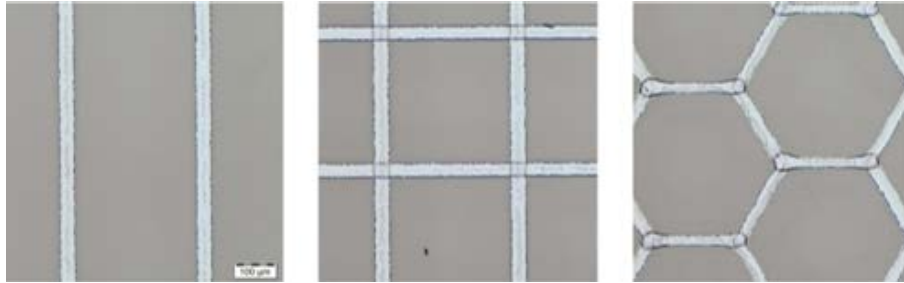
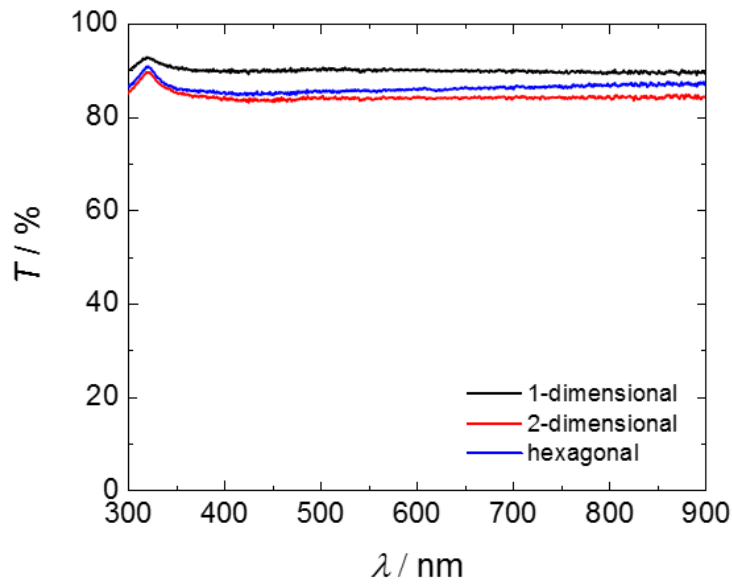


(b)

Figure 5.13.: Microscope images and transmittance spectra of 1-dimensional, 2-dimensional (squared), and hexagonal AJ printed Ag grids printed on a 100 nm thick highly conductive PEDOT:PSS (PH1000) covered glass substrate with symmetry radii of  $100 \mu m$ .

Table 5.4.: Sheet resistances measured at  $1 \times 1 \text{ cm}^2$  AJ printed 1-dimensional, 2-dimensional, and hexagonal Ag grids from formulation #3. Grids printed at  $5 \text{ mms}^{-1}$  with a line width of  $\sim 20 \mu m$

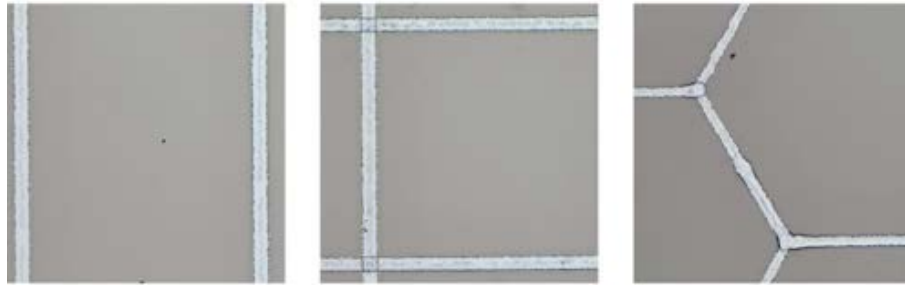
$r_{sym}$	$R_{sheet,M}$ [ $\Omega/\square$ ]		
	1-dimensional	2-dimensional	hexagonal
$100 \mu m$	$3.0(\pm 0.2)$	$2.8(\pm 0.3)$	$2.7(\pm 0.1)$
$200 \mu m$	$5.0(\pm 1)$	$4.9(\pm 1)$	$5.0(\pm 1)$
$400 \mu m$	$10.0(\pm 2.5)$	$10.0(\pm 2)$	$10.1(\pm 1)$

(a)  $r_{sym} = 200 \mu m$ 

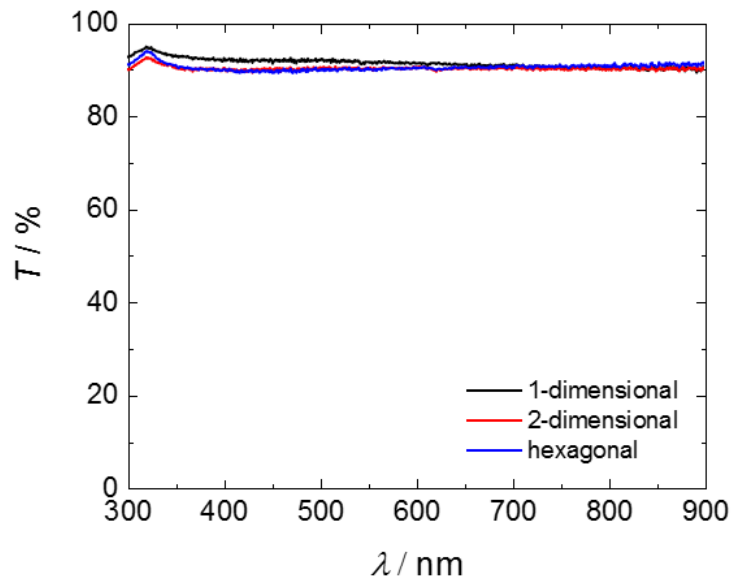
(b)

Figure 5.14.: Microscope images and transmittance spectra of 1-dimensional, 2-dimensional, and hexagonal AJ printed Ag grids printed on a 100 nm thick highly conductive PEDOT:PSS (PH1000) covered glass substrate with symmetry radii of  $200 \mu m$ .

## 5. AJ Printed Grid Electrodes for Organic Solar Cells



(a)  $r_{sym} = 400 \mu m$



(b)

Figure 5.15.: Microscope images and transmittance spectra of 1-dimensional, 2-dimensional, and hexagonal AJ printed Ag grids printed on a 100 nm thick highly conductive PEDOT:PSS (PH1000) covered glass substrate with symmetry radii of  $400 \mu m$ .

### 5.2.1. Summary

The accuracy of the printed structures has a key role for transmittance and resistance relevant applications. In case of transparent electrode systems two important factors have to be considered. In this section, three different grid geometries (1-dimensional, 2-dimensional, and hexagonal) were fabricated with different symmetry radii ranging from  $100\ \mu\text{m}$  to  $400\ \mu\text{m}$  and Ag line widths of  $\sim 20\ \mu\text{m}$ . Unsurprisingly, the 1-dimensional grids demonstrated the highest transparency. However, the measured *equivalent*  $R_{sheet,M}$  resulted similar for all geometries. This has the trivial background, that the  $R_{sheet,M}$  was measured between opposing sides of a square grid area, which considers only the current flow in this particular direction and orthogonal interconnections only show minor influence. A tendency to lower statistical deviations in the  $R_{sheet,M}$  can be observed for the 2-dimensional and hexagonal grids, which arises from the existence of interconnecting current paths, which compensate possible line disruptions in single lines.

## 5.3. Mechanical Stability

As described in Section 2 on page 6, the organic soft matter properties enable the printing of flexible devices. ITO, the commonly used TC in organic solar cells, is mechanically stiff and therefore constitutes a weak spot in terms of device flexibility due to the formation of cracks while bending or stretching. Even low mechanical stress already provokes irreparable losses in conductivity and directly impacts the device performance. Other sources of material fatigue constitute buckling and delamination processes, which mainly occur at very high mechanical loadings. Hence, optical and electrical measurements during strain and bending experiments were conducted in cooperation with the Institute of Applied Materials (IAM, KIT campus North) and give valuable information about the fatigue resistance of the different electrode systems. Further information can be found elsewhere.[86]

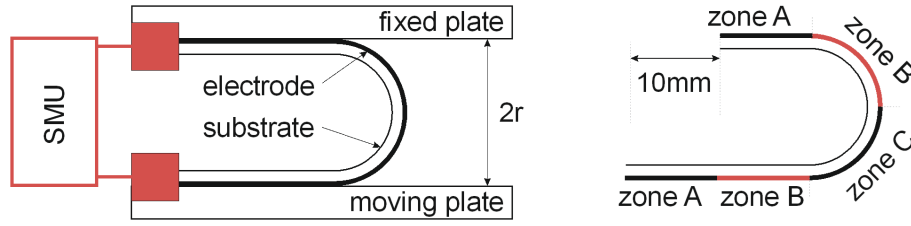
### 5.3.1. Bending Fatigue in Hybrid Electrodes

Cyclic bending experiments simulate the ongoing fatigue occurring mainly due to repetitive stress. This reflects the mechanical load applied in foldable or rollable applications. The mechanical load of repetitive actions can be much lower than the maximum sustainable stress of a device.

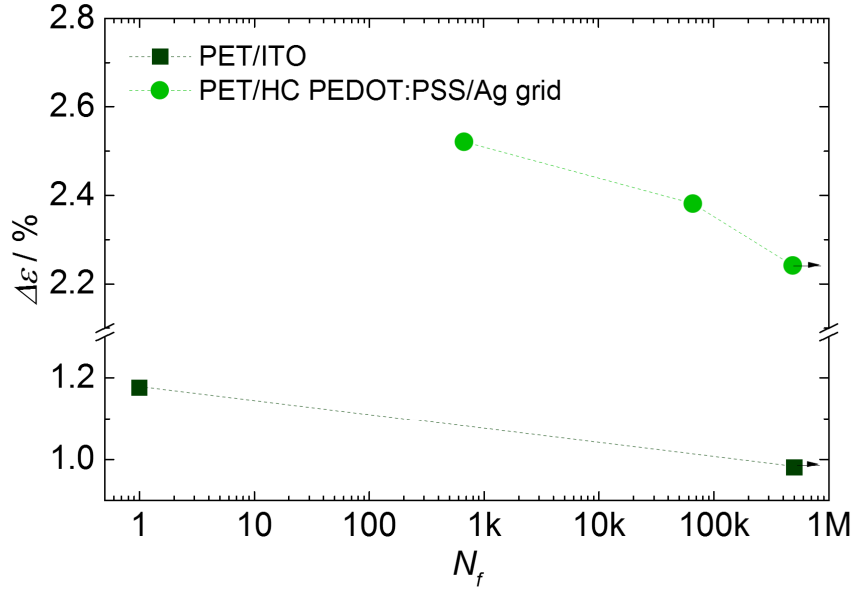
All mechanical fatigue measurements, including strain and bending fatigue, were performed in cooperation with the Institute of Applied Materials (IAM, KIT campus North) by Thomas Haas.

**Figure 5.16(a)** presents a schematic drawing of the apparatus („CK-770FET“, *CK Trading Co.*), which was used for the automated resistance measurements (4-point, Agilent 34410A) as a function of bending cycles  $N_f$  at defined bending radii  $r$ . The sample is

## 5. AJ Printed Grid Electrodes for Organic Solar Cells



(a) Schematic of the bending apparatus



(b) Manson-Coffin-Plot

Figure 5.16.: Mechanical stability measurements using an automated resistivity measurement as a function of bending cycles. a) Schematic drawing of measurement setup. b) Fatigue tests: Calculated lateral strain  $\Delta\varepsilon$  in % as a function of number of bending cycles  $N_f$ . [86]

attached between a fixed and a moving plate, where the distance between the two plates corresponds to twice the bending radius  $2 \cdot r$ . The moving plate displaces 10 mm with an oscillation frequency of 5 Hz driven by a linear eccentric action machine. The cyclic fatigue was recorded simultaneously using a source measurement unit (SMU). The experiment was conducted for ITO covered PET foil and for the hybrid electrodes comprising AJ printed Ag grids and blade coated PEDOT:PSS covered PET foil. Further information about the investigated electrode systems can be found in Table 5.5. Since the ITO covered PET comprises a different substrate thickness compared to the PEDOT:PSS and hybrid electrode, the different substrate thicknesses were considered in Eq. 5.1:

$$\Delta\varepsilon = \frac{d_{el} + d_{sub}}{2r} \quad (5.1)$$

where  $d_{el}$  is the thickness of the conductive matter; and  $d_{sub}$  is the thickness of the substrate.

Table 5.5.: Material list of different electrode systems.

<i>Electrode System</i>	<i>Compound Thicknesses</i>	<i>Additional Information</i>
<i>flexible ITO</i>	PET: 125 $\mu\text{m}$ ITO: 50 nm	ITOPET50, Visiontec
<i>Hybrid Electrode</i>	PET: 175 $\mu\text{m}$ PEDOT:PSS: 100 nm Ag grid: 300 nm	PH1000 (Heraeus) Ag MOD ink #3 (Inktec) PET (GN6400, Hostaphan)
<i>conductive PEDOT:PSS</i>	PET: 175 $\mu\text{m}$ PEDOT:PSS: 100 nm	PH1000 (Heraeus) PET (GN6400, Hostaphan)

Figure 5.16(b) presents in a Manson-Coffin-plot, the number of bending cycles before malfunction as a function of the relative elongation  $\Delta\varepsilon$ , arising from Equation 5.1.[87, 88] Noteworthy is, that ITO covered PET shows no significant fatigue at  $\Delta\varepsilon$  of 0.98% ( $r = 6.4$  mm), neither after 500,000 cycles. However, for a slightly decreased bending radius, represented by an increase in  $\Delta\varepsilon = 1.176\%$  ( $r = 5.3$  mm), the plot in Fig. 5.16(b) indicates a malfunction already at the first cycle, which means the stop criterion of 5% higher resistance compared to the initial value was reached. The bending fatigue in the printed hybrid electrodes, in contrast, occur at markedly higher relative strains. Thus, no irreversible bending fatigue after 500,000 cycles could be observed at a corresponding bending radius of 3.9 mm. A malfunction is however observable at  $r = 3.7$  mm after  $\sim 100,000$  cycles. Nonetheless, the hybrid electrode clearly demonstrate its mechanical robustness towards repetitive flexing. Furthermore, it appears that the fatigue mechanism differs from the one in ITO. The latter indicates abrupt formations of cracks due to the brittleness. The results from the hybrid electrode instead point rather to a more subtle process, where the soft PEDOT:PSS partly compensates or attenuates the fatigue.

### 5.3.2. Strain Fatigue in Hybrid Electrodes

To further investigate, which kind of processes are prevalent during mechanical stress and hence cause the fatigue, the samples were optically and electrically analyzed, while applying a monotonous ascending strain.

Therefore, the samples were placed between the electrically connected substrate clamps. The electrical resistance was then recorded by a 4-probe measurement during the elongation of the electrodes. The strain velocity was set to  $2 \mu\text{ms}^{-1}$ . The compact apparatus could also be placed under an optical or scanning electron microscope for a simultaneous observation of damage, e.g. by crack formation in the sub-micrometer regime.

**Figure 5.17(a)** presents the change in resistance as a function of mechanical strain conducted for ITO covered PET, conductive PEDOT:PSS, and the hybrid electrodes. The substrate specifications can be gathered from Table 5.5. The theoretical values (dashed line) describe the increase in resistance due to the geometrical changes in cross-section of

## 5. AJ Printed Grid Electrodes for Organic Solar Cells

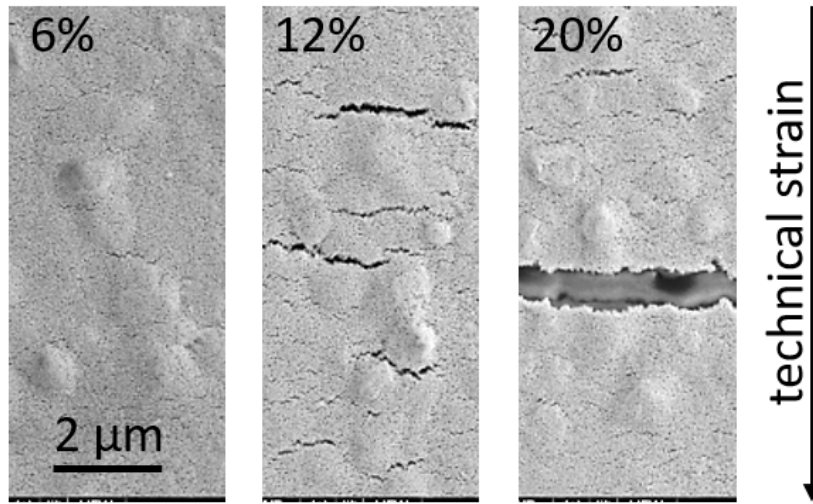
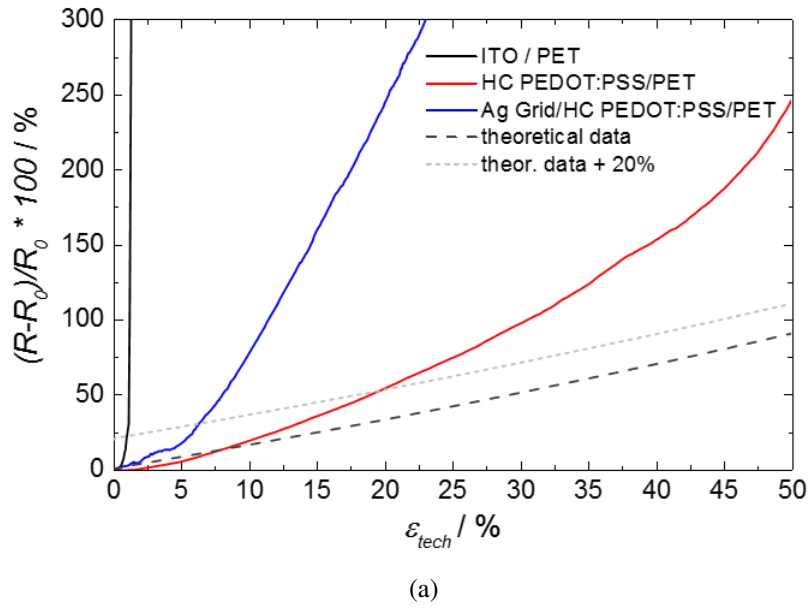


Figure 5.17.: Mechanical stability measurements using an automated resistivity measurement as a function of elongation. a) Fatigue tests: Increase in resistivity in % as a function of lateral strain in %. b) SEM images of during elongation showing the PET/PEDOT:PSS/Ag sample at 6 %, 12 %, and 20 %. [86]

the conductor during elongation and assumes a constant specific resistivity  $\rho$  and volume of the material. The initial resistance  $R_0$  can be described as followed:

$$R_0 = \rho \frac{l_0}{A_0} \quad (5.2)$$

where  $l_0$  is the initial length in the relaxed state;  $A_0$  is the cross-sectional area of the

conducting layer. The relative change of the resistance  $R$  due to the elongation is then given by equation 5.3:

$$\frac{R}{R_0} = \left(\frac{l}{l_0}\right)^2 \quad (5.3)$$

where  $l$  is the length of the conductor under mechanical stress. The normalized change in resistance is then given by equation 5.4, where the technical strain is revealed by  $\varepsilon_{tech} = (l - l_0)/l_0$ :

$$\frac{R - R_0}{R_0} = 2\varepsilon_{tech} + \varepsilon_{tech}^2 \quad (5.4)$$

The criteria of an electrode malfunction was defined by an increase in resistance of 20% compared to the theoretical curve (dashed black line), which is shown in Fig. 5.17(a) as a gray dashed line. It turned out that the relative change in resistance for the conductive PEDOT:PSS electrode survived very high mechanical strain and started to fail at 19.7%, a calculated bending radius of only  $\sim 444 \mu\text{m}$ , according to the equation  $2r = d/\varepsilon_{tech}$ . In contrast, the ITO reference electrode forms irreversible cracks at a relative elongation of 1.05%, or a bending radius of  $\sim 6 \text{ mm}$ . The hybrid electrode instead, comprising a 1-dimensional AJ printed Ag grid on conductive PEDOT:PSS, shows first nano-scopic cracks at around 6%, that steadily enlarge, as can be seen in the images taken at 12% and 20% elongation. Apparently, the cracks in the MOD Ag layer seem to be partly bridged by the PEDOT:PSS. Nevertheless, a mechanical strain of 6% corresponds to a bending radius of 1.45 mm and demonstrates the outstanding flexibility of the hybrid electrodes composed of conductive PEDOT:PSS and a AJ printed MOD Ag grid.

### 5.3.3. Summary

Since one of the main motivators of printed electronics, especially large area applications, such as OPVs and OLEDs, is the possibility of fabrication of light weight and flexible devices, the strain and bending fatigue of AJ printed hybrid electrodes was investigated.

In summary, a superb mechanical robustness was observed for the hybrid TCs consisting of the conductive PEDOT:PSS and the aerosol printed MOD ink. While brittle ITO electrodes tend to crack at relatively small substrate elongations of  $\sim 1.1\%$ , corresponding to a bending radius of 6 mm, the hybrid electrodes withstand  $> 6\%$  elongations on PET, which correspond to a bending radius smaller than  $\sim 1.45 \text{ mm}$ . One of the reasons for this might lie in the fact that PEDOT:PSS acts as an elastomeric soft layer between the substrate and the metal grid, which minimizes the mechanical load on the metal structures. In addition to this, the mesoporous interlayer that forms between the PEDOT:PSS and the metal conceivably contributes to an improved bonding. Compared to the pure PEDOT:PSS electrode, the hybrid electrode reveals a significant improvement of the electrical conductivity with a small drawback on the mechanical flexibility.

The cyclic bending fatigue further demonstrated the outstanding mechanical resistance

against over and over repeating flexure of the electrode system. The bending tests were stopped after 500k cycles and showed no increase in resistance and hence no fatigue at a radius of 3.9 mm. Nevertheless, for smaller radii the criterion for malfunction was reached at  $\sim 100k$  cycles.

## 5.4. Solar Cells Comprising AJ Printed Hybrid Transparent Conductors

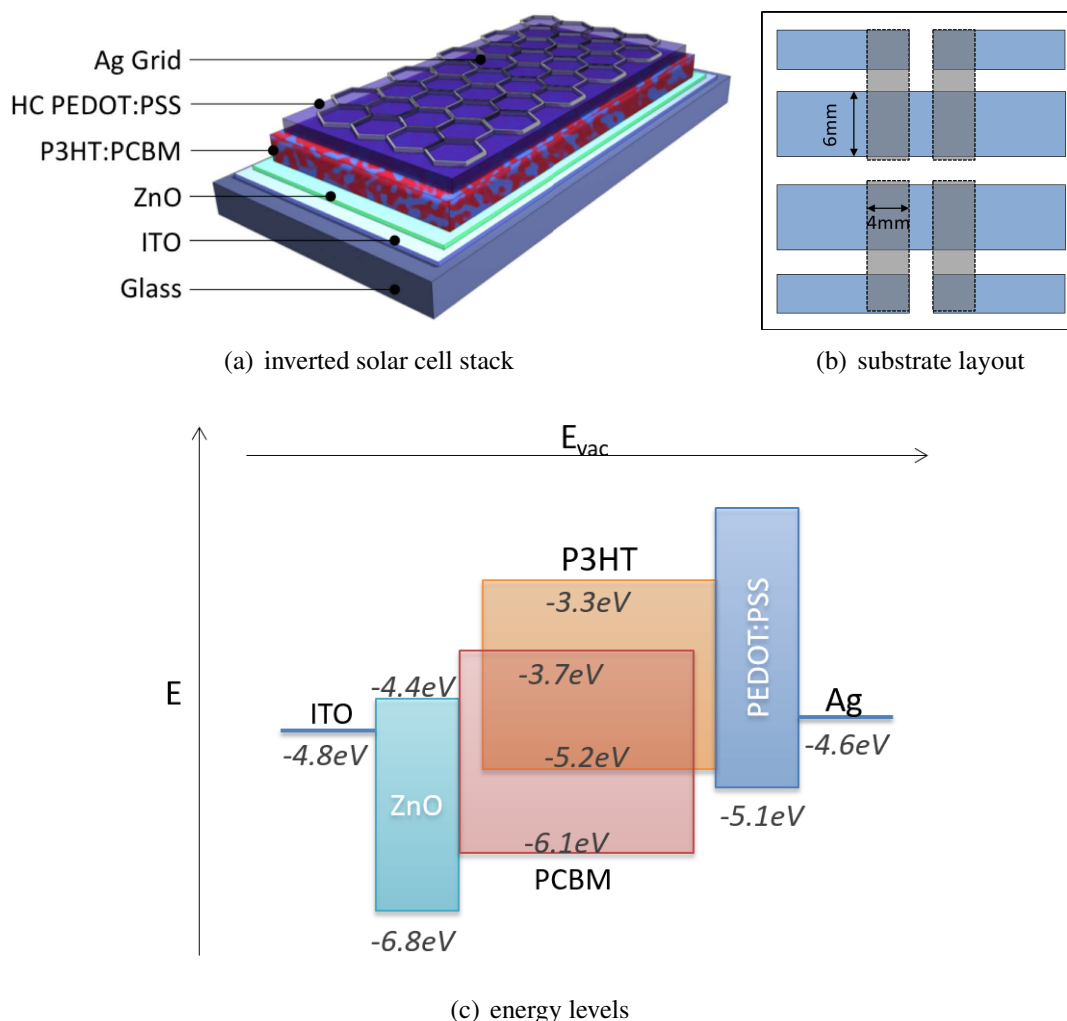


Figure 5.18.: a) Schematics of an inverted organic solar cell stack comprising an ITO/ZnO cathode on a glass substrate, P3HT:PCBM active layer, and the conductive PEDOT:PSS/Ag-grid top anode. b) Substrate layout comprising a structured ITO electrode. The dashed rectangles illustrate the shape of the top contact, where the overlap of the ITO and the top contact form the active area. c) Energy levels of the different materials with corresponding values for metal work functions, HOMO, LUMO, conduction and valence bands.

## 5.4.1. Device Preparation

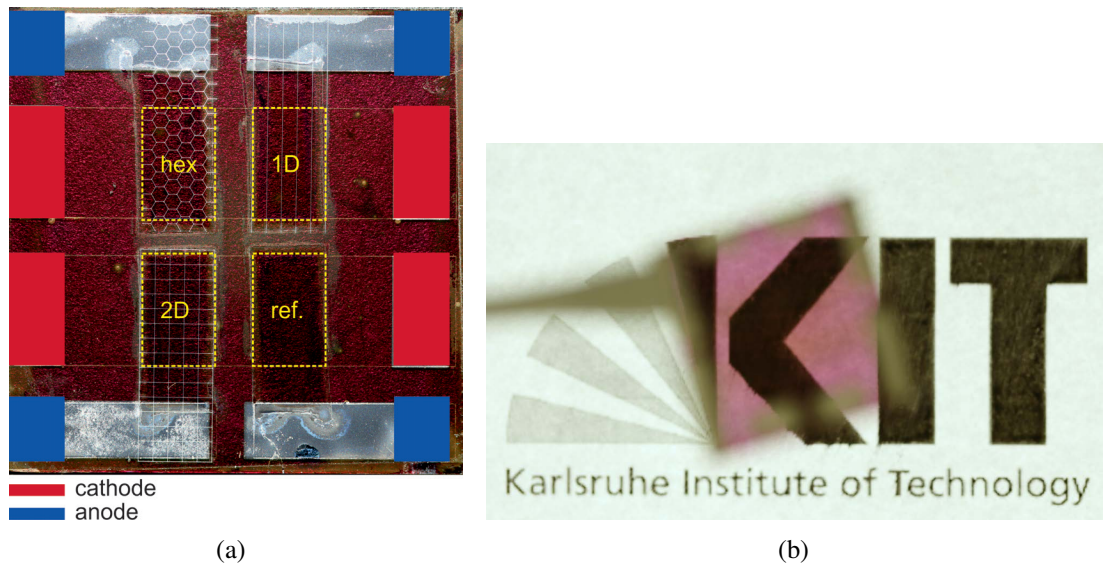


Figure 5.19.: a) Photograph of a substrate containing a PEDOT:PSS reference pixel, and hybrid electrodes with 1-dimensional, 2-dimensional, and hexagonal grids ( $r_{sym} = 400 \mu\text{m}$ ). b) Photograph of a semi-transparent OSC in front of a KIT-logo.

Thus far, the electrical and mechanical performance of AJ printed grids were characterized in previous sections. To further investigate the performance enhancement in organic solar cells, the hybrid TC's were implemented in final devices. Therefore, a standardized substrate layout was utilized, as shown in Figure 5.18(b), with a pre-structured 6 mm wide ITO electrode stripe. The device stack is presented in Figure 5.18(a), where the zinc oxide layer was prepared from a  $Zn(acac)_2$  hydrate precursor, as described elsewhere.[89] The active layer was spin cast for 20 s from a 40 g/L 1,4-dichlorobenzene solution of P3HT:PC60BM in a ratio of 1 : 0.9 in ambient conditions. The still wet film was then solvent annealed under a Petri dish until a color change from orange to dark violet was observed and the film was visibly dry. The resulting thickness was measured to be 180 nm. The top electrode was structured by utilizing a pre-patterned heat release tape, which was stuck to the P3HT:PCBM layer in advance to the spin coating process. The subsequent conductive PEDOT:PSS film (Clevios PH1000, Heraeus), containing 5% dimethyl sulfoxide (DMSO) and 1% Zonyl (FS-300) as wetting agent, was spin cast onto the active layer. The film was then annealed at 140 °C for 15 min inside a nitrogen filled glove box resulting in a 100 nm thick layer. Supplemental measurements revealed an average  $\sigma_{PEDOT:PSS}$  of  $\sim 550 \text{ S/cm}$  for films prepared the same way on glass slides. Ultimately, the MOD ink (formulation #3) was AJ printed at a speed of 5 mm/s onto the conductive PEDOT:PSS area in ambient conditions and subsequently annealed at 140 °C for 1 min in air. The line width and height was determined to be 25 – 30  $\mu\text{m}$  and  $\sim 250 \text{ nm}$ , respectively.

Figure 5.19 shows photographs of a  $25 \times 25 \text{ mm}^2$  sample having four pixels, where one comprises only PEDOT:PSS as the anode (ref.), and the remaining pixel show 1-dimensional

(1D), 2-dimensional (2D), and hexagonal (hex) Ag grids with  $r_{sym} = 400 \mu\text{m}$  and a line width,  $w = 25 - 30 \mu\text{m}$ . The right photograph shows the sample in front of the KIT-logo and demonstrates their semi-transparency due to the transparent ITO and hybrid TC.

## 5.4.2. Device Characterization and Discussion

### 1-Dimensional Grids

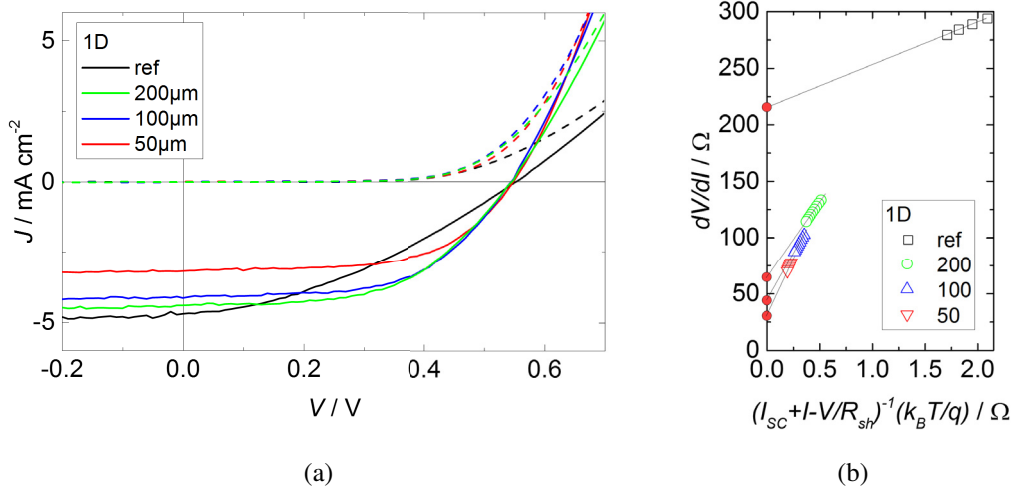


Figure 5.20.: a) J-V characteristics of top illuminated inverted P3HT:PCBM solar cells comprising a conductive PEDOT:PSS top electrode as reference, and AJ printed 1-dimensional Ag grids with symmetry radii of  $r_{sym} = 50, 100$  and  $200 \mu\text{m}$ . b) Plot of  $dV/dI$  as a function of  $(I_{SC} + I - V/R_{sh})^{-1}/(k_B T/q)$ , where  $R_s$  can be extracted from the intersect of a linear fit with the y-axis (red dot).

**Figure 5.20(a)** presents the  $J-V$  characteristics of a sample comprising one PEDOT:PSS reference pixel and three pixels with 1-dimensional hybrid TCs with varying  $r_{sym}$  from 50 to  $200 \mu\text{m}$ . The devices were illuminated through the hybrid TC and the data clearly demonstrates the influence of the different shadings on the  $J_{SC}$  originating from the different transparencies of the grids. Although, the reference pixel comprised the highest  $J_{SC}$ , the contribution of the high series resistance  $R_s$  led to a poor device performance.  $R_s$  was obtained from the intercept of the linear fit with the y-axis, as shown in Figure 5.20(b), which was introduced on page 13 in Equation 2.6.

The fine 1-dimensional hybrid TC with  $r_{sym} = 50 \mu\text{m}$  in combination with a  $25 - 30 \mu\text{m}$  line width drastically reduced the illuminated active area to around  $70 - 75 \%$ , which correlates well with the reduction of the photo current of  $\sim 30 \%$ . Nevertheless, the reduction in photo current was mainly compensated by the reduced series resistance, which decreased from  $\sim 215 \Omega$  (PEDOT:PSS reference) to below  $30 \Omega$ . This even induced a

Table 5.6.: Device efficiency  $\eta$ , fill factor  $FF$  and series resistance  $R_s$  of P3HT:PCBM solar cells comprising 1-dimensional hybrid TCs.

1D	$\eta$ [%]	$FF$ [%]	$R_s$ [ $\Omega$ ]
PEDOT:PSS reference	1.62	35	214.9
50 $\mu\text{m}$	1.81	60	28.8
100 $\mu\text{m}$	2.23	56.4	42.7
200 $\mu\text{m}$	2.28	53	63.7

slight increase in device efficiency  $\eta$  from 1.62% to 1.81% with a fill factor ( $FF$ ) of 60%. The  $J - V$  characteristics of the devices with 100 and 200  $\mu\text{m}$  symmetry radii exhibited an even more pronounced increase in  $\eta$  caused by the significantly increased transparency and very good  $FF > 53\%$ .  $R_s$  values for the devices are summarized in Table 5.6.

### Hexagonal Grids

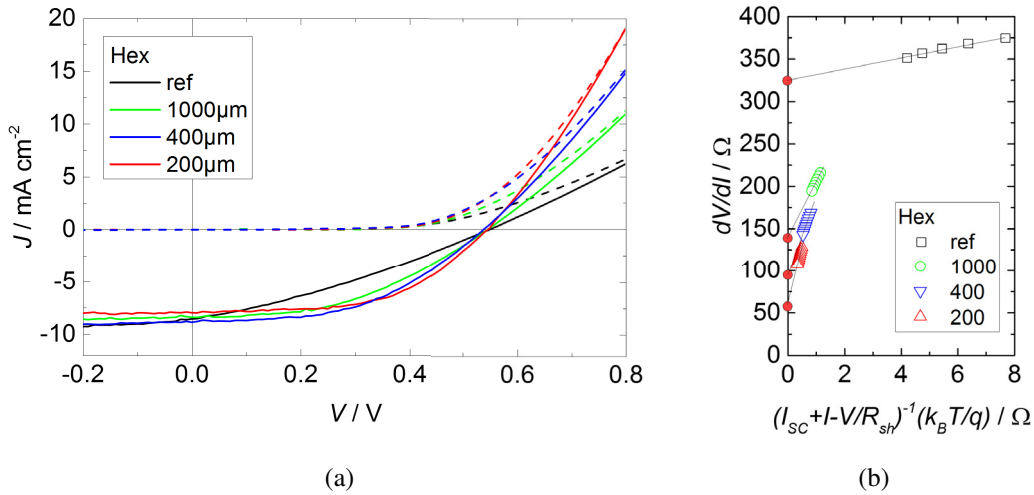


Figure 5.21.: J-V characteristics of top illuminated inverted P3HT:PCBM solar cells comprising a conductive PEDOT:PSS top electrode as reference, and AJ printed 1-dimensional Ag grids with symmetry radii of  $r_{sym} = 50, 100$  and  $200 \mu\text{m}$ . b) Plot of  $dV/dI$  as a function of  $(I_{SC} + I - V/R_{sh})^{-1}/(k_B T/q)$ , where  $R_s$  can be extracted from the intersect of a linear fit with the y-axis (red dot).

**Figure 5.21** shows the  $J - V$  characteristics and the corresponding  $R_s$  plot of inverted P3HT:PCBM cells with hexagonal hybrid TCs. For a  $r_{sym} = 200 \mu\text{m}$  the series resistances of cells with 1-dimensional and hexagonal grids were fairly congruent. And a distinguishable influence of the different grid geometries for similar  $r_{sym}$  could not be confirmed, since manufacturing inaccuracies, such as variations in line widths or overspray, may reduce the impact of the geometrical design. The line heights and widths were similar for all hexagonal grids, thus a higher  $r_{sym}$  mainly caused on the one hand higher

## 5. AJ Printed Grid Electrodes for Organic Solar Cells

Table 5.7.: Device efficiency  $\eta$ , fill factor  $FF$  and series resistance  $R_s$  of P3HT:PCBM solar cells comprising hexagonal hybrid TCs.

HEX	$\eta$ [%]	$FF$ [%]	$R_s$ [ $\Omega$ ]
PEDOT:PSS reference	1.49	31.1	325.2
200 $\mu\text{m}$	2.34	54.9	58.5
400 $\mu\text{m}$	2.30	47.9	92.1
1000 $\mu\text{m}$	2.05	44.1	133.9

transparencies and on the other hand higher series resistances. The counteracting influences are represented in the  $J_{sc}$ , and the  $R_s$  or FF, respectively. A good balance was found with  $r_{sym}$  between 200 and 400  $\mu\text{m}$ . A further increase in  $r_{sym}$  resulted in decreasing of the FF and hence in a reduction of  $\eta$ .

### Comparison of 1-Dimensional, 2-Dimensional and Hexagonal Grids

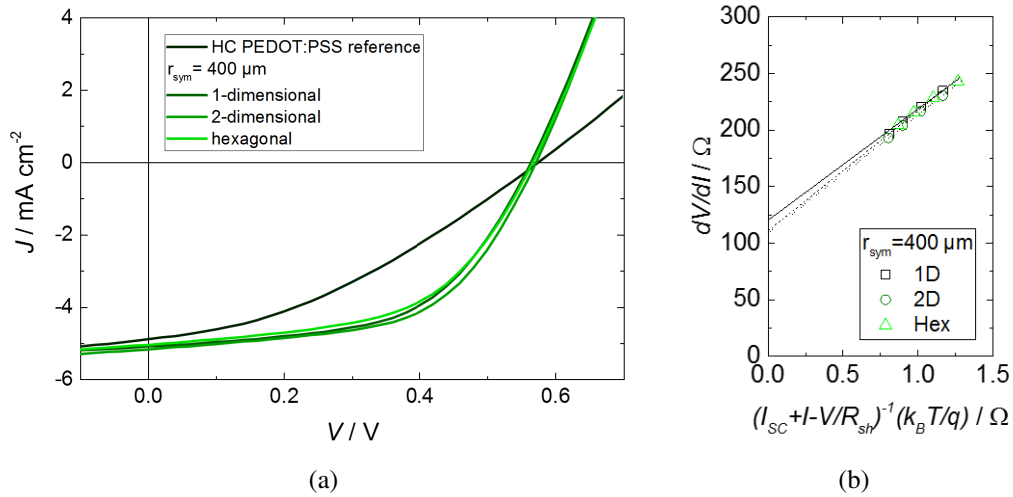


Figure 5.22.: a) J-V characteristics of bottom illuminated inverted P3HT:PCBM solar cells with a PEDOT:PSS reference, and AJ printed 1-dimensional, 2-dimensional, and hexagonal Ag grids with symmetry radii of  $r = 400 \mu\text{m}$ . b) Plot of  $dV/dI$  as a function of  $(I_{SC} + I - V/R_{sh})^{-1}(k_B T/q)$ , where  $R_s$  can be extracted from the intersect of a linear fit with the y-axis.

**Figure 5.22** shows the results of inverted organic solar cells comprising a pure PH1000 top electrode as the reference pixel, and 1-dimensional, 2-dimensional, and hexagonal grids with  $r_{sym} = 400 \mu\text{m}$  printed from the modified MOD ink (#3). The samples were illuminated through the glass/ITO. Since the reduction of the photo current due to shading was neglected by illuminating through the ITO electrode, the results focus solely on the influence on the device performance from the reduction of the sheet resistance due to the supporting metal grids. In case of the PEDOT:PSS reference cell a huge lack in device efficiency was detected, mainly caused by the relatively high series resistance ( $\sim 740 \Omega$ ).

Table 5.8.: Characteristic device parameter extracted from the  $J - V$  characteristics of inverted OSCs comprising solution processed top electrodes with PEDOT:PSS and printed Ag grids. (\* value could not be determined by the described method and was therefore calculated by the slope at  $\sim 0.9$  V)

<i>Pixel</i>	$\eta$ (%)	$FF$ (%)	$V_{OC}$ (V)	$J_{SC}$ ( $mAcm^{-2}$ )	$R_s$ ( $\Omega$ )
<i>PEDOT:PSS ref.</i>	0.83	35.2( $\pm 3$ )	0.567( $\pm 0.07$ )	4.32( $\pm 0.8$ )	740*
<i>1-dim</i>	1.43( $\pm 0.25$ )	50.6( $\pm 3$ )	0.567( $\pm 0.05$ )	4.92( $\pm 0.62$ )	112.9
<i>2-dim</i>	1.64( $\pm 0.1$ )	54.6( $\pm 1$ )	0.572( $\pm 0.03$ )	5.24( $\pm 0.2$ )	111.7
<i>Hex</i>	1.54( $\pm 0.02$ )	53.7( $\pm 1$ )	0.568( $\pm 0.02$ )	5.1( $\pm 0.05$ )	121.2

This again resulted in a low  $FF$  of 36 %.

All additional contributions, such as the contact resistance to the terminals, the ITO sheet resistance, interface resistances, were assumed to be similar for all samples, regardless for the cell with or without the hybrid TC. The  $J$ - $V$  characteristics of the 1-dimensional, 2-dimensional and hexagonal grids show similar behaviors. In all cases, the device performance led to a significant improvement by a factor of 1.7 to 2, as summarized in Table 5.8. We note that the shading by the grids was not considered, since the devices were illuminated through the ITO electrode. A clear decrease in series resistance from  $\sim 740 \Omega$  down to  $\sim 110 \Omega$  could be measured.

### Light Beam Induced Current Measurement

Light beam induced current measurements give a qualitative insight into the spatially resolved current flows within a specified active area. The measurement results in **Figure 5.23** were recorded for OSCs comprising a hexagonal grid with  $r_{sym} = 400 \mu m$  illuminated through the hybrid electrode. The brighter (yellow) areas account for higher local currents, where the dark reddish areas correspond to lower local currents. These results support the previous  $J$ - $V$  measurements and clearly identify the printed metal structures as current collecting grids. However, the laser spot size was larger than the nominal line width, which explains why no reduction of the local current on top of the Ag structures could be observed.

### 5.4.3. Summary

In summary, transparencies of 90 % between 400 and 800 nm wavelength with sheet resistances of  $10 \Omega/\square$  were achieved for the AJ printed grids with  $r_{sym} = 400 \mu m$  and line widths of  $\sim 20 - 30 \mu m$  on PEDOT:PSS covered glass. Furthermore, the electrical performance of OSCs with conductive PEDOT:PSS electrodes could be significantly improved by the addition of AJ printed current collecting grids on top of the OSCs. Different symmetry radii for 1-dimensional and hexagonal grids were demonstrated, as well as a comparison of 1-dimensional, 2-dimensional and hexagonal grids with equal  $r_{sym}$  of  $400 \mu m$

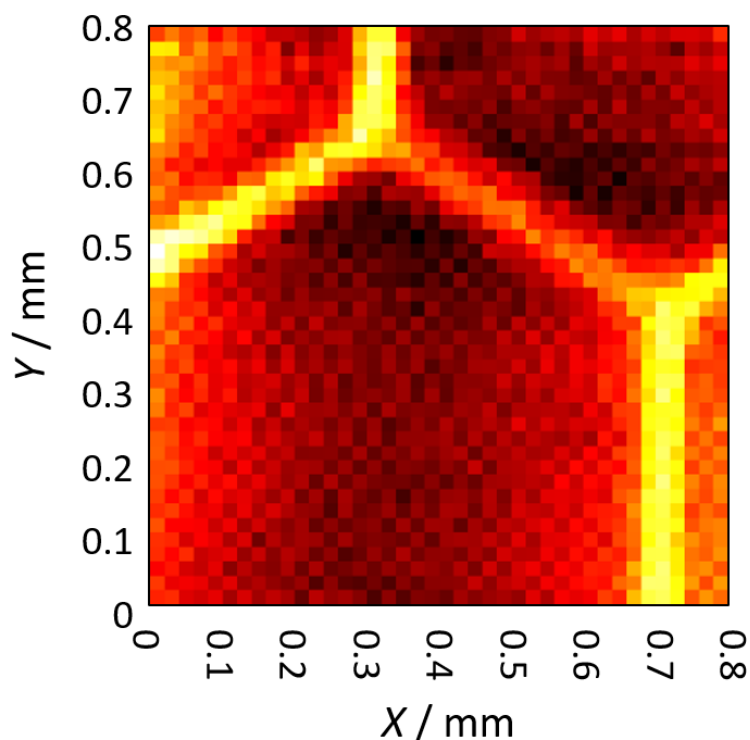


Figure 5.23.: Light beam induced current measurements (LBIC) of organic P3HT:PCBM solar cells comprising a hybrid top electrode with an AJ printed hexagonal grid.

was shown. The LBIC measurements further demonstrated an increased photo current close to the metal structures, showing the current collecting properties of the metal mesh. The qualitative examination revealed an efficiency improvement of up to 57% compared to the PEDOT:PSS reference devices. However, a quantitative comparison of the grid geometries could not be made due to a certain combination of factors in manufacturing inaccuracies and the relatively small active area of  $0.24 \text{ cm}^2$ .

## 5.5. Electrode and Device Modeling

The successful application of AJ printed top grids for OSC markedly demonstrates the potential of additive digital manufacturing techniques on top of sensitive organic matter. In a first step, the large improvement of OSC performance due to the reduction of series resistance was accomplished. Furthermore, the excellent prototyping capabilities in combination with the contact-free deposition of the material of interest allowed for an empirical study of different electrode parameters, such as symmetry radius and grid geometry. Nevertheless, certain inaccuracies from laboratory fabrication processes, such as influences of fluctuations in the ambient conditions and other reproducibility issues,

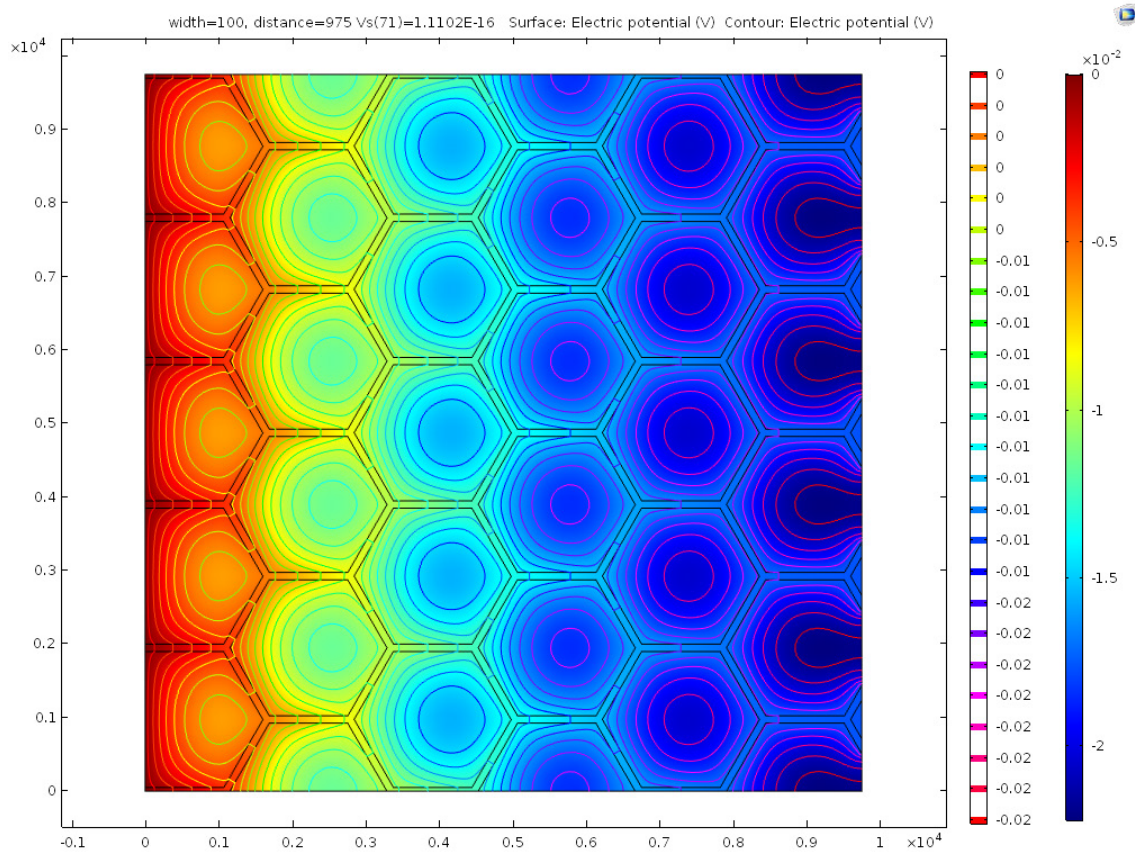


Figure 5.24.: Example of an OPV (comprising a hexagonal grid) device modeling with anode and cathode contacts on opposing sides (left and right). The false-color code and the isolines represent the electrical potential in the hybrid TC at 0 V.

obscure the effect of interest. Moreover, the theoretical analysis of hybrid TCs for specific applications, such as solar cells or light-emitting devices, can provide a profound understanding of device specific requirements, such as the series resistance. Therefore, different figures of merit have emerged to somehow predict the suitability of TCs for an application.[85, 90, 91]

The following section will first introduce a physical and geometrical model, based on the *COMSOL* simulation software presented in section 4.4 on page 40. An example of a device simulation is shown in **Figure 5.24**, where the electrical potential within the hexagonal hybrid TC was calculated and plotted. It basically illustrates the complex local dependencies between the applied bias, the current density, the built-in voltage, the resulting voltage drop and the local resistance of the polymeric or supportive metallic matter. Finally, these device simulations can be used to re-evaluate the requirements of hybrid TCs with focus on practicality and printability.

### 5.5.1. Physical Model

Within *COMSOL* the physical module '*electric current*' was chosen, which provides all the necessary tools for simulating currents, potentials, and electric fields. The model is capable of solving the differential equations spatially according to the defined mesh resolution. The model assumes a uniform illumination through the top electrode. This requires a consideration of local shading by the Ag grid within the physical model, as illustrated in **Figure 5.25**. The model can be separated into two modules. Module 1 comprises the hybrid TC based on a homogeneously conductive polymer layer (PEDOT:PSS) supported by a current collecting Ag grid. Module 2 defines the back electrode (cathode). The specific conductivity of the cathode was set to  $10^{12} \text{ S m}^{-1}$ , which constitutes an unrealistically high value. However, it guarantees a simulation result, where the influence of the back-electrode can be neglected. In between the two electrode modules, the illuminated areas are linked by  $J - V$  characteristic of a solar cell under illumination.

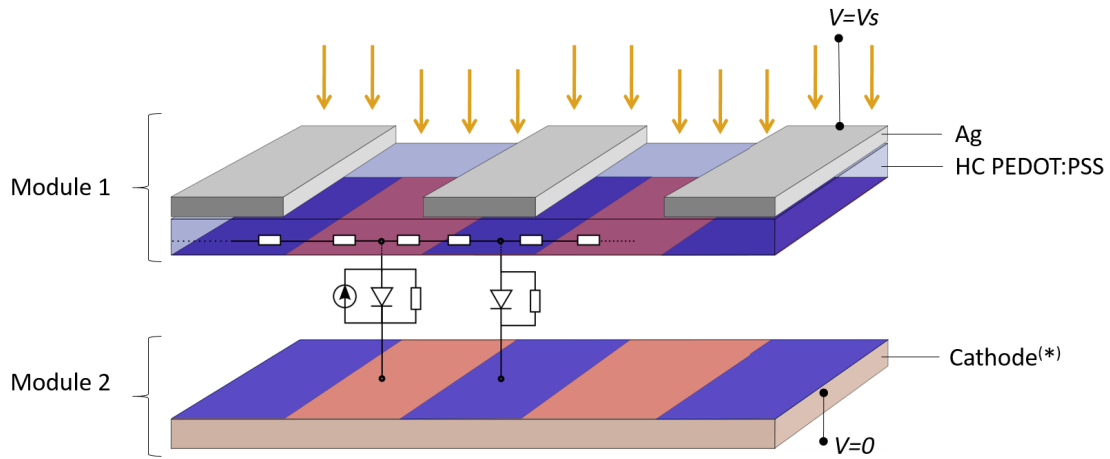


Figure 5.25.: Physical model of a solar cell with top hybrid TC and bottom electrode linked by an OPV equivalent circuit for illuminated and shaded areas. (reprinted from master thesis Jan Preinfalk 2013)

The junction of both electrode modules is usually expressed by an implicit equation, as already described in section 2.3 on page 11, which cannot be solved by the FEM. The implicit diode equation is therefore transcribed into an explicit form, where the potential drop  $R_s \cdot J$  within module 1 and 2 is calculated by *Comsol* itself, according to Eq. 5.5 and Eq. 5.6 between neighboring vertexes, as a function of the specific conductivities and layer thicknesses.

$$V_0 - R_s \cdot J = V_1(x, y, z) \quad (5.5)$$

$$- R_s \cdot J = V_2(x, y, z) \quad (5.6)$$

Now, after eliminating the implicit dependencies, the explicit  $J - V$  characteristics for the shaded  $J_{dark}$  and illuminated  $J_I$  regions can be expressed as follows:

Table 5.9.: Physical parameter of the diode equation.

<i>Parameter</i>	<i>Value</i>
$q$	$1.602 \cdot 10^{-19} [C]$
$A$	1.53
$J_0$	$1.9 \cdot 10^5 [Am^{-2}]$
$k_B$	$1.38 \cdot 10^{-23} [JK^{-1}]$
$T$	293.17 [K]
$G$	0 [ $S m^{-2}$ ]

$$J_{dark}(V_1, V_2) = J_0 \left( \exp \left( \frac{q(V_2 - V_1)}{nk_B T} \right) - 1 \right) + G(V_2 - V_1) \quad (5.7)$$

$$J_I(V_1, V_2) = J_0 \left( \exp \left( \frac{q(V_2 - V_1)}{nk_B T} \right) - 1 \right) + G(V_2 - V_1) - J_L \quad (5.8)$$

where  $J_0$  presents the reverse bias saturation current density;  $q$  is the electronic charge;  $n$  the ideality factor (between 1 and 2); and  $G$  the conductance, which is equatable to the inverse of the parallel resistance  $R_P$  of the absorber. In a 2-dimensional simulation the generation of photo current within the absorber layer is represented by a current source with  $\nabla \cdot J = J(V_1, V_2)$ . The principle parameters used for the simulations are summarized in Table 5.9.

### 5.5.2. Grid Geometries

In a first reflection, a vast quantity of interesting geometries emerge to be applied in hybrid TCs. Starting with 1-dimensional and symmetrical 2-dimensional grids, continuing with more sophisticated geometries like triangular, rhomboid, or hexagonal structures. However, I focused on two main geometries. 1-dimensional and hexagonal grids, as illustrated in **Figure 5.26**. To explain why, lets pick first the scenario of a symmetrical 2-dimensional grid, which essentially represents a 1-dimensional grid superposed by an orthogonally aligned identical 1-dimensional grid. Assuming now a preferential current flow from opposing anode and cathode contacts, as typically the case in solar cell modules, the additional shadowing due to the orthogonal 1D grid does not mainly contribute to a better conductivity. A definite advantage however constitute asymmetric interconnects between parallel lines, which in practice compensate possible line disruptions, which can occur during the fabrication process or from later handling of the devices. However, the latter scenario was not investigated. One can now discuss the reasonableness of rhomboid geometries, which opens a vast diversity of possible combinations of angles and symmetry dependencies and which are conceptually located somewhere between 1-dimensional and 2-dimensional grids in terms of shading. Furthermore, the resistance increases due to an increase in current path length. In the same way, the triangular geometry results from

## 5. AJ Printed Grid Electrodes for Organic Solar Cells

superimposed rhomboid and orthogonal 1-dimensional grids and has not been considered in this work.

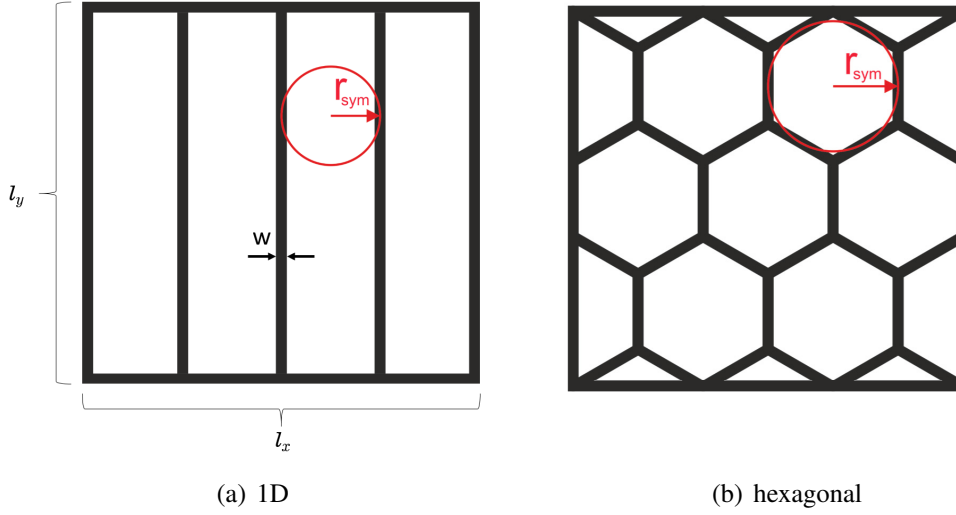


Figure 5.26.: Grid geometries. a) 1-dimensional, and b) hexagonal.

The shading from the metal grid can be calculated for squared areas as followed:

$$T_{1D} = \left(1 - \frac{w}{2r_{sym}}\right) [\%] \quad (5.9)$$

where  $w$  is the line width; and  $r_{sym}$  the symmetry radius. This is valid, assuming the metal to be 100 % opaque and the remaining areas to be 100 % transparent. For hybrid TCs the homogeneous PEDOT:PSS layer, as shown before, contributes to the shading with an approximately constant absorption of around 5 to 10 %. However, the same conditions persist for all electrode geometries and can therefore in a first assumption be neglected. For hexagonal grids the equations 5.10 and 5.11 lead to the total transmittance (5.12).

$$A_{HEX} = 2r_{sym}^2 \sqrt{3} \quad (5.10)$$

$$A_{subtract} = 2 \left(r_{sym} - \frac{w}{2}\right)^2 \sqrt{3} \quad (5.11)$$

$$T_{HEX} = \frac{A_{HEX} - A_{subtract}}{A_{HEX}} [\%] = 1 - \frac{r_{sym}w - 0.25w^2}{r_{sym}^2} [\%] \quad (5.12)$$

where  $A_{HEX}$  is the area of a hexagon;  $A_{subtract}$  is than the area to be subtracted from  $A_{HEX}$ , having an inner radius  $w/2$  smaller than  $A_{HEX}$ ;  $T_{HEX}$  depicts the transparency

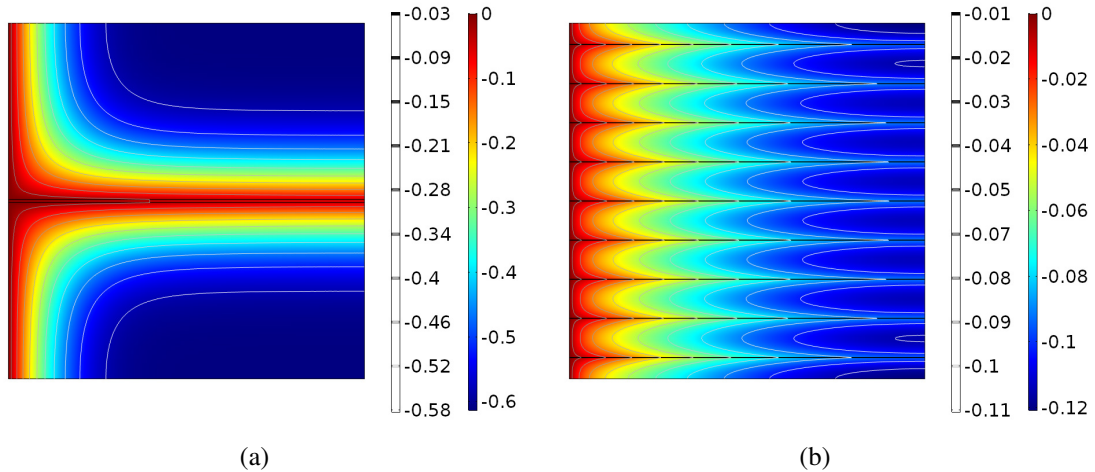


Figure 5.27.: *COMSOL* device simulations of  $1 \text{ cm}^2$  large solar cells comprising a) one  $100 \mu\text{m}$  wide and b) nine  $11 \mu\text{m}$  wide Ag lines. The false-color code illustrates the voltage potential distribution over the area.

arising from the normalized subtraction of  $A_{HEX}$  and  $A_{subtract}$ .

One issue, faced with experimental data from solar cells including a hybrid TC is that it is not trivial to gain information about the potential distribution under operation, which plays a key role for the cell performance. The simplest scenario is illustrated in **Figure 5.27**, where in both cases the same amount of Ag covers the surfaces. While in 5.27(a) only one  $100 \mu\text{m}$  wide line is present, in 5.27(b) the Ag is equally distributed in nine  $11 \mu\text{m}$  wide lines. The potential of the grid with one line drastically drops by  $0.6 \text{ V}$ , which equals the open circuit voltage of the device. A much more homogeneous potential was achieved by the device simulation in 5.27(b). The maximum voltage drop here accounts for  $0.12 \text{ V}$ . Since the charge generation is equally distributed over the whole area, except for the shaded Ag covered areas, the average path length of the current through the higher resistive PEDOT:PSS is in case 1 much longer than in case 2. Thus, a more homogeneous potential distribution allows, therefore, for more efficient charge extraction even though the transparency and *effective* sheet resistance  $R_{sheet,M}$  stays constant. Furthermore, device simulations can be used to evaluate and optimize symmetry radii with printing relevant feature sizes ( $\geq 10 \mu\text{m}$ ) while maintaining satisfactory cell performance.

### 5.5.3. Boundary Conditions

The result of changing  $r_{sym}$ , while  $w$  is kept constant can be seen in **Figure 5.28(a)** for a device simulation for a solar cell comprising a 1-dimensional hybrid TC. Both the transparency  $T$  and the *effective* sheet resistance  $R_{sheet,M}$  change simultaneously with an increase of  $r_{sym}$ , with the two parameters affecting the device performance (Fig. 5.28(b))

## 5. AJ Printed Grid Electrodes for Organic Solar Cells

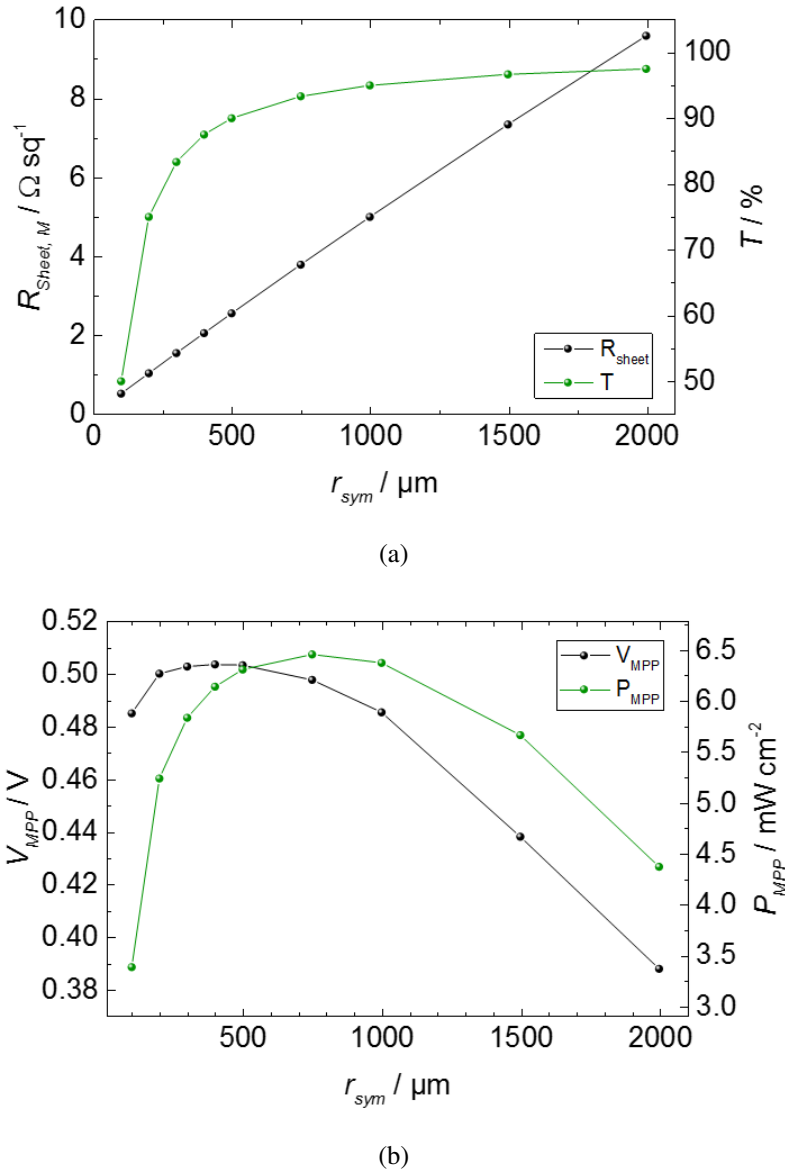


Figure 5.28.: a) Sheet resistance  $R_{sheet, M}$  and transmittance  $T$  of a 1-dimensional hybrid TC as a function of the symmetry radius  $r_{sym}$ . b) Voltage and power in the maximum power point of simulated solar cells as a function of  $r_{sym}$ . The line width  $w$  was fixed to  $100 \mu\text{m}$ .

in an opposing manner, as demonstrated by the changing voltage and power at the maximum power point. This approach is less expedient, since the transmittance on the one hand and the resistances of the metal and the polymeric matter on the other hand superimpose each other, which makes a discrimination of the contradictory influences problematic. The major aspect, however, is given by the different grid geometries, which have distinct transmittances and potential distributions for a similar  $r_{sym}$ .

**Figure 5.29** shows the calculated transparency for 1-dimensional and hexagonal grids comprising similar line widths of  $10 \mu\text{m}$  and  $30 \mu\text{m}$  as a function of  $r_{sym}$ . The transparency of 1-dimensional grids is significantly higher for smaller  $r_{sym}$  compared to the

hexagonal grids, which is illustrated by the compact ( $w = 10 \mu\text{m}$ ) and dashed ( $w = 30 \mu\text{m}$ ) green and black lines.

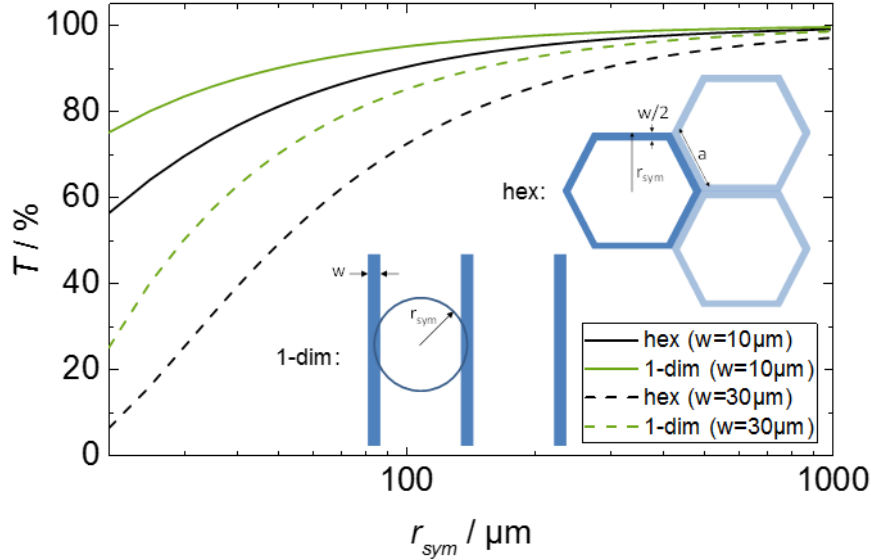
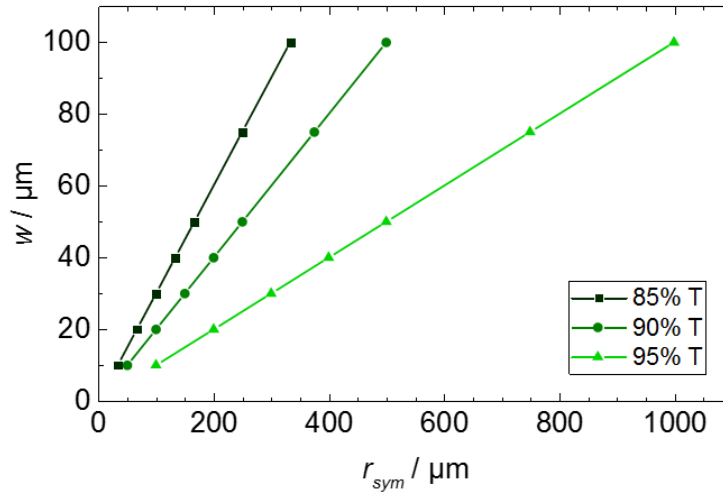


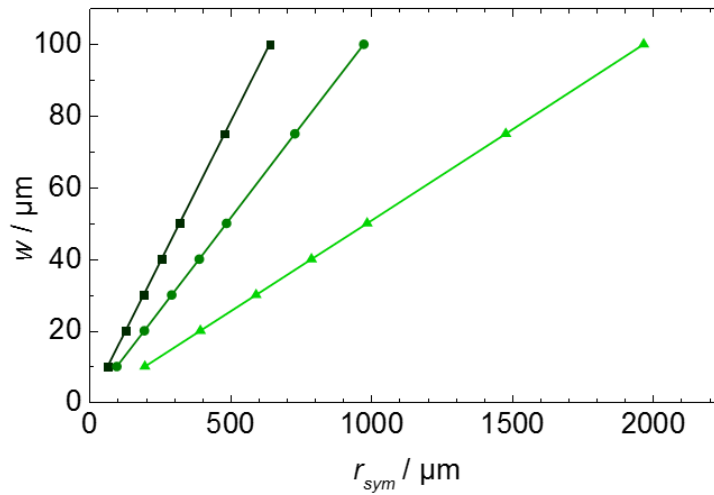
Figure 5.29.: Transmittance of 1-dimensional and hexagonal grid symmetries for different  $w$  as a function of  $r_{sym}$ .

Thus, the question to be raised is, *how can we compare different grid geometries and symmetries and their influences on distinguishable parameters?* To do so, several geometric and electric boundary conditions must be properly set. A parameter set defining the minimum requirements was found by Rowell *et al.* with an effective sheet resistance of  $\leq 10 \Omega/\square$  and a transmittance  $\geq 90\%$ . [91] These values were found to be crucial for monolithic thin film modules. For standard modules even lower transparencies and resistances should be sufficient according to the authors.

In this work an approach was chosen, where the transmittance was kept constant for varying line widths, which are relevant for printing, by adjusting the symmetry radius  $r_{sym}$ . **Figure 5.30** shows the dependencies between the width and  $r_{sym}$  in 1-dimensional and hexagonal grid geometries. The *effective* sheet resistance  $R_{sheet,M}$  can be kept constant by adjusting  $\sigma_{Ag}$  and/or the line height  $h$ . Regardless of whether  $\sigma_{Ag}$  or  $h$  is tuned, the values must only stay within a reasonable geometric range for printed structures. This means, that neither a conductivity of bulk Ag, nor a line height of several tens of  $\mu\text{m}$  would be representative for a practical application with commonly used inks. Therefore, the simulations were performed using a realistic  $\sigma_{Ag}$  of  $1.6 \cdot 10^7 \text{ S m}^{-1}$ , which was measured for the MOD Ag ink. And  $h$  was then adjusted properly to the desired  $R_{sheet,M}$  (Table 5.11), as can be found in Table 5.11.



(a) 1D



(b) hexagonal

Figure 5.30.: Dependencies between line width  $w$  and symmetry radius  $r_{sym}$  for fixed transparencies in a) 1-dimensional, and b) hexagonal hybrid TCs. These dependencies are independent of the effective sheet resistance.

#### 5.5.4. Effective Sheet Resistance and PEDOT:PSS Conductivity

I first focused on the conductivity of the polymeric component and the *effective* sheet resistance of the current collecting grid. Device simulations were conducted comprising a 1-dimensional hybrid TC with a transmittance of 90% according to Eq. 5.9. The current density generated within the active layer was set to  $15 \text{ mA cm}^{-2}$ . **Figure 5.31** shows now the influence of  $r_{sym}$ ,  $\sigma_{PEDOT:PSS}$  and  $R_{sheet,M}$  on the normalized device efficiency  $\eta$ . Simulating hybrid TCs under the conditions of 90% transparencies and symmetry radii

Table 5.10.: Parameters for line width  $w$  and symmetry radius  $r_{sym}$  with respect to the grid geometry and different  $T$ .

$w$ [ $\mu\text{m}$ ]	$r_{sym}$ [ $\mu\text{m}$ ] (1D)			$r_{sym}$ [ $\mu\text{m}$ ] (HEX)		
	85%	90%	95%	85%	90%	95%
10	33.3	50	100	64	97	197
20	66.6	100	200	128	195	394
30	99.9	150	300	192	292	592
40	133.2	200	400	256	390	789
50	166.5	250	500	320	487	987
75	249.5	375	750	480	730	1480
100	333	500	1000	640	975	1970

Table 5.11.: Line heights for 1-dimensional and hexagonal symmetries with different  $T$ , adjusted to the desired  $R_{sheet,M}$ . Values were revealed from FEM simulations.

$R_{sheet,M}$ [ $\Omega/\square$ ]	$h$ [ $\text{nm}$ ] (1D)			$h$ [ $\text{nm}$ ] (HEX)		
	85%	90%	95%	85%	90%	95%
2.5	160	240	480	290	440	904
5	80	120	240	145	216	452
10	38.7	57.5	115	72.5	108	216

smaller than  $100 \mu\text{m}$  require line widths below  $10 \mu\text{m}$ , which is smaller than the minimum AJ printable feature size. Nevertheless, as can be seen in the graph, this further decrease in  $r_{sym}$  and hence  $w$  shows no effect on the device efficiency. A drop in device efficiency could be observed not until symmetry radii above  $100 \mu\text{m}$ . These findings connote, that line widths  $> 10 \mu\text{m}$  are suitable for highest performing hybrid TCs. Furthermore, even a very low  $\sigma_{PEDOT:PSS}$  of  $200 \text{ S cm}^{-1}$ , which corresponds to a PEDOT:PSS sheet resistance of  $500 \Omega/\square$  at  $100 \text{ nm}$  layer thickness, yielded a relative decay in efficiency of only  $\sim 3.3\%$  at  $r_{sym} = 1000 \mu\text{m}$ .

The parameter space was then extended to the hexagonal grid geometry and a variation in the transmittance between  $85\%$  and  $95\%$ . As was introduced earlier, the transparency was varied by relating a fixed  $w$  to a variable  $r_{sym}$ , as listed in Table 5.10. **Figure 5.32(a)** and **5.32(b)** show both for 1-dimensional and hexagonal grids the influence of the different transparencies by a constant offset in the normalized  $\eta$ , which could be attributed to the effect of shading. Moreover, larger  $r_{sym}$  connote a very pronounced drop in  $\eta$  for large values. To achieve the same transmittance for hexagonal and 1-dimensional grids, the  $r_{sym}$  had to be set to  $1970 \mu\text{m}$  for hexagonal and  $1000 \mu\text{m}$  for the 1-dimensional grids at  $w = 100 \mu\text{m}$ . Hence, the electrode with the hexagonal grid experiences a higher impact from the resistive PEDOT:PSS, which results in a very large decay in normalized efficiency of more than  $60\%$  at  $r_{sym} = 1970 \mu\text{m}$  and  $\sigma_{PEDOT:PSS} = 200 \text{ S cm}^{-1}$ .

The simulations additionally include a variation in  $\sigma_{PEDOT:PSS}$  ranging from  $200$  to  $1000 \text{ S cm}^{-1}$ , which can be also expressed as a variation in the sheet resistance  $R_{sheet,PEDOT}$  for similar layer thicknesses. The sheet resistances would then correspond to  $100 \Omega/\square$  for

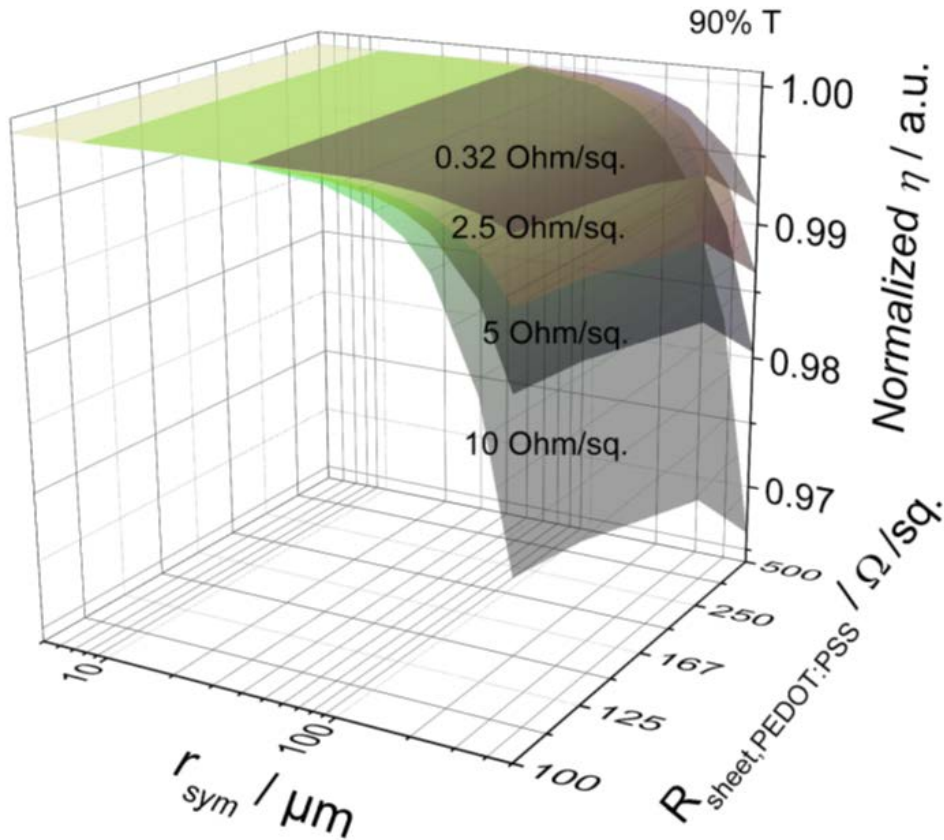
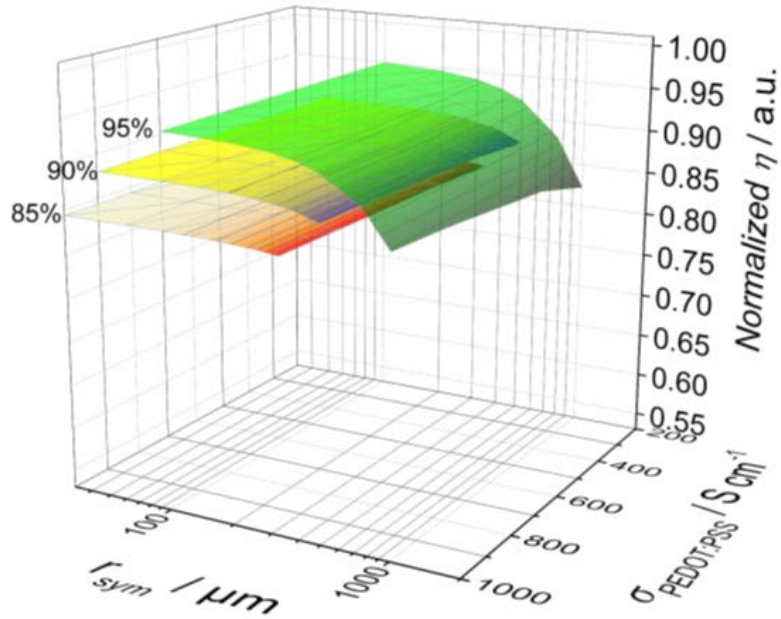


Figure 5.31.: 1-dimensional hybrid TC: Influence of symmetry radius  $r_{sym}$ , PEDOT:PSS conductivity  $\sigma_{PEDOT:PSS}$  and  $R_{sheet,M}$  on the normalized device efficiency  $\eta$ . (Boundary conditions:  $J = 15 \text{ mA cm}^{-2}$ ,  $T = 90 \%$ )

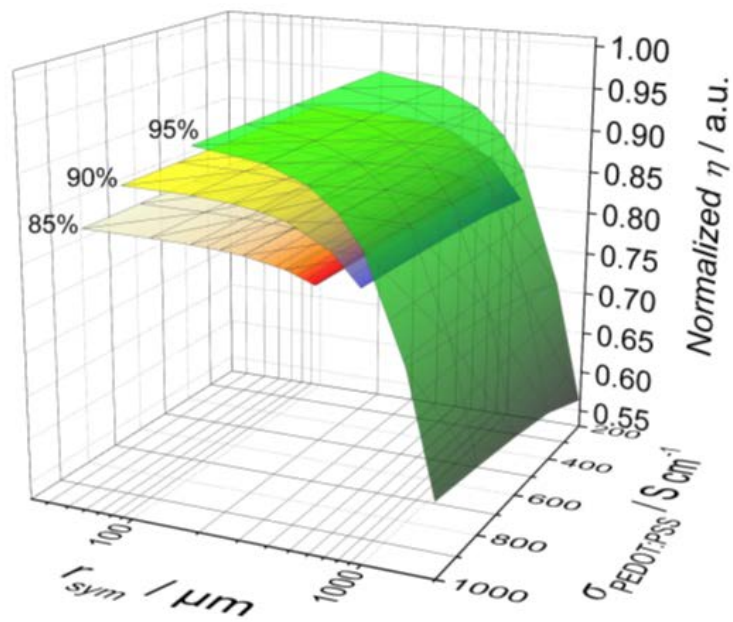
the highest specific conductivity and to  $500 \Omega/\square$  for the lowest specific conductivity. This range reflect realistic values, where the large variations can be attributed to different PEDOT:PSS formulations, printing and post-treatment processes, or the addition of wetting agents.[92–97]

The device efficiency was found to decrease linearly with the amount of shaded area, which corresponds to the reduction of the transmittance. That was confirmed by **Figure 5.33(a)**, where the normalized efficiency  $\eta$  as a function of  $r_{sym}$ ,  $R_{sheet,M}$  and  $\sigma_{PEDOT:PSS}$  was plotted neglecting the aforementioned influence of the different transparencies for a device comprising a 1-dimensional hybrid TC. The curve shapes of 85, 90 and 95 % transparency perfectly overlap. Nonetheless, it should be pointed out again, that this plot neither compares the absolute nor relative efficiencies and only illustrates the constant offset arising from the transparency.

Figure 5.33(b) presents the simulated normalized  $\eta$  as a function of the line width (left) and the symmetry radius (right) of devices with 1-dimensional and hexagonal hybrid HC and 95 % transmittance and  $10 \Omega/\square$  effective sheet resistance. The hexagonal grid (orange) revealed marginally higher normalized efficiencies for the low conductive PE-



(a) 1-dimensional



(b) hexagonal

Figure 5.32.: Influence of  $r_{sym}$ ,  $\sigma_{PEDOT:PSS}$ , and  $T$  on the normalized device efficiency  $\eta$  in hybrid TCs comprising a) 1-dimensional, and b) hexagonal grids. PEDOT:PSS layer thickness was set to 100 nm, and  $R_{sheet,M}$  to  $10 \Omega/\square$ .

## 5. AJ Printed Grid Electrodes for Organic Solar Cells

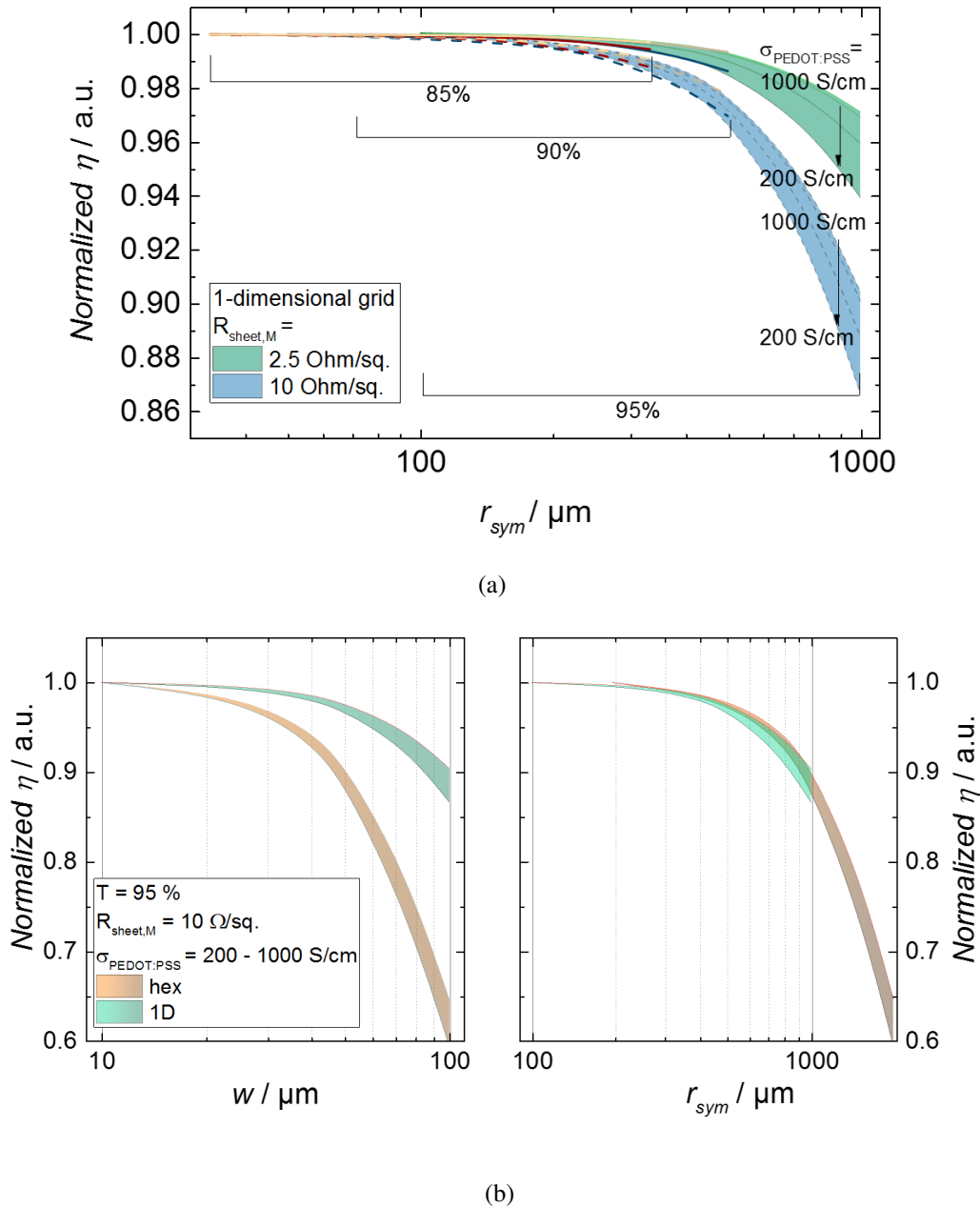
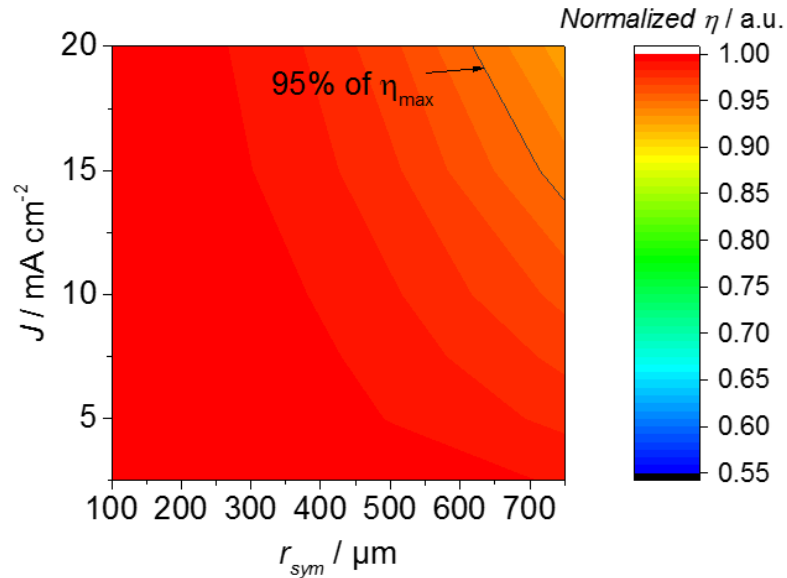


Figure 5.33.: a) 1-dimensional hybrid TCs: Normalized efficiency  $\eta$  reduced to the influencing parameter  $r_{sym}$  (transparency neglected) for different  $R_{sheet,M}$  and different  $\sigma_{PEDOT:PSS}$ . b) Influence of grid geometry (1-dimensional vs. hexagonal) and  $\sigma_{PEDOT:PSS}$  on the normalized efficiency  $\eta$  as a function of line width  $w$  (left) and symmetry radius  $r_{sym}$  (right).  $R_{sheet,M}$  and  $T$  were set to  $10 \text{ Ohm/sq.}$  and  $95\%$ , respectively.

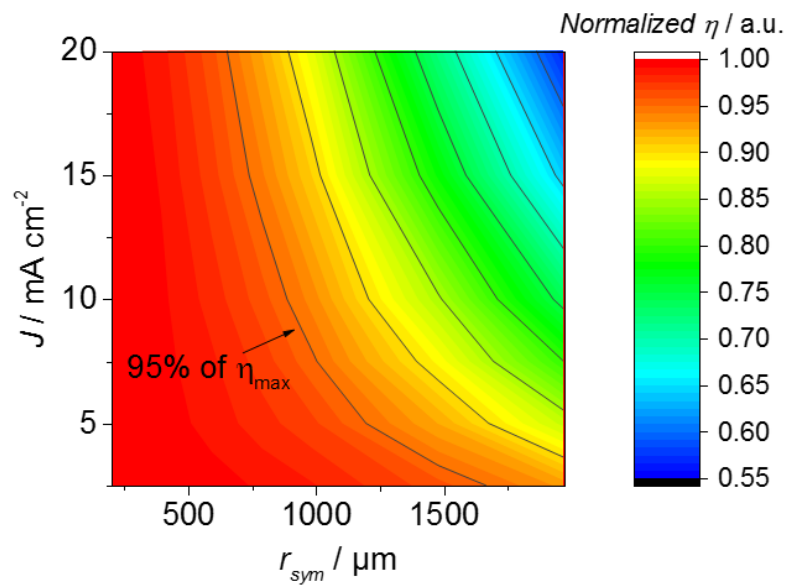
DOT:PSS simulations ( $200 \text{ S m}^{-1}$ ) compared to the 1-dimensional grid. This can be attributed to the more uniform distribution of the Ag mesh, which causes a lower average potential drop within the TC.[90] The same simulation data presented in an efficiency–line width plot (left) uncovers the stronger influence of  $w$  on the device efficiency for the

hexagonal geometry. As a result, already slightly increased line widths occurring during the printing process would utter an starker decrease in transmittance in case of hexagonal grids than for 1-dimensional grid.

### 5.5.5. Current Densities



(a) 1-dimensional



(b) hexagonal

Figure 5.34.: Influence of current density  $J$  on the normalized device efficiency as a function of  $r_{sym}$ . ( $T = 95\%$ ,  $R_{sheet,M} = 10 \Omega/\square$ ,  $\sigma_{PEDOT:PSS} = 850 \text{ S cm}^{-1}$ )

## 5. AJ Printed Grid Electrodes for Organic Solar Cells

Until here, the influence of geometrical factors,  $T$ ,  $R_{sheet,M}$ , as well as of  $\sigma_{PEDOT:PSS}$  have been targeted under the premise of practical application in printed organic solar cells. Albeit, no considerations were bestowed on the current density of the devices. Thus, **Figure 5.34** illustrates in false color graphs the impact of the current density  $J$  on the normalized efficiency  $\eta$  as a function of  $r_{sym}$  for 1-dimensional and hexagonal grids. The boundary conditions for these simulations included  $R_{sheet,M} = 10 \Omega/\square$ ,  $\sigma_{PEDOT:PSS} = 850 \text{ S cm}^{-1}$ , and  $T = 95 \%$ . For current densities below  $5 \text{ mA cm}^{-2}$  the  $r_{sym}$  shows no significant impact. Hence, with  $r_{sym} = 1970 \mu\text{m}$  in a hexagonal geometry a loss of  $\sim 10 \%$  in device efficiency has to be taken. Figure 5.34(a), which plots the influence of current densities up to  $20 \text{ mA cm}^{-2}$  and  $r_{sym}$  up to  $750 \mu\text{m}$  in 1-dimensional geometries, nicely shows a maximum efficiency drop of  $5 - 6 \%$ . The extended range of  $r_{sym}$  in hexagonal geometries resulted in a further efficiency drop down to  $45 \%$ . This basically shows the importance of the potential distribution, where at large  $r_{sym}$  the resistance of the PEDOT:PSS limits the efficiency due to the long high-resistive current paths. Choosing a criterion for a critical efficiency loss of  $5 \%$ ,  $r_{sym} \leq 650 \mu\text{m}$  suits very well for the entire range of simulated current densities.

### 5.5.6. Summary

In the here presented studies on hybrid TCs for organic solar cells, the boundary conditions were set according to the practicality in realistic printing applications. That means, that geometrical restrictions incorporating a minimum line width of  $10 \mu\text{m}$ , and physical restrictions with realistic conductivities for PEDOT:PSS and printed Ag were considered. Furthermore, the focus was set on a comparability of effective sheet resistances and constant transparencies. Interestingly, simulations confirmed that line widths below  $10 \mu\text{m}$  do not necessarily further improve the device performance, which satisfies the feature size capabilities of the AJ printing technology. Under consideration of a broad range of current densities, it was shown that for higher current densities smaller symmetry radii are necessary, which can be explained by a change in the potential distribution within the hybrid TC due to Ohm's law.

In general, the transparency shows a linear dependency of the device performance, the potential distribution instead is influenced by the current density  $J$ ,  $R_{sheet,M}$  and  $\sigma_{PEDOT:PSS}$  and shows a non-linear influence on the device performance. The hexagonal geometry revealed marginally better performances especially for lower PEDOT:PSS conductivities, compared to 1-dimensional grids, which has to be, however, paid by a stronger dependency on the line width to fulfill the requirements of highest possible transparencies. Nevertheless,  $r_{sym} \leq 650 \mu\text{m}$  caused a maximum efficiency loss of  $\leq 5 \%$  for 1-dimensional and hexagonal patterns, considering a  $R_{sheet,M} = 10 \Omega/\square$ ,  $\sigma_{PEDOT:PSS} = 850 \text{ S/m}$ , and  $T = 95 \%$ . That implies a maximum line width of  $\sim 30 \mu\text{m}$  and  $\sim 60 \mu\text{m}$  for hexagonal and 1-dimensional lines, respectively.

## 6. Fully AJ Printed Organic Photodiodes

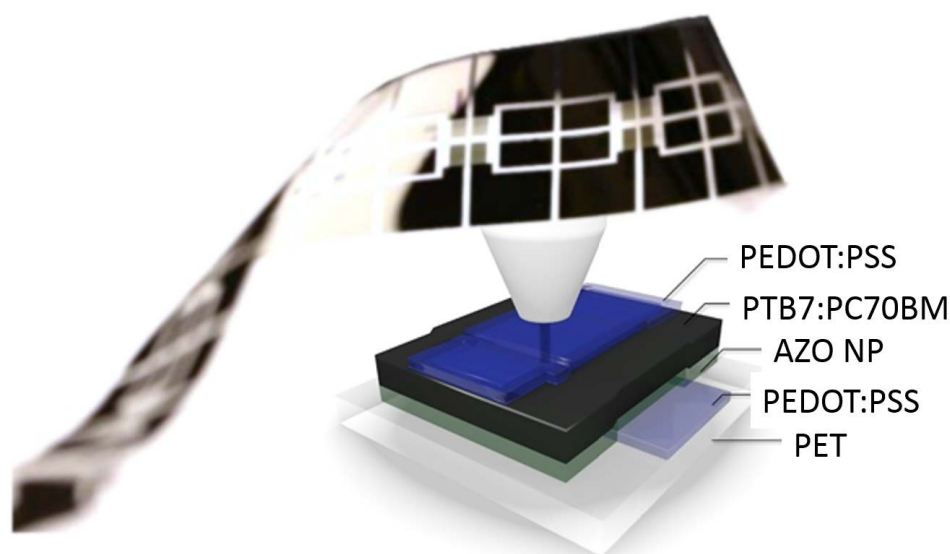


Figure 6.1.: Schematic drawing and photograph of an AJ printed organic photodiode comprising two polymeric PEDOT:PSS electrodes, an aluminum doped zinc oxide (AZO) electron extraction layer, and the PTB7:PC70BM active layer blend.

*The following chapter addresses the fabrication of photodiodes by the additive and digital Aerosol Jet technology. This will be demonstrated by fully printed organic photodiodes (OPDs), as depicted in Figure 6.1. The processing of miniaturized polymeric photodetectors provides large potential for a broad spectrum of future application, e.g. in environmental monitoring systems, automotive applications, optical communication systems or in ubiquitous technologies such as wearables, or portable medical diagnostic systems. In a first instance, the impact of printing parameters on the layer homogeneity will be discussed in section 6.1. The fabrication and characterization of photodiodes printed on ITO back-electrodes and fully printed ITO-free organic photodiodes are presented in the*

## 6.1. Optimization of AJ Printing Parameters for Smooth Functional Layers

**Figure 6.1** illustrates schematically a printed OPD based on two conductive and transparent PEDOT:PSS top and bottom electrodes, an aluminum doped zinc oxide (AZO) electron transport layer, and the PTB7:PC70BM active material sandwiched between the anode and cathode. Nevertheless, all consecutively deposited layers need to accomplish a high degree of layer homogeneity to ensure a proper device functionality and to avoid pin holes and short cuts, which can diminish the device performance. While spin coating makes use of centrifugal forces, AJ printing uses a sequential path of narrowly printed lines, which result in a closed and dense layer. The homogeneity and thickness of the AJ printed active layer strongly depends on the printing parameters, such as material and sheath gas flow, as well as on the substrate-fluid interactions and the drying kinetics during the film formation. To obtain smooth layers from an initially wavy modulated wet film, one crucial condition needs to be satisfied, namely, the drying time needs to exceed leveling time. Influencing factors are here, for instance, the solvent's boiling point and vapor pressure, the ink's viscosity and surface tension, the wet film thickness and the periodicity of the thickness modulation. A profound study on rheology and drying considerations based on linear stability analysis of the Navier-Stokes equation can be found elsewhere.[98] However, it was found that by adjusting the printing parameters very smooth layers could be acquired.

### 6.1.1. Impact of Printing Speed and Multi-Pass Printing

The utilized active material consisted of a blend of PTB7 and PC70BM. The materials were dissolved separately in 1,2-dichlorobenzene (DCB) with a concentration of  $10 \text{ g L}^{-1}$  and then blended in a ratio of 1 : 1.5. Additionally, 2.5 vol.% diiodooctane (DIO) was added to improve the film morphology as reported in literature.[99] The relatively low solid concentration was chosen to fulfill the requirements of low viscosity for a proper ultrasonic atomization.

To examine the influence of the printing speed on the layer homogeneity, areas of  $2 \times 3 \text{ mm}^2$  were printed using a sequential filling pattern with a line pitch of  $50 \mu\text{m}$ . The number of printing passes was adjusted to the printing speed. This means, that for the lowest printing speed of  $2 \text{ mm s}^{-1}$  only one printing pass was used. For the highest printing speed of  $16 \text{ mm s}^{-1}$  the number of passes was increased to 8 passes, which resulted in equal nominal thicknesses by keeping the deposited ink volume constant for all areas. For multi-pass printing, an intermission of 10 sec was set between each path. All other printing related

## 6.1. Optimization of AJ Printing Parameters for Smooth Functional Layers

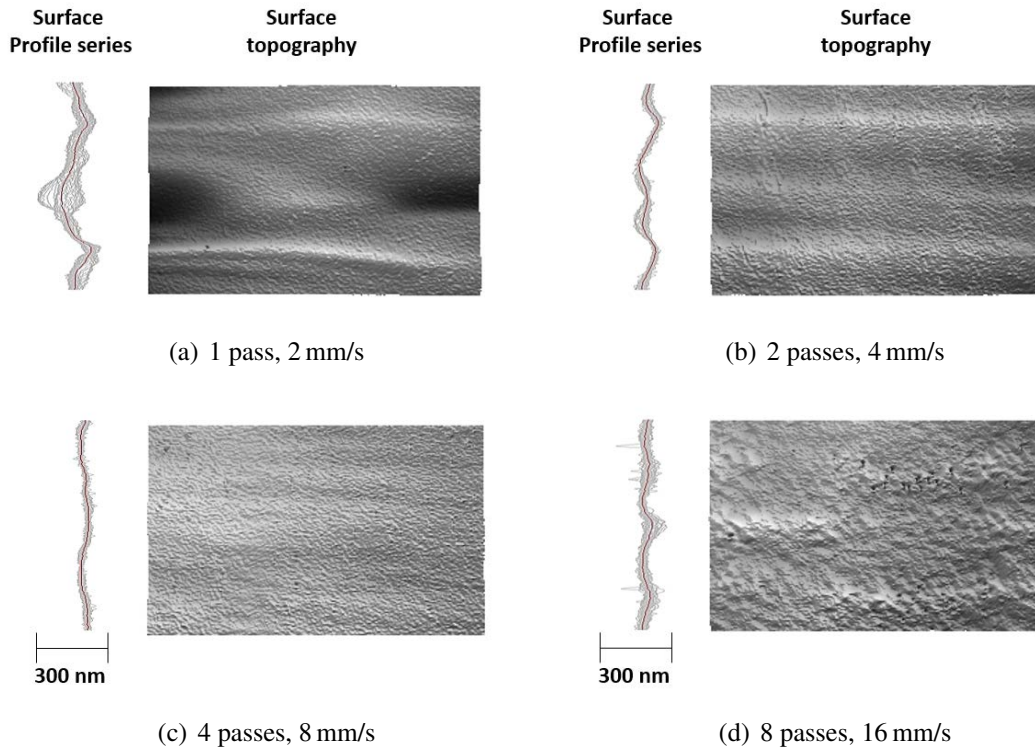


Figure 6.2.: Influence of printing speed on sequentially printed PTB7:PC70BM layers (10 g/L DCB + 2.5 % DIO) on ITO covered glass, where the number of passes were adjusted to keep the deposited ink volume constant for all samples. (sh/atm: 10/17 sccm, tube T./platen T.: 60 ° C/22 ° C). The images show areas of 255  $\mu\text{m}$  x 160  $\mu\text{m}$ . The scale bars are valid only for the surface profiles.

Table 6.1.: Rms roughness  $r$  of areas of 255  $\mu\text{m}$  x 190  $\mu\text{m}$  AJ printed PTB7:PC70BM layers for different printing velocities and printing repetitions at constant atomizer to sheath gas flow of 10 sccm to 17 sccm, and different atomizer gas flow rates

vel [mm/s] / repetitions	$r_{rms}$ [nm]	sh [sccm]/ atm [sccm]	$r_{rms}$ [nm]
2 mm/s / 1x	60.0	10 / 13	64.2
4 mm/s / 2x	26.2	10 / 14	56.5
8 mm/s / 4x	14.5	10 / 15	10.2
16 mm/s / 8x	21.7	10 / 16	6.21

parameters, such as material concentration, ink formulation, sheath (10 sccm) and atomizer (17 sccm) flows, tube (60 ° C) and platen temperature (RT), as well as the tool path remained unchanged.

The wet film after one slow printing pass, as shown in **Figure 6.2(a)**, revealed a very inhomogeneous surface topography, which was caused by the sequential filling pattern. Explanations for that could be found in the dry nitrogen flow from the sheath gas. One explanation is, that as a consequence of the continuously impinging nitrogen gas, the de-

posited ink was partially surface dried or the viscosity drastically increased due to the increasing solid concentration, which then shortens the drying time significantly, and the drying time decreases below the necessary leveling time. Additionally, the sheath and atomizer gas flow can cause fluid displacements in the wet film due to the high pressure emitted from the nozzle.

An increasing printing speed paired with a higher number of passes considerably improved the layer homogeneity, as shown in Fig. 6.2 (b) and (c). An optimal parameter window in due consideration of the utilized ink formulation was hence found between  $4 \text{ mm s}^{-1}$  and  $16 \text{ mm s}^{-1}$  for the given material volume flow. Table 6.1 summarizes the rms values of the printed areas. The rms roughness was hereby reduced from 60 nm (a) to 14.5 nm (c). A further increase in printing speed and number of passes, as shown Fig. 6.2(d), revealed a deterioration of the layer homogeneity. This can be referred to a lack of material supply at high printing speed.

### 6.1.2. Impact of Material Flow Rate

**Figure 6.3** presents surface topographies and the corresponding line profile series, measured with a white light interferometer, show the impact of the material volume flow rate on the layer homogeneity of AJ printed PTB7:PC70BM layers. A quantitative measurement of the volume flow rate however could not be determined since the mist density was unknown. Nevertheless, a variation in the material flow rate at a fixed sheath gas results in an effect on the surface smoothness in a qualitative manner. The films were printed with four consecutively printed passes to ensure a densely closed film. The measured field of view ( $255 \times 190 \mu\text{m}^2$ ) corresponds to four sequentially printed lines next to each other. The lines, however, were not perceptible anymore due to an optimization of printing speed in advance, which was found optimum at  $12 \text{ mm s}^{-1}$ .

In comparison to the previous experiment slightly lower material flow rates were chosen, ranging from 13 sccm to 16 sccm. The results from Fig. 6.3 illustrate markedly the vast difference in surface roughness of the different samples, which did not arise from the modulation of the sequentially printed lines, but affected more the micro morphology of the surfaces. The lowest material flow yielded an rms roughness value of around 64 nm. By increasing the material flow this could be reduced significantly to  $\sim 6 \text{ nm}$ . The roughness data can also be found in Table 6.1. It stands to reason, that the low material flow led to an advancing solvent evaporation in the aerosol already in the nitrogen stream. Thus, an increase in viscosity was accompanied by a finally faster drying of the deposited film.

### 6.1.3. Impact of Ultrasonic Atomization on Functional Polymeric Matter

The AJ printing technique is making use of a high power ultrasonic bath to atomize the functional inks. In case of polymers the mechanical forces could eventually harm the

## 6.1. Optimization of AJ Printing Parameters for Smooth Functional Layers

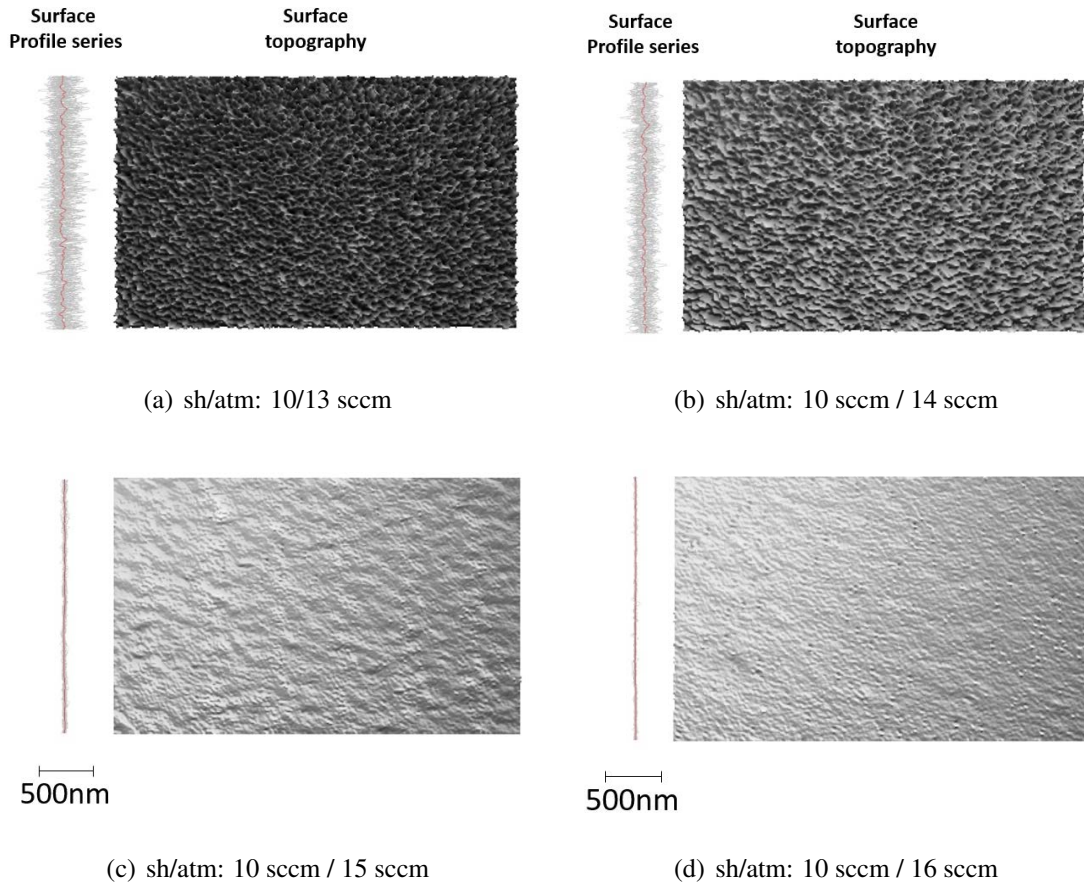


Figure 6.3.: Topography ( $255 \mu\text{m} \times 190 \mu\text{m}$ ) and line series profile measurements (left side of the topography image) of AJ printed PTB7:PC70BM layers using different flow ratios for sheath (sh) and atomizer (atm) gas flows. The scale bars are valid only for the surface profiles.

molecular structure and consequently impact its electronic properties. Furthermore, the ink composition, for instance the ratio of blended materials, as in case of PTB7:PC70BM, could be eventually influenced by the atomization process.

Therefore, near-infrared (NIR) spectroscopic measurements at AJ printed and spin cast (SC) PTB7, PC70BM, and PTB7:PC70BM layers were performed by Tobias Glaser in cooperation with the Kirchhoff-Institute for Physics (University of Heidelberg). **Figure 6.4** shows the relative transmission spectra over the wavenumber for SC (top) PTB7 and PC70BM (bottom) layers deposited on silicon wafer. The SC and AJ printed blended materials are shown in blue and red. The characteristic peaks for PTB7 and PC70BM can be retrieved in the material blends, where absorption bands above  $1600 \text{ cm}^{-1}$  can be ascribed to oscillations of specific functional groups. In Figure 6.4 the double bonded oxygen atoms in the PTB7 and the PC70BM molecules are exemplarily highlighted. The spectral region between  $600$  and  $1600 \text{ cm}^{-1}$  is called the *finger print region*, which is unique for every molecule and arises from a superposition of oscillations of the molecule. Both, the spin cast and the AJ printed blended PTB7:PC70BM layers show a linear su-

## 6. Fully AJ Printed Organic Photodiodes

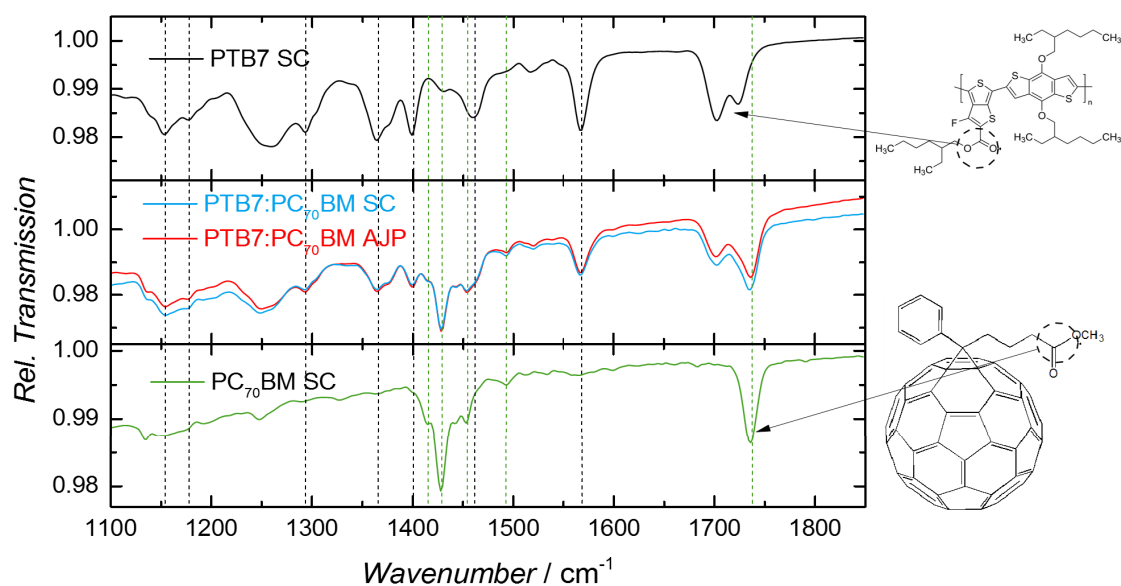


Figure 6.4.: Infrared spectroscopy of spin cast (SC) PTB7, SC and AJ printed PTB7:PC70BM blends, and SC PC70BM layers on silicon wafer.

position of the individual spectra, which implies that no interactions, such as charge transfer between donor and acceptor took place. Furthermore, the unique unchanged *finger prints* let assume, that no decomposition of the materials occurred during the ultrasonic atomization. The differences at wavenumbers above 1600 cm<sup>-1</sup> could be ascribed to baseline effects influenced by the ambient temperature or thin-film interferences, while deviations below 1250 cm<sup>-1</sup> arose from the measurement setup.[100, 101] Merely minor deviations in the peak heights lead to the assumption that a slight variation in blend composition is possible.

### 6.1.4. Summary

The AJ printing technique was used to print areas of the PTB7:PC70BM blend. It could be shown, that by adjusting the relevant parameters very smooth layers could be achieved with this sequential printing technique. In particular, the printing velocity in combination with multi-pass printing opens a broad process window customizable to specific requirements. Additionally, a variation in the material flow rate revealed a concise impact on the roughness in the micrometer regime, which was not related to a height modulation due to the sequential printing.

NIR-spectroscopy measurements were performed at spin coated and AJ printed PTB7:PC70BM layers, which showed almost identical finger print regions indicating that no molecular or compositional derogation took place, which is of major importance for functional materials and hence for the final application in optoelectronic devices.

## 6.2. ITO comprising Photodetectors

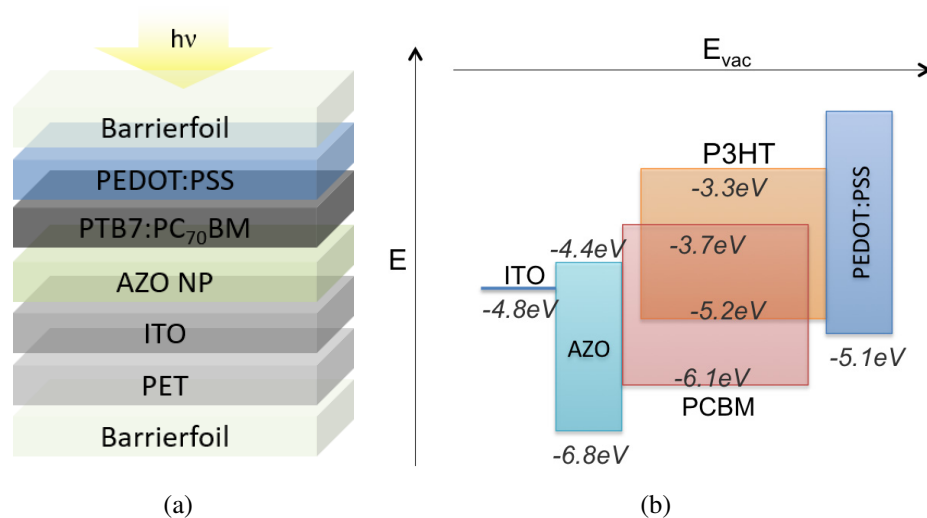


Figure 6.5.: a) Schematic drawing of the device stack and b) photograph of fully AJ printed devices with c) the corresponding energy levels of the different materials.

### 6.2.1. Device Preparation

After examining the printing related issues in the optimization of printed smooth and homogeneous active layers devices were fabricated, as shown in **Figure 6.5(a)**. The stack comprised, beside the ITO already covering PET foil, only AJ printed layers. The energy levels in Fig. 6.5(b) presents the energetic properties of the functional layers of an inverted device architecture.[102] Aluminum doped zinc oxide was utilized as the electron transport layer (ETL), since it offers an electrical conductivity three orders of magnitude higher than intrinsic zinc oxide, which allowed for a broader processing window for the ETL thickness.[103]

In a first instance, the indium-tin oxide (ITO) coated 175  $\mu\text{m}$  thick PET foil ( $20 - 30 \Omega/\square$ , Kintec, Japan) was pre-structured using an inkjet printed (Dimatix, DMP-2831, 10 pL cartridge) poly(methyl methacrylate) (PMMA) etching mask illustrated in **Figure 6.2.1**. After etching with a 10 % hydrochloric acid, the substrates were cut and finally cleaned for 15 min in acetone and 2-propanol.

An AZO nanoparticle dispersion from 2-propanol (N10X, Nanograde) was used as the electron transport layer. The 2.5 wt.% dispersion was further diluted in a ratio of 1:1 with mesitylene to adjust the final layer thickness and to additionally affect the wetting and drying behavior on the ITO, as it revealed a higher boiling point of 164.7 °C and a slightly increased surface tension of 28 mN m<sup>-1</sup> compared to 2-propanol with 82.3 °C and 21 mN m<sup>-1</sup>, respectively. After depositing the AJ printed sequentially filled layer a thermal annealing step at 80 °C for 5 min was applied. The final layer thickness was

## 6. Fully AJ Printed Organic Photodiodes

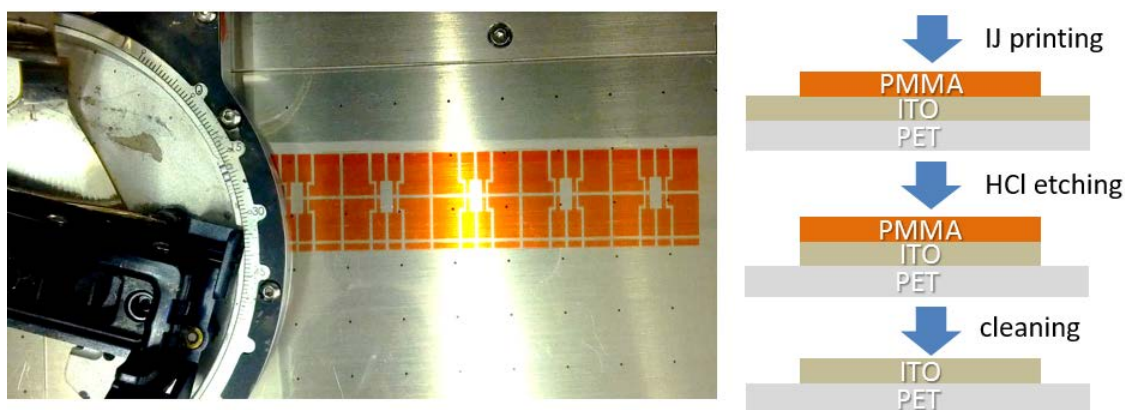


Figure 6.6.: Structuring process of ITO covered PET foil by using inkjet printed PMMA (orange) as etching mask.

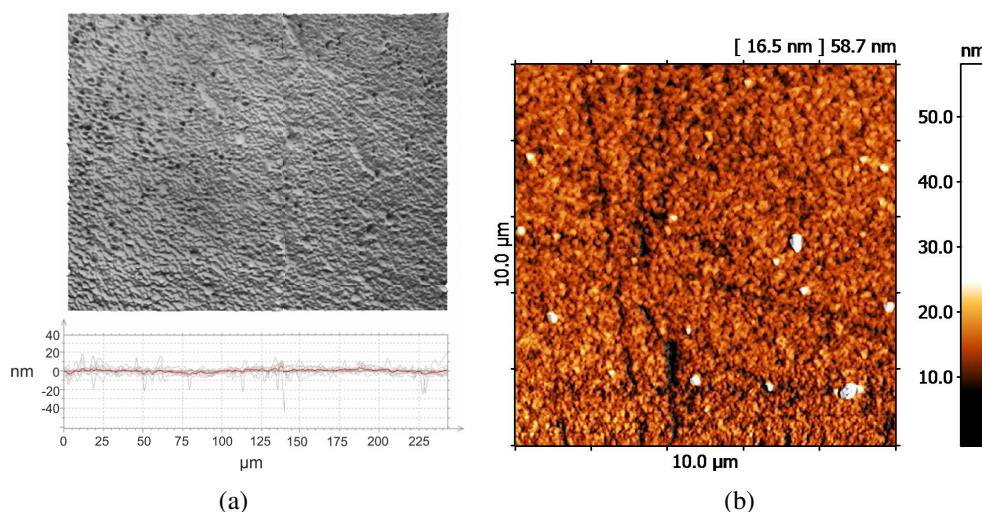


Figure 6.7.: a) Topography image ( $243 \mu\text{m} \times 191 \mu\text{m}$ ) and profile series and b) AFM topography image ( $10 \mu\text{m} \times 10 \mu\text{m}$ ) of an AJ printed Al-doped ZnO layer on ITO covered glass.

measured to be 50 nm with an rms roughness of 5 nm, as presented in the **Figure 6.7(a)**. The surface topography image of an AJ printed AZO layer on ITO covered glass substrate recorded with a white light interferometer revealed the presence of drying fronts arising from the sequential printing process and indicated tiny pin holes, as can be observed in the corresponding profile series. The AFM image presented in Fig. 6.7(b) uncovered artefacts in form of particles on the AZO surface with peak heights around 20 – 30 nm, which could originate from dust particles or even AZO agglomerates. The latter could be possible, since nanoparticle agglomeration can be induced by a change in the pH value of the dispersion, which can be bred at the surface of the glass vial.[104]

The active material with PTB7:PC70BM was deposited by AJ printing on top of the

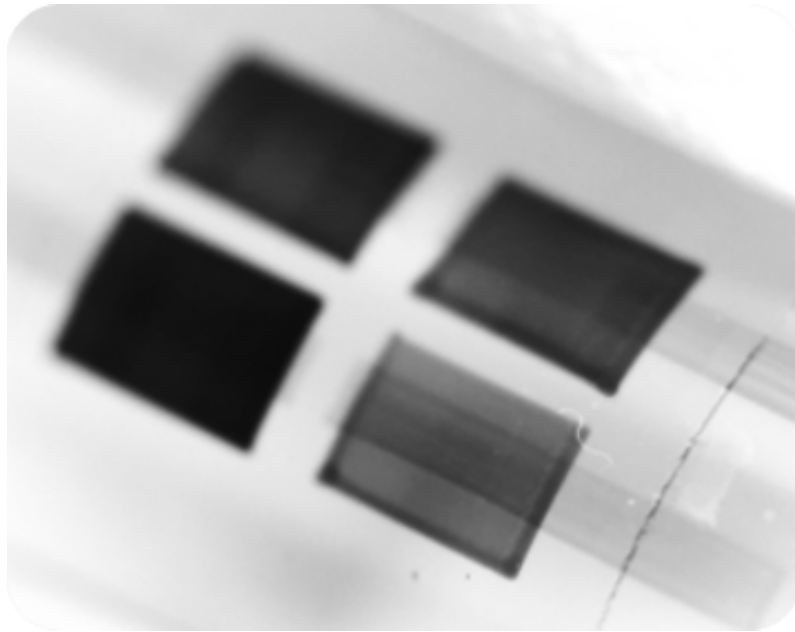


Figure 6.8.: Photograph of organic photodiode samples comprising different active layer thicknesses fabricated by multi-pass printing.

PET/ITO/AZO cathode, as presented earlier in the text. The consecutive deposition of thin absorber layers in a multi-pass process allowed for a defined variation in the final active layer thickness, as illustrated in **Figure 6.8**. The active layer was printed with a tube temperature of  $60\text{ }^{\circ}\text{C}$ , while the atomizer and sheath gas flows were adjusted to attain a dense but thin layer in one single pass. The tool path parameters were set to  $50\text{ }\mu\text{m}$  pitch and  $10\text{ mm s}^{-1}$ . After a drying procedure in vacuum for at least 15 min, the polymeric transparent anode was printed on top of the PTB7:PC70BM from a diluted conductive PEDOT:PSS formulation (F HC Solar, Heraeus) with water in a ratio of 2:1. The 1 mm wide ITO cathode stripe and the orthogonal 1 mm wide PEDOT:PSS stripe determine the  $1\text{ mm}^2$  active area of the AJ printed OPDs. The completed devices were then dried in vacuum in an ante-chamber for 1 h at 15 mbar and  $20\text{ }^{\circ}\text{C}$  and afterwards directly transferred into a nitrogen filled glove box for encapsulation, where an adhesive barrier foil (3M) against oxygen and humidity penetration was stuck on top of the samples.

## 6.2.2. Characterization of Semi-Transparent ITO comprising OPDs

### Dependency of Layer Thickness on the Device Performance

The dark current density, as can be seen in **Figure 6.9**, revealed a significant dependency on the active layer thickness. It was found to follow an exponential decay, as shown in Fig. 6.9(b). This relationship could be ascribed to the change in the electric field, which changed depending on the applied bias and the distance  $d$  between the anode and cathode.

## 6. Fully AJ Printed Organic Photodiodes

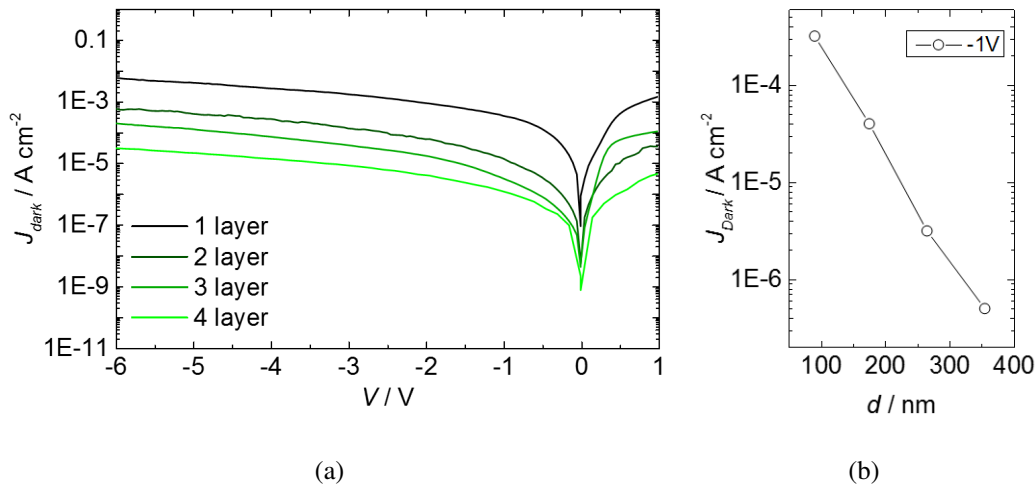


Figure 6.9.: a) Dark current densities recorded for OPDs comprising different PTB7:PC70BM layer thicknesses. b) Dark current density at  $-1\text{ V}$  reverse bias as a function of layer thickness.

Fig. 6.10 unveiled that the decrease in dark current density was at least supported by the electric-field, which provokes an enhancement the charge carrier injection from the contacts into the active layer, where the effective field was calculated using the following equation 6.1:[105]

$$F_{eff.} = \frac{V_{bi} + V_{applied}}{d} \quad (6.1)$$

where  $V_{bi}$  is the built-in voltage and  $V_{applied}$  the applied bias voltage;  $d$  refers to the active layer thickness.  $V_{bi}$  was estimated to  $0.9\text{ V}$  extracted from the electrochemical potential difference of the anode and cathode, as shown in the energy levels in Fig. 6.5(b).

**Figure 6.10** shows the dark current density as a function of the film thickness dependent effective electric field in a log-log plot at different reverse bias voltages. #1 to #4 account for the number of consecutively printed layers of active material. The electric field was calculated according to equation 6.1. The dark current density increases with the effective field, as expected with decreasing active layer thickness.

The transmission spectra in **Figure 6.11(a)** of the active printed active layers was measured using a UV-Vis spectrometer to confirm, that additional printing passes and thus an incremental increase in layer thickness lead to a linear decrease in transmittance, as shown in Fig. 6.11(b). That could be again used to estimate the active layer thickness by just measuring the transmittance at  $550\text{ nm}$  ranging from 15 to 60 %.

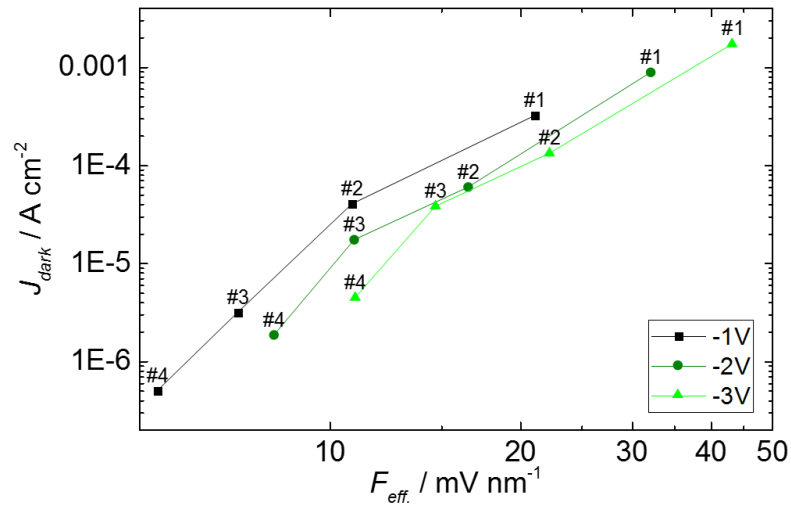


Figure 6.10.: Dark current density as a function of the calculated effective electric field.

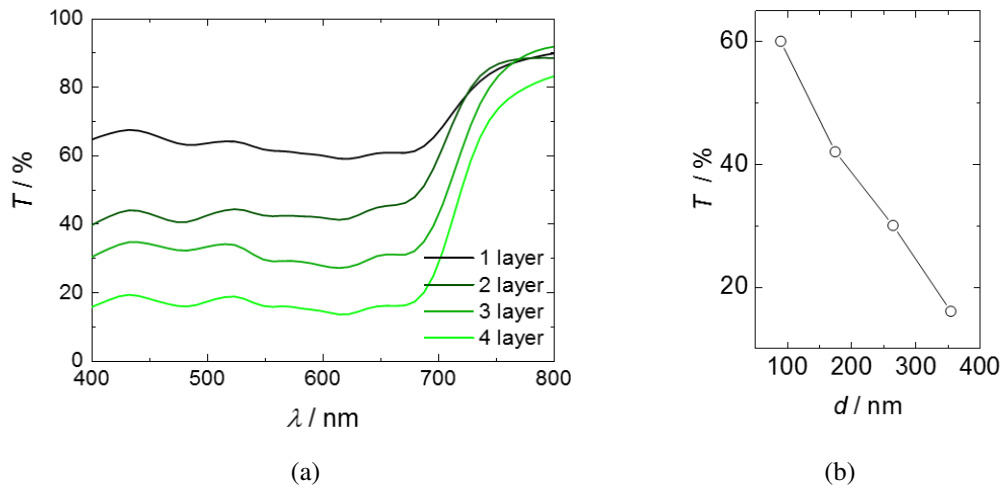


Figure 6.11.: a) Transmittance spectra recorded for OPDs comprising different PTB7:PC70BM layer thicknesses with 1 to 4 consecutively printed passes. b) Transmittance at 550 nm wavelength as a function of layer thickness.

### Steady State Analysis

We now examine in particular two AJ printed OPDs with different active layer thicknesses, which will be dubbed in the following as *Device A* with  $\sim 200$  nm and *Device B* with  $\sim 300$  nm. The layer thicknesses were achieved by adjusting the thickness of a single pass to  $\sim 100$  nm, where *Device A* comprised two and *Device B* three consecutively printed layers. Furthermore, the measured transmittance spectra (dashed) in **Figure 6.12** nicely confirmed the findings, which accounted for  $\sim 40\%$  and  $\sim 20\%$  for the active layers including the PEDOT:PSS top of *Device A* and *Device B*, respectively. The absorption of the PEDOT:PSS top electrode could be assumed to be constant for both

## 6. Fully AJ Printed Organic Photodiodes

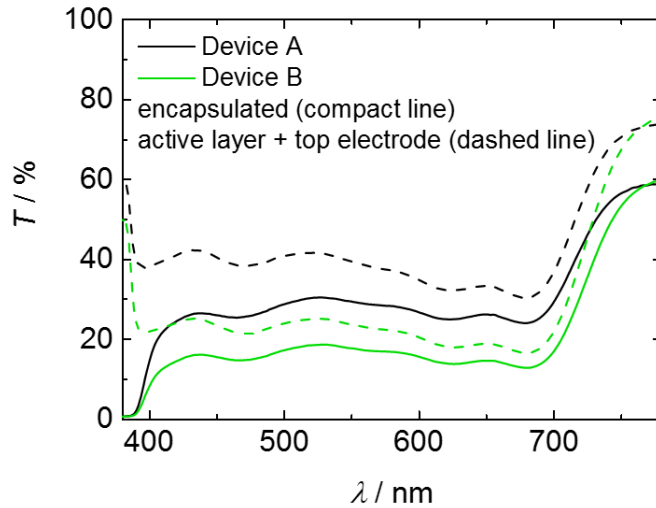


Figure 6.12.: Transmission spectra of active layers with PEDOT:PSS top electrode and completed and encapsulated Device A (black) and Device B (green).

devices. The graph additionally shows the transmittance of the completed both-sided encapsulated photodiodes. The strong absorption below  $\lambda = 400$  nm was assigned to the encapsulation foil, which provided a UV cut-off filter at  $\sim 400$  nm to protect from harmful UV-degradation of the active material and the PEDOT:PSS.[106]

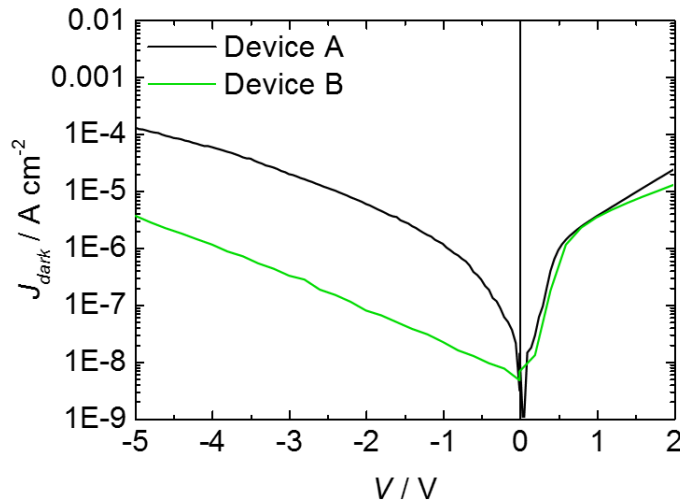


Figure 6.13.: a) Transmission spectra of active layers with PEDOT:PSS top electrode and completed and encapsulated Device A (black) and Device B (green). b) Corresponding dark current densities.

Special considerations were bestowed upon the dark current, which is directly related to the on-off ratio, as well as the detectivity of photodetectors, and therefore mainly defines

its performance. The difference in dark current density in **Figure 6.13** on the one hand arose from the difference in the effective field, as already introduced in the preliminary results in Fig. 6.10. But on the other hand, thinner active layers also tend to exhibit pin holes or locally reduced thicknesses leading to lower parallel resistances and thus to higher leakage currents. However, dark current densities of  $1.17 \mu\text{A cm}^{-2}$  and  $21.9 \text{ nA cm}^{-2}$  at  $-1 \text{ V}$  reverse bias could be achieved for *Device A* and *Device B*, respectively.

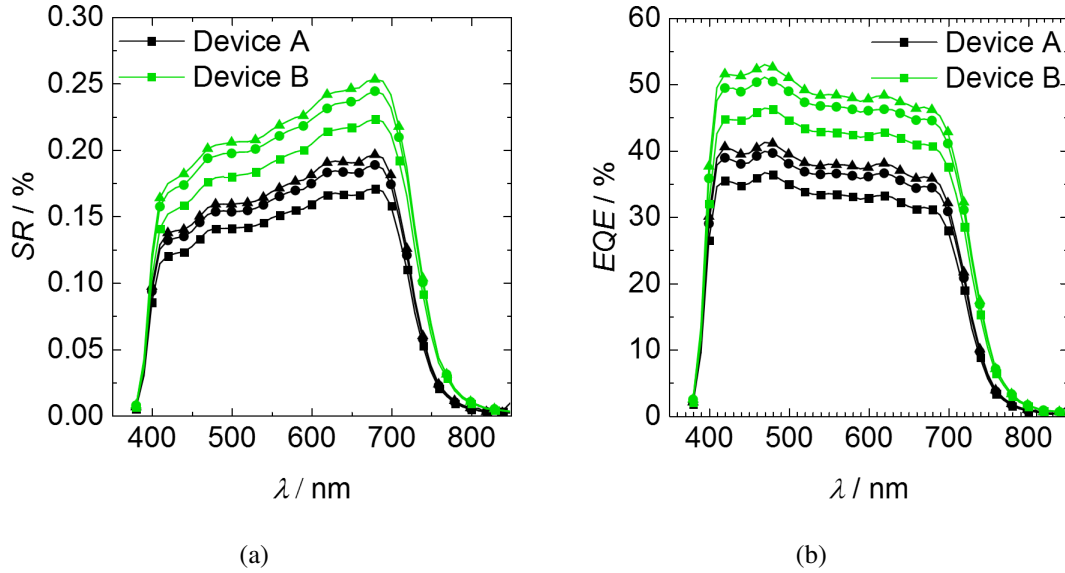


Figure 6.14.: Spectral responsivity and external quantum efficiency of ITO comprising Device A (black) and Device B (green) recorded at  $-1 \text{ V}$  (circle),  $-2 \text{ V}$  (triangle), and  $-3 \text{ V}$  (rhomb) reverse bias.

The spectral responsivity  $SR$  and the corresponding external quantum efficiency  $EQE$  are shown in **Figure 6.14**. The measurements were recorded at reverse biases of  $-1 \text{ V}$  (circles),  $-2 \text{ V}$  (triangles), and  $-3 \text{ V}$  (rhombs). An increase in  $SR$  and  $EQE$  for increasing bias voltages could be observed, which was attributed to the increase in the effective field leading to a more efficient extraction of the generated charge carriers.  $SR$ s of  $0.25 \text{ A W}^{-1}$  and  $EQE$ s of up to  $55 \%$  were achieved for *Device B*, which was found to be in good agreement with state-of-the-art values for spin cast devices in literature.[107] However, to mention in particular, quantum efficiencies up to  $85 \%$  have been demonstrated in literature for optimized spin cast PTB7:PC70BM photodetectors with evaporated charge selective transport and electrode layers, which shows the large potential of this material system.[108]

The specific detectivity  $D^*$  is plotted for *Device A* and *Device B* at reverse bias voltages ranging from  $-1 \text{ V}$  to  $-3 \text{ V}$  in **Figure 6.15**. Thereby,  $D^*$  of  $2 \cdot 10^{11}$  Jones and  $2 \cdot 10^{12}$  Jones were achieved over a wide spectral region for *Device A* and *Device B* at  $-1 \text{ V}$  bias, respectively. Explicitly mentioned, these values considered a calculated shot noise contribution as described in Equation 2.16 on page 18, which could differ from the

## 6. Fully AJ Printed Organic Photodiodes

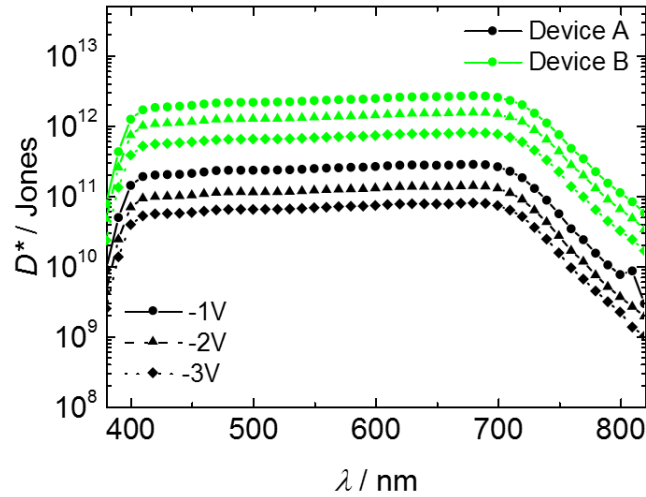


Figure 6.15.: Calculated specific detectivity for the ITO comprising AJ printed OPDs Device A (black) and Device B (green) recorded at  $-1\text{ V}$  (circle),  $-2\text{ V}$  (triangle), and  $-3\text{ V}$  (rhomb) reverse bias.

Table 6.2.: Specification list of ITO comprising AJ printed OPDs recorded at  $-3\text{ V}$  reverse bias. Maximum Detectivity  $D^*$  also given at  $-1\text{ V}$ .

<b>Parameter (@-3V, @550nm)</b>	<b>DeviceA</b>	<b>DeviceB</b>
<i>Active layer thickness [nm]</i>	$\sim 200\text{ nm}$	$\sim 300\text{ nm}$
<i>Transparency [%]</i>	30	18
$J_d [A\text{ cm}^{-1}]$	$19.5E-6$	$0.32E-6$
$SR [A\text{ W}^{-1}]$	0.168	0.225
$D^* [Jones](@-1V)$	$6.7E10 (2.4E11)$	$6.7E11 (2.2E12)$
$EQE [\%]$	38	48

actual noise equivalent power. The differences in  $D^*$  for *Device A* and *Device B* referred to diverging dark currents, as well as the differences in  $SR$  The device characteristics from the static analysis are summarized in Table 6.2.

## Speed of Response

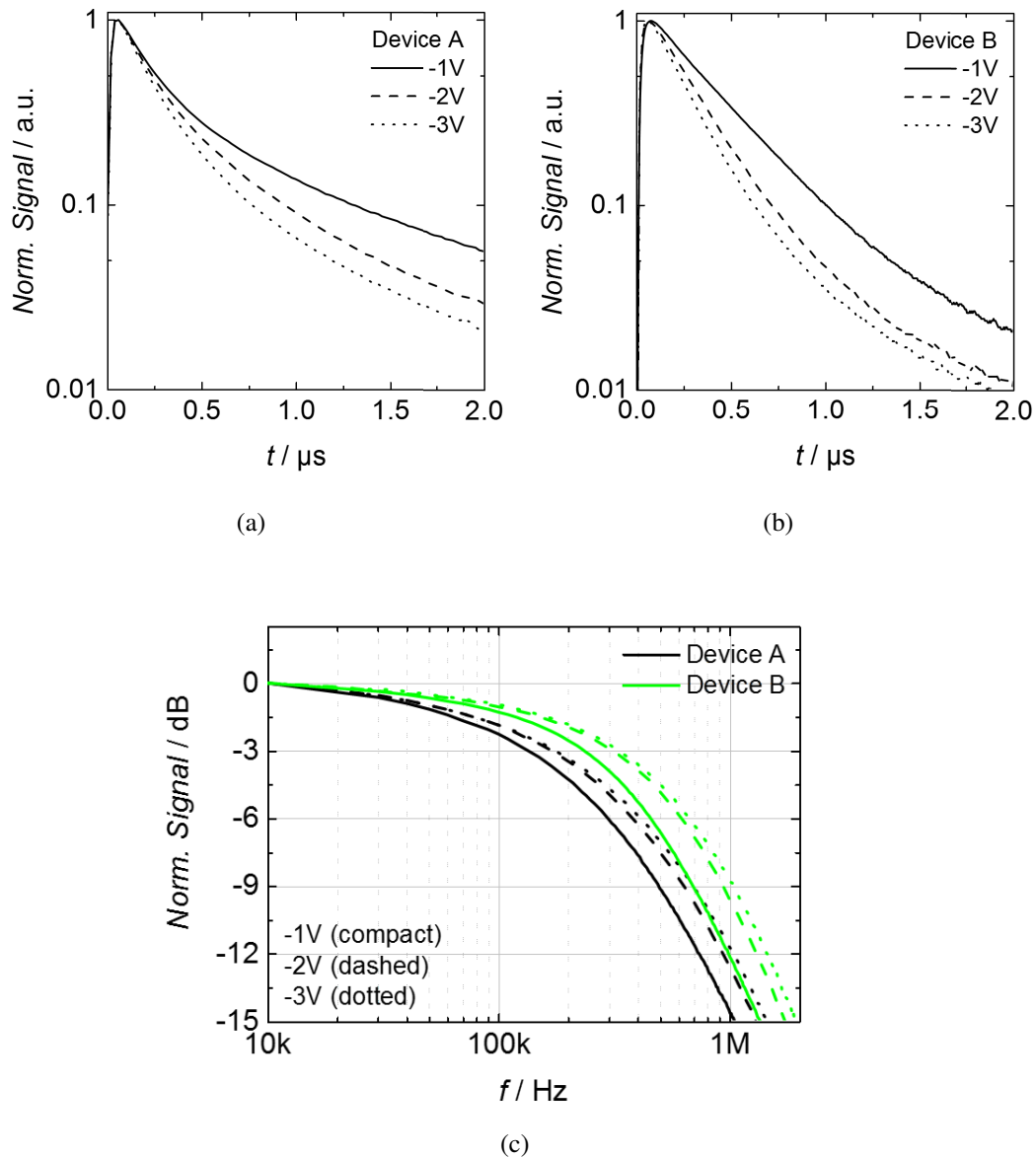


Figure 6.16.: Transient photo current measurements for a) Device A and b) Device B and c) the corresponding FFT of the normalized signal as a function of frequency.

For measuring the dynamic response, the devices were excited with a very short ( $< 1.1$  ns) laser pulse (1Q355-2, Crylas) at  $\lambda = 532$  nm. Detailed information about the setup can be found in section 4.3.3 on page 38. **Figure 6.16** exhibits the photo response recorded for *Device A* (a) and *Device B* (b) at a power density of  $5 \cdot 10^{11} \text{ W m}^{-2}$ . The measurements were conducted again for reverse bias voltages from  $-1$  V to  $-3$  V. The rise time was determined to be below 30 ns for all devices. Albeit, the fall time and thus the bandwidth (*BW*) clearly changed with the active layer thickness and the applied reverse bias. *Device*

## 6. Fully AJ Printed Organic Photodiodes

Table 6.3.: Dynamic Analysis of ITO comprising OPDs with different active layer thicknesses.

Parameter	Device A			Device B		
	-1V	-2V	-3V	-1V	-2V	-3V
$t_{FWHM}$ [ns]	243	220	199	325	240	205
$t_{9010}$ [ns]	1189	837	672	868	605	523
$BW$ [kHz]	133	170	175	238	312	330

A revealed a significantly longer  $t_{fall}$  compared to *Device B*. The detection speed limiting factors for photodiodes can be roughly broke down into three main contributions. The slowest one depicts the diffusion of the charge carriers through the active layer outside the depletion region. The second one refers to the drift of charge carriers through the depletion region, which can be influenced by the reverse bias.[109–111] And the last one is the  $RC$  time constant, where the capacitance of the device is influenced by the active layer thickness and the resistance composed of the series and the load resistance of the circuit. Having a look at the values from Table 6.3 give evidence that the devices are by  $RC$  limited.[112] Based on the theory explained in section 2.3.3 on page 19 the fall time depends on  $t_{RC}$ , which relates the dependency to the series resistance and the device capacitance. Since the series and contact resistances can be estimated to be similar for both devices, the capacitance constitute the influencing factor. By increasing the active layer thickness the capacitance decreases according to Eq. 2.20 on page 19.

### 6.2.3. Summary

In conclusion, semi-transparent ITO-containing PTB7:PC70BM photodetectors were demonstrated, where all consecutive layers were AJ printed. At the beginning, a strong focus was set on the fabrication of very smooth functional layers, while the final layer thickness adjustment was accomplished by multi-pass printing. The static and dynamic characterization of the fully printed OPDs with different active layer thicknesses revealed device performances comparable to state-of-the-art values reported in literature.[107] The semi-transparency of 20 – 30 % allows for imperceptible applications, but also limits the  $SR$  and thus  $D^*$  due to a reduced photon absorption. Nevertheless,  $SR$  up to  $0.25 \text{ A W}^{-1}$ ,  $D^*$  over  $10^{12}$  Jones and  $BW$  up to  $330k$  Hz were achieved.

## 6.3. Fully Printed OPDs

ITO embodies one of the weak spots in organic optoelectronic devices for flexible application. On the one hand, the processing and following patterning steps are causing high production costs.[113] On the other hand, the brittle electrode system constitutes mechanical stability issues. Therefore, the transparent metal oxide electrode was replaced by AJ printed conductive and also transparent PEDOT:PSS. **Figure 6.17** shows a photograph of

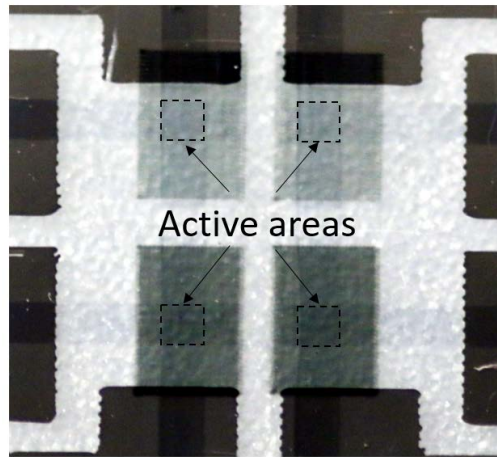


Figure 6.17.: Photograph of fully AJ printed semi-transparent OPDs comprising active areas of  $1\text{ mm}^2$ . The sample shows two different thicknesses of the active material.

fully AJ printed OPDs comprising PTB7:PC70BM sandwiched between two polymeric PEDOT:PSS electrodes.

### 6.3.1. Device Preparation

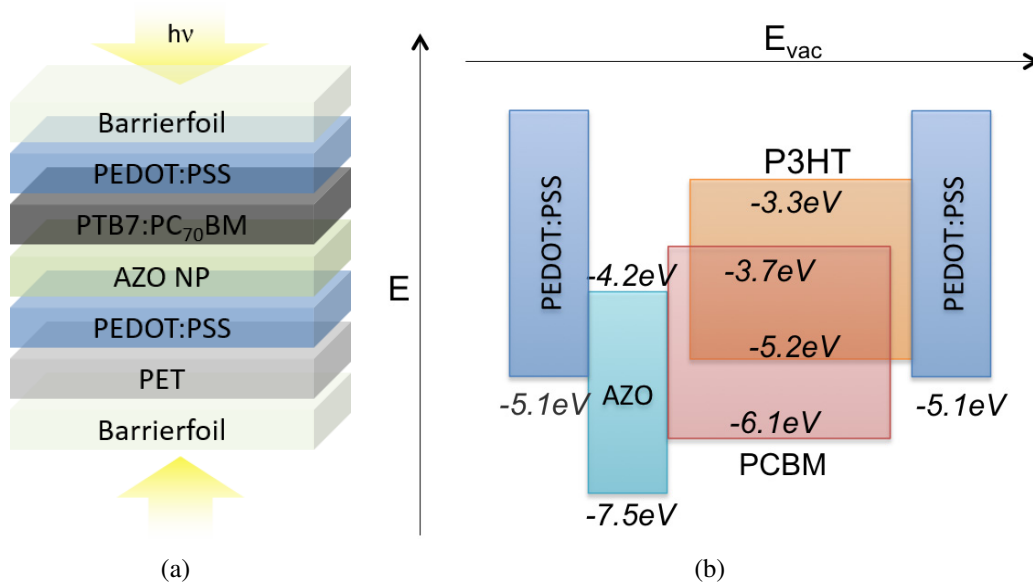


Figure 6.18.: a) Schematic device architecture and b) photograph of fully AJ printed devices with c) the corresponding energy levels of the different materials.

The device stack and the energy levels are shown in **Figure 6.18**. Due to the fact that PET is permeable to water and oxygen, the samples were encapsulated from both sides with adhesive 3M barrier foil, as already described in section 6.2.1 for the ITO comprising

## 6. Fully AJ Printed Organic Photodiodes

devices.

The question to be raised is how the energetic properties of the hole conducting PEDOT:PSS match with the ones of the electron transport layer AZO. Fortunately, this material configuration has already been investigated elsewhere.[114]



Figure 6.19.: a) Inkjet printed Ag contact pads on PET. b) PET stripe comprising several fully AJ printed OPDs.

Since PEDOT:PSS reveals a relatively low lateral conductivity compared to ITO or metals, the contact pads and feed lines were inkjet printed on PET foil using a Dimatix Fujifilm DMP-2831 using a commercial Ag ink (Silverjet DGP-40LT-15C, Sigma-Aldrich), as illustrated in **Figure 6.19(a)**.

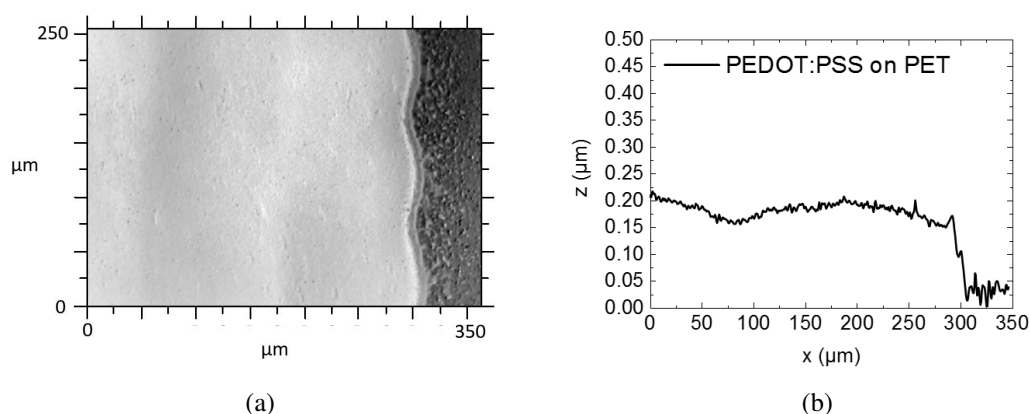


Figure 6.20.: AJ printed PEDOT:PSS stripe on PET foil. a) Topography and b) surface profile

The polymeric bottom electrode was AJ printed from a PEDOT:PSS (F HC Solar, Heraeus) formulation diluted with water in a ratio of 2:1. As mentioned before, the dilution of inks was principally used to adjust the ink's viscosity for a proper ultrasonic atomization. **Figure 6.20** exhibits the topographical quality of the AJ printed film. The surface modulation observable in Fig 6.20(b) arose from the sequential printing path. The electrodes had

an average thickness of  $\sim 200$  nm to ensure an acceptable conductivity paired with a high transparency. The PEDOT:PSS layer was afterwards dried in a vacuum oven for 30 min at  $100^\circ\text{C}$ . The following layers were printed according to the previously presented device preparations for the ITO comprising OPDs (page 75) with nominal layer thicknesses as followed: PEDOT:PSS ( $\sim 200$  nm) / AZO (50 nm) / PTB7:PC70BM ( $\sim 310$  nm) / PEDOT:PSS ( $\sim 200$  nm). The flexible printed OPDs are presented in Figure 6.19(b).

### 6.3.2. Characterization of ITO-free OPDs

#### Steady State Analysis

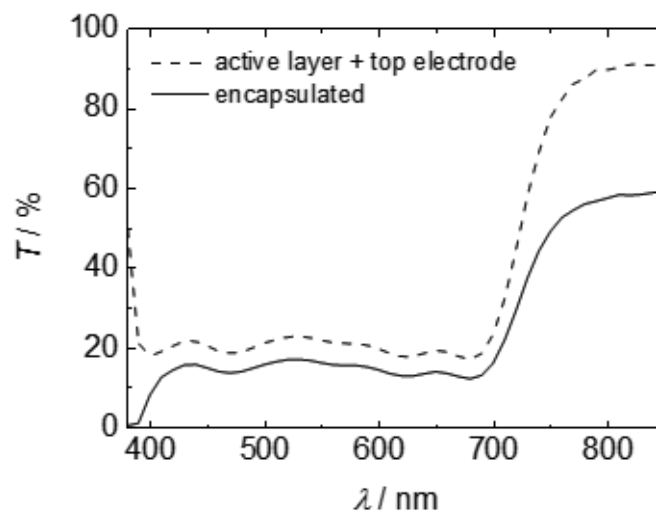


Figure 6.21.: Transmission spectra of the active layer including the PEDOT:PSS top electrode, and the encapsulated device.

**Figure 6.21** shows the transmittance spectra of the encapsulated semi-transparent device and the PTB7:PC70BM active layer including the PEDOT:PSS top electrode. Analogous to the results for the ITO comprising *Device B*, the ITO-free Device possessed a similar active layer thickness and a similar transmittance spectra. The spectra shows close resemblance to the transmittance spectra of the previously studied *Device B*, which is in very good agreement with the measured film thickness of 310 nm of the active layer.

The dark current density, as shown in **Figure 6.22**, of the ITO free (black) compared to the previously characterized *Device B* (red), exhibited a significant increase in dark current. However, due to the very weak slope in reverse bias, it can be excluded that the higher current density is introduced by pin holes in the active layer. Nevertheless, pin holes in the AZO layer due to wetting issues on the PEDOT:PSS could play a major role in the current density increase. Hence, a PEDOT:PSS/PTB7/PEDOT:PSS hole only current path

## 6. Fully AJ Printed Organic Photodiodes

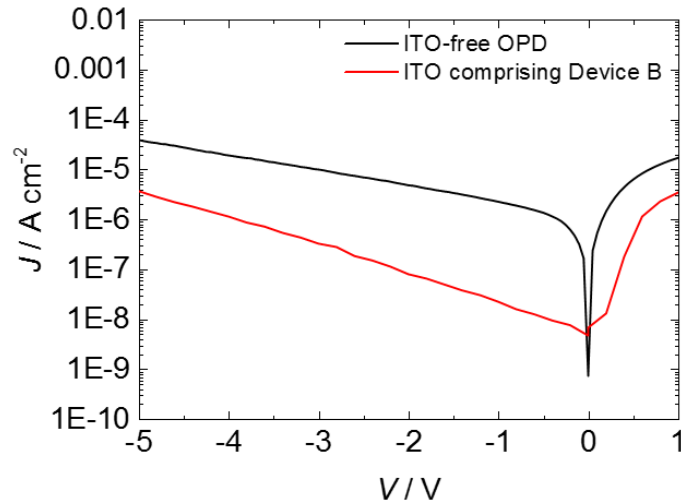


Figure 6.22.: Dark current density of a fully AJ printed semi-transparent OPD.

would be formed. Another explanation could be found in the higher step edge between PEDOT:PSS and PET ( $\sim 200$  nm) compared to ITO and PET ( $50$  nm), which could evoke a reduction in active layer thickness at the bottom electrode rim.

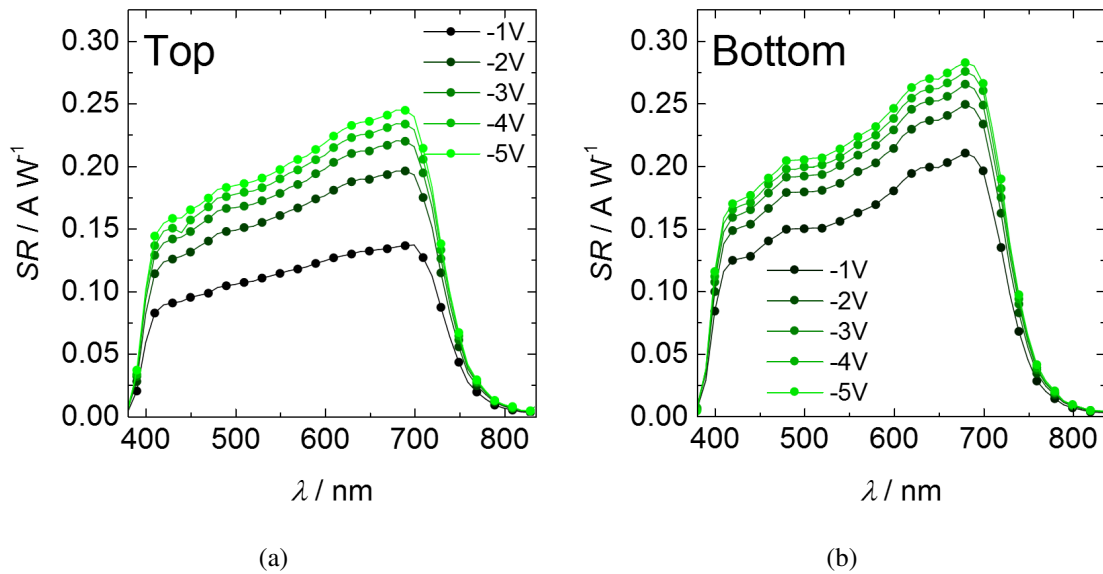


Figure 6.23.: Spectral responsivity (SR) measured at sample illuminated through a) top electrode and b) bottom electrode.

**Figures 6.23** and **6.24** present the  $SR$  and  $EQE$  of the ITO-free OPD illuminated through the top and bottom PEDOT:PSS electrode, respectively, and recorded for reverse bias voltages ranging from  $-1$  V to  $-5$  V. It is evident that the device showed similar performance for both illumination sides. The highest performance with an  $SR$  of  $0.26$   $\text{A W}^{-1}$

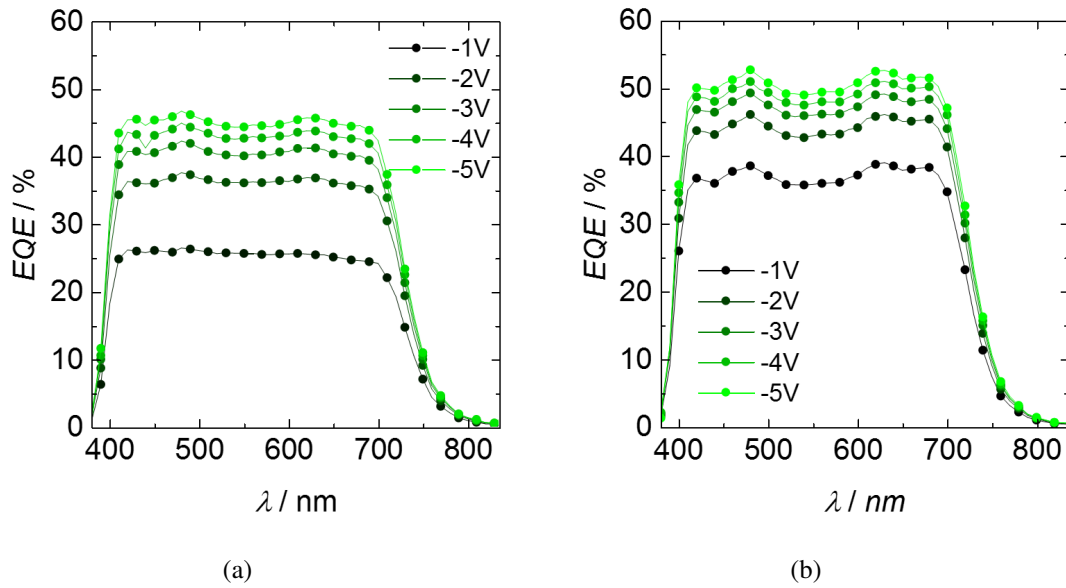


Figure 6.24.: External quantum efficiency (EQE) measured at sample illuminated through a) top electrode and b) bottom electrode.

at  $\lambda = 680$  nm and an EQE of over 50% over the entire absorption range was achieved for the bottom illumination. However, the discrepancy can be explained by thin film interferences, where the different optical paths through the device act as distinctive optical spacers.[114]

A considerably lower *SR* and *EQE* at the low reverse bias voltage of  $-1$  V gives evidence for a electric field dependent recombination process, i.e. geminate or bimolecular recombinations. Furthermore, the high series resistance of the PEDOT:PSS electrodes significantly impact the photo current at low reverse bias voltages, which would also entail a reduction in *SR* and *EQE*.

To further investigate the evidence of dominant geminate recombination processes, atomic force microscopy (AFM) images were conducted and show the micromorphology of an AJ printed PTB7:PC70BM layer in **Figure 6.25**. The  $50 \mu\text{m}$  by  $50 \mu\text{m}$  area revealed an rms roughness of  $3.5 \text{ nm}$  and on the one hand confirms the very good surfacial homogeneity of the AJ printed films. But on the other hand, the topography and phase images indicate the formation of PTB7 and PC70BM rich domains in the micrometer range. The high boiling point solvent diiodooctane (DIO) was added to the initial blend, which supposedly distributes the PC70BM uniformly, as investigated elsewhere.[99] This effect could not be observed for the AJ printed samples. However, these observations raise the suspicion that the PTB7:PC70BM blend and particularly the amount of additive needs to be adjusted to the AJ printing technology, which on that point, will be addressed in future work. Further AFM measurements of samples printed with different parameter sets can be found in the Appendix A on page 115, where principally the influence of the tube temperature was investigated.

## 6. Fully AJ Printed Organic Photodiodes

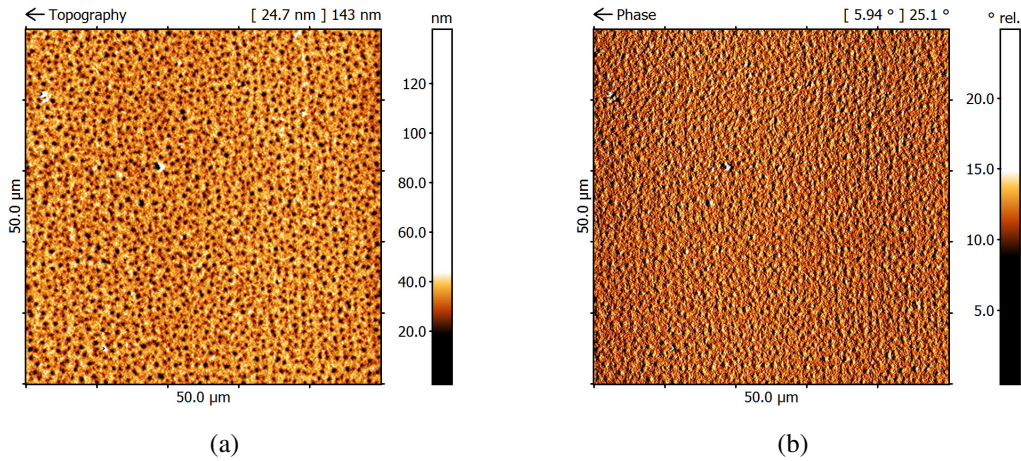


Figure 6.25.: AFM image with a) topography and b) phase of a AJ printed PTB7:PC70BM layer.

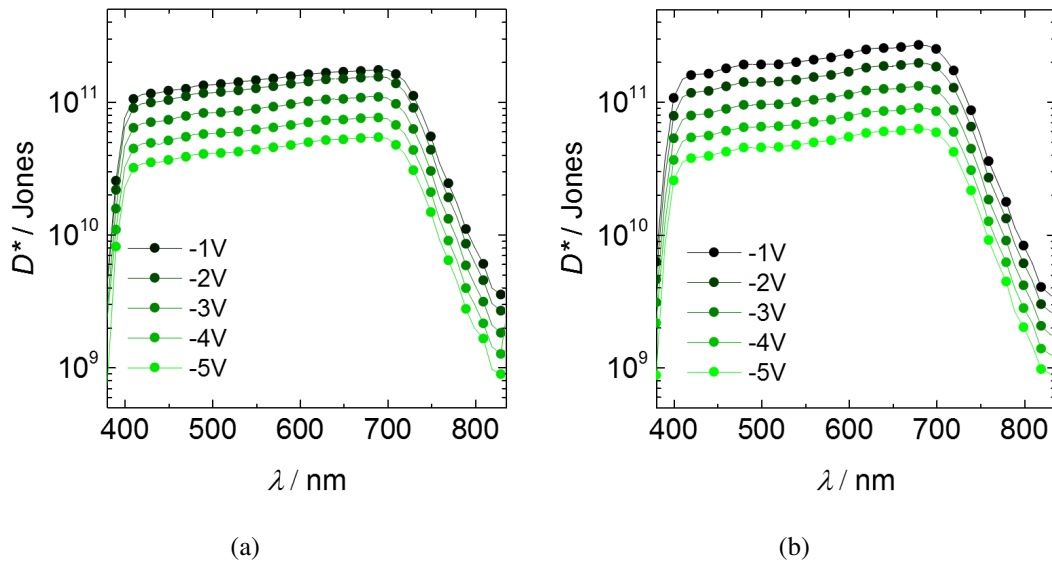


Figure 6.26.: Specific detectivity  $D^*$  recorded for a) top and b) bottom illuminated sample.

As a consequence of the higher dark current compared to the ITO comprising *Device B*, also the specific Detectivity of the ITO-free device suffers, as can be seen in **Figure 6.26**. Hence,  $D^*$  of  $2.7 \cdot 10^{11}$  Jones and  $1.7 \cdot 10^{11}$  Jones for the bottom and the top illumination, respectively, were achieved at  $-1$  V bias and  $\lambda = 680$  nm.

Simple mechanical stress tests were performed for the ITO free printed OPD. Therefore, the device was bent to a radius of 2 mm. As demonstrated in section 5.3.2 in Fig. 5.17(a) (p. 54), ITO covered PET is very brittle and consequently exhibits irreversible harm even at bending radii of  $\sim 6$  mm. **Figure 6.27** shows two photographs of the ITO free device bent in a radius of 2 mm. A further decrease in bending radius, however, lead to a delam-

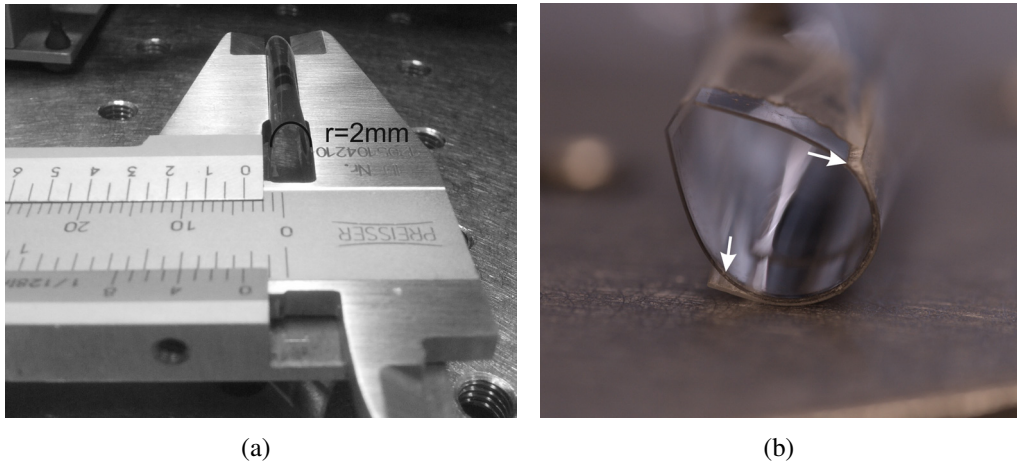


Figure 6.27.: a) Photograph of an OPD bended at a radius of 2 mm. b) Delamination of the encapsulation foil as a consequence of further reduction of the bending radius.

ination of the encapsulation foil, as shown in Fig. 6.27(b).

The  $SR$  and  $EQE$ , as shown in **Figure 6.28**, were recorded before and during the bending of the device at a reverse bias of  $-3\text{ V}$ . Almost no loss in performance could be observed, which is also confirmed by the calculated  $D^*$ .

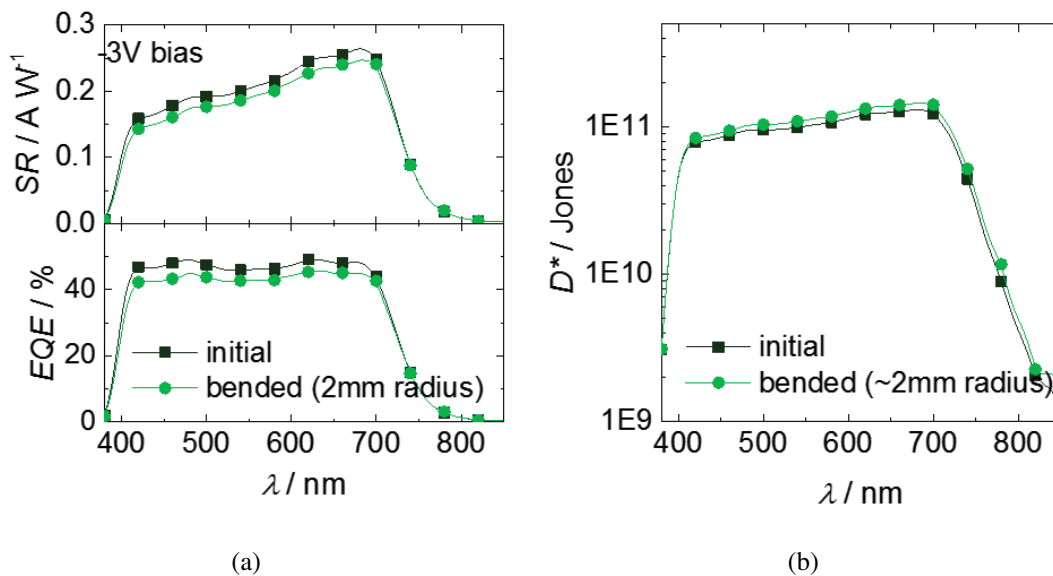


Figure 6.28.: a)  $SR$  and  $EQE$  (at  $-3\text{ V}$ ) recorded before and during bending of the fully AJ printed OPD with a radius of 2 mm. b) corresponding  $D^*$ .

Table 6.4.: Specification list of ITO-free AJ printed OPDs.

Parameter (@-3V, @550nm)	top illumination	bottom illumination
Active layer thickness [nm]		316
Transparency [%]		16
$J_a$ [ $A\ cm^{-1}$ ]		9.9E-6
SR [ $A\ W^{-1}$ ]	0.178	0.204
$D^*$ [Jones](@-1V)	8.9E10 (1.5E11)	1.0E11 (2.0E11)
EQE [%]	40	46

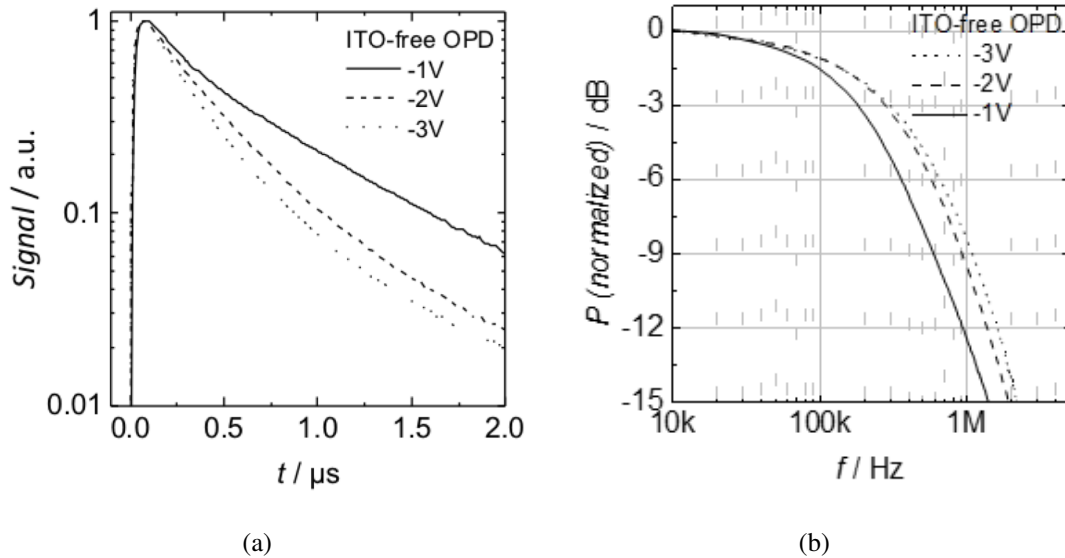


Figure 6.29.: a) Current signal measured at different reverse bias voltages of the ITO-free OPD after an excitation with a 1 ns laser pulse. b) Fast-Fourier-Transform of the time signal into the frequency spectrum. The cut-off frequency can be derived at  $-3$  dB.

### Speed of Response

For measuring the pulse response of the ITO-free OPD, the device was excited with a 1 ns laser pulse (1Q355-2, Crylas) at  $\lambda = 532$  nm, as described in section 4.3.3 on page 38. The transient photo current measurements in **Figure 6.29(a)** revealed a strong influence of the applied reverse bias on the current decay time, as it was already observed for the ITO comprising *Device B*. For the lowest applied bias voltage of  $-1$  V a small current decay was observed, while for increasing bias voltages the decay and thus the fall time  $t_{fall}$  markedly decreased. The time needed for the charge transport to the corresponding electrodes, namely the transit time for the dominant charge carriers, as introduced in chapter 2.3.3 on page 19, is mainly defined by the active layer thickness, the charge carrier mobility and the internal electric field.[111, 112] It can be assumed that a  $-3$  V the depletion region is not fully extended over the entire active layer thickness, which leads to a high probability, that diffusion of charge carriers limits the current decay. An RC limitation

Table 6.5.: Device characteristics of ITO free AJ printed OPDs extracted from transient measurements at different reverse bias voltages.

Parameter	ITO free OPD		
	-1V	-2V	-3V
$t_{FWHM}$ [ns]	388	306	266
$t_{fall}$ [ns]	883	572	464
$BW$ [kHz]	181	276	295

would have been expected at much higher reverse bias voltages.

However, in comparison to the ITO comprising *Device B* very similar characteristics for  $t_{FWHM}$ ,  $t_{fall}$  and  $BW$  were observed, which nicely demonstrate the feasibility of replacing the ITO by an additionally printed PEDOT:PSS layer. Finally, a  $BW$  of up to 295k Hz at  $-3$  V was observed. The transient characteristics are summarized in Table 6.5.

### 6.3.3. Summary

In summary, the fabrication of organic photodiodes by solely utilizing the AJ printing technique was demonstrated. Furthermore, the suitability of this technique for a local, precise and homogeneous deposition of functional materials could be revealed. Although, the nozzle size would be ideally adapted in industrial processes to the final device geometries to avoid sequential filling paths, the multi-pass printing approach allows for a precise adjustment of the final layer thickness. It was also shown that the atomization of the functional ink does not affect the electrical properties and no molecular harm was observed by the IR spectroscopic measurements. However, the printing technique seems to have a nominal influence on the ink composition. These concerns were raised due to the fact that AFM measurements indicated a phase separation of the PTB7 and the PC70BM, which ideally should have been suppressed by the high boiling point additive DIO.

At first, OPDs (PET/ITO/AZO/PTB7:PC70BM/PEDOT:PSS) with different active layer thicknesses were printed. The static and dynamic characterization of these devices delivered state-of-the-art performances with  $SR$  up to  $0.26 \text{ A W}^{-1}$  and  $BW$  at around 330k Hz. The replacement of 50 nm thick ITO by an additionally AJ printed conductive  $\sim 200$  nm thick PEDOT:PSS bottom electrode revealed considerably higher dark currents, which might be evoked by the higher step edge of the bottom electrode, the formation of pin holes due to a non-uniform PEDOT:PSS surface energy. Nevertheless, the semi-transparent devices consisting of four consecutively AJ printed layers revealed remarkable  $SR$  of  $0.2 \text{ A W}^{-1}$  and a  $BW$  of  $\sim 300$  k Hz. Besides that, a  $D^*$  of  $> 10^{11}$  Jones was achieved for the bottom as well as top illumination of the device. The results of the semi-transparent and flexible OPDs are comparable to state-of-the-art inorganic photodetectors, as illustrated in Figure 6.30. Bending tests indicated that devices made from purely soft matter (and AZO NP) might not constitute the limiting factors in flexible applications. The mechanical limitation was rather set by the substrate and the adhesive encapsulation. Nonetheless, semi-transparency and flexibility depict unique features of organic electronics, which paired with additive manufacturing techniques, could play a significant role in

## 6. Fully AJ Printed Organic Photodiodes

future applications.

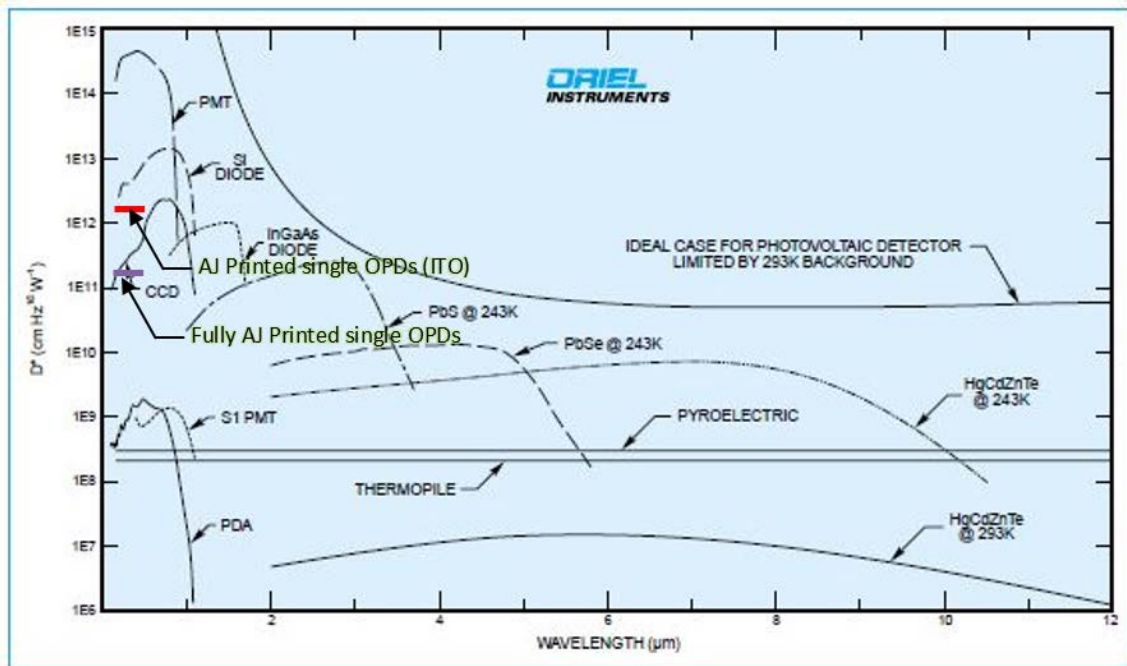


Figure 6.30.: Specific detectivity of common inorganic photodetectors and the AJ printed OPD (red) in comparison to them. (Adapted and reprinted from <http://www.azooptics.com>)

## 7. Digitally Printed Dewetting Patterns for Self-Organizing Microelectronics



Figure 7.1.: Fully printed flexible photodiode array comprising 36 pixel with dimensions of  $45 \times 175 \mu\text{m}^2$ .

*This chapter addresses a novel patterning technique for digitally printed metal microstructures by using the additive AJ manufacturing technique. Herein, the fabrication of Ag micro-structures by AJ printed low-surface-energetic epoxy resin (SU-8, 2000 Series, MircoChem) as dewetting patterns on PET is investigated. The use of the digital small feature-size capability of the printing technique enabled the manufacturing of complex patterns and multi-layered devices, which will be exemplified in fully printed micrometer-sized OPD pixels, as shown in **Figure 7.1**. Even integrated circuits could be fabricated in form of ring oscillators, which can be found in the Appendix B.3.*

## 7.1. The Dewetting Process

The intense research on printed electronics, such as sensors,[115] transistors,[116–118] light-emitting diodes,[98] and batteries[119] enable a bright future for low-cost integrated systems, such as for smart packaging,[120–122] remote sensing, [123, 124] consumer electronics, [125–127] or medical diagnostics. This ongoing transfer from lab-scale processes to industry relevant printing processes is indispensable for the success of printed electronics. It can be nicely observed, that the development and improvement of fabrication processes, as well as the effort to overcome technical hurdles of printing related issues gain more and more center stage in the past years. This implies in particular the downscaling of printed structures, the reproducibility of small features and the registration accuracy of microscale multi-layer devices, e.g. by direct-printing of small feature patterns, [117, 128, 129] or spray deposition of photodiodes [130, 131]. Apart from that, substrate modification processes for tuning the selective wetting have been developed to obtain highly accurate small-features. Concerning this appertain hydrophobic self-assembled monolayers (SAM)[132], electron-beam direct writing [133], and mechanical surface modifications like nano-imprinting [134]. In general, the success of printed electronics will rise and fall with the ease of processing combined with the reliability of the fabricated devices.

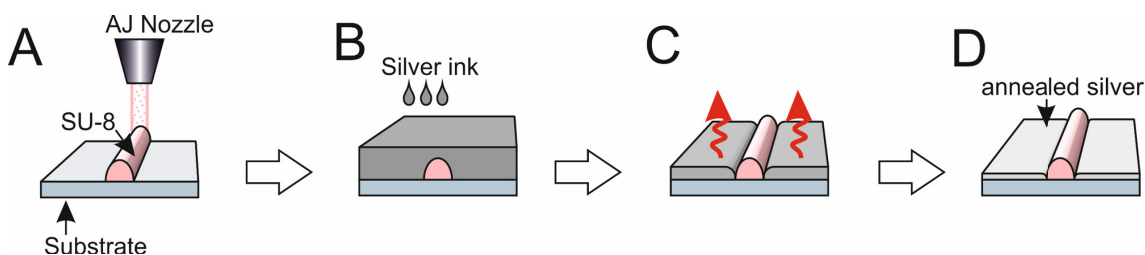


Figure 7.2.: Schematic drawing of the patterning process of Ag electrodes.

The patterning process, as depicted in **Figure 7.2**, starts with (A) the printing of hydrophobic SU-8, which was a priori diluted with  $\gamma$ -butyrolactone (GBL) and 3-heptanone in a ratio of 1:1:1 ( $\sim 23\%$  solid loading) to achieve a printable ink formulation. The printed pattern of epoxy resin was then exposed to UV light (365 nm) for 5 min and afterwards baked on a hotplate at  $120^\circ\text{C}$  for 15 min. The subsequently deposited Ag ink (B) was done by inkjet, brushing, spray coating, and blade coating, which consequently allowed for a large diversity of processing options. Nevertheless, for reasons of reproducibility, most experiments were performed using the inkjet deposition technique. Finally, after self-organization of the Ag patterns, the samples were (C) vacuum dried at 15 mbar for 30 min and (D) thermally annealed on a hotplate at  $120^\circ\text{C}$  for 20 min.

The self-organization of the functional material commenced instantaneously, as can be observed from the image sequence over time in **Figure 7.3(a)**. Here, the Ag ink was brushed on top of the SU-8 patterned PET substrate using a swab. The dewetting started from a seed spot on the left side of the pattern advancing along the SU-8 lines until the dewetting was completed. After 30 s the assembly of the finger structures in the order

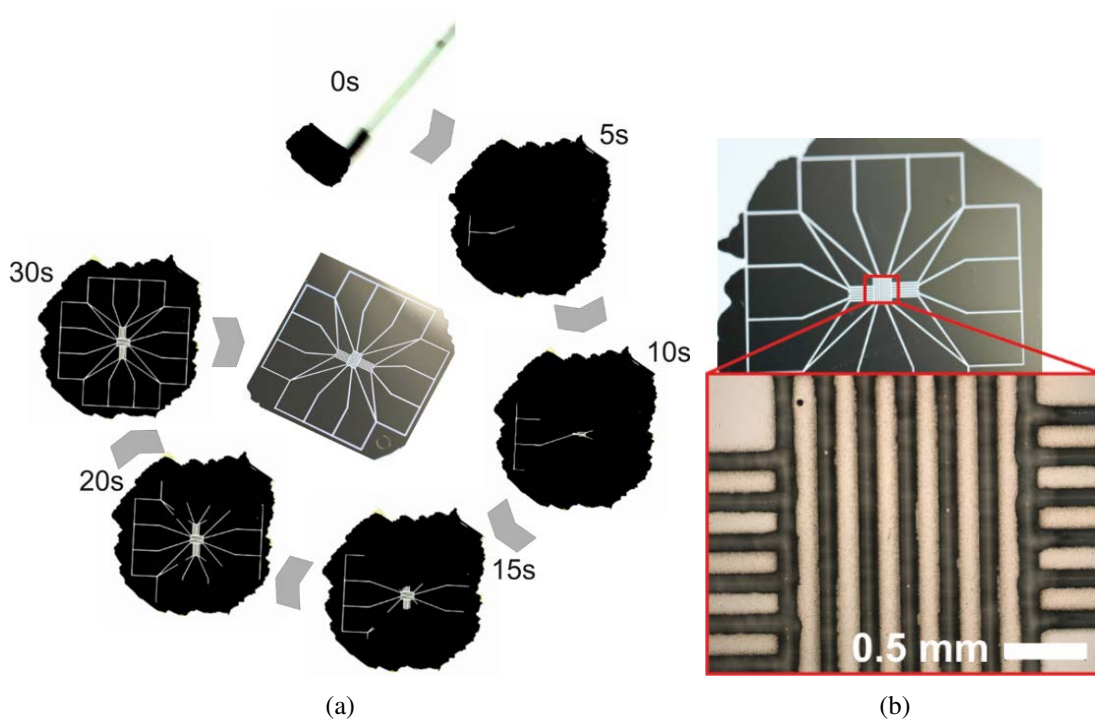


Figure 7.3.: a) Image sequence over time showing the self-organization of a brushed Ag ink on an SU-8 patterned PET substrate. b) Magnification of the annealed Ag finger structures.

of  $\sim 100 \mu\text{m}$  was completed. Figure 7.3(b) presents a micrograph of the self-aligned interdigitated Ag structures. The seemingly random starting point could be attributed to a locally low wet film thickness, which presumably result from either inhomogeneous and imprecise deposition technique or by protruding SU-8 peaks arising from the SU-8 line crossings. The relation between an observable dewetting phenomena and the necessary framework conditions will be discussed in the following paragraphs.

**Figure 7.4** shows an inkjet printed Ag stripe, which was separated by two  $\sim 11 \mu\text{m}$  wide SU-8 lines, where a line width of  $\sim 10 \mu\text{m}$  represents the lower resolution limit of the AJ printer. These fine structures were enough to be used for separating a continuously printed Ag stripe. The Ag was printed using a drop spacing of  $45 \mu\text{m}$ . This nicely demonstrates the feasibility of small feature size printing in combination with the repelling SU-8.

## 7.2. Wetting Morphologies

### 7.2.1. Contact Angles and Work of Adhesion

Dewetting mechanisms by exploiting hydrophobic SAMs or nanoimprinted micro and nanostructures have been intensively investigated in the past years.[133–135] The fundamental effect is caused by a difference in attracting and repelling forces between the

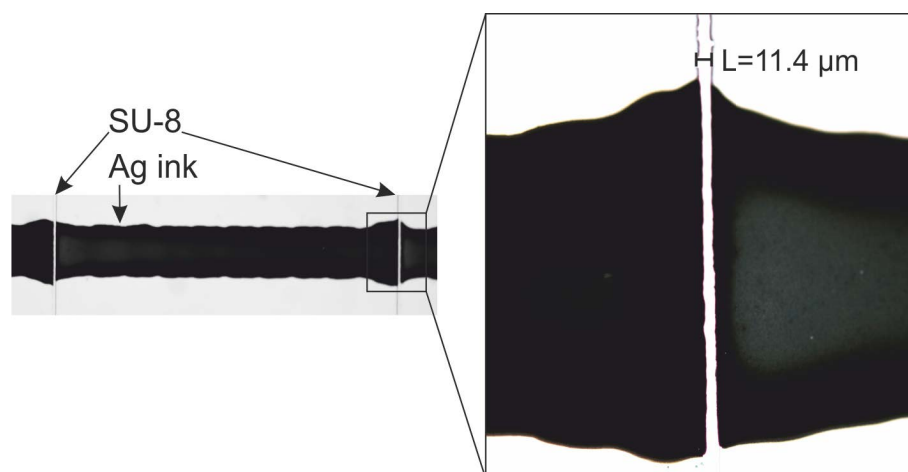


Figure 7.4.: Inkjet printed Ag stripe across two AJ printed  $11\ \mu\text{m}$  wide SU-8 lines on a PET substrate.

ink and the respective surfaces, which denotes a low contact angle (CA) on the *wetting* surface and a high CA on the *dewetting* surface. Furthermore, key factors were found in the ink viscosity, as well as in the solid concentration.[133, 136]

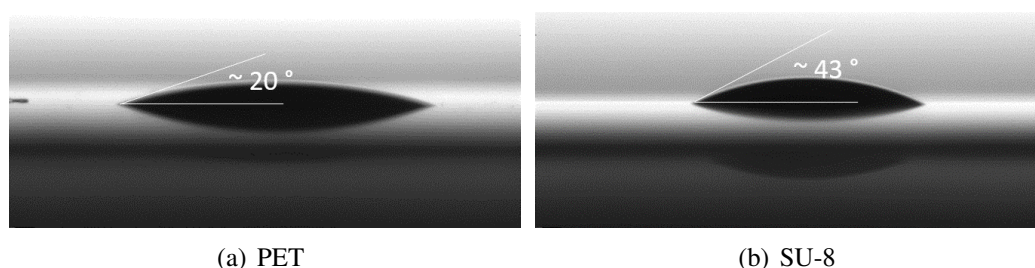


Figure 7.5.: Image of Ag ink droplets on a) PET and b) SU-8 surfaces showing contact angles of  $\sim 20^\circ$  and  $\sim 43^\circ$ , respectively.

The equilibrium CA of the Ag NP ink on PET ( $\sim 20^\circ$ ) and SU-8 ( $\sim 43^\circ$ ), shown in **Figure 7.5**, contains information about the fluid-solid interactions. The CA on a particular surface theoretically correlates with the surface tension of the fluid expressed by the *work of adhesion*  $W_A$  (Equation 4.3 on page 34). This again is based the Young-Dupré equation, which describes how much work needs to be expended to separate a the fluid from a particular solid surface. The surface tension  $\sigma_{l,Agink}$  of the nanoparticulate Ag ink was therefore determined, as described in section 4.1.1 on page 33, to  $35.5\ \text{mN m}^{-1}$  using the Young's equation (Eq. 4.1). Consequently,  $W_{A,SU-8}$  was calculated to  $60.6\ \text{mJ m}^{-2}$  and  $W_{A,PET}$  to be  $67.9\ \text{mJ m}^{-2}$  revealing a lower work necessary for the separation of the ink from the SU-8 than from the PET. The work of adhesion for a fluid on a specific surface is according to Packham *et al.* strongly influenced by the presence of solvent vapor, which affects the equilibrium states and spreading pressure. Furthermore, the interface between fluid and solid surface can be affected by chemical heterogeneities and geometrical

non-uniformities.[137] The latter basically concerns a discrepancy between theoretically assumed perfectly flat surfaces and *real* systems with nano- and micro-scopic inhomogeneities. AFM measurements from AJ printed SU-8 line surface uncovered (Appendix B.1) tiny ink residues remaining on the dewetted SU-8 surface. The roughness was found to have a minor impact on the dewetting process in this case, since roughness of both the SU-8 and the PET revealed merely nano-scopic values of  $\sim 0.2 - 0.4$  nm. However, the ink residues on the SU-8 line backs indicate the presence of local surface energetic inhomogeneities, which could evoke from an imperfect cross-linking of the SU-8.

### 7.2.2. Correlation between Ink Volume and Normalized Wetting Area

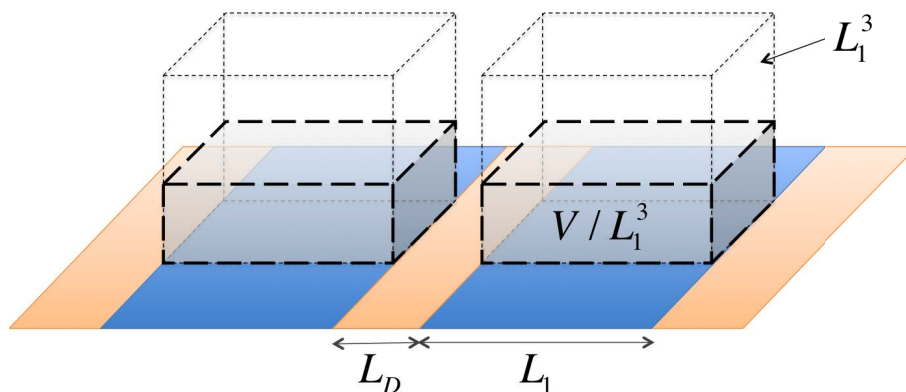


Figure 7.6.: Illustration of the reduced fluid volume on patterned substrates comprising lyophilic (blue) and lyophobic (orange) stripes of the width  $L_1$  and  $L_D$ , respectively, where the dashed cube represents the nominal volume  $L_1^3$ .  $V/L_1^3$  [136]

Brinkmann and Lipowsky delivered a theoretical study on the wetting and dewetting of chemically patterned surface domains back in 2002.[136] Their study on the influence of geometrical and volumetrical analysis of fluid management on low and high surface energetic stripes revealed systematically the crucial parameters for a successful dewetting. Namely, the gap between the two wetting stripes  $L_D$  (here the SU-8 line width), the CA of the wetting surface, the CA of the repelling surface, and the reduced fluid volume  $V/L_1^3$ , as illustrated in **Figure 7.6**. The latter correlates therefore to the maximum ink volume applicable without causing liquid bridging over the dewetting regions. These crucial parameters also determined whether liquid bridging emerges or not, which means that the ink bridges two parallel but separated high surface energetic regions of the width  $L_1$  across a low surface energetic region of the width  $L_D$ .

Albeit, these studies were carried out on flat, chemically modified surfaces, the findings can be transferred with a clear conscience to the here reported dewetting process. Thereby, the protruding structures could be regarded as a nominally increased gap between two wetting stripes, as it is illustrated by the *actual* area in **Figure 7.7(a)**. Figure

## 7. Digitally Printed Dewetting Patterns for Self-Organizing Microelectronics

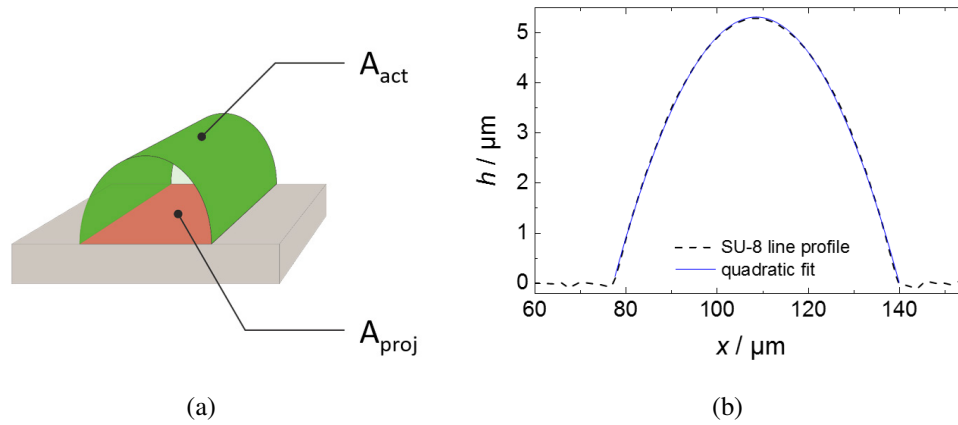


Figure 7.7.: a) Schematic illustration of the actual area,  $A_{act}$ , (green) of an SU-8 line and the projected area  $A_{proj}$  (red). b) Cross-section of an AJ printed SU-8 line (dashed) and a parabolic fit (blue).

7.7(b) shows a typical cross-sectional profile of a printed line, which almost ideally follows a parabolic function. However, the arc length from the line cross-section resulted in a marginal increase of 2.2% from  $\sim 60 \mu\text{m}$  for a perfectly flat dewetting area to  $61.32 \mu\text{m}$  for the protruding areas. Nevertheless, the line  $w$  and hence the aspect ratio can be tuned in a wide range by varying the printing parameters, as described already in section 3.1.2 on page 23. Thereby, SU-8 line heights of over  $15 \mu\text{m}$  were achieved via multi-pass AJ printing. Thus, considering a line with  $h = 5 \mu\text{m}$  and  $w = 20 \mu\text{m}$  would already lead to an increase in area of  $\sim 15\%$ . More important, however, appears the SU-8 line height, since the protrusions drastically decrease the wet film thickness of the Ag ink.

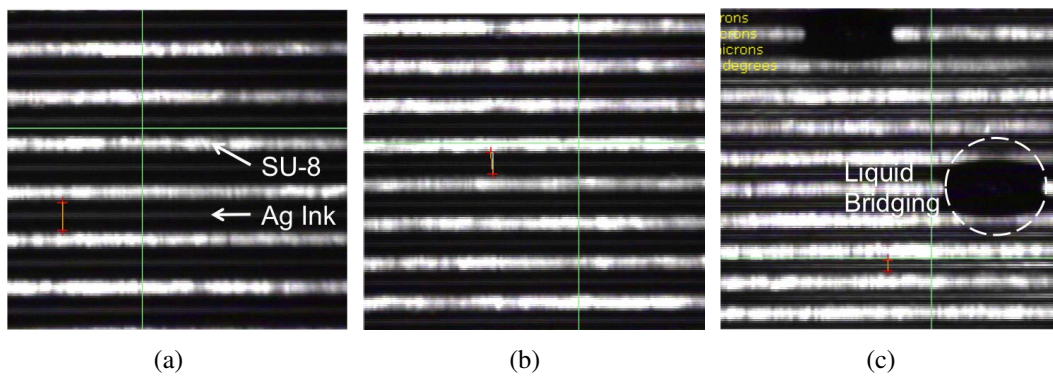


Figure 7.8.: Images of inkjet printed Ag ink (dark areas) with a drop spacing of  $50 \mu\text{m}$  on PET substrate, comprising a)  $65 \mu\text{m}$ , b)  $50 \mu\text{m}$ , and c)  $25 \mu\text{m}$  gaps between the SU-8 lines (bright areas).

To investigate the correlation of ink volume to the feature size of the dewetting SU-8 and the wetting PET regions the following experiment was conducted. SU-8 lines with line widths of  $L_D = 25 \mu\text{m}$  were AJ printed with different gap sizes of  $L_{1(a)} = 65 \mu\text{m}$ ,

$L_{1(b)} = 50 \mu\text{m}$ , and  $L_{1(c)} = 25 \mu\text{m}$  on a PET substrate. Hence, samples with different proportions of wetting to dewetting areas ( $L_D/L_1$ ) were created, accounting for values of 0.38, 0.5, and 1, respectively. Subsequently, the Ag ink was inkjet printed using a constant drop spacing of  $50 \mu\text{m}$ . Assuming a constant drop volume of  $10 \text{ pL}$  revealed a total nominal ink volume of  $4 \mu\text{L}/\text{mm}^2$  deposited on each pattern illustrated in **Figure 7.8**. Albeit, the ink volume per *wetting* region changed regarding the prevalent gap size  $L_D$ . As aforementioned, Brinkmann *et al.* (2002) related the reduced liquid volume ( $V/L_1^3$ ) to the ratio of wetting and non-wetting areas ( $L_D/L_1$ ).[136] Similar observations could be made from the experiment in Figure 7.8, where bulge-like bridging of the Ag ink from one *wetting* area to a neighboring *wetting* area was observed, as presented in c). That implied, that a critical ink volume was exceeded, leading to a certain instability. Hence, a bulge-like bridging was observed for a  $L_D/L_1 = 1$ ,  $V/L_1^3 = 160$ , and CAs of  $\theta_{SU-8} = 43^\circ$  and  $\theta_{PET} = 20^\circ$ .

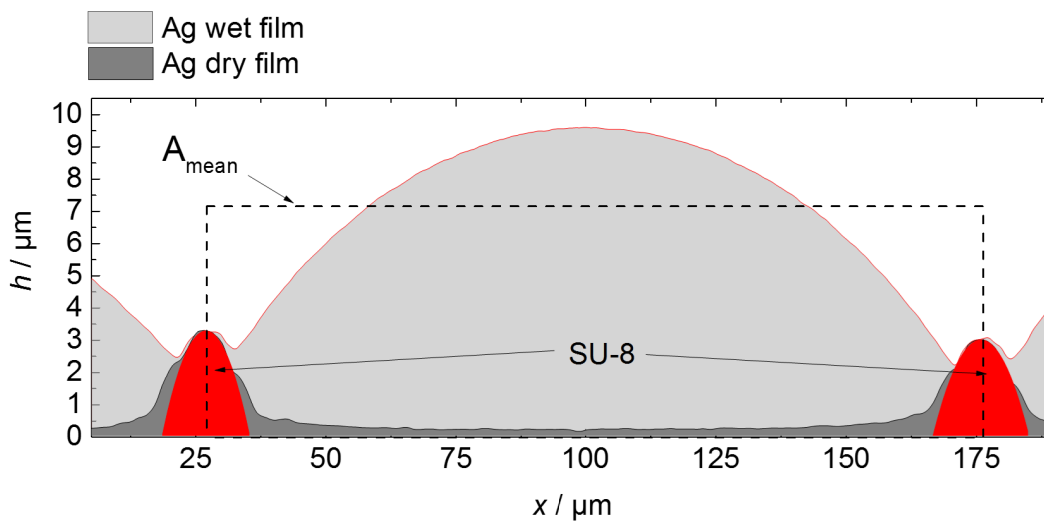


Figure 7.9.: Cross-sectional profile of inkjet printed Ag ink on top of an SU-8 patterned PET substrate. SU-8 lines are colored in red, the wet Ag film in light grey, and the dried Ag film in dark grey.

Wet films can easily achieve tens of micrometers, which basically depend on the desired layer thickness of the dried film and the solid loading of the ink. **Figure 7.9** shows cross-sectional profiles of an SU-8 patterned PET foil comprising an inkjet printed Ag layer before and after annealing. The red areas highlight the AJ printed SU-8 pattern that was composed of two parallel  $\sim 3.5 \mu\text{m}$  tall lines at a  $150 \mu\text{m}$  pitch. After inkjet printing the NP Ag ink, the substrate was directly transferred to the 3D profilometer (Neox PLu, Sensofar) 3 min to record the topography comprising the self-organized but still wet Ag pattern. Within this short carrying time, it was assumed that the ink volume remained constant and no significant evaporation took place. This assumption is justifiable since the main solvent of the Ag NP ink *triethylen glycol monomethyl ether* comprises a very low vapor pressure of  $< 0.0013 \text{ kPa}$  and a boiling point of around  $250^\circ \text{C}$ . The light grey area illustrates the wet Ag film, which clearly exhibits a dewetting on top of the SU-

8 structures and therefore forms a very pronounced meniscus. Assuming that the light grey area corresponds to an initial mean cross-sectional area  $A_{mean}$  between the two SU-8 lines, as indicated by the dashed line, the wet film thickness could be determined to  $\sim 7 \mu\text{m}$ . After annealing the sample on a hotplate, the same spot was measured again, which is indicated as the dark grey area. The nominal thickness of the annealed Ag film of  $\sim 250 \text{ nm}$  additionally perfectly supported the assumption for the aforementioned mean wet film thickness and equals to the calculated Ag film thickness ( $h_{dry}$ ).  $h_{dry}$  was calculated, considering a solid loading of  $c_{Ag} = 30 - 35 \text{ wt.}\%$ , a density of the main solvent of  $\rho_{solvent} = 1.09 \text{ g cm}^{-3}$ , as well as the density of Ag ( $\rho_{Ag} = 10.49 \text{ g cm}^{-3}$ ), as followed:

$$h_{dry} = h_{wet} \cdot c_{Ag} \cdot \frac{\rho_{solvent}}{\rho_{Ag}} \quad (7.1)$$

**Figure 7.10** presents application examples with various geometries for the dewetting structures. The surface profiles and corresponding line profiles of rectangular, ring and spiral patterns were recorded directly after inkjet printing of the Ag ink, after drying in a vacuum chamber and subsequently annealing at  $120^\circ \text{C}$  for 10 min. These complex patterns elucidate some possibilities with squared areas comprising well-defined gaps, or ring and spiral structures in the hundred micrometer range, e.g. enabling the fabrication of antennas in the high GHz or THz range. Immediately after printing of the Ag with a drop spacing of  $45 \mu\text{m}$  on a Dimatix DMP-2800 and a cartridge with a 10 pL drop volume a pronounced meniscus could be observed. To homogeneously dry the high wet films, a vacuum step at room temperature was introduced. This vacuum step suppressed unpredictable drying effects, which would significantly diminish the pattern quality. The dried films were then annealed at  $120^\circ \text{C}$  for 15 min. However, a decrease in Ag film thickness towards the SU-8 structures was observed. A concave Ag shape, however, was achieved by a fast annealing without vacuum drying on a hotplate, as shown in Fig. 7.9.

### 7.2.3. Interface Energetic Dependencies

To gain further insight into the principles of the dewetting and its applicability with other solvent systems, the dependencies on polar and non-polar surface tension and energy was investigated. Various solvents, which constitute classic representatives used in inks and formulations in the field of printed electronics, were examined considering the polar and dispersive surface tensions, the boiling point, the viscosity and the vapor pressure, as can be seen in Table 7.1.

In a first place, a basic experiment was performed, where a  $2 \mu\text{L}$  solvent droplet was deposited on a PET/SU-8 step edge. Therefore, a clean PET substrate was partly blade coated with SU-8 forming a rim, as illustrated in **Figure 7.11(a)**. Although, the solvent's vapor pressure and thus the evaporation speed play an undeniable role, the experiment elucidates the potential application of a variety of inks with this dewetting process, since these fluid properties will always be present.

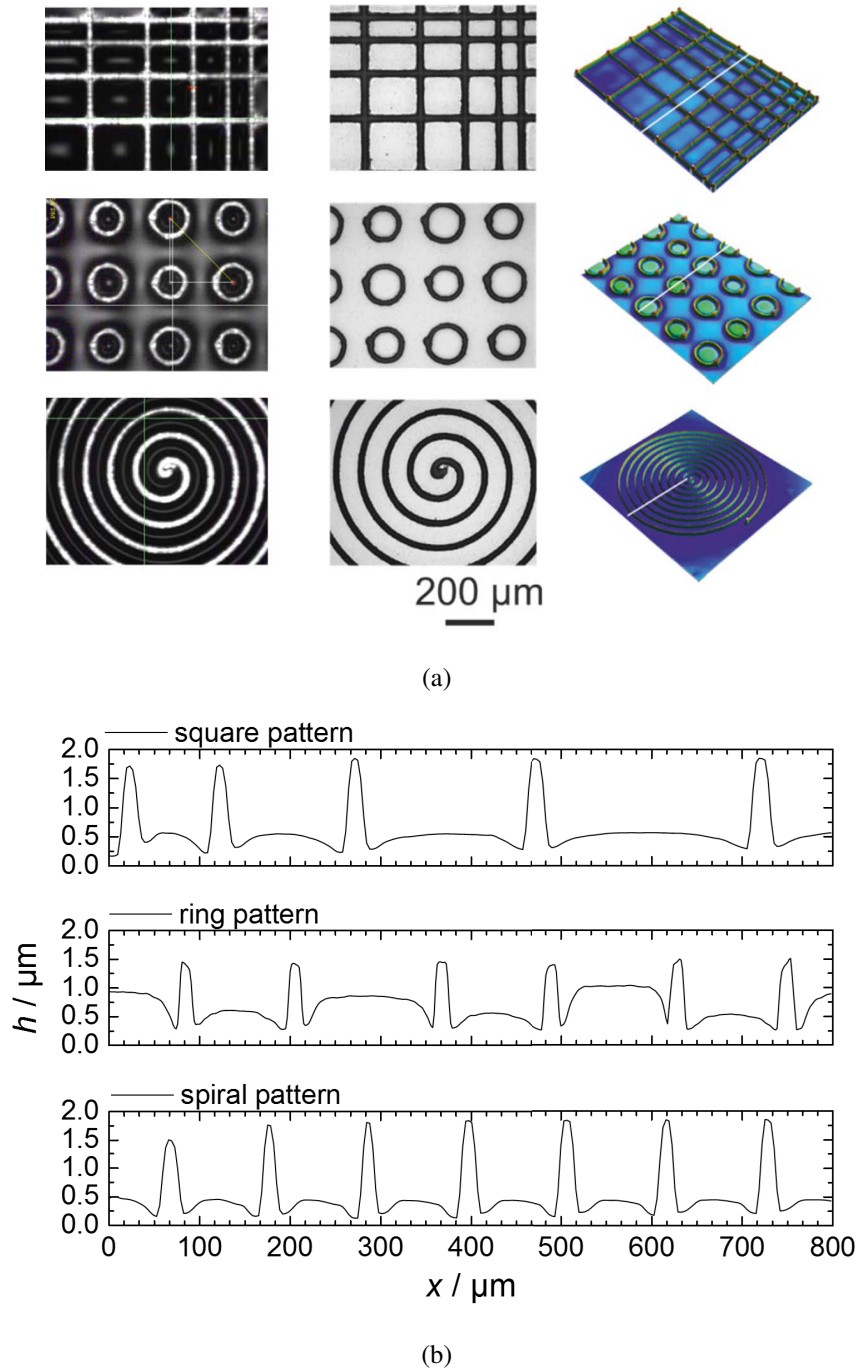


Figure 7.10.: Examples of dewetting Ag structures showing square, ring and spiral patterns with a) image directly recorded after Ag deposition via inkjet, microscope image recorded after annealing the Ag ink, and 3D topographies. b) Extracted line profiles of the corresponding patterns.

The repelling effect of the Ag ink from the SU-8 surface towards the PET surface is demonstrated in a image sequence over time in Figure 7.11(b). The step edge is visualized by the black line. Already after 2 s the Ag ink droplet was fully vanished from the

## 7. Digitally Printed Dewetting Patterns for Self-Organizing Microelectronics

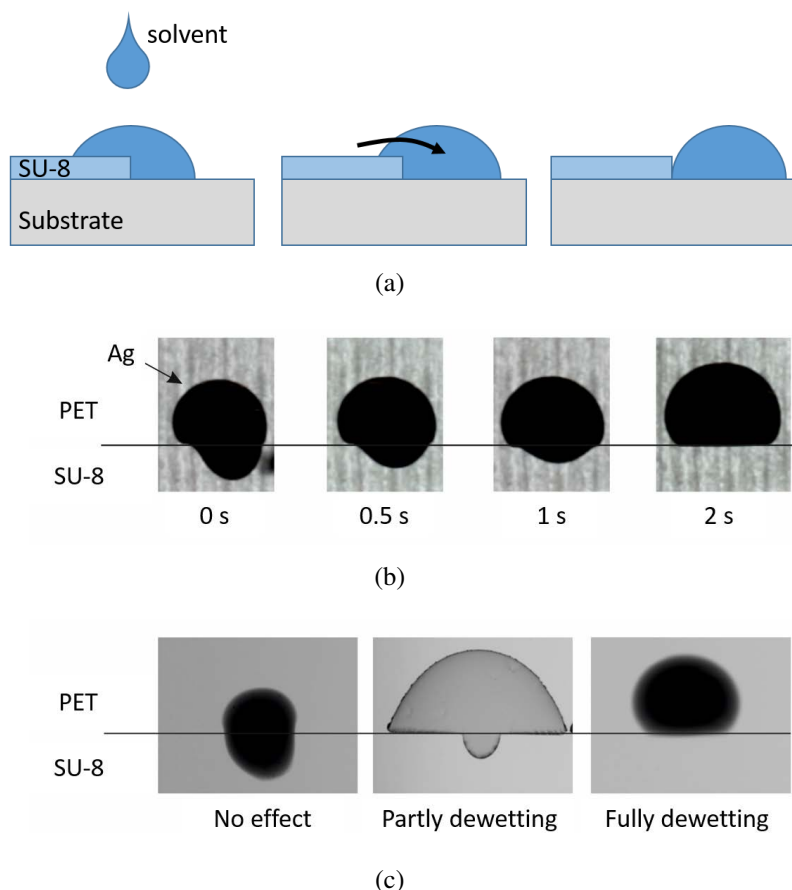


Figure 7.11.: a) schematic drawing of the experimental assembly. The solvent droplet of  $2 \mu\text{L}$  is deposited on the SU-8/PET step edge. In case of dewetting, the droplet moves towards the PET. b) Image sequence over time of the experiment using Ag ink. c) Examples of a solvent showing no effect (left), partly dewetting (center), and fully dewetting (right).

SU-8 side and formed a straight front at the interface of the of the PET and SU-8. Nonetheless, as illustrated in Figure 7.11(c), three possible results could be obtained, which were: *No effect*, where the droplet remained in its initial position; *Partly dewetting*, where a dewetting behavior was clearly observable, but due to fast solvent evaporation residues (here black dye) remained on the SU-8 surface; and *Fully dewetting*, where after a certain time the solvent droplet fully repelled from the SU-8.

Water ( $H_2O$ ) compared to alcohols and organic solvents exhibits a very high polar surface tension, which often causes wetting issues on substrates. However, it is miscible with alcohols whereby the polar and dispersive surface tensions can be tuned in a broad range, as shown in **Figure 7.12(a)** for different volume fractions  $\chi_{MeOH}$  of  $MeOH$  in  $H_2O$ . These mixtures, as well as the solvents listed in Table 7.1, were tested by means of its dewetting properties on a PET/SU-8 step edge. The graph in Figure 7.12(b) shows the wetting envelopes of a cleaned PET surface and SU-8 and the polar ( $\sigma^P$ ) and dispersive ( $\sigma^D$ ) surface tensions, where circles indicate a proper repelling effect and triangles

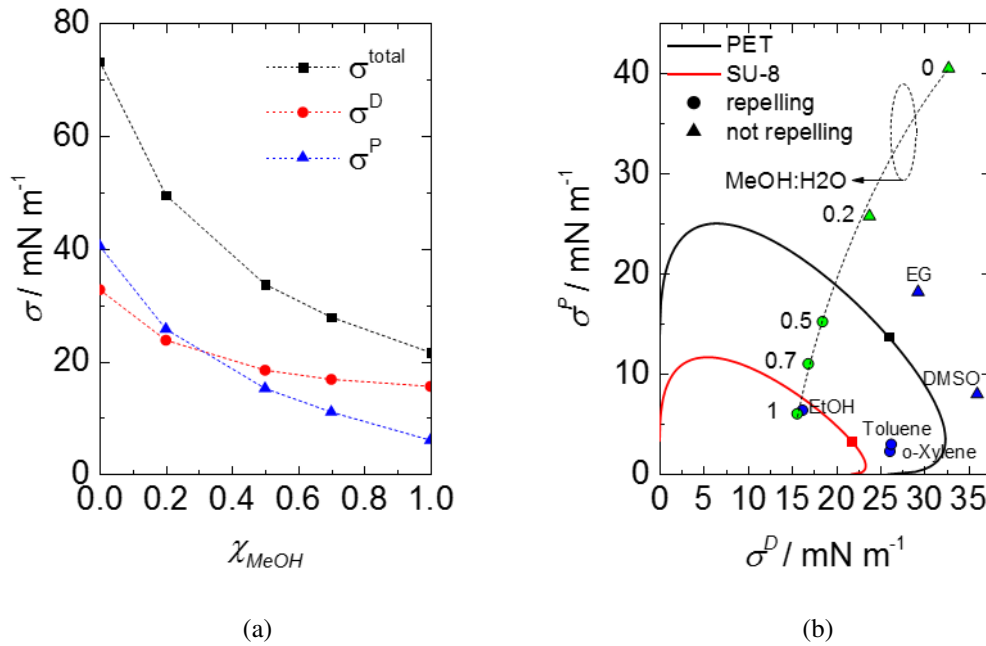


Figure 7.12.: a) Total, polar, and dispersive surface tensions of water:methanol mixtures blended in various ratios  $\chi_{\text{MeOH}}$ . b) Wetting envelopes of PET and SU-8 surfaces and complex surface tensions of solvents and  $\text{H}_2\text{O}:\text{MeOH}$  blends. Circles represent a proper dewetting, while triangles represent no or insufficient dewetting from the SU-8.

indicating no or insufficient dewetting. Breaking down the theory of wetting envelopes would lead to the simple statement that fluids with surface tension values inside the envelope tend to fully wet the surface, while solvents with values outside lean towards an increase in CA or even to a dewetting. Although, wetting envelopes have to be regarded somewhat skeptically due to their theoretical assumptions of a CA of  $0^\circ$ , it visualized at least a tendency for solvents to wet or dewet on a given surface. Interesting to see that the all solvents and mixtures located within the wetting envelope of the PET succeeded the dewetting effect. In contrast, all solvents outside the wetting envelope of PET were unperturbed by the different surface energies and remained on both surfaces. This could originate from multiple reasons, e.g. that both materials provide a more or less unfavorable surface energy, or a high viscosity, which counteracts with the repelling forces from the SU-8. Furthermore, solvents with values close to the wetting envelope of SU-8, are still stronger attracted by the PET.

**Figure 7.13(a)**, in comparison to the graph in Fig. 7.12(b), includes the wetting envelope of an  $\text{O}_2$  pre-treated PET substrate and the corresponding wetting behaviors of the same solvents and mixtures. The initial wetting envelope of PET (dashed line) was maintained in the graph to highlight the influence of the plasma treatment on the substrate's surface energy. Against expectations, all tested fluids, even pure  $\text{H}_2\text{O}$ , EG, and DMSO, repelled from the SU-8. These observations, likewise the considerations above, further confirmed

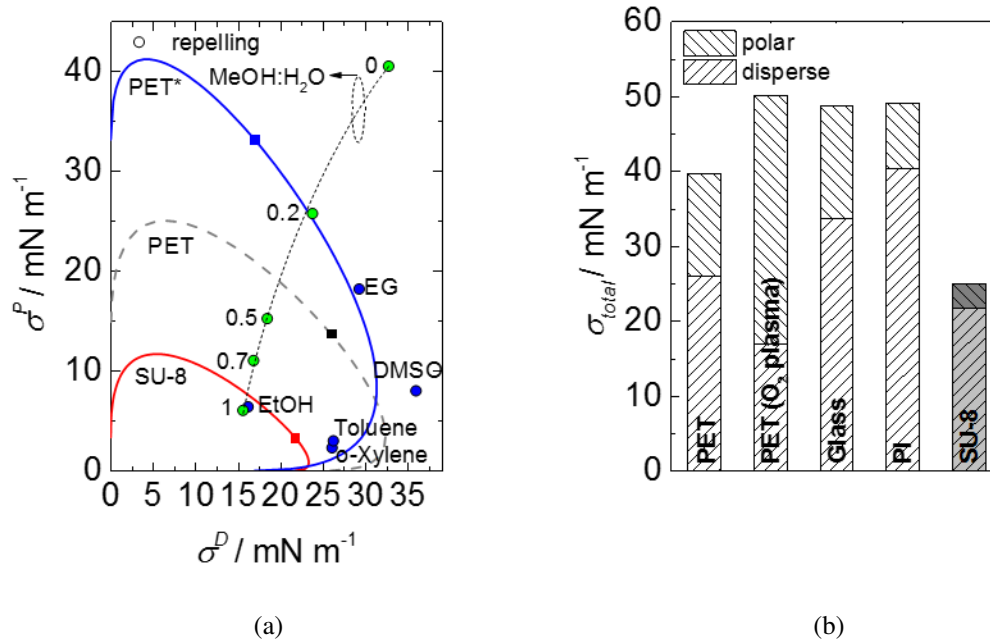


Figure 7.13.: a) Wetting envelopes of PET,  $O_2$  plasma treated, and SU-8 surfaces and complex surface tensions of solvents and  $H_2O:MeOH$  blends. Circles represent a proper dewetting, while triangles represent no or insufficient dewetting from the SU-8. b) Total surface energies split in polar and dispersive parts for PET,  $O_2$  plasma treated PET, glass, polyimide (PI), and SU-8.

the theory already stated by Wang *et al.* that a low CA on the wetting surface constitutes a key parameter for the dewetting.[133]

Furthermore, beside the variation of solvents and the plasma-treatment of the PET, other substrates were tested. Test structures were fabricated on also on glass and polyimide (PI), where photographs can be found in the Appendix B.2. The surface energies of these substrates are shown in Figure 7.13(b), where glass and PI tendentially have higher surface energies compared to PET.

### Versatility of Ag Deposition

At the beginning of this chapter the dewetting process was illustrated by brushing the ink over the SU-8 patterned substrate. In the subsequent progression the ink was then deposited using inkjet printing, to fully control the amount of ink deposited per area, which was defined by the drop volume and the drop spacing. According to the positive results using those deposition techniques, other complementary widespread methods, such as spray coating with an airbrush or blade-coating.

**Figure 7.14(a)** shows the deposition of Ag ink on SU-8 patterned PET using blade coating. The patterns consisted of *Split Ring Resonators*, which were investigated in cooperation with Jerzy Kowalewski from the Institute of Radio Frequency Engineering and Electronics (IHE, KIT). The film thickness of blade coated layers is mainly determined by

Table 7.1.: Summary of surface tensions ( $\sigma$ ) including polar ( $\sigma^P$ ) and dispersive part ( $\sigma^D$ ), vapor pressure ( $p$ ), boiling point ( $T_{bp}$ ), and viscosity ( $\eta$ ) for different solvents and the Ag NP ink. Additionally, surface energies for PET, plasma treated PET, and SU-8 (2025 Series).

	$\sigma [mNm^{-1}]$			$p [kPa]$ (@20 ° C)	$T_{bp} [° C]$	$\eta [cP]$ (@20 ° C)	dewetting* [yes/no]
	$\sigma^T$	$\sigma^P$	$\sigma^D$				
<b>Solvent</b>							
Water (H2O)	72.6	50.8	21.8	2.4	100.0	0.98	no
Ethylene Glycol (EG)	47.5	18.2	29.3	0.5	198.0	26	no
Methanol (MeOH)	24.0	5.1	18.9	13.0	64.7	0.55	yes
Ethanol (EtOH)	24.6	6.4	16.2	5.95	78.0	1.2	yes
Dimethylsulfoxide (DMSO)	44.0	8.0	36.0	0.55	189.0	2.14	no
Toluene	28.4	2.3	26.1	5.4	110.0	0.59	yes
o-Xylene	29.3	3.0	26.3	0.7	144.5	0.76	yes
<b>Ink</b>							
Ag ink <sup>a)</sup>	35.5	6.8	28.7	0.0013	249.5	10-18	yes
<b>Substrates</b>							
SU-8	27.4	3.1	24.3	-	-	-	-
PET <sup>b)</sup>	45.1	12.2	32.9	-	-	-	-
O2 plasma treated PET	50.2	33.2	17.0	-	-	-	-

<sup>a)</sup> Silverjet DGP-40LT-15C, <sup>b)</sup> Hostaphan GN-4600, \*on cleaned PET/SU-8

the coating speed and the gap between the substrate and the knife. Nevertheless, the focus of this experiment was not set to find optimal deposition parameters, for what reason the gap was fixed to  $50 \mu\text{m}$  and the coating speed to  $10 \text{ mm s}^{-1}$ . Against the anticipations, a very homogeneous surface was observed after the Ag film was deposited, showing no surface disruptions from the SU-8 patterns. Not until after 1 min the SU-8 patterns got visible, as shown in Figure 7.14(b). The inertia of this dewetting process was not further investigated, but could be either explained by an approaching spreading of the ink on the substrate, which resulted in a reduction of the wet film thickness and thus came below a critical wet film thickness, or from the absence of the previously mentioned seed spots.

The widespread deposition of the Ag ink was additionally realized using an airbrush pistol, which is shown in the image in **Figure 7.15(a)**. This rudimentary version of professional spray coating processes was used to confirm its aptitude for this patterning process. Unlike in the blade coating experiment, the spray coated Ag film immediately dewetted on the SU-8 patterns. The image taken directly after the deposition of the Ag ink (Fig. 7.15(b)) shows already completely dewetted SU-8 patterns.

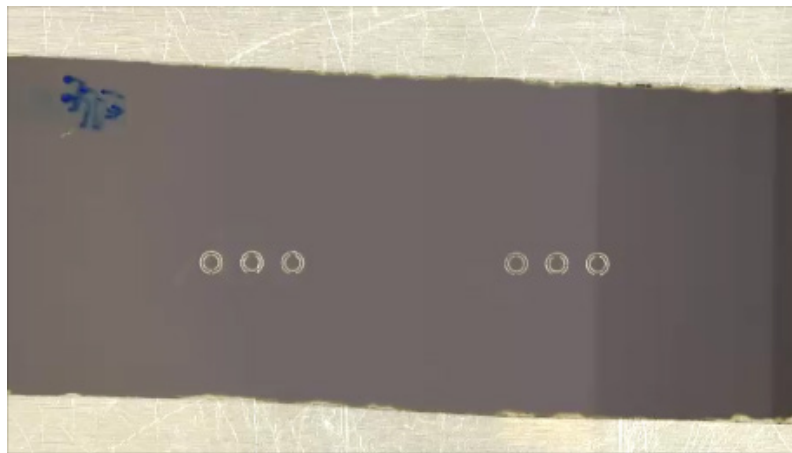
## Summary

The fabrication of self-organizing metal structures in the micrometer scale was successfully demonstrated, where dewetting features of  $\sim 10 \mu\text{m}$  could be realized. The protrusion of the SU-8 lines reduced the resulting local wet film thickness, which appeared to

## 7. Digitally Printed Dewetting Patterns for Self-Organizing Microelectronics



(a)

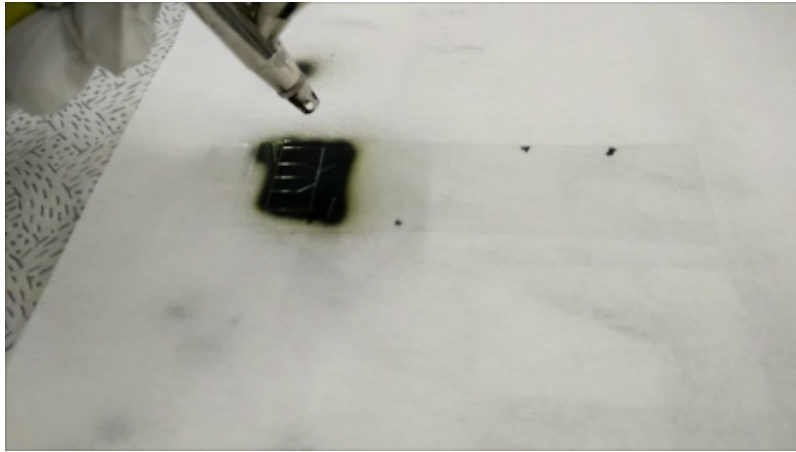


(b)

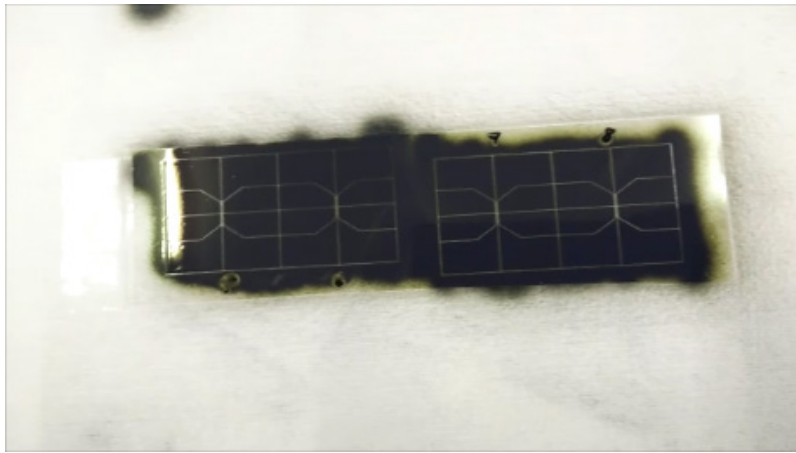
Figure 7.14.: Blade coating of Ag ink on top of SU-8 patterned PET foil using an *Erichsen Coatmaster 510*. a) Image recorded during coating process. b) Image recorded after SU-8 structures were dewetted ( $\sim 1$  min).

be advantageous for the effect. Additionally, the wetting morphology and thus the correlation between fluid volume and the features sizes of wetting and dewetting regions was investigated. Instabilities in form of liquid bridging were observed for excess Ag ink. The correlation between the observed dewetting effect and the surface tensions for different solvents was examined by a simple step edge experiment. A low contact angle on the wetting regions was found to be very important, which could be demonstrated by an  $O_2$  plasma treatment of the PET prior to the SU-8 and Ag printing. Nevertheless, no clear evidence for a major impact of polar or dispersive surface energies or tensions could be determined.

The deposition of the subsequent Ag layer was beside the brushing and ink jet printing also successfully demonstrated by blade coating and widespread spray coating.



(a)



(b)

Figure 7.15.: Spray coating of Ag ink using an airbrush on top of an SU-8 patterned PET foil. a) Image recorded during spray coating process. b) Image recorded directly after finishing the coating process.

### 7.3. Application Examples

The key benefits of contact-free digital printing, the simple two-step additive manufacturing, and the feasibility of fabrication on a large variety of substrates, as well as the potential use of a wide range of solvents, have been elucidated so far. The following paragraphs will first address the fabrication of fully printed micrometer scaled photodiodes, which embody the requirements needed for microelectronic applications, especially in terms of precise layer depositions and registration accuracy. Beyond that, the fabrication of self-organized source-drain transistor electrodes will be demonstrated, which in addition to it were integrated into electronic circuits in form of ring oscillators.

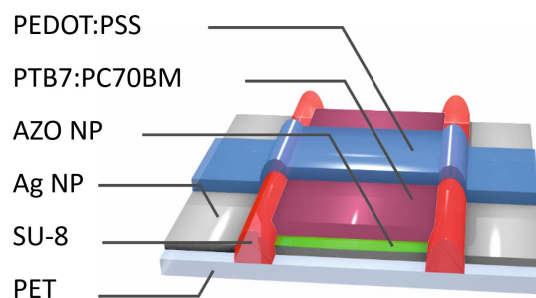


Figure 7.16.: Schematic drawing of a photodetector pixel comprising an Ag back-electrode fabricated by the introduced dewetting technique. The Ag electrode was inkjet printed, while all subsequently printed layers were AJ printed.

### 7.3.1. Fully Printed Organic Photodetectors

The patterned Ag electrodes exhibit a still considerable protrusion of the SU-8 lines, which varies depending on the AJ printing parameters from sub-micrometer to several micrometers. These protruding structures can be very useful for the alignment of subsequently printed layers, as illustrated in the schematic of an OPD in **Figure 7.16**, where the volume between two physical SU-8 barriers was exploited as a reservoir for the subsequently printed materials. Moreover, this reservoir ensures an excellent registration accuracy for any subsequently printed functional material. An related approach for fluid management and guidance for printed microelectronics was published recently by Mahajan *et al.*[138] However, they utilized lithographically fabricated micro-channels that were filled by capillary forces. The approach here instead aims for an utterly digital fabrication of the devices, where also the capillarity plays a minor role.

The SU-8 pattern was designed to reveal separated Ag stripes comprising a width of  $\sim 175 \mu\text{m}$ , as presented in **Figure 7.17(a)**. After the deposition of the AZO electron extraction layer, the PTB7:PC70BM ( $10 \text{ g L}^{-1}$ , DCB + 3 vol.% DIO) was then printed inside the reservoirs confined by the SU-8 boundaries, as can be depicted in Figure 7.17(b). The reservoir was therefore excessively filled with the active material revealing a layer thickness of  $\sim 1 \mu\text{m}$ , reducing the dark currents and avoid the formation of possible pin holes or short cuts.[139] The active layer was then dried in an antechamber under vacuum (15 mbar) for 15 min. The transverse PEDOT:PSS anode (IJ 1005, Orgacon) was AJ printed from a diluted formulation in a ratio of 1:1 with  $H_2O$  and 1 vol.% of Zonyl (FS-300). The overlap of the Ag back-contact and the PEDOT:PSS top-contact yielded a pixel size of  $175 \times 45 \mu\text{m}^2$  resulting in an active area of solely  $7.9 \cdot 10^{-3} \text{ mm}^2$ . To mention in particular, the confinement during the filling of PTB7:PC70BM into the reservoir was mainly of physical nature. Also the PEDOT:PSS from aqueous dispersion was not significantly affected by the underlying surface energies of the SU-8 and the PTB7:PC70BM, since both exhibit relatively equally hydrophobic surfaces. The wetting of PEDOT:PSS was however guaranteed by the addition of 1 vol.% of the fluorosurfactant *Zonyl*. Finally, a closed PEDOT:PSS stripe with a width of  $\sim 45 \mu\text{m}$  and an average height of  $\sim 400 \text{ nm}$

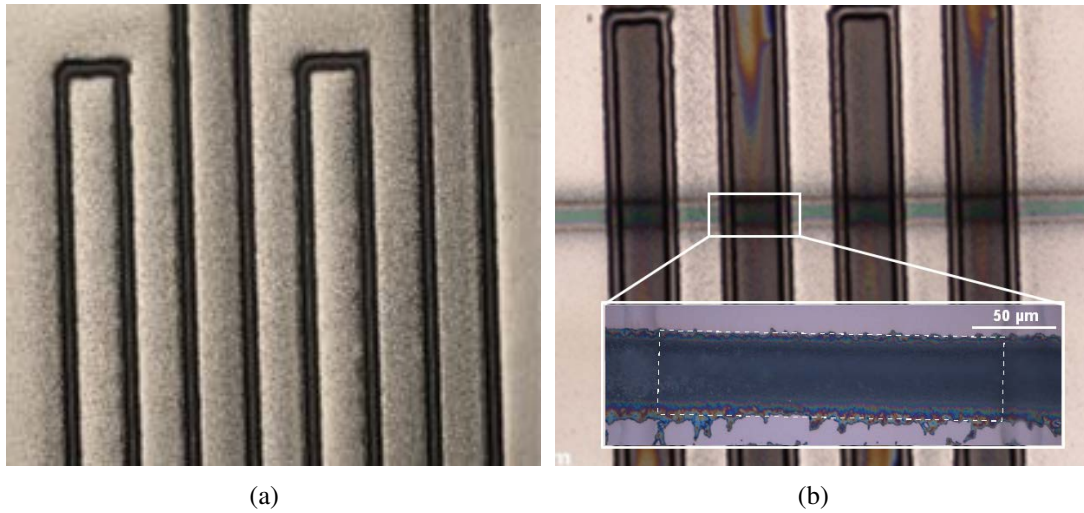


Figure 7.17.: a) Self-organized Ag electrodes on SU-8 patterned PET foil. b) Completed organic photodiodes with PTB7:PC70BM active material and a transverse highly conductive PEDOT:PSS anode stripe. The magnification shows one single pixel with a size of  $175 \times 45 \mu\text{m}^2$ .

was achieved, as illustrated in the 3D false color image in **Figure 7.18**. The samples were afterwards again dried in an antechamber under vacuum (15 mbar) for 15 min before transferring them into the nitrogen filled glove box to apply the encapsulation foil (3M).

Dark current densities were measured with an Agilent 4155C semiconductor network analyser in a electrically and optically shielded probe station. The OPDs revealed very low dark current densities of  $\sim 2 \cdot 10^{-7} \text{ A cm}^2$  at  $-3 \text{ V}$  reverse bias, as presented in **Figure 7.19(a)**, which could be referred to the active layer thickness of  $\sim 1 \mu\text{m}$ . Thus, an on-off ratio between dark and  $1000 \text{ W cm}^{-2}$  of  $\sim 10^5$  could be achieved. Furthermore, photocurrents were recorded under different optical intensities. These were varied by inserting neutral density filters (Thorlabs) into the optical path. The linearity of the OPD's response as a function of light intensity is shown in Figure 7.19(b) for  $-1 \text{ V}$  and  $-2 \text{ V}$  reverse bias.

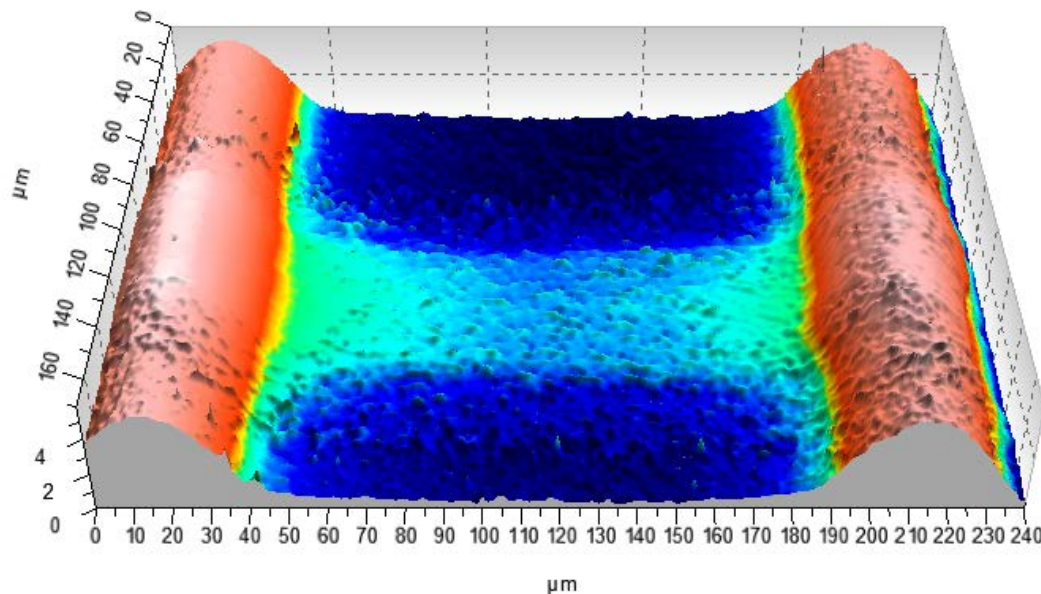


Figure 7.18.: 3D topography image of an OPD pixel recorded with a confocal microscope (Neox PLu, Sensofar, 50x, Ap. 0.95).

### 7.3.2. Fully Printed 256 Pixel Photodetector-Array

Printed organic electronics is predicted a very demanded market in the next years having a high potential for novel conformable or flexible applications, for instance for medical and health care, wearables, or gesture recognition systems.<sup>1</sup> Entirely printed high performing photodiodes have been demonstrated in the past.[22, 23]. Nevertheless, the change from a single device level to more complex and reproducible systems still bear a big challenge in terms of layer homogeneity and registration accuracy. Especially, since the requirements for specific application, such as finger print sensors, image scanners, or x ray detectors, require a high resolution with pixel sizes down to  $50\ \mu\text{m}$ .

In this section, I will present fully digitally printed OPD arrays composed of 256 single pixel, as shown in **Figure 7.20**. Furthermore, single pixels were opto-electronically characterized by  $J - V$ ,  $SR$ ,  $EQE$ , as well as  $BW$  measurements. To gain further insight into the reproducibility of the single pixel performance within a matrix of 256 individual devices, we evaluated the photo response of each pixel sequentially using a home-built read-out system. Additionally, the optical cross-talk was investigated by high resolution LBIC measurements under different Laser beam intensities.

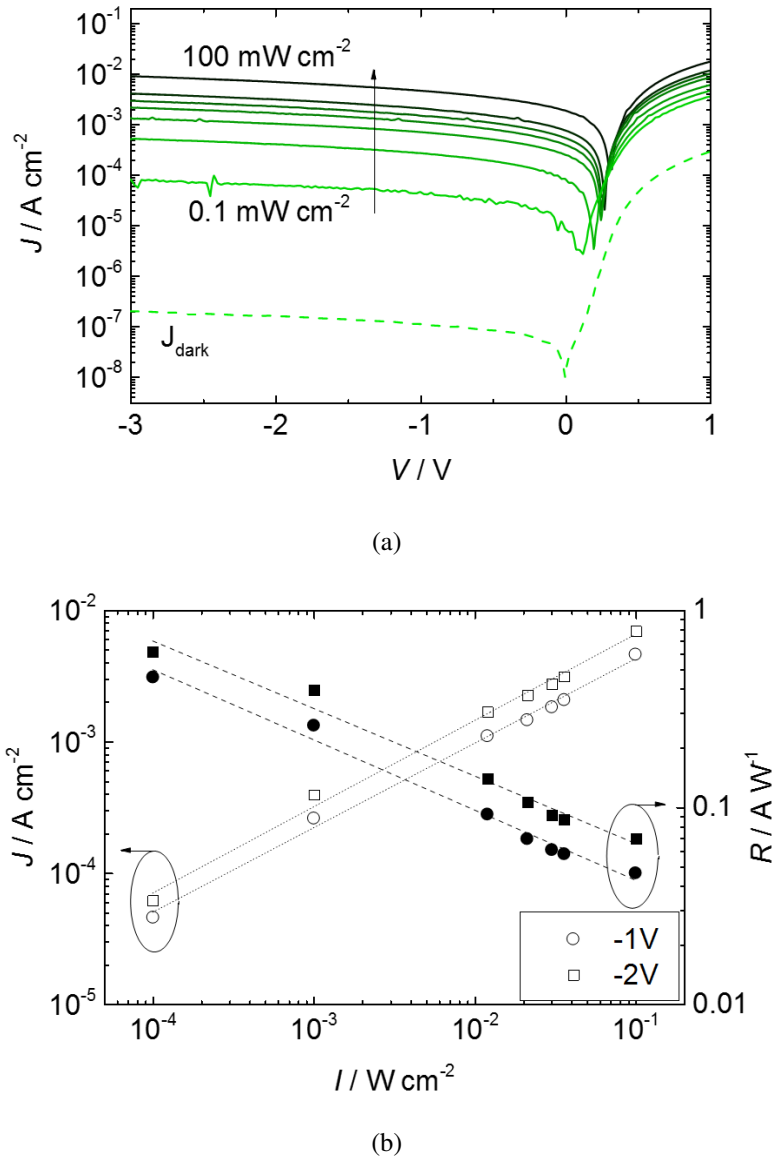


Figure 7.19.: a)  $J$ - $V$  Characteristics of a PTB7:PC70BM OPD pixel under different illumination intensities ranging from  $0.1 \text{ mW cm}^{-2}$  to  $100 \text{ mW cm}^{-2}$ . b) Current density over optical intensity and responsivity  $R$  at  $-1 \text{ V}$  and  $-2 \text{ V}$  bias.

## Device Fabrication

The Ag micro-electrodes were fabricated on glass slides (borofloat33, Schott), which were cleaned with acetone and IPA and  $\text{O}_2$  plasma treated for 5 min prior to the SU-8 printing. The lyophobic SU-8 patterns were printed as described before on page 87. **Figure 7.3.2** presents the height profile of SU-8 and Ag structures measured at the indicated region from the photograph in the left upper corner, revealing a very uniform Ag layer thickness of 250 nm and a protrusion of the SU-8 of  $3 \mu\text{m}$ . The protruding SU-8 ideally serves as

<sup>1</sup>IDTechEx Research Market Forecast

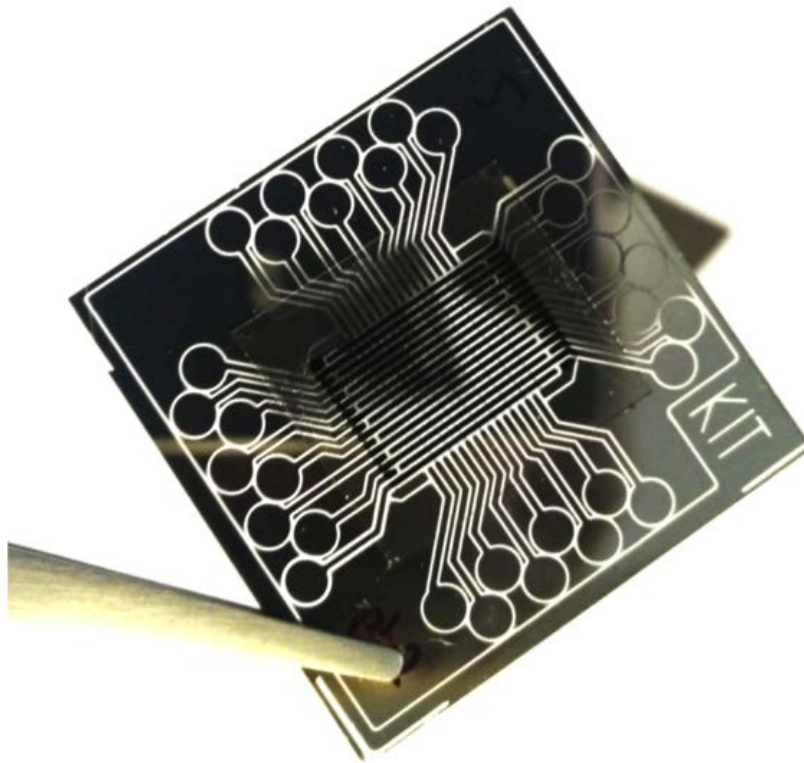


Figure 7.20.: Photograph of a fully printed OPD array with 256 pixel.

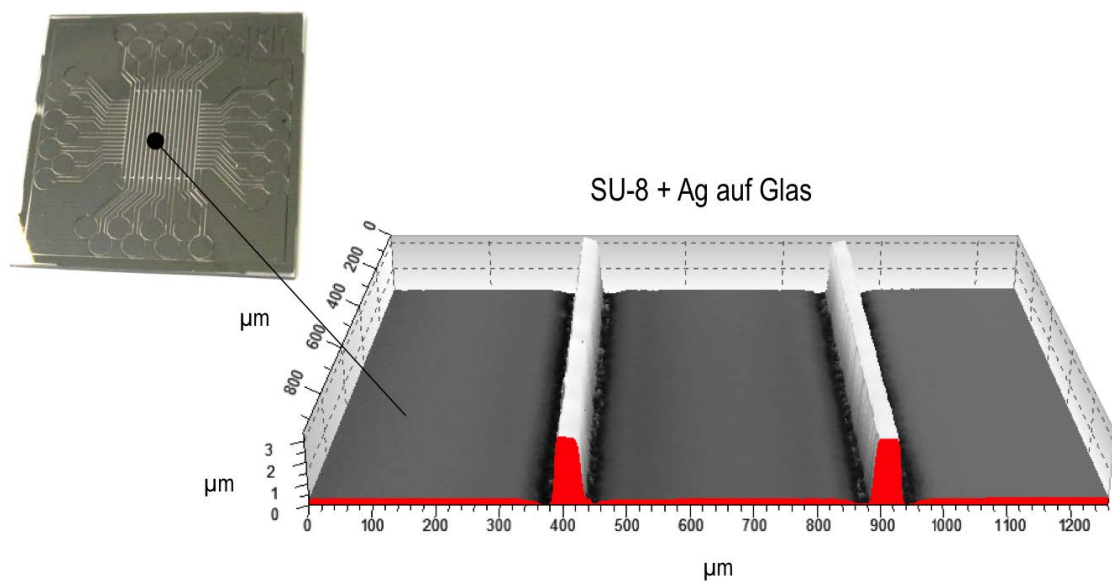


Figure 7.21.: Photograph of patterned Ag back-electrodes on glass (left) and height profile measured with confocal microscopy, Sensofar Neox (right).

wells for the subsequently printed layers.

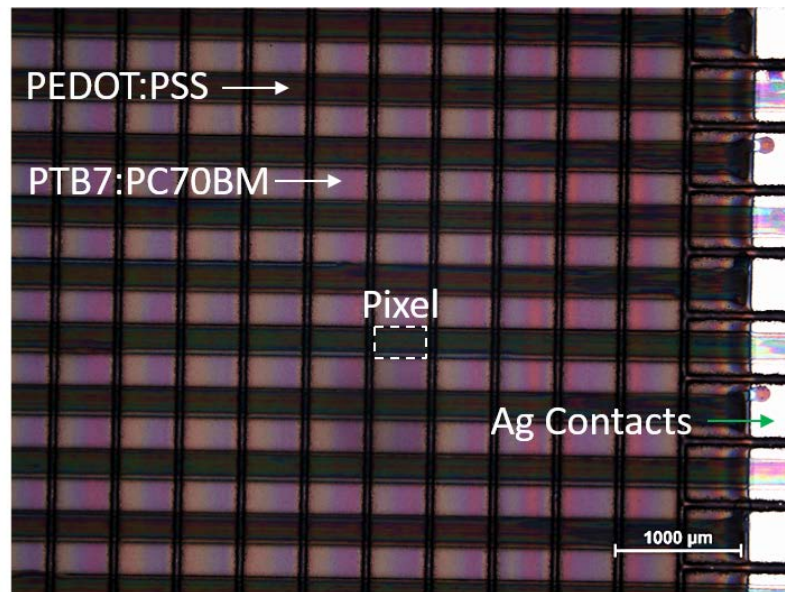


Figure 7.22.: Micrograph of a an Ag/ZnO/PTB7:PC70BM/PEDOT:PSS OPD array.

After the vacuum drying and annealing of the Ag patterns, a 50 nm ZnO layer was AJ printed from a NP dispersion (N11, Nanograde) and serves as an electron transport layer. Subsequently, a PTB7:PC70BM blend ( $10 \text{ g L}^{-1}$ , DCB, ratio 1:1.5) containing 3 vol.% of DIO was used as the absorber material and was printed in two passes to reveal a layer thickness of 250 nm. A 250 nm PEDOT:PSS (F HC Solar, Heraeus) top electrode was printed orthogonally to the Ag stripes to define the pixel size. The finalized OPD arrays, as shown in the micrograph in **Figure 7.22**, were then stored over night in vacuum and encapsulated the next day with 3M barrier foil.

### Device Characterization

The  $J - V$  measurements, as shown in **Figure 7.23(a)**, were performed for single pixels using a solar simulator. Therefore, the array was masked to ensure an illumination of only one pixel to avoid influence of optical and electrical cross-talk. The light intensity was varied by placing neutral density filters into the light beam and revealed an on-off ratio of  $10^5$ . The scattered light was mainly blocked by an optical shielding from the sides and the bottom. The current density ( $J$ ) over light intensity ( $I$ ) plot in Fig. 7.23(b) illustrates the linearity of the measured device in the range of six orders of magnitudes. This corresponds to a linear dynamic range ( $LDR$ ) of more than 100 db at 0 V and 90 dB at a reverse bias of  $-1 \text{ V}$ , which was calculated according to Equation 2.17 on page 18.

Furthermore, the spectral responsivity ( $SR$ ) and external quantum efficiency ( $EQE$ ) at bias voltages from 0 V to  $-1 \text{ V}$  were recorded for the masked pixel, as shown in **Figure 7.24**. The  $SR$  and  $EQE$  revealed a strong dependency on the applied bias. Thus, the  $SR$  increased from  $0.15 \text{ A/W}$  up to  $0.3 \text{ A/W}$  at a peak wavelength of 710 nm. Analogously, the  $EQE$  increased from 32 % to  $> 65 \%$  at  $-1 \text{ V}$ , which shows a very good performance

## 7. Digitally Printed Dewetting Patterns for Self-Organizing Microelectronics

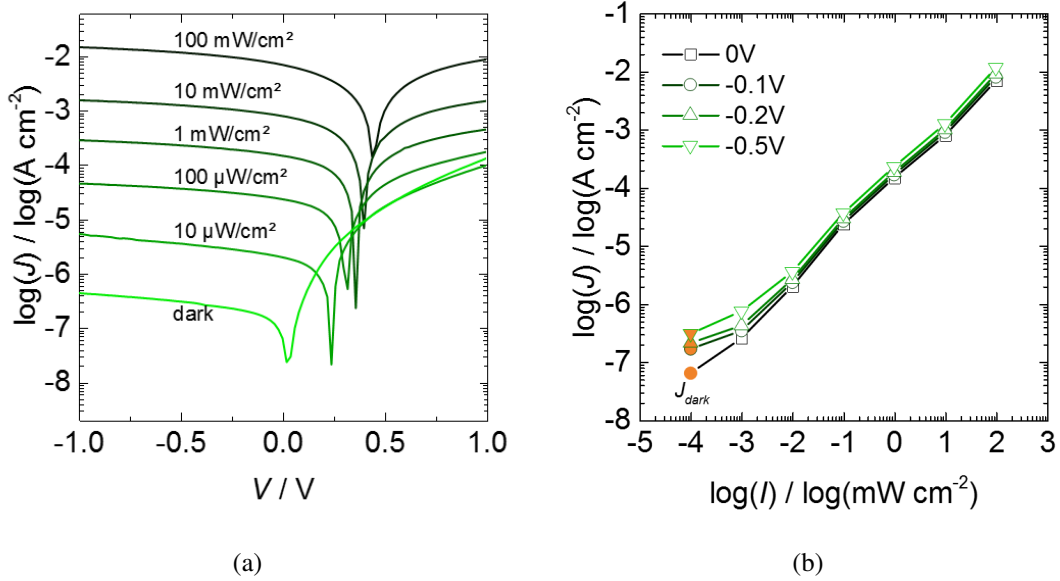


Figure 7.23.: a)  $J - V$  characteristics measured at a single pixel under different illumination intensities and in dark. b) log-log plot current density as a function of the light intensity  $I$ .

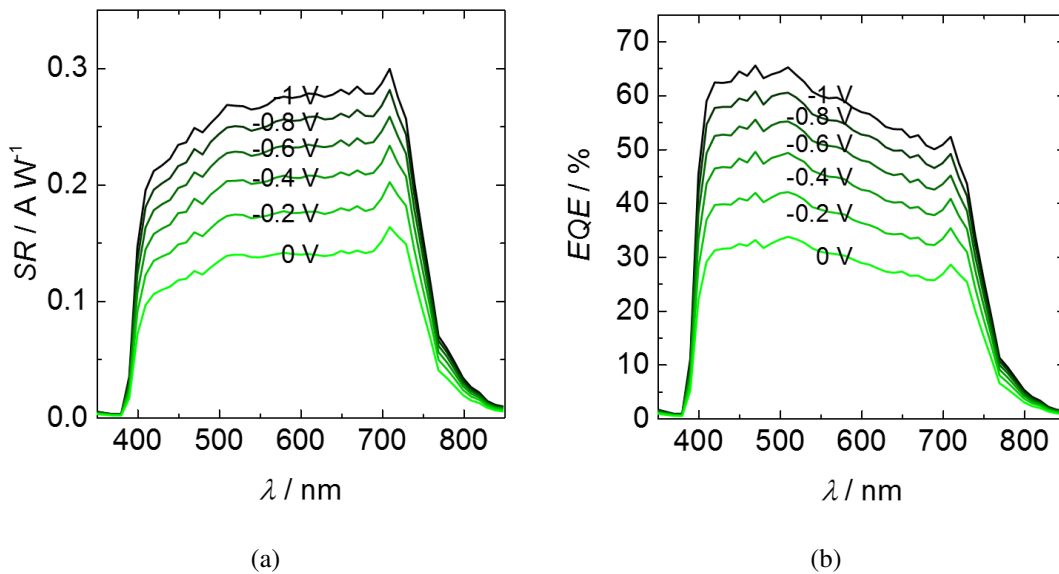


Figure 7.24.: a) Spectral responsivity ( $SR$ ) and b) external quantum efficiency ( $EQE$ ) of a masked OPD pixel.

mainly limited by the series resistance coming from the PEDOT:PSS stripe.

Additionally, the specific detectivity ( $D^*$ ) was calculated, as shown in **Figure 7.25(a)** and revealed  $8 \cdot 10^{11}$  Jones at  $\lambda = 710$  nm. These results are comparable to the results

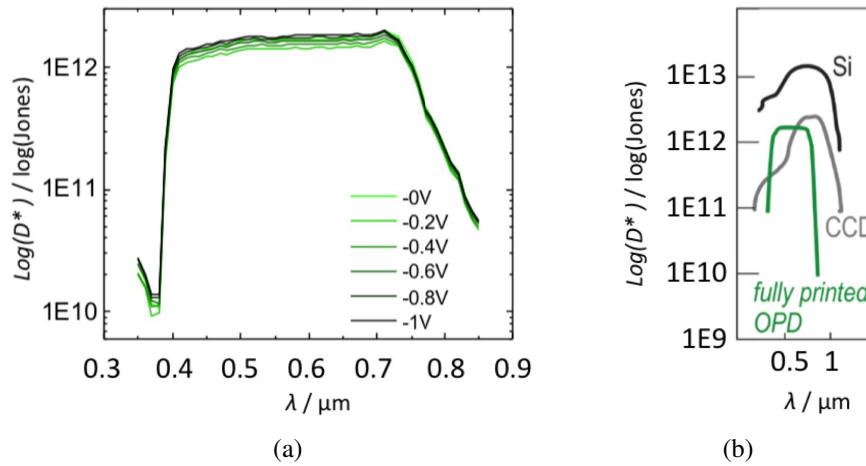


Figure 7.25.: a) Specific detectivity  $D^*$  calculated from the  $SR$  and  $J_d$  of the OPD pixel. b) Comparison of  $D^*$  with inorganic silicon based photodetectors.

from chapter 6 for fully printed single devices, where the slightly increased  $D^*$  could be ascribed to the opaque back-electrode. Furthermore, the achieved  $D^*$  can be nicely compared to conventional inorganic silicon based photodetectors, as shown in Fig. 7.25(b).

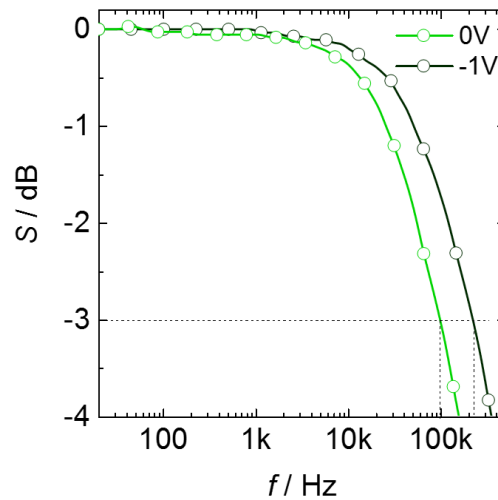


Figure 7.26.: Signal response ( $S$ ) in normalized dB to a modulated rectangular light signal measured at frequencies from 20 to 500k Hz.

The bandwidth, as illustrated in **Figure 7.26** was determined for the 256 pixels connected in parallel, which was realized by short cutting all anode and all cathode contacts, respectively. This procedure obviously leads to a dramatic increase in device capacitance, which hence lowers the measured BW. The BW of a single pixel can therefore be estimated larger. The device was then measured as described in paragraph 4.3.3 on page 38 and revealed a  $-3$  dB cut-off frequency of 100 kHz at 0 V and up to 220 kHz at  $-1$  V, as

demonstrated in Fig. 7.26.

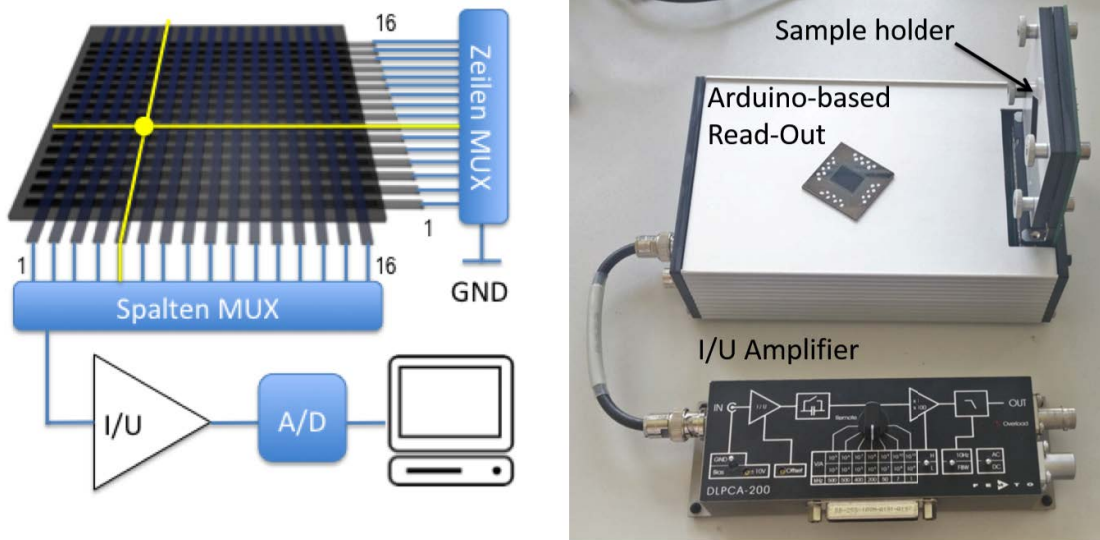
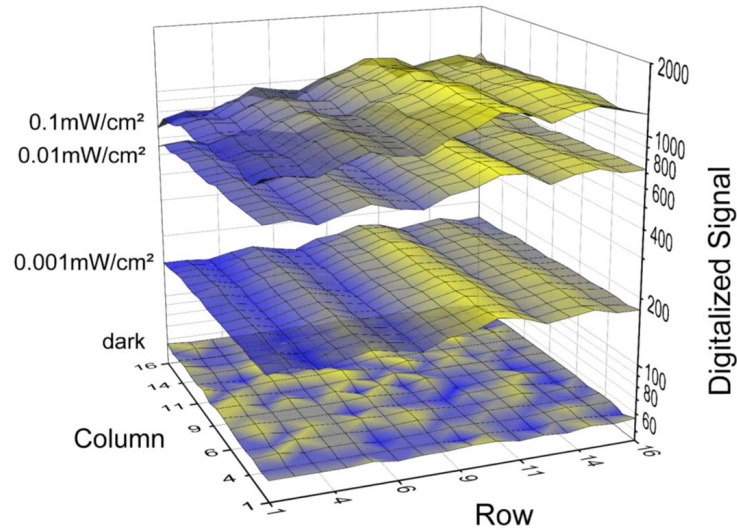


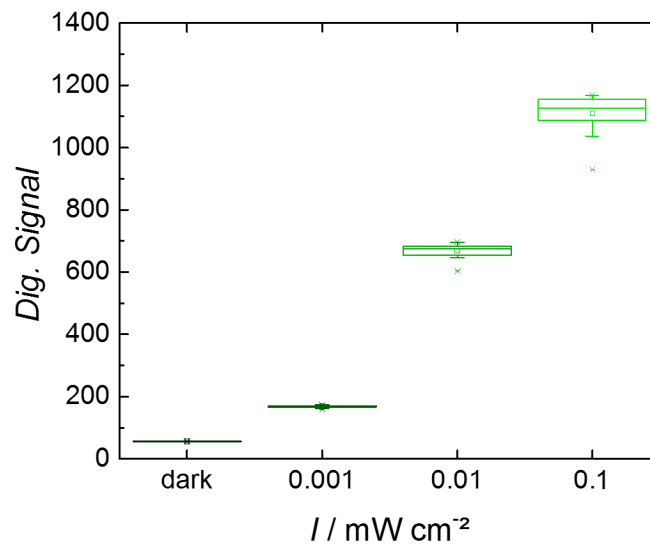
Figure 7.27.: Schematic drawing and photograph of a home-built Arduino based passive matrix read-out system. The pixels are sequentially addressed by transistor circuits and then amplified using an external transimpedance amplifier (FEMTO). The amplified signal is then digitized with an ADC and transmitted to a computer.

For a more statistical inspection of the printed array, a passive matrix read-out was built, as can be seen in **Figure 7.27**, which sequentially addresses the OPD pixel using one 16 channel multiplexing unit for the columns and rows, respectively. The current signal was read out at 0V and was then amplified by an externally connected trans-impedance amplifier (FEMTO, DLPCA-200). The amplified voltage signal was then processed by an analog-digital-converter (ADC) on an Arduino Due. The digitized signal (amplification factor of  $10^7$ ), recorded in dark and under low light intensities from  $0.1 \text{ mW/cm}^2$  to  $10 \text{ mW/cm}^2$ , is illustrated in a 3D map in **Figure 7.28(a)**. The array was therefore homogeneously illuminated using a solar simulator and the intensity was adjusted using neutral density filters. The graph shows a very homogeneous distribution of the dark current. However, seemed evident that the dark current is superimposed by the relatively high noise floor of the read-out system. Under illumination a slight modulation was observable, which could be caused by either small deviations in the active layer thickness and consequently arising thin-film interference effects, differences in the series resistances evolving from the printing process, or due to unwanted light coupling in the substrate and the SU-8 structures. In addition, the mean value and standard deviation is plotted in Fig. 7.28(b), which demonstrates the narrow signal deviation and elucidate the very small deviation between the pixels. However, an increase in signal deviation with light intensity can be observed. The reason for that could not clearly be identified.

Since photodetector arrays are supposed to be used for a local detection of light signals,



(a)



(b)

Figure 7.28.: a) Mapping of the digitized signal of the sequentially read-out OPD pixels in dark and under light intensities of 0.1, 1, and 10  $\text{mW}/\text{cm}^2$  and b) the corresponding digitized average signal and standard deviations.

the influence of optical and electrical cross-talk on the signal detection in a single OPD was investigated. Therefore, the active area of the OPD array was masked except for one OPD pixel, using an adhesive copper foil with a pinhole with a diameter of  $\sim 400 \mu\text{m}^2$ , as illustrated in the left schematic drawing in **Figure 7.29**. Apart from the single pixel, also the substrate, including feed lines and contact pads, was illuminated. The pixel map in

## 7. Digitally Printed Dewetting Patterns for Self-Organizing Microelectronics

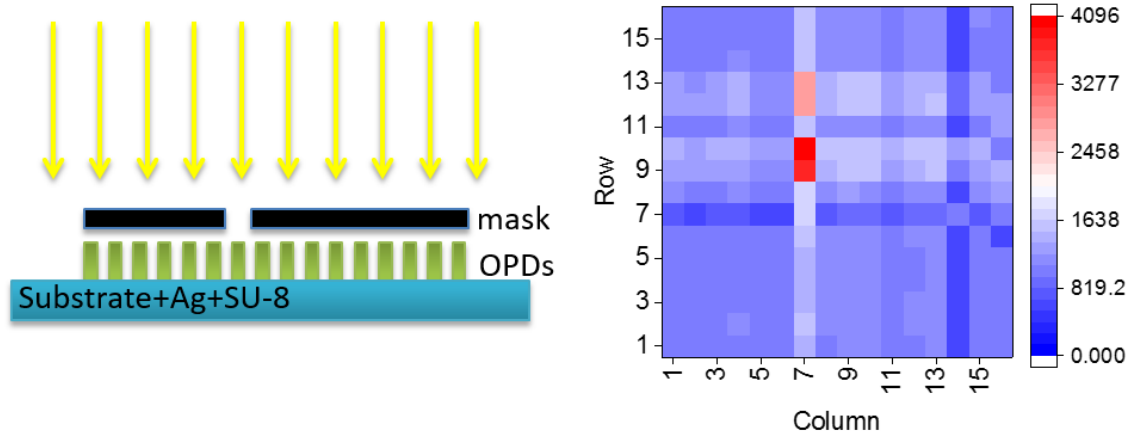


Figure 7.29.: Schematic and pixel map of a signal pixel excitation: Illumination of a single pixel by shading only the active area except for one pixel.

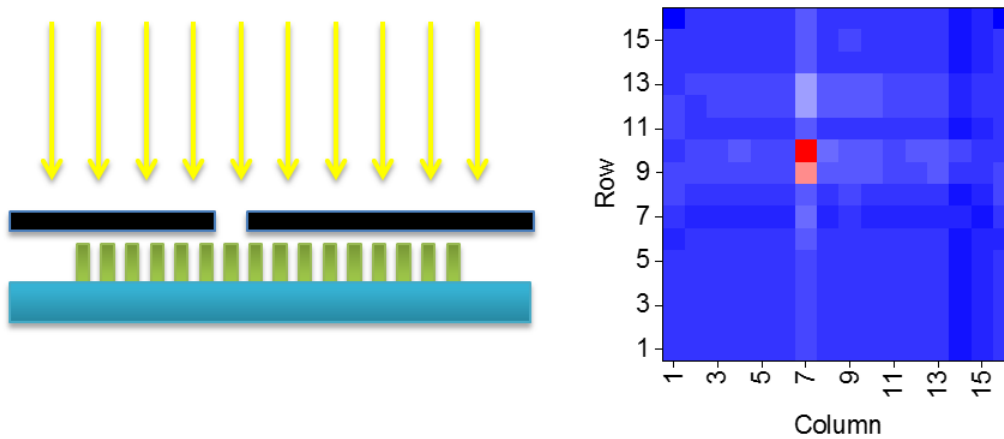


Figure 7.30.: Schematic and pixel map of a signal pixel excitation: Illumination of a single pixel by shading the active area, the feed lines and the contact pads.

Fig. 7.29 unveiled a peak for two adjacent pixels, which arose from a slight misalignment of the pinhole. However, a significant noise floor was present, which could be attributed to scattered light, or even incoupled light into the substrate or the SU-8 patterns. As shown in **Figure 7.30**, by expanding the mask over the complete topside of the substrate reduced the noise floor significantly. An additional shading of the backside of the glass substrate, as shown in **Figure 7.31**, resulted in a pronounced signal from the illuminated pixel and almost no measurable signal from the remaining pixels. These results indicate the importance of scattered and incoupled light, which by all means needs to be considered in a final application. To avoid an optical cross-talk colored substrates and even colored SU-8 should be utilized for top illuminated devices.

Furthermore, light beam induced current measurements were performed with the help of

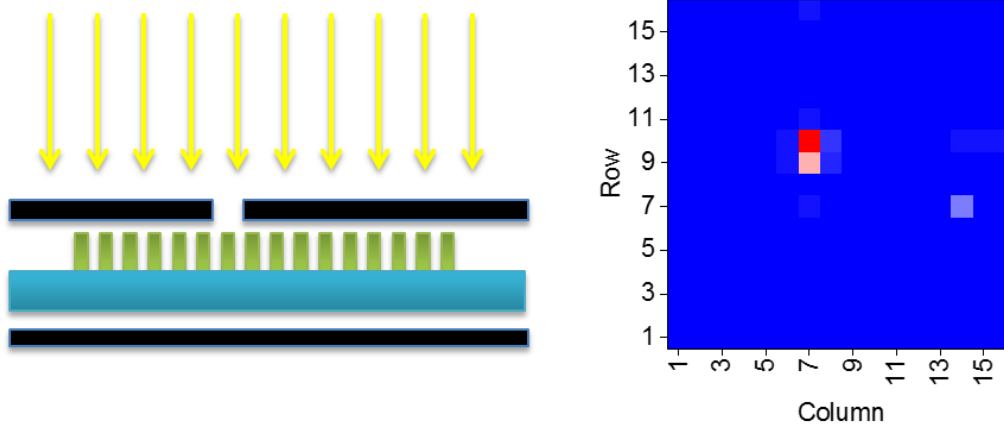


Figure 7.31.: Schematic and pixel map of a signal pixel excitation: Illumination of a single pixel by a) shading the active area, the feed lines and the contact pads, and additionally the backside.

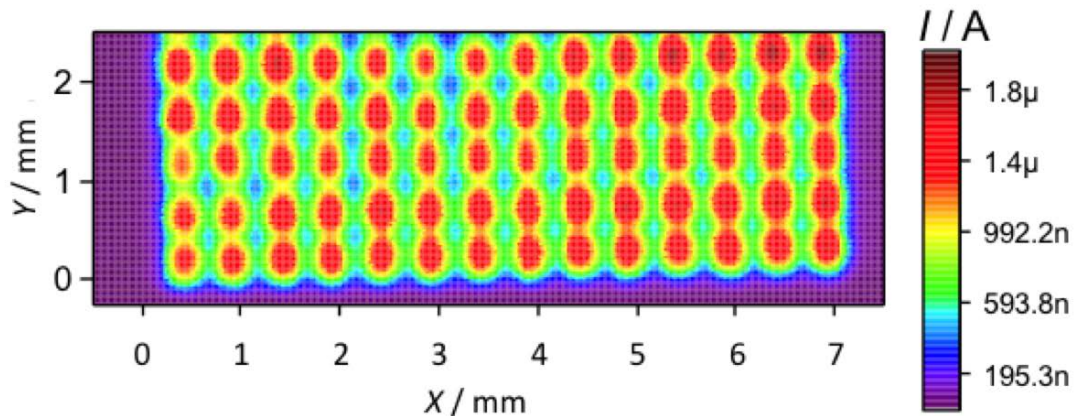


Figure 7.32.: LBIC measurements recorded for  $5 \times 14$  pixel at an illumination intensity of  $1.23 \text{ mW/cm}^2$  and a mapping resolution and spot diameter of  $40 \mu\text{m}$ .

Konstantin Glaser (LTI, KIT). The high resolution LBIC image in **Figure ??** was recorded using a laser (Newport, R-30972, 543 nm) focused with a 4x magnification objective to a beam diameter of  $40 \mu\text{m}$  yielding a peak power density of  $\sim 123 \text{ W/cm}^2$ . The intensity was reduced using neutral density filter to  $1.23 \text{ mW/cm}^2$ .

Finally, the LBIC measurement was performed for a  $3 \times 8 \text{ mm}^2$  image section of the  $16 \times 16$  pixel array, as presented in **Figure 7.32**. The two outer columns of the array were not contacted due to connection issues with the sample holder. However, the image demonstrates nicely the uniformity of 70 out of 256 printed OPD pixels. The uniformity of the pixel could be mainly ascribed to the homogeneity of the active layer thickness, which was achieved by a filling of the SU-8 wells serving as physical barriers for the ink. Furthermore, the separation of individual OPD pixels with protruding SU-8 structures also yields

## *7. Digitally Printed Dewetting Patterns for Self-Organizing Microelectronics*

a high registration accuracy.

### 7.3.3. Digitally Patterned Source-Drain Electrodes for Organic Field-Effect Transistors and Circuits

The research area of printed electronics embrace a vast diversity of possible applications, which besides the extensively discussed organic photodiodes also shows a keen interest in biological sensors,[140] light-emitting devices,[98, 141] and organic field-effect transistors (OFETs). The latter depicts a key component for almost all electrical logic circuitry, which is relevant for sensing, switching, regulating or modulating signals. It is therefore of great interest to yield highly reproducible devices even at the limits of the printing resolution of a few micrometers. Here, I will demonstrate OFETs and integrated circuits comprising source-drain (S/D) contacts fabricated with the presented self-organizing Ag patterning technique.

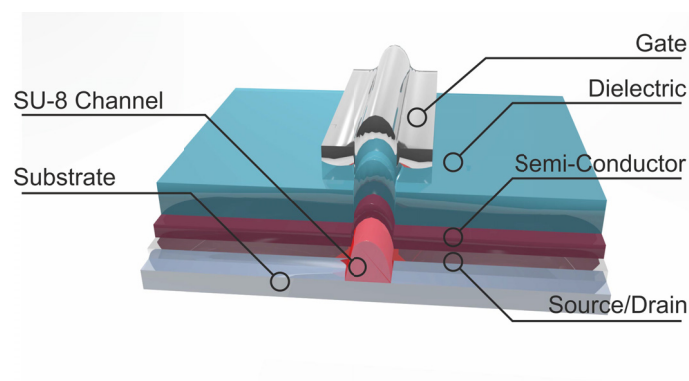


Figure 7.33.: Schematic drawing of an OFET comprising a channel length defined by the SU-8 line width.

The device architecture of OFETs comprising bottom S/D and top gate Ag contacts is illustrated in **Figure 7.33**, where the OFET's channel length, defined by the distance between the source and drain contacts, is determined by the SU-8 line width. Hence, the SU-8 pattern constitutes the later transistor channel, as well as the outer boundaries of the source and drain contacts.

Examples of the digitally patterned S/D layer and a magnification of the S/D finger structures are illustrated in **Figure 7.34(a)** and 7.34(b). However, in order to improve the charge carrier injection from the metal contacts into the semi-conductor (SC), the contacts were treated with a self-assembled mono-layer (SAM) forming molecule *julolidyl disulfide*, which lowers the work function of the Ag surface by  $\sim 1$  eV.[142] Therefore, the S/D contacts on the PET substrate were immersed in a 0.75 mM ethanol solution for 1 min. The n-type SC (N2200, Polyera) was then spin cast inside a  $N_2$  filled glovebox revealing a nominal thickness of 80 nm from an  $8 \text{ g L}^{-1}$  chlorobenzene (CB) solution.[143] The dielectric was chemical vapor deposited (PDS2010, Specialty Coating Systems, IN, USA) ParyleneC with a layer thickness of 250 nm, which ensures a highly conformal

## 7. Digitally Printed Dewetting Patterns for Self-Organizing Microelectronics

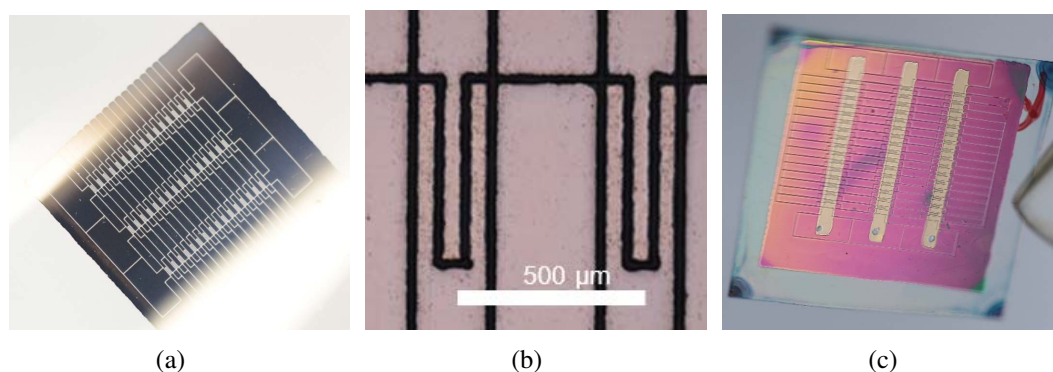


Figure 7.34.: a) Photograph of a PET substrate covered with 48 S/D finger structures. b) Magnification of two S/D structures, where the dark lines depict the SU-8 pattern. c) Photograph of completed OFETs with three inkjet printed top gate contacts.

and dense coverage of the layers below. ParyleneC possesses, compared to other commonly used dielectrics, such as the amorphous fluoropolymer Cytop (AGC Chemicals), a very high surface energy. This brings clear advantages for inkjet printing the Ag top gate contact. The printed gate was then vacuum dried for 15 min and afterwards annealed at  $120^{\circ}\text{C}$  for 10 min also in vacuum (15 mbar).

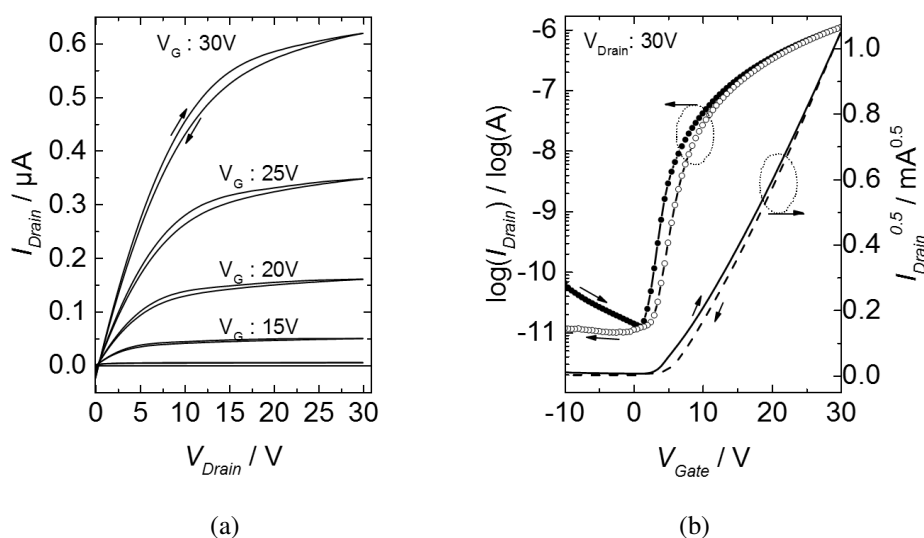


Figure 7.35.: OFETs with digitally patterned and SAM treated S/D electrodes. a) Output I–V characteristics. b) Transfer I–V characteristics.

The output and transfer characteristics of transistors comprising a channel width of  $\sim 1.15\text{ mm}$  and length of  $\sim 25\ \mu\text{m}$  are shown in **Figure 7.35**. The devices exhibited a very low threshold voltage of  $\sim 1\text{ V}$ , which could be ascribed to the previous SAM treatment. Furthermore, on-off ratios on the order of  $10^5$  were achieved.

### Digitally Patterned Source-Drain Layers for Organic Ring Oscillators

To further demonstrate the aptitude for building integrated circuitry ring-oscillators were fabricated, whose functionality strongly relies on the equality of each repetitive component. Therefore, unipolar ring oscillators were chosen in order to emphasize and demonstrate the process reliability and the reproducibility within a certain amount of interconnected transistors. Furthermore, this application example nicely demonstrates the benefits of utilizing solely digital deposition techniques with aerosol and inkjet printing for the S/D level, which allows for quick adjustments of geometrical factors and hence effective prototyping.

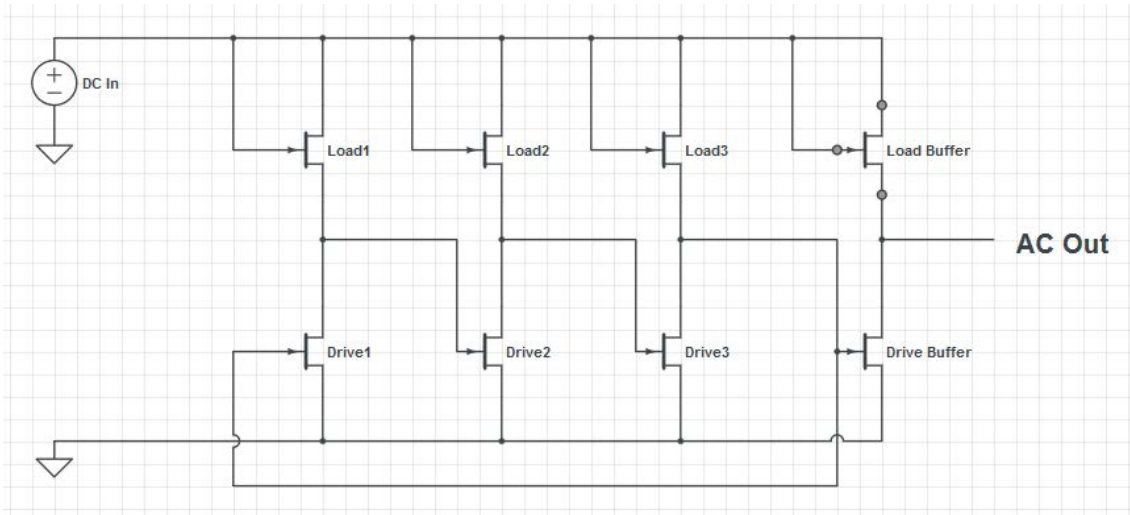


Figure 7.36.: Circuit diagram of a 3-stage unipolar ring oscillator.

First of all, a unipolar ring oscillator is an integrated transistor circuit comprising an odd number of inverter stages, which transforms a DC input voltage into an oscillating AC output voltage. The unipolarity implies, that only p- or n-type transistors are utilized. **Figure 7.36** shows the circuit diagram of a 3-stage ring oscillator, as it was fabricated within this work. The last stage is an additional buffer stage and serves as a output signal driver. Every inverter stage constitutes of one load and one drive transistor, meaning that the input signal gets negated at the output of each stage. Consequently, an odd number of inverters connected in a ring leads to an oscillation of  $V_{out}$ .

Due to the complex and entangled dependency of an integrated circuit's electrical behavior to the single OFET performance, gate-leakage currents, overlap capacities, and contact resistances, we opted for a Simulation Program with Integrated Circuit Emphasis (*SPICE*) simulation prior to the fabrication of the SU8 structures. Further information about the model can be found elsewhere[144] and in the Appendix B.3. The transconductance  $g_m$ , which depicts a tunable parameter by varying the channel width of the transistors, was found to be one of the key parameters for the success of an oscillating circuit:

$$g_m = \frac{\Delta I_D}{\Delta V_G} \quad (7.2)$$

## 7. Digitally Printed Dewetting Patterns for Self-Organizing Microelectronics

where  $I_D$  is the drain current; and  $V_G$  depicts the gate voltage. Simulation results exhibited the  $g_m$  of the load transistor to be 100 times smaller than the  $g_m$  of the drive transistor. According to these findings, the channel widths and hence the AJ printer's tool path, comprising the geometries of the SU-8 pattern for the transistor circuitry were adjusted properly. Consequently, the channel widths were defined for load and drive transistors as followed:  $L_{1-3} = 400 \mu\text{m}$  and  $L_{BS} = 800 \mu\text{m}$ ;  $D_{1-3} = 40 \text{ mm}$  and  $D_{BS} = 40 \text{ mm}$ . Further information about the SU-8 tool path, as well as coarse inkjet patterns can be found in the Appendix B.4.

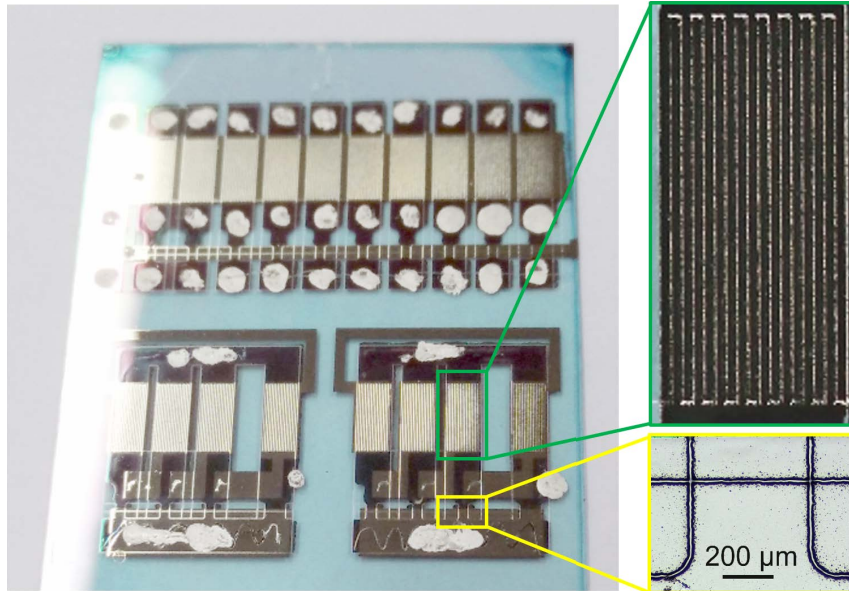


Figure 7.37.: (left) Photograph of a PET substrate comprising two ring oscillators and each 10 single load and drive transistors above. (right) magnification of a drive transistor with a 40 mm and a load transistor with a 0.4 mm channel width.

**Figure 7.37** shows a photograph of a PET substrate comprising two digitally patterned ring oscillators on the bottom, and each 10 single load and drive transistors at the top. The magnifications demonstrated the enormous channel width of the drive transistor with 40 mm and a channel length of  $\sim 30 \mu\text{m}$ .

The transfer characteristics and the corresponding gate leakage are depicted in **Figure 7.38**. The drain current ( $I_{Drain}$ ) as a function of the gate voltage  $V_{Gate}$  almost perfectly scaled with the channel width, as expected. Fig. 7.38(b) reveals the gate leakage, which clearly showed an increased leakage current for the larger drive transistor. However, since the gate leakage seemed to depend not only on the dielectric properties and  $V_{Gate}$ , but also on the semi-conductor properties,[144] this effect could in principle be diminished by printing the semi-conductor only in the channel, which would be nothing else than the SU-8 tool path. These continuative experiments however has to be postponed to future work.

The previously mentioned  $g_m$  was plotted over the  $V_{Gate}$ , as shown in **Figure 7.39** and correlate well with desired  $g_m$  from the *SPICE* modeling and the geometric adjustments

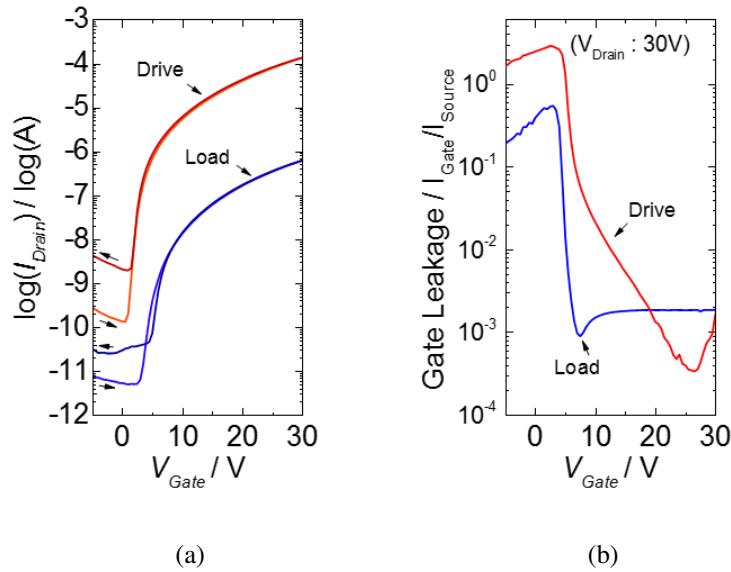


Figure 7.38.: a) Transfer characteristics of a drive and a load transistor. b) Corresponding gate leakage derived at  $V_{Drain} = 30V$ .

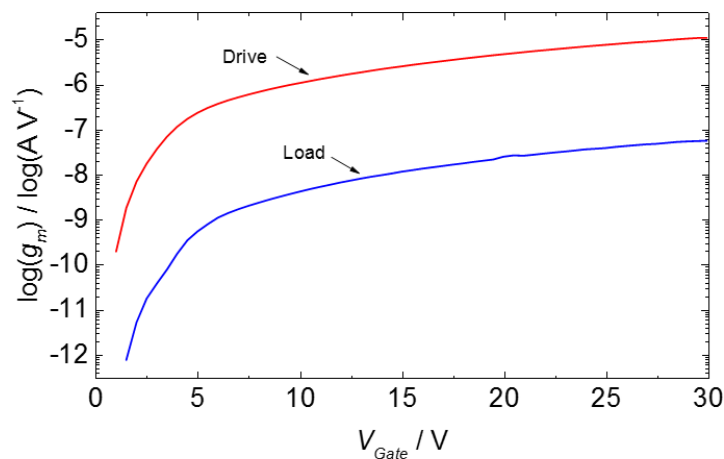


Figure 7.39.: Transconductance of drive and load transistors.

of the drive and load transistors. Furthermore, the graph shows a dependency of  $g_m$  from  $V_{Gate}$ , which consequently influences the AC output frequency as a function of the DC input voltage.

To further test the reproducibility of the OFETs, a statistical evaluation was carried out with each 8 transfer curves ( $V_D = 30V$ ) of load and drive transistors, as shown in **Figure 7.40**, which were located on one substrate. The difference in channel width of a factor of 100 corresponds well to the recorded currents in the *on* state at  $V_{Gate} = 30V$ , as already shown in Fig. 7.38. More interestingly, almost no deviation in the transfer curves was observed for the  $400\mu m$  wide load transistors. By contrast, the  $40\mu m$  wide drive transistors comprised deviating currents in the *off* state in the range of one order of magnitude.

## 7. Digitally Printed Dewetting Patterns for Self-Organizing Microelectronics

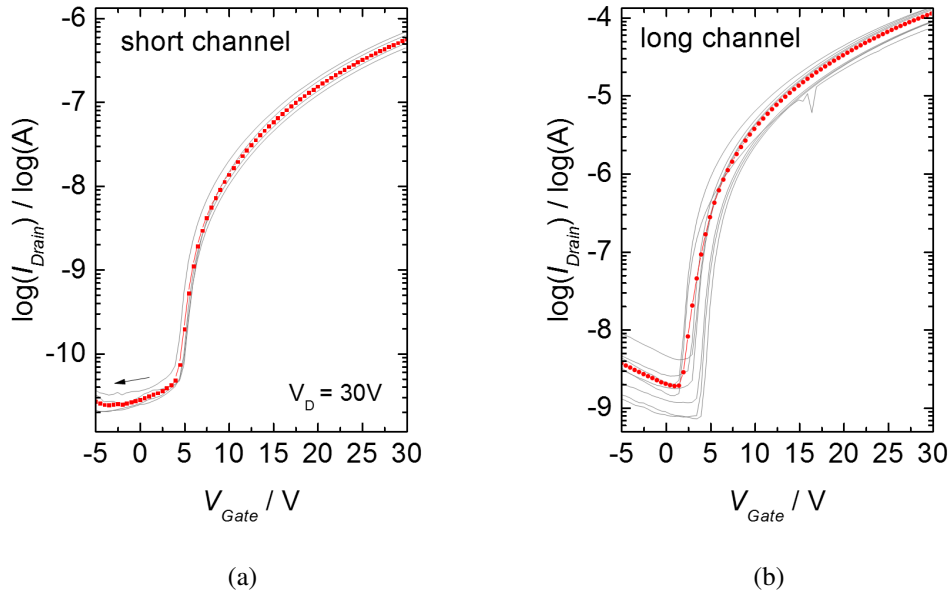


Figure 7.40.: Transfer characteristics measured at  $V_D = 30\text{ V}$  for a) 8 different load transistors, and b) of 8 different drive transistors. (red curve = average)

For larger  $V_{Gate}$  the  $I$ - $V$  transfer curves showed only nominal deviations.

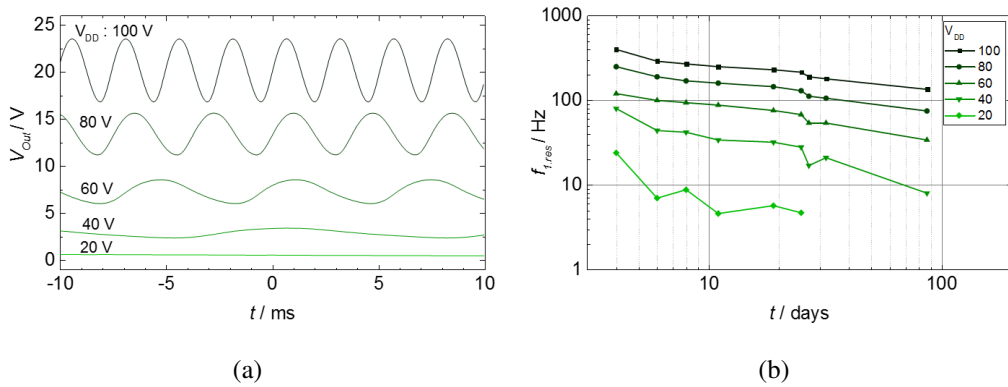


Figure 7.41.: a) Oscillating output signal at different DC input voltages  $V_{DD}$ . b) Oscillation frequency at different  $V_{DD}$  measured over a period of 87 days.

The statistically proven equity of the measured single transistors could be reflected by the output signal of the ring oscillator, as shown in **Figure 7.41(a)**. The AC signal was recorded using an oscilloscope (DSO6102A, Agilent) at different input voltages  $V_{DD}$  ranging from 20 V to 100 V. That confirms the previously stated dependency of input voltage to output frequency by a change in  $g_m$  with  $V_{Gate}$ . The oscillation frequency for an input voltage of 100 V reached up to 400 Hz. Fig. 7.41(b) presents additionally the oscillation frequency measured at different  $V_{DD}$  over a period of 87 days. The ring oscillators in the meantime were stored under ambient conditions. A frequency decrease, as well as a decrease in amplitude could be observed, which could be referred to the oxida-

tion of the Ag top gate and to a penetration of oxygen and water into the dielectric and semi-conductor. Nonetheless, the overall working time appeared to be quite long, considering that the device was not actively encapsulated. Certain oxygen and humidity barrier properties could be ascribed to the ParyleneC dielectric.[145]

#### 7.3.4. Summary

The process reliability was demonstrated by fully printing organic photodiodes, where the advantages of the patterning process was exploited to fill the emerging reservoirs with active material and consequently achieve an outstanding registration accuracy. Pixels in the micrometer scale were fabricated and revealed on-off ratios of  $10^5$ . Furthermore, fully digitally printed OPD arrays with 256 pixels were fabricated and revealed  $D^*$  up to  $8 \cdot 10^{11}$  Jones, a  $BW$  up to 220 kHz, and an  $LDR$  of more than 90 dB. The uniformity of the individual OPD pixel with an active area of  $150 \times 350 \mu\text{m}^2$  was demonstrated by a sequential mapping of the OPD signals, as well as by LBIC measurements. Nevertheless, an issue constitutes the cross-talk between pixels that was mainly caused by incoupled light into the glass substrate.

Beyond that, the fabrication of unipolar ring oscillators was successfully demonstrated. The complete source-drain electrode layer was structured using AJ printed SU-8. Thus the channel width and length were defined by the SU-8 pattern. The profound device characterization emphasizes the suitability of this patterning process, where single device and statistic measurements, and also lifetime measurements were performed.



## 8. Summary and Outlook

In the presented work, the versatility of the digital Aerosol Jet (AJ) manufacturing technology was demonstrated in a variety of optoelectronic and electronic applications. Starting with the fabrication of lines, sequentially printed layers, towards devices and even more complex electronic systems. The versatility of this method was shown for a plenitude of functional materials, such as conductive metal and polymer inks, semi-conducting metal oxides, as well as organic absorber materials. A strong expertise was developed on the optimization of printing relevant processes, such as technical processing parameters and the formulation of functional inks for the fabrication of functional layers and electronic devices. Furthermore, the introduction of a novel digital patterning method for self-organizing metal structures could be exploited to fabricate electronic systems, e.g. with integrated circuitry and 2-dimensional OPD arrays with 16x16 pixels in the micrometer regime.

In chapter 5, I investigated the feasibility of AJ printing for the fabrication of transparent conductors (TCs) as top electrodes for organic solar cells. The AJ printing method allows for a very precise deposition of tailored fine features in a contact-free and digital manner, which can be perfectly used for prototyping, as well as the fabrication of more complex grid designs with the special requirements of contacting the top of organic functional layers. Thermogravimetric measurements revealed that a considerable amount of organic residues still remain in the annealed film, which however evidently is located in a mesoporous interface between the Ag and the substrate, as could be visualized by cross-section SEM image. The utilized commercial low temperature metal organic deposition (MOD) Ag ink formulation was further adapted by adding 10 vol.% anisole to meet the requirements of the AJ printer and the underlying organic matter in terms of printability, reproducibility and compatibility with annealing conditions of 140 °C and  $\leq 1$  min. The as printed Ag grids on top of conductive PEDOT:PSS were then evaluated by its equivalent sheet resistance, transparency, as well as mechanical robustness. 1-dimensional, 2-dimensional, as well as hexagonal grids with  $\geq 90\%$  transmittance and an equivalent sheet resistance of  $10 \Omega/\square$  could be achieved. The mechanical stability was measured for the hybrid TC by performing cyclic bending and strain test revealing a significantly improved resistance to fatigue processes compared to conventionally used ITO covered PET allowing for non-destructive bending radii of  $\sim 1.45$  mm. The application of these hybrid TCs with 1-dimensional, 2-dimensional and hexagonal layouts as top electrodes for P3HT:PCBM solar cells lead to a remarkable improvement of the device efficiency by up to 57% compared to a pure PEDOT:PSS top electrode. Nevertheless, since fluctuations in the laboratory fabrication processes interfered with the analysis of geometrical and electrical influences, a physical finite element device model was set up. This enabled

## 8. Summary and Outlook

a large number of factors, such as the transmittance, specific conductivity of the respective materials, or the geometrical factors depending on the grid design, always considering reasonable material sets, such as Ag and PEDOT:PSS conductivities, or Ag line width and height, which reflect the practicality and applicability for printing, to be tested. By that, it could be shown, that hybrid TC's with line widths of  $\geq 10 \mu\text{m}$ ,  $R_{sheet,M} = 10 \Omega/\square$ , and a transmittance of 95 % merely reduce the power conversion efficiency by  $\sim 5 \%$ , as long as the symmetry radius of the grid is kept below  $650 \mu\text{m}$ . These results are valid for photocurrent densities up to  $20 \text{ mA cm}^{-2}$ , which also meets most requirements of organic solar cells.

In chapter 6, I focused on the fabrication of multi-layered organic photodiodes using AJ printing. Therefore, expertise in printing of functional layers was gained with special requirements to the control over the final layer thickness and the layer homogeneity. Beside that, near infrared measurements were conducted to confirm that no molecular destruction took place during the ultrasonic atomization of the source material. In comparison to printing lines, layers were printed by a sequential filling of the desired area, where the printing speed and material throughput mainly affected the layer quality. It was also found that the layer thickness could be adjusted by multi-pass printing of thin single layers, which in addition improved significantly the layer homogeneity. Finally, organic photodiodes with ITO / AZO / PTB7:PC70BM / PEDOT:PSS revealed a spectral responsivity of up to  $0.25 \text{ A/W}$ , a specific detectivity of  $10^{12}$  Jones, and a bandwidth of  $330 \text{ kHz}$  under consideration of an overall device transparency of 20 %. The commonly used ITO was then exchanged in a further step by a PEDOT:PSS layer resulting in an inverted devices stack with PEDOT:PSS / AZO / PTB7:PC70BM / PEDOT:PSS. The devices were characterized optoelectronically from the top and the bottom side. Furthermore, its mechanical robustness was tested. The fabricated ITO-free photodetector performance tests revealed  $SR = 0.2 \text{ A/W}$ ,  $D^* = 2 \cdot 10^{11}$  Jones, and  $BW = 295 \text{ kHz}$  at a transparency of 16 %. The digital fabrication of almost imperceptible optical sensors with a very simple, but efficient device stack, demonstrated its remarkable potential for novel applications, such as the integration in novel sensing devices, e.g. in gesture recognition user interfaces.

In chapter 7, the previously gained expertise on photodiodes on a single-device level was transferred to more complex printed systems. Here, I presented a digital patterning method, where Ag micro-structures could be accurately fabricated in a simple two-step process. Therein, a lyophobic pattern was AJ printed from SU-8 and a Ag nanoparticulate ink coated on top in a consecutive pass. For reasons of reproducibility and control over the ink volume, inkjet printing was used for the Ag deposition, although many other coating techniques, such as blade coating and spray coating, were proven to be suitable for this process. It was found, that an excessive ink volume led to liquid bridging, which according to Brinkmann *et al.* is determined by the following four parameters: the reduced ink volume  $V/L_1^3$ , the ratio of dewetting to wetting area  $L_D/L_1$ , and the contact angles  $\theta_D$  and  $\theta_1$ . That hints to a correlation between minimum feature size and maximum layer thickness. Besides, successful dewetting could also be correlated to the substrate's surface energy and the solvent's surface tension, where a low contact angle on the wetting

regions was found to be of high importance. Conversely, no clear evidence could be found for a major impact of either the polar or dispersive surface energies or tensions. Finally, different application examples were fabricated to elucidate the versatility of the printing technique and the applied dewetting process with a high self-registration accuracy and a high reproducibility. The high registration accuracy was demonstrated by the local deposition of thick active layers ( $\sim 1 \mu\text{m}$ ) by exploiting the physical barriers given by the protruding SU-8 structures, shown by fully printed photodiode pixels with dimensions in the sub-millimeter regime. Based on these findings, photodiode arrays with 256 pixels were printed to emphasize the high reproducibility that could be achieved for these optoelectronic systems. Furthermore, its high qualification for accuracy critical applications was then also highlighted in the fabrication of self-organized source-drain electrode structures for 3-stage ring oscillators. With this, a big step towards the digital manufacturing of integrated circuitry was demonstrated, which shows one route for the successful fabrication of complex integrated systems.

The AJ technique is a relatively new deposition technique, which was demonstrated to be highly suitable for manufacturing of conductive lines, electronic devices and systems on flexible and stiff substrates. AJ printing offers different techniques to generate the aerosol, which are the pneumatic and ultrasonic atomization. While the pneumatic system has its advantages in the handling of a wide ink viscosity range and a high material throughput, the ultrasonic system shows clear benefits in terms of low material consumption, precise small-feature printing, and thus for rapid prototyping. These very distinct atomization possibilities cover the viscosity range of almost all inks, dispersions or precursor solutions used in printed electronics and hence make it a unique and versatile technique compared to other digital deposition techniques, such as Inkjet or conventional spray coating. However, from my understanding AJ printing does not directly compete with other techniques, but rather bridges the established deposition methods. Optomec, a global supplier of additive AJ manufacturing systems, announced in 2015, that the core AJ technology will be integrated in the line of Inkjet Printers by Ceradrop, France, to merge the technology strengths and further increase the system's versatility.

The fabrication of sensors on a single-device level, as well as basic integrated circuits and sensor arrays comprising organic semi-conductors have been demonstrated so far. Nevertheless, the demand for flexible, imperceptible, or stretchable devices and integrated systems require a fabrication on highly diverse substrate materials. This again carries a variety of different surface properties and qualities with it, including local energetic inhomogeneities. This diversity of substrate materials and also of the functional inks lead to very high process complexity, leaving out the additional influences of humidity, dust particles and room temperature. Therefore, future work has to address the very sensitive variables with influences on the surface and interface kinetics, such as pinning, wetting, spreading, and drying. This could be tackled for instance by specific surface treatments with surface silanizations, or planarization layers. Another aspect addresses the drying and annealing of functional materials. It was found that in many cases a drying under vacuum conditions prior to the annealing drastically improves the layer homogeneity and thus the device performance, which could be ascribed to a lack of saturated solvent atmospheres in close

## 8. Summary and Outlook

proximity to the wet surface. However, the effect and process parameters need further investigation.

Furthermore, the protection of organic and metallic layers against oxidation and degradation due to water and oxygen penetration is still one of the main issues for printed organic electronics. Depending on the application, adhesive encapsulation foils or solution-processable materials would need match also the mechanical requirements. Fortunately, in recent years the importance of this research area was identified by several research groups, such as the group around Edman.[146] Nevertheless, the required moisture vapour transmission rates (MVTR) and oxygen transmission rates (OTR) of  $\sim 10^{-6}$  g/m<sup>2</sup>/day and  $\sim 10^{-6}$  cm<sup>3</sup>/m<sup>2</sup>/day, respectively, are still very challenging and not reached, besides glass or metals.

I'm very confident and anticipating that printed and flexible electronics will be successful in future markets, as recent forecasts already impressively predict with a market volume of more than *\$US 8 billion* within the next 10 years only in sensor applications. These predictions rely mainly on the already ongoing transition from research and development to mass production and will mainly be driven by the novel functionalities such as flexibility, imperceptibility, light-weight and customizability for up-coming sectors, i.e. the internet of things, ubiquitous sensing, wearables or smart packaging.

# Appendix



# A. Appendix: Fully AJ Printed Organic Photodiodes

## A.1. AJ Printed Active Material: Influence of Tube Temperature on Film Homogeneity

Figure A.1 shows AFM images taken from PTB7:PC70BM layers on ITO covered glass, printed with different tube temperatures ranging from 40 °C up to 90 °C. The tube heater is located directly before the nozzle head. Its assignment is composed of a condensation of the aerosol droplets, which allows for a printing of higher concentrated inks. As can be seen in the images, which present the topography and phase of each layer, the tube temperature comprises a certain influence on the film morphology, as well as the film homogeneity. For lower tube temperatures ( $\leq 70$  °C) a very smooth and dense layer could be observed. Additionally, as indicated by the dark and brighter areas, a phase separation with PTB7 (bright areas) and PC70BM (dark spots) rich domains occurred, which is supported by the similar pattern in the phase image. An utterly different image was however constituted by the layer printed with 90 °C tube temperature. Surprisingly, the phase separation changed significantly, resulting in larger PC70BM domains. Hence, using the tube temperature as a printing parameter to optimize the print image, such as the layer homogeneity, requires a careful consideration of the morphological aspects taking place in especially functional material blends, such as organic BHJ absorbers.

## A.2. Linearity of ITO-free OPDs

Figure A.2 shows a linear behavior of the fully AJ printed photodetector under different excitation wavelengths and different reverse bias voltages. Red, green and blue LED arrays were used for the excitation. The intensity, measured with a power meter (1936-C, 818-UV, Newport), was varied by changing the current. The results nicely correlate with the *SR* measurements from Fig. ???. The linearity however suffers somewhat at  $-3$  V. The open symbols in the graph show the current density with subtracted dark current, which prove that the higher dark current and increased bias voltages dominates the current density at low intensities.

A. Appendix: Fully AJ Printed Organic Photodiodes

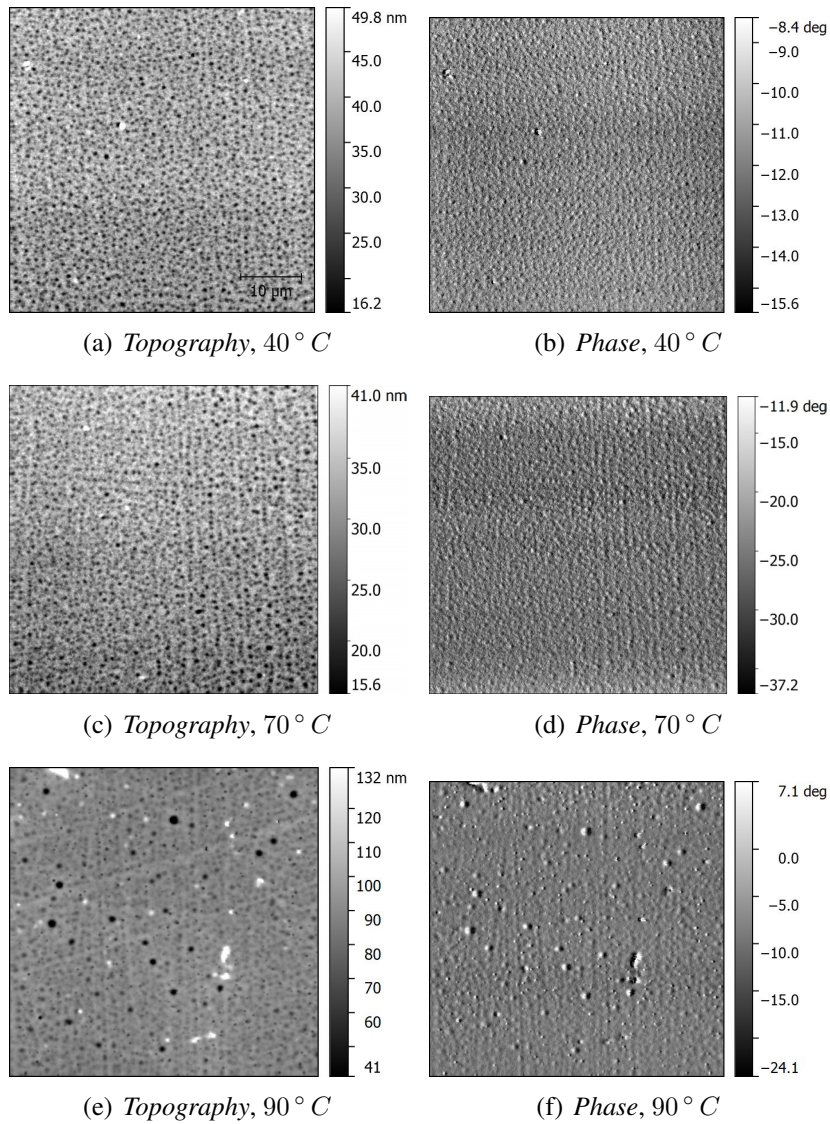


Figure A.1.: AFM image with topography and phase of AJ printed PTB7:PC70BM layers.

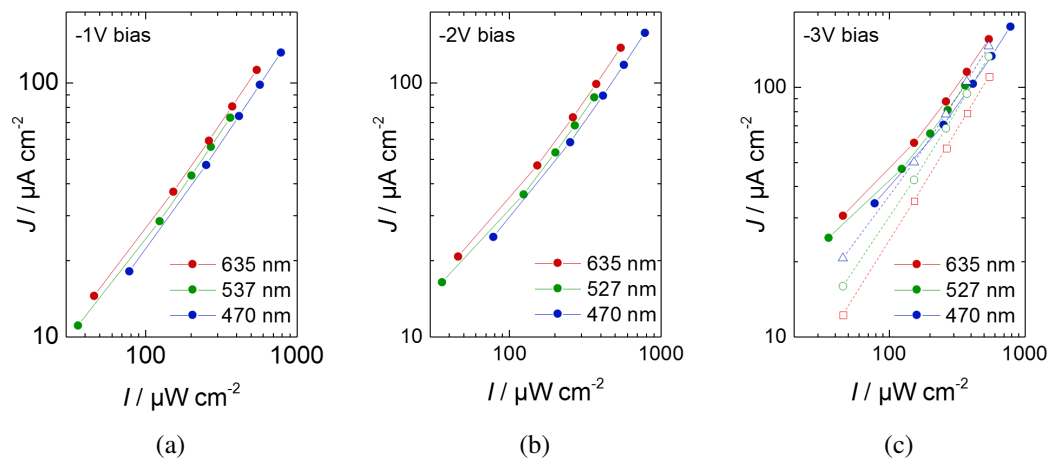


Figure A.2.: Intensity dependent current density measurements at a)  $-1\text{ V}$ , b)  $-2\text{ V}$ , and c)  $-3\text{ V}$  reverse bias voltages for red, green, and blue LED light sources.



## B. Appendix: Digitally Printed Dewetting Patterns for Self-Organizing Microelectronics

*In this Appendix the reader will find further supplemental information to the data shown in chapter 7.*

### B.1. Surface Topography of AJ-Printed SU-8

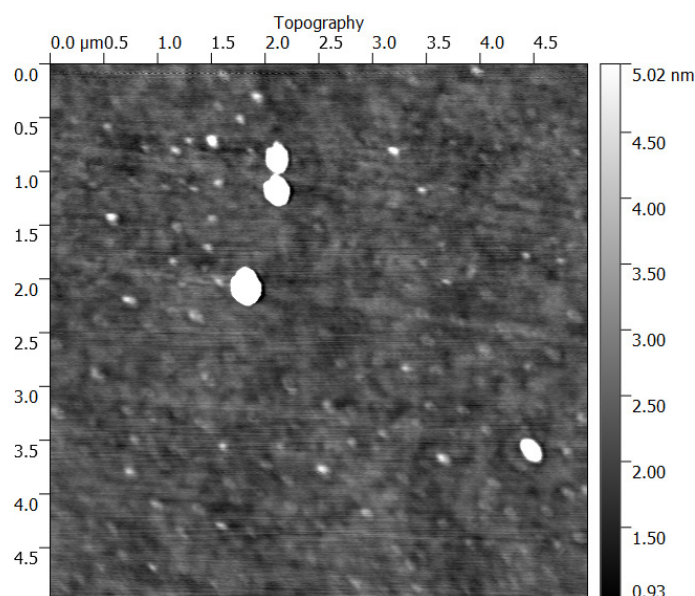


Figure B.1.: AFM image of an AJ printed SU-8 line back.

Figure B.1 presents an AFM image from a SU-8 line back taken after the deposition and dewetting of Ag. Hence, the bright spots constitute Ag ink residues on the SU-8, which could emerge from locally diverging surface energies caused by intrinsic defects. The rms roughness was determined to 0.4 nm for this surface area (Ag residues excluded).

## B.2. Substrate Variation for Self-Organized Ag Patterns

The AJ printing of low surface energetic epoxy resins, such as SU-8, as dewetting patterns for self-organizing functional materials, e.g. Ag ink, was extensively demonstrated on PET. It was shown, that mainly the high surface energy of the substrate, which provokes a low contact angle of the fluid, is crucial for the success of this process. Therefore, further commonly utilized substrates with high surface energies were tested. Information about the exact surface energies of polyimide (PI, Kapton), glass (Borofloat33, Schott), and  $O_2$  plasma-treated PET were already presented in the main text. The surface energy of substrates has a considerable influence the wetting behavior of printed structures. This again can lead on the one hand to a spreading of the ink, which prevents the fabrication of small features, e.g. source-drain contacts for OFETs or antenna structures. On the other hand, too low surface energies would cause a dewetting of the ink, which could prevent the fabrication of homogeneous layers. Hence, the feasibility or performance of printed devices or circuits depends vigorously on the ink-substrate interactions. However, the substrate choice is often determined by the final application, e.g. dielectric substrate losses,[147] and fabrication relevant necessities, e.g. solvent resistivity and thermal loading.

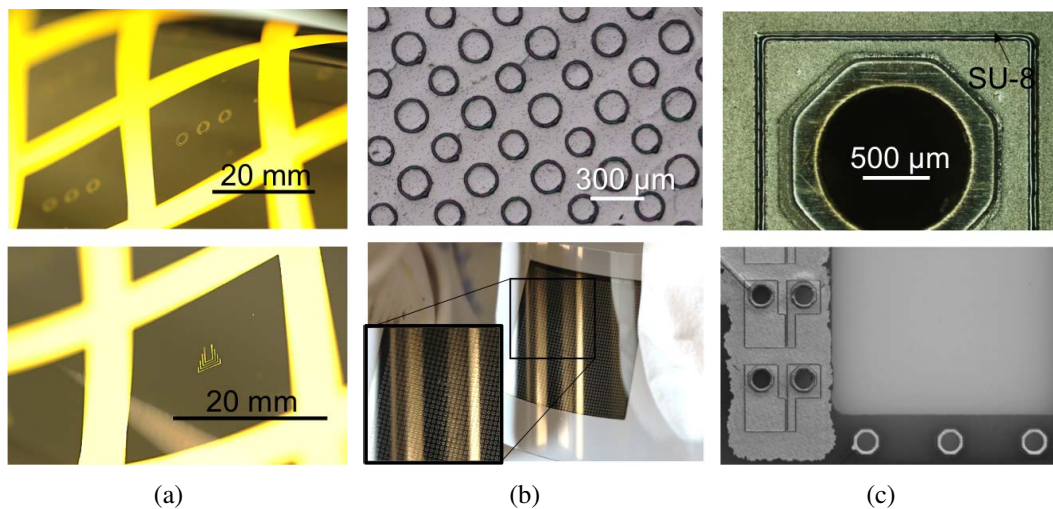


Figure B.2.: a) AJ printed split ring resonator and RF slot antenna structures with inkjet printed Ag areas on polyimide (PI). b) Ring structures for THz applications printed on  $1.4 \mu\text{m}$  tick PET foil (left) and on  $175 \mu\text{m}$  thick PET (right) covered with subsequently inkjet printed Ag ink. c) AJ printed SU-8 lines on FR-4 (printed circuit board) comprising dewetted brushed Ag ink.

Figure B.2(a) illustrates photographs of inverted split ring resonator (top) and slot antenna (bottom) structures printed with SU-8 and subsequently inkjet printed Ag on PI foil. The SU-8 patterns comprise line widths of  $\sim 50 \mu\text{m}$ . Figure B.2(b) depicts in the top image an array of ring structures with alternating radii of  $\sim 70 \mu\text{m}$  and  $\sim 80 \mu\text{m}$  and a lattice

of  $\sim 250 \mu\text{m}$  printed on a  $\sim 1.4 \mu\text{m}$  thick PET foil. The bottom image shows the same pattern on a  $\sim 175 \mu\text{m}$  thick PET foil. In Figure B.2(c), SU-8 was AJ printed on a conventional printed circuit board (FR-4 epoxy resin), which also exhibits the described dewetting effect.

## B.3. Unipolar Ring Oscillators

### B.3.1. SPICE Model

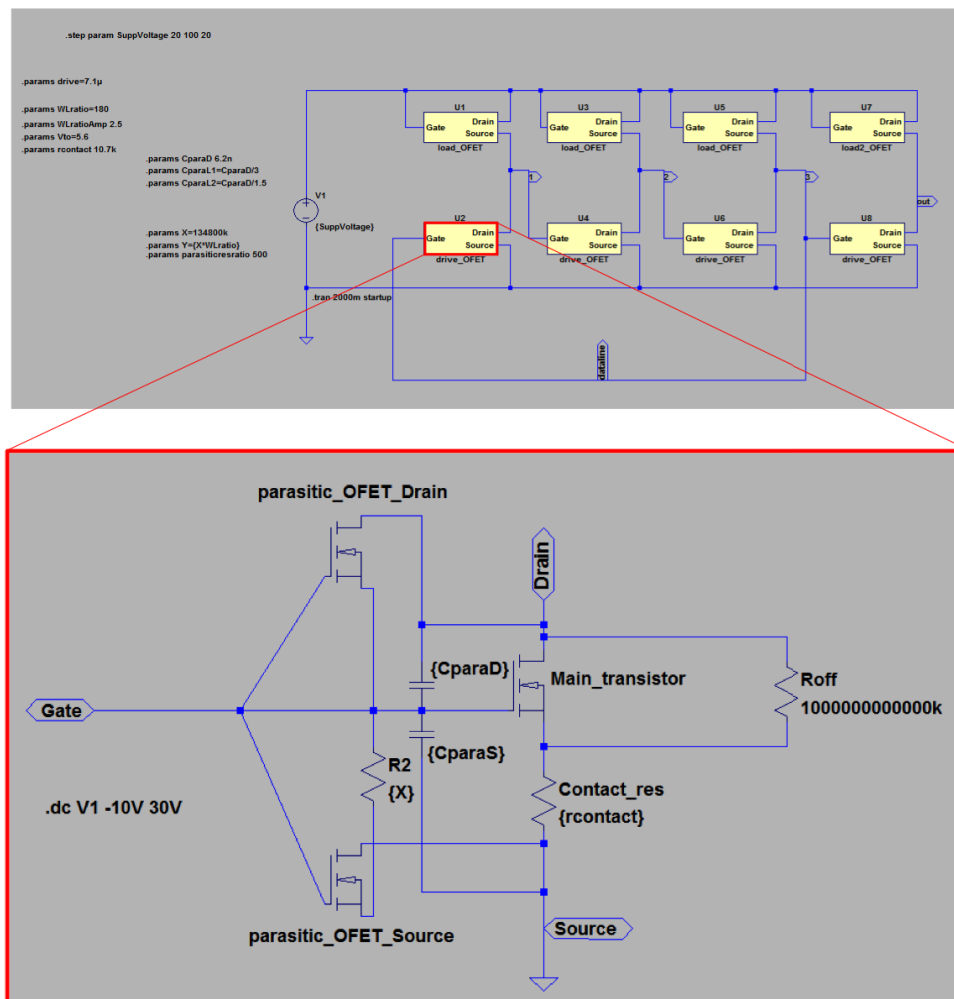


Figure B.3.: SPICE model of a 3-stage + buffer stage ring oscillator (top) and equivalent circuit including parasitic effects of an OFET. (bottom).

The ring oscillator circuit was simulated using a SPICE model, as illustrated in Figure B.3, prior to the device fabrication. Therefore, an OFET equivalent circuit was applied, which considers for the major parasitic currents, such as the gate leakage currents. Considering these parasitic effects allows for a more robust circuit design. A detailed model

description can be found elsewhere.[144]

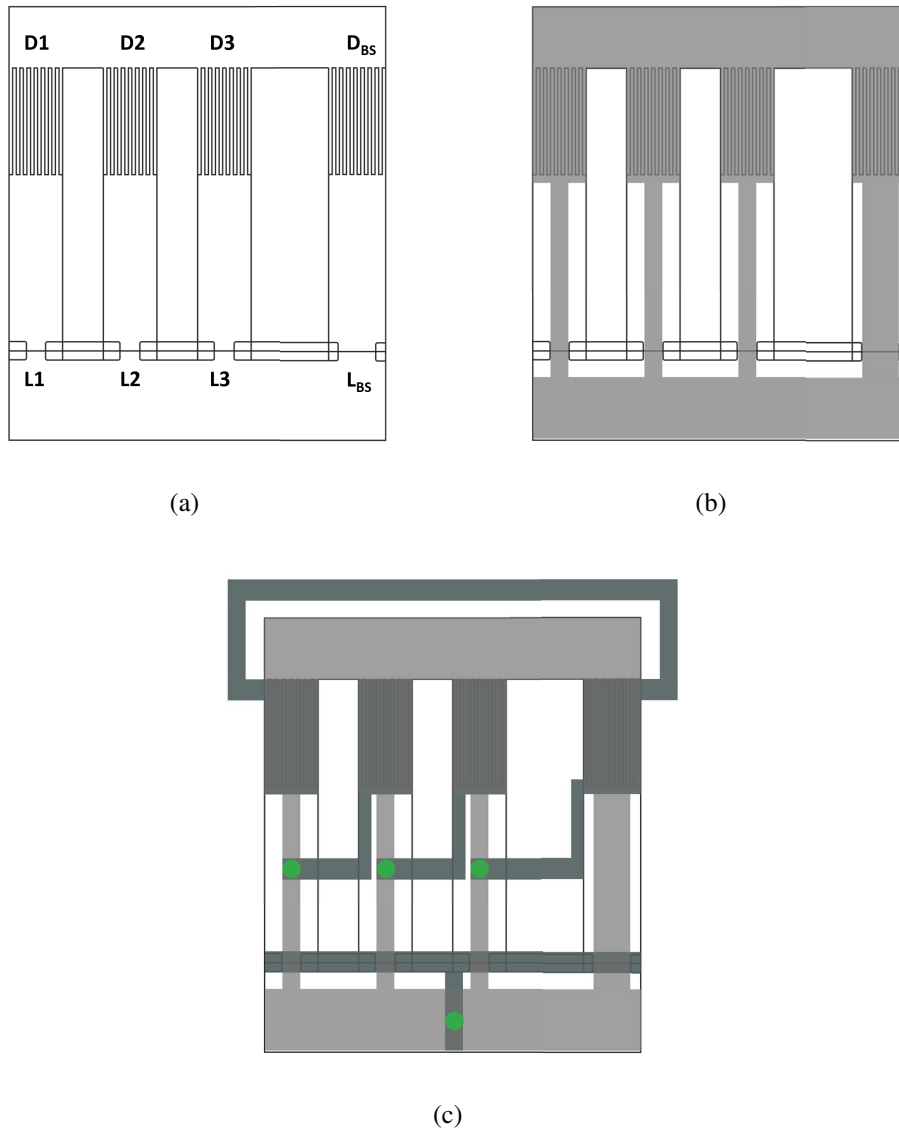


Figure B.4.: Ring oscillator layout: a) SU-8 tool path with dewetting pattern for S/D Ag layer. b) The light grey area depicts the coarse inkjet pattern for the Ag deposition. c) The dark grey area depicts the final gate layer, where the green dots highlight the through-contacts to the bottom S/D layer.

Figure B.4(a) reveals the SU-8 tool path, which was used to pattern the source-drain (S/D) layer comprising channel widths of 40 mm for drive and 0.4 mm for load transistors, except the load transistor of the buffer stage dimensioned to 0.8 mm.  $D_{1-3}$ ,  $D_{BS}$ ,  $L_{1-3}$  and  $L_{BS}$  indicate the positions of each transistor within the circuit. Fig.B.4(b) illustrates the coarse Ag pattern in light grey, which was subsequently inkjet printed. The final gate layer, as shown in Fig. B.4(c) in dark grey, was through-contacted through the semi-

conductor and dielectric layer by mechanical scratching to the S/D layer, indicated by the green dots.



# List of Abbreviations

<i>q</i>	electron charge ( $1.602 \cdot 10^{-19}$ eV)
<i>k</i>	Boltzmann constant ( $1.38064852 \cdot 10^{-23}$ m <sup>2</sup> kg s <sup>-2</sup> K <sup>-1</sup> )
<i>RT</i>	room temperature
<i>sccm</i>	standard cubic centimeters (ccm/min)
<i>P3HT</i>	Poly(3-hexylthiophene-2,5-diyl) (MaDrix)
<i>PTB7</i>	polythieno[3,4- b ]-thiophene-co-benzodithiophene (1-Material)
<i>PCBM</i>	Phenyl-C61-butyric acid methyl ester (Solenne)
<i>PC70BM</i>	Phenyl-C70-butyric acid methyl ester (Solenne)
<i>MEH-PPV</i>	Poly[2-methoxy-5-(2-ethylhexyloxy)-1,4-phenylenevinylene]
<i>PEDOT:PSS</i>	Poly(3,4-ethylenedioxythiophene) polystyrene sulfonate
<i>Au</i>	Gold
<i>Ag</i>	Silver
<i>Pt</i>	Platinum
<i>Cu</i>	Copper
<i>MOD</i>	Metal-organic decomposition
<i>PET</i>	Polyethylene Terephthalate
<i>PI</i>	Polyimide
<i>H<sub>2</sub>O</i>	Water
<i>EG</i>	Ethylene Glycol
<i>DMSO</i>	Dimethyl sulfoxide
<i>DIO</i>	1,8-Diiodooctane
<i>AJ</i>	Aerosol Jet
<i>HOMO</i>	Highest Occupied Molecular Orbital
<i>LUMO</i>	Lowest Unoccupied Molecular Orbital
<i>BHJ</i>	Bulk-Heterojunction

### *List of Abbreviations*

<i>OPD</i>	Organic Photodiode
<i>OPV</i>	Organic Photovoltaic
<i>OFET</i>	Organic Field-Effect Transistor
<i>CVD</i>	Chemical Vapor Deposition
<i>WF</i>	Work Function
<i>IR</i>	Infrared
<i>SAM</i>	Self-Assembled Monolayer
<i>SPICE</i>	Simulation Program with Integrated Circuit Emphasis

# List of Figures

2.1.	The photon energy as a function of wavelength. . . . .	6
2.2.	Schematic of $sp_2$ hybridized C-atom. . . . .	7
2.3.	a) Schematic illustration of electronic configuration of an ethen molecule with covalently bound strong $\sigma$ - and weak $\pi$ bonds. b) Energy levels of ethen. . . . .	8
2.4.	a) Typical representative for a polymer donor with P3HT (Poly(3-hexylthiophene-2,5-diyl) and an acceptor fullerene with PCBM ([6,6]-Phenyl $C_{60}$ butyric acid methyl ester). b) Schematic drawing of a bulk-heterojunction solar cell, showing (1) the generation of the exciton and its subsequent charge separation at the donor-acceptor interface, (2) a geminate recombination process, and non-geminate recombination processes with (3) and (4). . . . .	9
2.5.	Band diagram of a bulk-heterojunction architecture, where an intermixed donor-acceptor blend provides a highly dispersed network of donor-acceptor interfaces, which allows for an improved charge separation. The absorption of a photon within the donor material excites an electron into the $LUMO_D$ . The bound exciton then diffuses to a donor-acceptor interface, where the electron is collected by the acceptor $LUMO_A$ . The separated charge carriers then drift to the corresponding electrodes to be extracted, which leads to a current flow. . . . .	10
2.6.	One-diode equivalent circuit for solar cells and photodiodes.[43] . . . . .	12
2.7.	Current-voltage ( $I$ - $V$ ) and power-voltage ( $P$ - $V$ ) characteristic of a solar cell. The hatched area accentuates the maximum extractable electrical power out of the cell. . . . .	14
2.8.	$I - V$ characteristic of a OPD illuminated with $P_0$ , half the energy $P_0/2$ , and in dark. . . . .	15
2.9.	External quantum efficiency (EQE) plot of a polymer:fullerene BHJ device.	16
2.10.	Spectral responsivity ( $SR$ ) plot of a polymer:fullerene BHJ device. . . . .	17
2.11.	Calculated specific detectivity ( $D^*$ ) plot of a polymer:fullerene BHJ device. (Eq. 2.16) . . . . .	18
2.12.	Signal response of a photodiode to an impinging $1\text{ ns}$ short light pulse. . . . .	19

LIST OF FIGURES

3.1.	Aerosol Jet Printing System (Optomec, AJ300) . . . . .	21
3.2.	Schematic of AJ printing system with ultrasonic atomizer section. . . . .	22
3.3.	Schematic of the nozzle orifice flow profile with contributions of the sheath and atomizer gas flows. (left) small flow ratio, (right) high flow ratio. (Reprinted from Binder <i>et al.</i> [58]) . . . . .	23
3.4.	Schematics of different sheath gas flows. a) Low sheath gas flow causing low turbulences at the substrate front. b) High sheath gas flow causing higher aspect ratio, but also increased turbulences. c) Exceeding sheath gas flow causing <i>overspray</i> due to turbulences at the orifice front . . . . .	24
3.5.	Microscope images of AJ printed nanoparticulate silver ink on glass of an a) moderate, b) high, and c) exceedingly high sheath-to-atomizer flow ratio. . . . .	25
3.6.	Cross-sectional line profiles as a function of the printing velocity and multi-passes. (Sheath and atomizer gas flow were kept constant during the experiment) . . . . .	25
3.7.	Test pattern with two approaching lines with and without rounded corners printed with nanoparticulate Ag ink on glass. a) Schematic of tool path. Microscope images of printing results with b) sharp corners printed at $5\text{ mm s}^{-1}$ , c) rounded corners printed at $5\text{ mm s}^{-1}$ , d) sharp corners printed at $10\text{ mm s}^{-1}$ , and e) rounded corners printed at $10\text{ mm s}^{-1}$ . . . . .	29
3.8.	Inkjet printer Dimatix Fujifilm DMP-2831 and cartridge. (Photos reprinted from <a href="http://www.fujifilmusa.com">www.fujifilmusa.com</a> ) . . . . .	29
3.9.	a) Example for a jetting waveform. b) Schematic drawing of a DoD inkjet nozzle comprising an ink reservoir, piezo electric actuators driven by an applied waveform, and an orifice with a defined diameter. . . . .	30
3.10.	Printability window of fluids and its relationship between the Weber and Reynolds number (reprinted from Derby <i>et al.</i> , 2010) [64] . . . . .	31
3.11.	Image of the Dimatix DMP-2800 drop watcher showing the ejection of droplets from the nozzles. . . . .	31
3.12.	a) Device without encapsulation foil, and b) with encapsulation foil. . . . .	31
4.1.	a) Image of a water droplet on Teflon. b) Image of a pendant drop hanging from a needle. . . . .	34
4.2.	4-wire electrode array for resistance measurements of thin films with a layer thickness $d$ . Current is applied at the outer pins and the voltage is measured at the inner pins. The array comprises equidistant pins with a spacing $s$ . . . . .	36
4.3.	EQE and bandwidth measurement setup. . . . .	38

4.4.	Pulse response of a photodiode with rise ( $t_r$ ) and fall ( $t_f$ ) time. The Fast-Fourier-Transform (FFT) reveals the signal (dB) as a function of frequency ( $f$ ) with the bandwidth $BW$ defined at $-3$ dB. . . . .	39
4.5.	Schematic drawing of transient photocurrent measurement setup using a 1.1 ns excitation laser pulse at 532 nm. The samples are mounted in a shielded probe station. The signal is measured by an oscilloscope. The reverse bias voltage is applied using a wavegenerator. . . . .	40
4.6.	Example of a geometrical layout for simulating a hybrid electrode comprising a hexagonal grid (blue). In each vertex the differential equations are solved according to the boundary conditions using the finite element method. . . . .	42
5.1.	Photograph of a P3HT:PCBM solar cell comprising AJ printed hexagonal Ag grids. . . . .	43
5.2.	Specific conductivity of spin-coated MOD Ag ink for different annealing temperatures and annealing durations. . . . .	44
5.3.	Thermo-gravimetric analysis (TGA) of MOD ink at $120^\circ\text{C}$ . . . . .	44
5.4.	SEM images of Aerosol Jet printed and subsequently annealed ( $120^\circ\text{C}$ ) Ag layers on glass a) from the MOD ink, and b) from a nano-particulate Ag ink (Cabot Ink). . . . .	45
5.5.	Line width and height of Aerosol Jet printed (AJP) Ag lines from MOD ink on PEDOT:PSS covered glass. The dashed lines are allometric and exponential fits to the line height, as well as an allometric fit to the line width. . . . .	46
5.6.	False color topography images of the line heights and cross-sectional profiles of AJP Ag lines at various printing speeds recorded with white light interferometry. . . . .	47
5.7.	Specific conductivity measurements of the diluted pristine MOD ink and the formulations with 10% additional co-solvent as a function of the additive's boiling point. The annealing temperature was set to $140^\circ\text{C}$ . The ambient conditions were varied with 10 min in air and 1 h in a vacuum oven. . . . .	47
5.8.	Specific conductivity measurements of the pristine MOD ink, annealed in air and under nitrogen ( $N_2$ ) atmosphere, at $120^\circ\text{C}$ , as a function of annealing time ( $t$ ). (data obtained with permission from Dr. A. Morfa, LTI, KIT) . . . . .	48
5.9.	Microscope images of AJ printed Ag lines at $5\text{ mm s}^{-1}$ . without co-solvent (#1), with 10% toluene (#2), 10% anisole (#3), and 10% ethylene glycol (EG) (#4). (Scale bar $20\ \mu\text{m}$ ) . . . . .	48
5.10.	Specific conductivity of MOD ink as a function of anisole fraction. . . . .	48

## LIST OF FIGURES

5.11. Transmittance spectra of a $\sim 160$ nm thick PEDOT:PSS TC, a Ag grid with a symmetry radius $r_{sym}$ of $200 \mu\text{m}$ and $\sim 30 \mu\text{m}$ wide lines, and the hybrid electrode with Ag grid and PEDOT:PSS layer. . . . .	50
5.12. Transmittance spectra of hybrid electrodes with an Ag grid symmetry radius $r_{sym}$ of $200 \mu\text{m}$ and line width $w$ of $\sim 25 \mu\text{m}$ comprising different PEDOT:PSS layer thicknesses by different spin speeds. . . . .	50
5.13. Microscope images and transmittance spectra of 1-dimensional, 2-dimensional (squared), and hexagonal AJ printed Ag grids printed on a $100$ nm thick highly conductive PEDOT:PSS (PH1000) covered glass substrate with symmetry radii of $100 \mu\text{m}$ . . . . .	50
5.14. Microscope images and transmittance spectra of 1-dimensional, 2-dimensional, and hexagonal AJ printed Ag grids printed on a $100$ nm thick highly conductive PEDOT:PSS (PH1000) covered glass substrate with symmetry radii of $200 \mu\text{m}$ . . . . .	51
5.15. Microscope images and transmittance spectra of 1-dimensional, 2-dimensional, and hexagonal AJ printed Ag grids printed on a $100$ nm thick highly conductive PEDOT:PSS (PH1000) covered glass substrate with symmetry radii of $400 \mu\text{m}$ . . . . .	51
5.16. Mechanical stability measurements using an automated resistivity measurement as a function of bending cycles. a) Schematic drawing of measurement setup. b) Fatigue tests: Calculated lateral strain $\Delta\varepsilon$ in % as a function of number of bending cycles $N_f$ . [86] . . . . .	53
5.17. Mechanical stability measurements using an automated resistivity measurement as a function of elongation. a) Fatigue tests: Increase in resistivity in % as a function of lateral strain in %. b) SEM images of during elongation showing the PET/PEDOT:PSS/Ag sample at 6 %, 12 %, and 20 %. [86] . . . . .	54
5.18. a) Schematics of an inverted organic solar cell stack comprising an ITO/ZnO cathode on a glass substrate, P3HT:PCBM active layer, and the conductive PEDOT:PSS/Ag-grid top anode. b) Substrate layout comprising a structured ITO electrode. The dashed rectangles illustrate the shape of the top contact, where the overlap of the ITO and the top contact form the active area. c) Energy levels of the different materials with corresponding values for metal work functions, HOMO, LUMO, conduction and valence bands. . . . .	56
5.19. a) Photograph of a substrate containing a PEDOT:PSS reference pixel, and hybrid electrodes with 1-dimensional, 2-dimensional, and hexagonal grids ( $r_{sym} = 400 \mu\text{m}$ ). b) Photograph of a semi-transparent OSC in front of a KIT-logo. . . . .	57

5.20. a) J-V characteristics of top illuminated inverted P3HT:PCBM solar cells comprising a conductive PEDOT:PSS top electrode as reference, and AJ printed 1-dimensional Ag grids with symmetry radii of  $r_{sym} = 50, 100$  and  $200 \mu\text{m}$ . b) Plot of  $dV/dI$  as a function of  $(I_{SC} + I - V/R_{sh})^{-1}/(k_B T/q)$ , where  $R_s$  can be extracted from the intersect of a linear fit with the y-axis (red dot). . . . . 57

5.21. J-V characteristics of top illuminated inverted P3HT:PCBM solar cells comprising a conductive PEDOT:PSS top electrode as reference, and AJ printed 1-dimensional Ag grids with symmetry radii of  $r_{sym} = 50, 100$  and  $200 \mu\text{m}$ . b) Plot of  $dV/dI$  as a function of  $(I_{SC} + I - V/R_{sh})^{-1}/(k_B T/q)$ , where  $R_s$  can be extracted from the intersect of a linear fit with the y-axis (red dot). . . . . 58

5.22. a) J-V characteristics of bottom illuminated inverted P3HT:PCBM solar cells with a PEDOT:PSS reference, and AJ printed 1-dimensional, 2-dimensional, and hexagonal Ag grids with symmetry radii of  $r = 400 \mu\text{m}$ . b) Plot of  $dV/dI$  as a function of  $(I_{SC} + I - V/R_{sh})^{-1}/(k_B T/q)$ , where  $R_s$  can be extracted from the intersect of a linear fit with the y-axis. . . . 59

5.23. Light beam induced current measurements (LBIC) of organic P3HT:PCBM solar cells comprising a hybrid top electrode with an AJ printed hexagonal grid. . . . . 60

5.24. Example of an OPV (comprising a hexagonal grid) device modeling with anode and cathode contacts on opposing sides (left and right). The false-color code and the isolines represent the electrical potential in the hybrid TC at 0 V. . . . . 61

5.25. Physical model of a solar cell with top hybrid TC and bottom electrode linked by an OPV equivalent circuit for illuminated and shaded areas. (reprinted from master thesis Jan Preinfalk 2013) . . . . . 62

5.26. Grid geometries. a) 1-dimensional, and b) hexagonal. . . . . 64

5.27. COMSOL device simulations of  $1 \text{ cm}^2$  large solar cells comprising a) one  $100 \mu\text{m}$  wide and b) nine  $11 \mu\text{m}$  wide Ag lines. The false-color code illustrates the voltage potential distribution over the area. . . . . 64

5.28. a) Sheet resistance  $R_{sheet,M}$  and transmittance  $T$  of a 1-dimensional hybrid TC as a function of the symmetry radius  $r_{sym}$ . b) Voltage and power in the maximum power point of simulated solar cells as a function of  $r_{sym}$ . The line width  $w$  was fixed to  $100 \mu\text{m}$ . . . . . 65

5.29. Transmittance of 1-dimensional and hexagonal grid symmetries for different  $w$  as a function of  $r_{sym}$ . . . . . 65

5.30. Dependencies between line width  $w$  and symmetry radius  $r_{sym}$  for fixed transparencies in a) 1-dimensional, and b) hexagonal hybrid TCs. These dependencies are independent of the effective sheet resistance. . . . . 66

LIST OF FIGURES

5.31. 1-dimensional hybrid TC: Influence of symmetry radius  $r_{sym}$ , PEDOT:PSS conductivity  $\sigma_{PEDOT:PSS}$  and  $R_{sheet,M}$  on the normalized device efficiency  $\eta$ . (Boundary conditions:  $J = 15 \text{ mA cm}^{-2}$ ,  $T = 90 \%$ ) . . . . . 67

5.32. Influence of  $r_{sym}$ ,  $\sigma_{PEDOT:PSS}$ , and  $T$  on the normalized device efficiency  $\eta$  in hybrid TCs comprising a) 1-dimensional, and b) hexagonal grids. PEDOT:PSS layer thickness was set to 100 nm, and  $R_{sheet,M}$  to  $10 \Omega/\square$ . . . . . 67

5.33. a) 1-dimensional hybrid TCs: Normalized efficiency  $\eta$  reduced to the influencing parameter  $r_{sym}$  (transparency neglected) for different  $R_{sheet,M}$  and different  $\sigma_{PEDOT:PSS}$ . b) Influence of grid geometry (1-dimensional vs. hexagonal) and  $\sigma_{PEDOT:PSS}$  on the normalized efficiency  $\eta$  as a function of line width  $w$  (left) and symmetry radius  $r_{sym}$  (right).  $R_{sheet,M}$  and  $T$  were set to  $10 \Omega/\square$  and 95 %, respectively. . . . . 68

5.34. Influence of current density  $J$  on the normalized device efficiency as a function of  $r_{sym}$ . ( $T = 95 \%$ ,  $R_{sheet,M} = 10 \Omega/\square$ ,  $\sigma_{PEDOT:PSS} = 850 \text{ S cm}^{-1}$ ) . . . . . 69

6.1. Schematic drawing and photograph of an AJ printed organic photodiode comprising two polymeric PEDOT:PSS electrodes, an aluminum doped zinc oxide (AZO) electron extraction layer, and the PTB7:PC70BM active layer blend. . . . . 71

6.2. Influence of printing speed on sequentially printed PTB7:PC70BM layers (10 g/L DCB + 2.5 % DIO) on ITO covered glass, where the number of passes were adjusted to keep the deposited ink volume constant for all samples. (sh/atm: 10/17 sccm, tube T./platen T.:  $60^\circ \text{ C}/22^\circ \text{ C}$ ). The images show areas of  $255 \mu\text{m} \times 160 \mu\text{m}$ . The scale bars are valid only for the surface profiles. . . . . 72

6.3. Topography ( $255 \mu\text{m} \times 190 \mu\text{m}$ ) and line series profile measurements (left side of the topography image) of AJ printed PTB7:PC70BM layers using different flow ratios for sheath (sh) and atomizer (atm) gas flows. The scale bars are valid only for the surface profiles. . . . . 73

6.4. Infrared spectroscopy of spin cast (SC) PTB7, SC and AJ printed PTB7:PC70BM blends, and SC PC70BM layers on silicon wafer. . . . . 74

6.5. a) Schematic drawing of the device stack and b) photograph of fully AJ printed devices with c) the corresponding energy levels of the different materials. . . . . 75

6.6. Structuring process of ITO covered PET foil by using inkjet printed PMMA (orange) as etching mask. . . . . 76

6.7. a) Topography image ( $243 \mu\text{m} \times 191 \mu\text{m}$ ) and profile series and b) AFM topography image ( $10 \mu\text{m} \times 10 \mu\text{m}$ ) of an AJ printed Al-doped ZnO layer on ITO covered glass. . . . . 76

6.8.	Photograph of organic photodiode samples comprising different active layer thicknesses fabricated by multi-pass printing. . . . .	76
6.9.	a) Dark current densities recorded for OPDs comprising different PTB7:PC70BM layer thicknesses. b) Dark current density at $-1 V$ reverse bias as a function of layer thickness. . . . .	77
6.10.	Dark current density as a function of the calculated effective electric field. . . . .	77
6.11.	a) Transmittance spectra recorded for OPDs comprising different PTB7:PC70BM layer thicknesses with 1 to 4 consecutively printed passes. b) Transmittance at 550 nm wavelength as a function of layer thickness. . . . .	78
6.12.	Transmission spectra of active layers with PEDOT:PSS top electrode and completed and encapsulated Device A (black) and Device B (green). . . . .	78
6.13.	a) Transmission spectra of active layers with PEDOT:PSS top electrode and completed and encapsulated Device A (black) and Device B (green). b) Corresponding dark current densities. . . . .	78
6.14.	Spectral responsivity and external quantum efficiency of ITO comprising Device A (black) and Device B (green) recorded at $-1 V$ (circle), $-2 V$ (triangle), and $-3 V$ (rhomb) reverse bias. . . . .	79
6.15.	Calculated specific detectivity for the ITO comprising AJ printed OPDs Device A (black) and Device B (green) recorded at $-1 V$ (circle), $-2 V$ (triangle), and $-3 V$ (rhomb) reverse bias. . . . .	79
6.16.	Transient photo current measurements for a) Device A and b) Device B and c) the corresponding FFT of the normalized signal as a function of frequency. . . . .	80
6.17.	Photograph of fully AJ printed semi-transparent OPDs comprising active areas of $1 \text{ mm}^2$ . The sample shows two different thicknesses of the active material. . . . .	81
6.18.	a) Schematic device architecture and b) photograph of fully AJ printed devices with c) the corresponding energy levels of the different materials. . . . .	81
6.19.	a) Inkjet printed Ag contact pads on PET. b) PET stripe comprising several fully AJ printed OPDs. . . . .	81
6.20.	AJ printed PEDOT:PSS stripe on PET foil. a) Topography and b) surface profile . . . . .	82
6.21.	Transmission spectra of the active layer including the PEDOT:PSS top electrode, and the encapsulated device. . . . .	82
6.22.	Dark current density of a fully AJ printed semi-transparent OPD. . . . .	82
6.23.	Spectral responsivity (SR) measured at sample illuminated through a) top electrode and b) bottom electrode. . . . .	83

LIST OF FIGURES

6.24. External quantum efficiency (EQE) measured at sample illuminated through a) top electrode and b) bottom electrode. . . . . 83

6.25. AFM image with a) topography and b) phase of a AJ printed PTB7:PC70BM layer. . . . . 83

6.26. Specific detectivity  $D^*$  recorded for a) top and b) bottom illuminated sample. . . . . 84

6.27. a) Photograph of an OPD bended at a radius of 2 mm. b) Delamination of the encapsulation foil as a consequence of further reduction of the bending radius. . . . . 84

6.28. a) SR and EQE (at  $-3$  V) recorded before and during bending of the fully AJ printed OPD with a radius of 2 mm. b) corresponding  $D^*$ . . . . . 84

6.29. a) Current signal measured at different reverse bias voltages of the ITO-free OPD after an excitation with a 1 ns laser pulse. b) Fast-Fourier-Transform of the time signal into the frequency spectrum. The cut-off frequency can be derived at  $-3$  dB. . . . . 85

6.30. Specific detectivity of common inorganic photodetectors and the AJ printed OPD (red) in comparison to them. (Adapted and reprinted from <http://http://www.azooptics.com>) . . . . . 86

7.1. Fully printed flexible photodiode array comprising 36 pixel with dimensions of  $45 \times 175 \mu\text{m}^2$ . . . . . 87

7.2. Schematic drawing of the patterning process of Ag electrodes. . . . . 88

7.3. a) Image sequence over time showing the self-organization of a brushed Ag ink on an SU-8 patterned PET substrate. b) Magnification of the annealed Ag finger structures. . . . . 88

7.4. Inkjet printed Ag stripe across two AJ printed  $11 \mu\text{m}$  wide SU-8 lines on a PET substrate. . . . . 88

7.5. Image of Ag ink droplets on a) PET and b) SU-8 surfaces showing contact angles of  $\sim 20^\circ$  and  $\sim 43^\circ$ , respectively. . . . . 89

7.6. Illustration of the reduced fluid volume on patterned substrates comprising lyophilic (blue) and lyophobic (orange) stripes of the width  $L_1$  and  $L_D$ , respectively, where the dashed cube represents the nominal volume  $L_1^3$ .  $V/L_1^3$  [136] . . . . . 90

7.7. a) Schematic illustration of the actual area,  $A_{act}$ , (green) of an SU-8 line and the projected area  $A_{proj}$  (red). b) Cross-section of an AJ printed SU-8 line (dashed) and a parabolic fit (blue). . . . . 90

7.8. Images of inkjet printed Ag ink (dark areas) with a drop spacing of  $50 \mu\text{m}$  on PET substrate, comprising a)  $65 \mu\text{m}$ , b)  $50 \mu\text{m}$ , and c)  $25 \mu\text{m}$  gaps between the SU-8 lines (bright areas). . . . . 91

7.9. Cross-sectional profile of inkjet printed Ag ink on top of an SU-8 patterned PET substrate. SU-8 lines are colored in red, the wet Ag film in light grey, and the dried Ag film in dark grey. . . . .	91
7.10. Examples of dewetting Ag structures showing square, ring and spiral patterns with a) image directly recorded after Ag deposition via inkjet, microscope image recorded after annealing the Ag ink, and 3D topographies. b) Extracted line profiles of the corresponding patterns. . . . .	92
7.11. a) schematic drawing of the experimental assembly. The solvent droplet of $2\ \mu\text{L}$ is deposited on the SU-8/PET step edge. In case of dewetting, the droplet moves towards the PET. b) Image sequence over time of the experiment using Ag ink. c) Examples of a solvent showing no effect (left), partly dewetting (center), and fully dewetting (right). . . . .	92
7.12. a) Total, polar, and dispersive surface tensions of water:methanol mixtures blended in various ratios $\chi_{MeOH}$ . b) Wetting envelopes of PET and SU-8 surfaces and complex surface tensions of solvents and $H_2O:MeOH$ blends. Circles represent a proper dewetting, while triangles represent no or insufficient dewetting from the SU-8. . . . .	93
7.13. a) Wetting envelopes of PET, $O_2$ plasma treated, and SU-8 surfaces and complex surface tensions of solvents and $H_2O:MeOH$ blends. Circles represent a proper dewetting, while triangles represent no or insufficient dewetting from the SU-8. b) Total surface energies split in polar and dispersive parts for PET, $O_2$ plasma treated PET, glass, polyimide (PI), and SU-8. . . . .	94
7.14. Blade coating of Ag ink on top of SU-8 patterned PET foil using an <i>Erichsen Coatmaster 510</i> . a) Image recorded during coating process. b) Image recorded after SU-8 structures were dewetted ( $\sim 1\ \text{min}$ ). . . . .	95
7.15. Spray coating of Ag ink using an airbrush on top of an SU-8 patterned PET foil. a) Image recorded during spray coating process. b) Image recorded directly after finishing the coating process. . . . .	95
7.16. Schematic drawing of a photodetector pixel comprising an Ag back-electrode fabricated by the introduced dewetting technique. The Ag electrode was inkjet printed, while all subsequently printed layers were AJ printed. . . .	96
7.17. a) Self-organized Ag electrodes on SU-8 patterned PET foil. b) Completed organic photodiodes with PTB7:PC70BM active material and a transverse highly conductive PEDOT:PSS anode stripe. The magnification shows one single pixel with a size of $175 \times 45\ \mu\text{m}^2$ . . . . .	97
7.18. 3D topography image of an OPD pixel recorded with a confocal microscope (Neox PLu, Sensofar, 50x, Ap. 0.95). . . . .	97

LIST OF FIGURES

7.19. a)  $J$ - $V$  Characteristics of a PTB7:PC70BM OPD pixel under different illumination intensities ranging from  $0.1 \text{ mW cm}^{-2}$  to  $100 \text{ mW cm}^{-2}$ . b) Current density over optical intensity and responsivity  $R$  at  $-1 \text{ V}$  and  $-2 \text{ V}$  bias. . . . . 97

7.20. Photograph of a fully printed OPD array with 256 pixel. . . . . 99

7.21. Photograph of patterned Ag back-electrodes on glass (left) and height profile measured with confocal microscopy, Sensofar Neox (right). . . . . 99

7.22. Microphaph of a an Ag/ZnO/PTB7:PC70BM/PEDOT:PSS OPD array. . . 99

7.23. a)  $J - V$  characteristics measured at a single pixel under different illumination intensities and in dark. b) log-log plot current density as a function of the light intensity  $I$ . . . . . 100

7.24. a) Spectral responsivity ( $SR$ ) and b) external quantum efficiency ( $EQE$ ) of a masked OPD pixel. . . . . 100

7.25. a) Specific detectivity  $D^*$  calculated from the  $SR$  and  $J_d$  of the OPD pixel. b) Comparison of  $D^*$  with inorganic silicon based photodetectors. . . . . 100

7.26. Signal response ( $S$ ) in normalized dB to a modulated rectangular light signal measured at frequencies from 20 to  $500k \text{ Hz}$ . . . . . 101

7.27. Schematic drawing and photograph of a home-built Arduino based passive matrix read-out system. The pixels are sequentially addressed by transistor circuits and then amplified using an external transimpedance amplifier (FEMTO). The amplified signal is then digitized with an ADC and transmitted to a computer. . . . . 101

7.28. a) Mapping of the digitized signal of the sequentially read-out OPD pixels in dark and under light intensities of  $0.1$ ,  $1$ , and  $10 \text{ mW/cm}^2$  and b) the corresponding digitized average signal and standard deviations. . . . . 101

7.29. Schematic and pixel map of a signal pixel excitation: Illumination of a single pixel by shading only the active area except for one pixel. . . . . 102

7.30. Schematic and pixel map of a signal pixel excitation: Illumination of a single pixel by shading the active area, the feed lines and the contact pads. 102

7.31. Schematic and pixel map of a signal pixel excitation: Illumination of a single pixel by a) shading the active area, the feed lines and the contact pads, and additionally the backside. . . . . 102

7.32. LBIC measurements recorded for  $5 \times 14$  pixel at an illumination intensity of  $1.23 \text{ mW/cm}^2$  and a mapping resolution and spot diameter of  $40 \mu\text{m}$ . . 102

7.33. Schematic drawing of an OFET comprising a channel length defined by the SU-8 line width. . . . . 104

7.34. a) Photograph of a PET substrate covered with 48 S/D finger structures. b) Magnification of two S/D structures, where the dark lines depict the SU-8 pattern. c) Photograph of completed OFETs with three inkjet printed top gate contacts. . . . . 104

7.35. OFETs with digitally patterned and SAM treated S/D electrodes. a) Output I–V characteristics. b) Transfer I–V characteristics. . . . . 105

7.36. Circuit diagram of a 3-stage unipolar ring oscillator. . . . . 105

7.37. (left) Photograph of a PET substrate comprising two ring oscillators and each 10 single load and drive transistors above. (right) magnification of a drive transistor with a 40 mm and a load transistor with a 0.4 mm channel width. . . . . 106

7.38. a) Transfer characteristics of a drive and a load transistor. b) Corresponding gate leakage derived at  $V_{Drain} = 30 V$ . . . . . 106

7.39. Transconductance of drive and load transistors. . . . . 106

7.40. Transfer characteristics measured at  $V_D = 30 V$  for a) 8 different load transistors , and b) of 8 different drive transistors. (red curve = average) . 107

7.41. a) Oscillating output signal at different DC input voltages  $V_{DD}$ . b) Oscillation frequency at different  $V_{DD}$  measured over a period of 87 days. . . . . 107

A.1. AFM image with topography and phase of AJ printed PTB7:PC70BM layers. . . . . 115

A.2. Intensity dependent current density measurements at a)  $-1 V$ , b)  $-2 V$ , and c)  $-3 V$  reverse bias voltages for red, green, and blue LED light sources. . . . . 116

B.1. AFM image of an AJ printed SU-8 line back. . . . . 117

B.2. a) AJ printed split ring resonator and RF slot antenna structures with inkjet printed Ag areas on polyimide (PI). b) Ring structures for THz applications printed on  $1.4 \mu m$  tick PET foil (left) and on  $175 \mu m$  thick PET (right) covered with subsequently inkjet printed Ag ink. c) AJ printed SU-8 lines on FR-4 (printed circuit board) comprising dewetted brushed Ag ink. . . . . 118

B.3. SPICE model of a 3-stage + buffer stage ring oscillator (top) and equivalent circuit including parasitic effects of an OFET. (bottom). . . . . 118

B.4. Ring oscillator layout: a) SU-8 tool path with dewetting pattern for S/D Ag layer. b) The light grey area depicts the coarse inkjet pattern for the Ag deposition. c) The dark grey area depicts the final gate layer, where the green dots highlight the through-contacts to the bottom S/D layer. . . . . 119



# List of Tables

5.1.	MOD ink (PR-010, Inktec) ingredients extracted from the MSDS . . . . .	46
5.2.	AJ printing parameter set for MOD:ethanol ink formulation. . . . .	47
5.3.	Specific conductivities $\sigma_{Ag}$ for annealed Ag layers at 140 °C on a hotplate (hp) for 10 min and in a vacuum oven (vac) for 1 h. Surface roughness $r_{rms}$ of $20 \times 20 \mu\text{m}^2$ areas of AJ printed Ag lines. . . . .	48
5.4.	Sheet resistances measured at $1 \times 1 \text{ cm}^2$ AJ printed 1-dimensional, 2-dimensional, and hexagonal Ag grids from formulation #3. Grids printed at $5 \text{ mms}^{-1}$ with a line width of $\sim 20 \mu\text{m}$ . . . . .	52
5.5.	Material list of different electrode systems. . . . .	54
5.6.	Device efficiency $\eta$ , fill factor $FF$ and series resistance $R_s$ of P3HT:PCBM solar cells comprising 1-dimensional hybrid TCs. . . . .	58
5.7.	Device efficiency $\eta$ , fill factor $FF$ and series resistance $R_s$ of P3HT:PCBM solar cells comprising hexagonal hybrid TCs. . . . .	59
5.8.	Characteristic device parameter extracted from the $J - V$ characteristics of inverted OSCs comprising solution processed top electrodes with PEDOT:PSS and printed Ag grids. (* value could not be determined by the described method and was therefore calculated by the slope at $\sim 0.9 \text{ V}$ ) . . . . .	60
5.9.	Physical parameter of the diode equation. . . . .	63
5.10.	Parameters for line width $w$ and symmetry radius $r_{sym}$ with respect to the grid geometry and different $T$ . . . . .	66
5.11.	Line heights for 1-dimensional and hexagonal symmetries with different $T$ , adjusted to the desired $R_{sheet,M}$ . Values were revealed from FEM simulations. . . . .	67
6.1.	Rms roughness $r$ of areas of $255 \mu\text{m} \times 190 \mu\text{m}$ AJ printed PTB7:PC70BM layers for different printing velocities and printing repetitions at constant atomizer to sheath gas flow of 10 sccm to 17 sccm, and different atomizer gas flow rates . . . . .	72
6.2.	Specification list of ITO comprising AJ printed OPDs recorded at $-3 \text{ V}$ reverse bias. Maximum Detectivity $D^*$ also given at $-1 \text{ V}$ . . . . .	79

*LIST OF TABLES*

6.3. Dynamic Analysis of ITO comprising OPDs with different active layer thicknesses. . . . . 80

6.4. Specification list of ITO-free AJ printed OPDs. . . . . 85

6.5. Device characteristics of ITO free AJ printed OPDs extracted from transient measurements at different reverse bias voltages. . . . . 85

7.1. Summary of surface tensions ( $\sigma$ ) including polar ( $\sigma^P$ ) and dispersive part ( $\sigma^D$ ), vapor pressure ( $p$ ), boiling point ( $T_{bp}$ ), and viscosity ( $\eta$ ) for different solvents and the Ag NP ink. Additionally, surface energies for PET, plasma treated PET, and SU-8 (2025 Series). . . . . 94

# Bibliography

- [1] Alan J Heeger. 25th Anniversary Article: Bulk Heterojunction Solar Cells: Understanding the Mechanism of Operation. *Adv. Mater.*, 26(1):10–28, jan 2014.
- [2] B. Kraabel, C.H. Lee, D. McBranch, D. Moses, N.S. Sariciftci, and A.J. Heeger. Ultrafast photoinduced electron transfer in conducting polymer—buckminsterfullerene composites. *Chem. Phys. Lett.*, 213(3-4):389–394, oct 1993.
- [3] Gang Yu, Jun Gao, Jan C Hummelen, Fred Wudl, and Alan J Heeger. Polymer photovoltaic cells: Enhanced efficiencies via a network of internal donor-acceptor heterojunctions. *Science (80-. )*, 270(5243):1789, dec 1995.
- [4] Ji Sun Moon, Jae Kwan Lee, Shinuk Cho, Jiyun Byun, and Alan J Heeger. “Columnlike” Structure of the Cross-Sectional Morphology of Bulk Heterojunction Materials. *Nano Lett.*, 9(1):230–234, jan 2009.
- [5] Jin Young Kim, Kwanghee Lee, Nelson E Coates, Daniel Moses, Thuc-Quyen Nguyen, Mark Dante, and Alan J Heeger. Efficient tandem polymer solar cells fabricated by all-solution processing. *Science (80-. )*, 317(5835):222–225, 2007.
- [6] H M Nur, J H Song, J R G Evans, and M J Edirisinghe. Ink-jet printing of gold conductive tracks. *J. Mater. Sci. Mater. Electron.*, 13(4):213–219, 2002.
- [7] Jolke Perelaer, Antonius W M de Laat, Chris E Hendriks, and Ulrich S Schubert. Inkjet-printed silver tracks: low temperature curing and thermal stability investigation. *J. Mater. Chem.*, 18(27):3209–3215, 2008.
- [8] Jolke Perelaer, Patrick J Smith, Dario Mager, Daniel Soltman, Steven K Volkman, Vivek Subramanian, Jan G Korvink, and Ulrich S Schubert. Printed electronics: the challenges involved in printing devices, interconnects, and contacts based on inorganic materials. *J. Mater. Chem.*, 20(39):8446–8453, 2010.
- [9] Xuan Wang, Linjie Zhi, and Klaus Müllen. Transparent, conductive graphene electrodes for dye-sensitized solar cells. *Nano Lett.*, 8(1):323–327, 2008.
- [10] Jung-Yong Lee, Seung-Bum Rim, Whitney Gaynor, Steve T. Connor, Brian E. Hardin, Han Sun Kim, Yi Cui, Michael D. McGehee, and Peter Peumans. Transparent and tandem solar cells using solution-processed metal nanowire transparent electrodes. *2009 34th IEEE Photovolt. Spec. Conf.*, pages 002200–002203, jun 2009.

## BIBLIOGRAPHY

- [11] Alexander Kamyshny and Shlomo Magdassi. Conductive Nanomaterials for Printed Electronics. *Small*, 10(17):3515–3535, 2014.
- [12] Shlomo Magdassi, Michael Grouchko, Oleg Berezin, and Alexander Kamyshny. Triggering the sintering of silver nanoparticles at room temperature. *ACS Nano*, 4(4):1943–1948, 2010.
- [13] J Y Kim, J H Jung, D E Lee, and Jinsoo Joo. Enhancement of electrical conductivity of poly (3, 4-ethylenedioxythiophene)/poly (4-styrenesulfonate) by a change of solvents. *Synth. Met.*, 126(2):311–316, 2002.
- [14] S Timpanaro, Martijn Kemerink, F J Touwslager, M M De Kok, and S Schrader. Morphology and conductivity of PEDOT/PSS films studied by scanning–tunneling microscopy. *Chem. Phys. Lett.*, 394(4):339–343, 2004.
- [15] Xavier Crispin, F L E Jakobsson, Annica Crispin, P C M Grim, Peter Andersson, A Volodin, Christian Van Haesendonck, Mark Van der Auweraer, William R Salaneck, and Magnus Berggren. The origin of the high conductivity of poly (3, 4-ethylenedioxythiophene)-poly (styrenesulfonate)(PEDOT-PSS) plastic electrodes. *Chem. Mater.*, 18(18):4354–4360, 2006.
- [16] Joshua Lessing, Ana C Glavan, S Brett Walker, Christoph Keplinger, Jennifer A Lewis, and George M Whitesides. Inkjet Printing of Conductive Inks with High Lateral Resolution on Omniphobic “RF Paper” for Paper-Based Electronics and MEMS. *Adv. Mater.*, 26(27):4677–4682, 2014.
- [17] Antonino Scandurra, Giuseppe Francesco Indelli, Noemi Graziana Spartà, Francesco Galliano, Sebastiano Ravesi, and Salvatore Pignataro. Low-temperature sintered conductive silver patterns obtained by inkjet printing for plastic electronics. *Surf. Interface Anal.*, 42(6-7):1163–1167, 2010.
- [18] Lakshminarayana Polavarapu, Kiran Kumar Manga, Hanh Duyen Cao, Kian Ping Loh, and Qing-Hua Xu. Preparation of conductive silver films at mild temperatures for printable organic electronics. *Chem. Mater.*, 23(14):3273–3276, 2011.
- [19] H Hofstraat. Will polymer electronics change the electronics industry?, 2001.
- [20] Beatrice Guerrier, Charles Bouchard, Catherine Allain, and Christine Benard. Drying kinetics of polymer films. *AIChE J.*, 44(4):791–798, 1998.
- [21] Dechan Angmo, Thue T Larsen-Olsen, Mikkel Jørgensen, Roar R Søndergaard, and Frederik C Krebs. Roll-to-Roll Inkjet Printing and Photonic Sintering of Electrodes for ITO Free Polymer Solar Cell Modules and Facile Product Integration. *Adv. Energy Mater.*, 3(2):172–175, 2013.
- [22] A Falco, A M Zaidi, P Lugli, and A Abdellah. Spray deposition of Polyethyleneimine thin films for the fabrication of fully-sprayed organic photodiodes. *Org. Electron.*, 23:186–192, 2015.

- [23] Ralph Eckstein, Tobias Rödlmeier, Tobias Glaser, Sebastian Valouch, Ralf Mauer, Uli Lemmer, and Gerardo Hernandez-Sosa. Aerosol-Jet Printed Flexible Organic Photodiodes: Semi-Transparent, Color Neutral, and Highly Efficient. *Adv. Electron. Mater.*, 1(8):1500101, 2015.
- [24] Albert Einstein and Leopold Infeld. *The evolution of physics: The growth of ideas from early concepts to relativity and quanta*. CUP Archive, re-issued edition, 1971.
- [25] Albert Einstein. The photoelectric effect. *Ann. Phys*, 17(132):4, 1905.
- [26] Holger Spanggaard and Frederik C. Krebs. A brief history of the development of organic and polymeric photovoltaics. *Sol. Energy Mater. Sol. Cells*, 83(2-3):125–146, jun 2004.
- [27] H Kallmann and M Pope. Photovoltaic effect in organic crystals. *J. Chem. Phys.*, 30(2):585–586, 1959.
- [28] H Kallmann and M Pope. Positive hole injection into organic crystals. *J. Chem. Phys.*, 32(1):300–301, 1960.
- [29] Peter Würfel. *Physik der Solarzellen*. Spektrum, Akad. Verlag, 1995.
- [30] Edward A. Silinsh and Vladislav Capek. Organic molecular crystals: interaction, localization and transport phenomena. *Acta Cryst*, 53:855, 1997.
- [31] Christian Uhrich. Strategien zur Optimierung organischer Solarzellen: dotierte Transportschichten und neuartige Oligothiophene mit reduzierter Bandluecke, 2008.
- [32] Wolfgang Brutting and Walter Rie. Grundlagen der organischen Halbleiter. *Phys. J.*, 7(5):33, 2008.
- [33] Martin Pope and Charles E Swenberg. Electronic processes in organic solids. *Annu. Rev. Phys. Chem.*, 35(1):613–655, 1984.
- [34] Brian A Gregg and Mark C Hanna. Comparing organic to inorganic photovoltaic cells: Theory, experiment, and simulation. *J. Appl. Phys.*, 93(6):3605–3614, 2003.
- [35] Oleksandr V Mikhnenko, Paul W M Blom, and Thuc-Quyen Nguyen. Exciton diffusion in organic semiconductors. *Energy Environ. Sci.*, 8(7):1867–1888, 2015.
- [36] H Bassler. Charge transport in disordered organic photoconductors a Monte Carlo simulation study. *Phys. status solidi*, 175(1):15–56, 1993.
- [37] J Takeya, Mf Yamagishi, Y Tominari, R Hirahara, Y Nakazawa, T Nishikawa, T Kawase, T Shimoda, and S Ogawa. Very high-mobility organic single-crystal transistors with in-crystal conduction channels. *Appl. Phys. Lett.*, 90(10):102120, 2007.
- [38] Harold W Kroto, James R Heath, Sean C O’Brien, Robert F Curl, and Richard E Smalley. C 60: buckminsterfullerene. *Nature*, 318(6042):162–163, 1985.

## BIBLIOGRAPHY

- [39] Gang Li, Vishal Shrotriya, Yan Yao, and Yang Yang. Investigation of annealing effects and film thickness dependence of polymer solar cells based on poly (3-hexylthiophene). *J. Appl. Phys.*, 98(4):43704, 2005.
- [40] Gang Li, Yan Yao, Hoichang Yang, Vishal Shrotriya, Guanwen Yang, and Yang Yang. "Solvent Annealing" Effect in Polymer Solar Cells Based on Poly (3-hexylthiophene) and Methanofullerenes. *Adv. Funct. Mater.*, 17(10):1636–1644, 2007.
- [41] Minze T Rispens, Auke Meetsma, Roman Rittberger, Christoph J Brabec, N Serdar Sariciftci, and Jan C Hummelen. Influence of the solvent on the crystal structure of PCBM and the efficiency of MDMO-PPV: PCBM plastic solar cells. *Chem. Commun.*, 17:2116–2118, 2003.
- [42] William Shockley and Hans J Queisser. Detailed balance limit of efficiency of p-n junction solar cells. *J. Appl. Phys.*, 32(3):510–519, 1961.
- [43] Javier Cubas, Santiago Pindado, and Carlos de Manuel. Explicit expressions for solar panel equivalent circuit parameters based on analytical formulation and the Lambert W-function. *Energies*, 7(7):4098–4115, 2014.
- [44] Chunfu Zhang, Jincheng Zhang, Yue Hao, Zhenhua Lin, and Chunxiang Zhu. A simple and efficient solar cell parameter extraction method from a single current-voltage curve. *J. Appl. Phys.*, 110(6):64504, 2011.
- [45] F Capasso, W T Tsang, A L Hutchinson, and G F Williams. Enhancement of electron impact ionization in a superlattice: A new avalanche photodiode with a large ionization rate ratio. *Appl. Phys. Lett.*, 40(1):38–40, 1982.
- [46] R. B. Emmons. Avalanche-Photodiode Frequency Response. *J. Appl. Phys.*, 38(9):3705, 1967.
- [47] Gerardo Hernandez-Sosa, Nelson. E Coates, Sebastian Valouch, and Daniel Moses. High Photoconductive Responsivity in Solution-Processed Polycrystalline Organic Composite Films. *Adv. Funct. Mater.*, 21(5):927–931, mar 2011.
- [48] Stephen O Rice. Mathematical analysis of random noise. *Bell Syst. Tech. J.*, 23(3):282–332, 1944.
- [49] Walter Schottky. Über spontane Stromschwankungen in verschiedenen Elektrizitätsleitern. *Ann. Phys.*, 362(23):541–567, 1918.
- [50] Aldert Van Der Ziel and A van der Ziel. Noise in solid-state devices and lasers. *Proc. IEEE*, 58(8):1178–1206, 1970.
- [51] Simon M Sze and Kwok K Ng. *Physics of semiconductor devices*. John wiley & sons, 2006.
- [52] Marc Ramuz, Lukas Bürgi, Carsten Winnewisser, and Peter Seitz. High sensitivity organic photodiodes with low dark currents and increased lifetimes. *Org. Electron.*, 9(3):369–376, jun 2008.

- [53] R Clark Jones. A method of describing the detectivity of photoconductive cells. *Rev. Sci. Instrum.*, 24(11):1035–1040, 1953.
- [54] Martin Punke, Sebastian Valouch, Student Member, Siegfried W Kettlitz, Martina Gerken, and Uli Lemmer. Optical Data Link Employing Organic Light-Emitting Diodes and Organic Photodiodes as Optoelectronic Components. *J. Light. Technol.*, 26(7):816–823, 2008.
- [55] Robert J Lang. Ultrasonic atomization of liquids. *J. Acoust. Soc. Am.*, 34(1):6–8, 1962.
- [56] R. Rajan and A.B. Pandit. Correlations to predict droplet size in ultrasonic atomisation. *Ultrasonics*, 39(4):235–255, jun 2001.
- [57] I S Akhatov, J M Hoey, O F Swenson, and D L Schulz. Aerosol flow through a long micro-capillary: collimated aerosol beam. *Microfluid. Nanofluidics*, 5(2):215–224, 2008.
- [58] Sebastian Binder, Markus Glatthaar, and Edda Rädlein. Analytical Investigation of Aerosol Jet Printing. *Aerosol Sci. Technol.*, 48(9):924–929, sep 2014.
- [59] Kye-Si Kwon and Wousik Kim. A waveform design method for high-speed inkjet printing based on self-sensing measurement. *Sensors Actuators A Phys.*, 140(1):75–83, 2007.
- [60] Daehwan Jang, Dongjo Kim, and Jooho Moon. Influence of fluid physical properties on ink-jet printability. *Langmuir*, 25(5):2629–2635, 2009.
- [61] Nuno Reis, Chris Ainsley, and Brian Derby. Ink-jet delivery of particle suspensions by piezoelectric droplet ejectors. *J. Appl. Phys.*, 97(9):94903, 2005.
- [62] Emine Tekin, Patrick J Smith, and Ulrich S Schubert. Inkjet printing as a deposition and patterning tool for polymers and inorganic particles. *Soft Matter*, 4(4):703–713, 2008.
- [63] Gareth H McKinley and Michael Renardy. Wolfgang von Ohnesorge. *Phys. Fluids*, 23(12):127101, 2011.
- [64] Brian Derby. Inkjet Printing of Functional and Structural Materials: Fluid Property Requirements, Feature Stability, and Resolution. *Annu. Rev. Mater. Res.*, 40:395–414, 2010.
- [65] Thomas Young. An Essay on the Cohesion of Fluids. *Philos. Trans. R. Soc. London*, 95:65–87, jan 1805.
- [66] D H Kaelble. Dispersion-polar surface tension properties of organic solids. *J. Adhes.* 2.2, pages 66–81, 1970.
- [67] Daniel K Owens and R C Wendt. Estimation of the surface free energy of polymers. *J. Appl. Polym. Sci.*, 13(8):1741–1747, 1969.

## BIBLIOGRAPHY

- [68] W Rabel. Einige Aspekte der Benetzungstheorie und ihre Anwendung auf die Untersuchung und Veränderung der Oberflächeneigenschaften von Polymeren. *Farbe und Lack*, 77(10):997–1006, 1971.
- [69] Horace Lamb. *Statics, including hydrostatics and the elements of the theory of elasticity*. The University Press, 1916.
- [70] F Hejda, P Solar, and J Kousal. Surface free energy determination by contact angle measurements—A comparison of various approaches. In *WDS*, volume 10, pages 25–30, 2010.
- [71] Junbo Wu, Mukul Agrawal, Héctor A Becerril, Zhenan Bao, Zunfeng Liu, Yongsheng Chen, and Peter Peumans. Organic light-emitting diodes on solution-processed graphene transparent electrodes. *ACS Nano*, 4(1):43–48, 2009.
- [72] Jongwoon Park, Jongho Lee, and Yong-Young Noh. Optical and thermal properties of large-area OLED lightings with metallic grids. *Org. Electron.*, 13(1):184–194, 2012.
- [73] Mi-Sun Lee, Kyongsoo Lee, So-Yun Kim, Heejoo Lee, Jihun Park, Kwang-Hyuk Choi, Han-Ki Kim, Dae-Gon Kim, Dae-Young Lee, and SungWoo Nam. High-performance, transparent, and stretchable electrodes using graphene–metal nanowire hybrid structures. *Nano Lett.*, 13(6):2814–2821, 2013.
- [74] K. Tvingstedt and O. Inganäs. Electrode Grids for ITO Free Organic Photovoltaic Devices. *Adv. Mater.*, 19(19):2893–2897, oct 2007.
- [75] Jingyu Zou, Hin-Lap Yip, Steven K. Hau, and Alex K.-Y. Jen. Metal grid/conducting polymer hybrid transparent electrode for inverted polymer solar cells. *Appl. Phys. Lett.*, 96(20):203301, 2010.
- [76] Jong-Su Yu, Inyoung Kim, Jung-Su Kim, Jeongdai Jo, Thue T Larsen-Olsen, Roar R Søndergaard, Markus Hösel, Dechan Angmo, Mikkel Jørgensen, and Frederik C Krebs. Silver front electrode grids for ITO-free all printed polymer solar cells with embedded and raised topographies, prepared by thermal imprint, flexographic and inkjet roll-to-roll processes. *Nanoscale*, 4(19):6032–40, sep 2012.
- [77] Pälvi Kopola, Birger Zimmermann, Aleksander Filipovic, Hans-Frieder Schleiermacher, Johannes Greulich, Sanna Rousu, Jukka Hast, Risto Myllylä, and Uli Würfel. Aerosol jet printed grid for ITO-free inverted organic solar cells. *Sol. Energy Mater. Sol. Cells*, 107:252–258, dec 2012.
- [78] Yulia Galagan, Birger Zimmermann, Erica W.C. Coenen, Mikkel Jørgensen, David M. Tanenbaum, Frederik C. Krebs, Harrie Gorter, Sami Sabik, Lenneke H. Slooff, Sjoerd C. Veenstra, Jan M. Kroon, and Ronn Andriessen. Current Collecting Grids for ITO-Free Solar Cells. *Adv. Energy Mater.*, 2(1):103–110, jan 2012.
- [79] Jacobus J. van Franeker, W.Pim Voorthuizen, Harrie Gorter, Koen H. Hendriks, René A.J. Janssen, Afshin Hadipour, Ronn Andriessen, and Yulia Galagan. All-solution-processed organic solar cells with conventional architecture. *Sol. Energy Mater. Sol. Cells*, 117:267–272, oct 2013.

- [80] Rafael Tadmor. Marangoni flow revisited. *J. Colloid Interface Sci.*, 332(2):451–4, apr 2009.
- [81] Hua Hu and Ronald G Larson. Marangoni effect reverses coffee-ring depositions. *J. Phys. Chem. B*, 110(14):7090–4, apr 2006.
- [82] Dongjo Kim, Sunho Jeong, Bong Kyun Park, and Jooho Moon. Direct writing of silver conductive patterns: Improvement of film morphology and conductance by controlling solvent compositions. *Appl. Phys. Lett.*, 89(26):264101, 2006.
- [83] Philipp Cavadini, Joachim Krenn, Philip Scharfer, and Wilhelm Schabel. INVESTIGATION OF SURFACE DEFORMATION DUE TO SURFACE TENSION DRIVEN FLOWS. In *Investig. Surf. Deform. DUE TO Surf. Tens. DRIVEN FLOWS*, 2012.
- [84] Kenjiro Fukuda, Tomohito Sekine, Daisuke Kumaki, and Shizuo Tokito. Profile Control of Inkjet Printed Silver Electrodes and Their Application to Organic Transistors. *ACS Appl. Mater. Interfaces*, 2013.
- [85] Daniel A Jacobs, Kylie R Catchpole, Fiona J Beck, and Thomas P White. A re-evaluation of transparent conductor requirements for thin-film solar cells. *J. Mater. Chem. A*, 4(12):4490–4496, 2016.
- [86] Thomas Haas. *Mechanische Zuverlässigkeit von gedruckten und gasförmig abgeschiedenen Schichten auf flexiblem Substrat*, volume 41. KIT Scientific Publishing, 2014.
- [87] L Fo Coffin Jr. A study of the effects of cyclic thermal stresses on a ductile metal. Technical report, 1953.
- [88] Samuel S Manson. *Behavior of materials under conditions of thermal stress*. 1954.
- [89] P. de Bruyn, D.J.D. Moet, and P.W.M. Blom. A facile route to inverted polymer solar cells using a precursor based zinc oxide electron transport layer. *Org. Electron.*, 11(8):1419–1422, aug 2010.
- [90] Kristiaan Neyts, Alfonso Real, Matthias Marescaux, Saso Mladenovski, and Jeroen Beeckman. Conductor grid optimization for luminance loss reduction in organic light emitting diodes. *J. Appl. Phys.*, 103(9):093113, 2008.
- [91] Michael W. Rowell and Michael D. McGehee. Transparent electrode requirements for thin film solar cell modules. *Energy Environ. Sci.*, 4(1):131, 2011.
- [92] Jianyong Ouyang, CW Chu, FC Chen, Qianfei Xu, and Yang Yang. High conductivity poly (3, 4 ethylenedioxythiophene) : poly (styrene sulfonate) film and its application in polymer optoelectronic devices. *Adv. Funct. Mater.*, 15(2):203–208, 2005.
- [93] Jingsong Huang, Paul F Miller, Jo S Wilson, Andrew J de Mello, John C de Mello, and Donal D C Bradley. Investigation of the effects of doping and post deposition treatments on the conductivity, morphology, and work function of poly

## BIBLIOGRAPHY

- (3, 4 ethylenedioxythiophene)/poly (styrene sulfonate) films. *Adv. Funct. Mater.*, 15(2):290–296, 2005.
- [94] Yinhua Zhou, Fengling Zhang, Kristofer Tvingstedt, Sophie Barrau, Fenghong Li, Wenjing Tian, and Olle Inganäs. Investigation on polymer anode design for flexible polymer solar cells. *Appl. Phys. Lett.*, 92(23):233308, 2008.
- [95] Marisol Reyes-Reyes, Isidro Cruz-Cruz, and Román López-Sandoval. Enhancement of the electrical conductivity in PEDOT: PSS films by the addition of dimethyl sulfate. *J. Phys. Chem. C*, 114(47):20220–20224, 2010.
- [96] Yinhua Zhou, Hyeunseok Cheun, Seungkeun Choi, William J Potscavage Jr, Canek Fuentes-Hernandez, and Bernard Kippelen. Indium tin oxide-free and metal-free semitransparent organic solar cells. *Appl. Phys. Lett.*, 97(15):153304, 2010.
- [97] Tsu-Ruey Chou, Szu-Hua Chen, Yen-Te Chiang, Yi-Ting Lin, and Chih-Yu Chao. Highly conductive PEDOT: PSS films by post-treatment with dimethyl sulfoxide for ITO-free liquid crystal display. *J. Mater. Chem. C*, 3(15):3760–3766, 2015.
- [98] Gerardo Hernandez-Sosa, Nils Bornemann, Ingo Ringle, Michaela Agari, Edgar Dörsam, Norman Mechau, and Uli Lemmer. Rheological and Drying Considerations for Uniformly Gravure-Printed Layers: Towards Large-Area Flexible Organic Light-Emitting Diodes. *Adv. Funct. Mater.*, 23(25):3164–3171, jul 2013.
- [99] Feng Liu, Wei Zhao, John R. Tumbleston, Cheng Wang, Yu Gu, Dong Wang, Alejandro L. Briseno, Harald Ade, and Thomas P. Russell. Understanding the morphology of PTB7:PCBM blends in organic photovoltaics. *Adv. Energy Mater.*, 4(5):1–9, apr 2014.
- [100] Olaf Stenzel. Das Dünnschichtspektrum. *Akad. Berlin*, page 127, 1996.
- [101] Tobias Glaser. *Infrarotspektroskopische Untersuchung der p-Dotierung organischer Halbleiter mit Übergangsmetalloxiden*. PhD thesis, Ruprecht-Karls-Universität Heidelberg, 2013.
- [102] Luyao Lu and Luping Yu. Understanding low bandgap polymer PTB7 and optimizing polymer solar cells based on IT. *Adv. Mater.*, 26:4413–4430, 2014.
- [103] Hyunchul Oh, Johannes Krantz, Ivan Litzov, Tobias Stubhan, Luigi Pinna, and Christoph J Brabec. Comparison of various sol-gel derived metal oxide layers for inverted organic solar cells. *Sol. Energy Mater. Sol. Cells*, 95(8):2194–2199, 2011.
- [104] A S Karakoti, P Munusamy, K Hostetler, V Kodali, S Kuchibhatla, G Orr, J G Pounds, J G Teeguarden, B D Thrall, and D R Baer. Preparation and Characterization Challenges to Understanding Environmental and Biological Impacts of Nanoparticles. *Surf. Interface Anal.*, 44(5):882–889, aug 2012.
- [105] Panagiotis E. Keivanidis, Peter K. H. Ho, Richard H. Friend, and Neil C. Greenham. The Dependence of Device Dark Current on the Active-Layer Morphology of Solution-Processed Organic Photodetectors. *Adv. Funct. Mater.*, 20(22):3895–3903, nov 2010.

- [106] Andreas Elschner, Stephan Kirchmeyer, Wilfried Lovenich, Udo Merker, and Knud Reuter. *PEDOT: principles and applications of an intrinsically conductive polymer*. CRC Press, 2010.
- [107] Kang Jun Baeg, Maddalena Binda, Dario Natali, Mario Caironi, and Yong Young Noh. Organic light detectors: Photodiodes and phototransistors. *Adv. Mater.*, 25:4267–4295, 2013.
- [108] Y R Lin, J H Chang, W L Tsai, C H Cho, and H W Lin. A high efficiency UV-VIS organic photodetector by an invertedPTB7: PC71BM bulk heterojunction structure, 2015.
- [109] Inchan Hwang, Christopher R McNeill, and Neil C Greenham. Drift-diffusion modeling of photocurrent transients in bulk heterojunction solar cells. *J. Appl. Phys.*, 106(9):94506, 2009.
- [110] Ross D Jansen-van Vuuren, Ardalan Armin, Ajay K Pandey, Paul L Burn, and Paul Meredith. Organic Photodiodes: The Future of Full Color Detection and Image Sensing. *Adv. Mater.*, 28(24):4766–802, jun 2016.
- [111] Nico Christ. *Modellierung und Simulation der Stromtransienten und UI-Kennlinien organischer Photodioden und Solarzellen*. KIT Scientific Publishing, 2013.
- [112] Sebastian Valouch, Mirco Nintz, Siegfried W. Kettlitz, Nico S. Christ, and Uli Lemmer. Thickness-Dependent Transient Photocurrent Response of Organic Photodiodes. *IEEE Photonics Technol. Lett.*, 24(7):596–598, apr 2012.
- [113] Rafael García-Valverde, Judith A Cherni, and Antonio Urbina. Life cycle analysis of organic photovoltaic technologies. *Prog. Photovoltaics Res. Appl.*, 18(7):535–558, 2010.
- [114] Ning Li, Tobias Stubhan, Derya Baran, Jie Min, Haiqiao Wang, Tayebah Ameri, and Christoph J Brabec. Design of the Solution-Processed Intermediate Layer by Engineering for Inverted Organic Multi junction Solar Cells. *Adv. Energy Mater.*, 3(3):301–307, 2013.
- [115] Koji Abe, Koji Suzuki, and Daniel Citterio. Inkjet-printed microfluidic multianalyte chemical sensing paper. *Anal. Chem.*, 80(18):6928–6934, 2008.
- [116] A C Arias, S E Ready, R Lujan, W S Wong, K E Paul, A Salleo, M L Chabinyc, R Apte, Robert A Street, Y Wu, and Others. All jet-printed polymer thin-film transistor active-matrix backplanes. *Appl. Phys. Lett.*, 85(15):3304–3306, 2004.
- [117] H Sirringhaus, T Kawase, R H Friend, T Shimoda, M Inbasekaran, W Wu, and E P Woo. High-Resolution Inkjet Printing of All-Polymer Transistor Circuits. *Sci.*, 290(5499):2123–2126, dec 2000.
- [118] Se Hyun Kim, Kihyon Hong, Keun Hyung Lee, and C Daniel Frisbie. Performance and stability of aerosol-Jet-printed electrolyte-gated transistors based on poly (3-hexylthiophene). *ACS Appl. Mater. Interfaces*, 5(14):6580–6585, 2013.

## BIBLIOGRAPHY

- [119] M. Hilder, B. Winther-Jensen, and N.B. Clark. Paper-based, printed zinc–air battery. *J. Power Sources*, 194(2):1135–1141, dec 2009.
- [120] Tomas Unander, Hans-Erik Nilsson, and Bengt Oelmann. Printed touch sensor for interactive packaging and display. In *Polym. Adhes. Microelectron. Photonics, 2007. Polytronic 2007. 6th Int. Conf.*, pages 12–17. IEEE, 2007.
- [121] Bambang Kuswandi, Yudi Wicaksono, Aminah Abdullah, Lee Yook Heng, Musa Ahmad, and Others. Smart packaging: sensors for monitoring of food quality and safety. *Sens. Instrum. Food Qual. Saf.*, 5(3-4):137–146, 2011.
- [122] Hwiwon Kang, Hyejin Park, Yongsu Park, Minhoon Jung, Byung Chul Kim, Gordon Wallace, and Gyoujin Cho. Fully Roll-to-Roll Gravure Printable Wireless (13.56 [emsp14] MHz) Sensor-Signage Tags for Smart Packaging. *Sci. Rep.*, 4, 2014.
- [123] Keat Ghee Ong and Craig A Grimes. A resonant printed-circuit sensor for remote query monitoring of environmental parameters. *Smart Mater. Struct.*, 9(4):421, 2000.
- [124] Rushi Vyas, Vasileios Lakafosis, Hoseon Lee, George Shaker, Li Yang, Giulia Orecchini, Anya Traille, Manos M Tentzeris, and Luca Roselli. Inkjet printed, self powered, wireless sensors for environmental, gas, and authentication-based sensing. *Sensors Journal, IEEE*, 11(12):3139–3152, 2011.
- [125] Ashu K Bansal, Shuoben Hou, Olena Kulyk, Eric M Bowman, and Ifor D W Samuel. Wearable Organic Optoelectronic Sensors for Medicine. *Adv. Mater.*, pages n/a–n/a, 2014.
- [126] Shanshan Yao and Yong Zhu. Wearable multifunctional sensors using printed stretchable conductors made of silver nanowires. *Nanoscale*, 6(4):2345–2352, 2014.
- [127] Kristy Jost, Daniel Stenger, Carlos R Perez, John K McDonough, Keryn Lian, Yury Gogotsi, and Genevieve Dion. Knitted and screen printed carbon–fiber supercapacitors for applications in wearable electronics. *Energy Environ. Sci.*, 6(9):2698–2705, 2013.
- [128] Yong-Young Noh, Ni Zhao, Mario Caironi, and Henning Sirringhaus. Downscaling of self-aligned, all-printed polymer thin-film transistors. *Nat Nano*, 2(12):784–789, dec 2007.
- [129] Huai-Yuan Tseng and Vivek Subramanian. All inkjet-printed, fully self-aligned transistors for low-cost circuit applications. *Org. Electron.*, 12(2):249–256, 2011.
- [130] Sandro F Tedde, Johannes Kern, Tobias Sterzl, Jens Fürst, Paolo Lugli, and Oliver Hayden. Fully Spray Coated Organic Photodiodes. *Nano Lett.*, 9(3):980–983, mar 2009.
- [131] Aniello Falco, Lucio Cinà, Giuseppe Scarpa, Paolo Lugli, and Alaa Abdellah. Fully-Sprayed and Flexible Organic Photodiodes with Transparent Carbon Nanotube Electrodes. *ACS Appl. Mater. Interfaces*, 6(13):10593–10601, jul 2014.

- [132] Zexin Zhang, Zhe Wang, Rubo Xing, and Yanchun Han. Patterning thin polymer films by surface-directed dewetting and pattern transfer. *Polymer (Guildf)*, 44(13):3737–3743, jun 2003.
- [133] J Z Wang, Z H Zheng, H W Li, W T S Huck, and H Sirringhaus. Dewetting of conducting polymer inkjet droplets on patterned surfaces. *Nat Mater*, 3(3):171–176, mar 2004.
- [134] Reinhard Lipowsky, Peter Lenz, and Peter S. Swain. Wetting and dewetting of structured and imprinted surfaces. *Colloids Surfaces A Physicochem. Eng. Asp.*, 161(1):3–22, jan 2000.
- [135] Etienne Menard, Matthew a Meitl, Yugang Sun, Jang-Ung Park, Daniel Jay-Lee Shir, Yun-Suk Nam, Seokwoo Jeon, and John a Rogers. Micro- and nanopatterning techniques for organic electronic and optoelectronic systems. *Chem. Rev.*, 107(4):1117–60, apr 2007.
- [136] Martin Brinkmann and Reinhard Lipowsky. Wetting morphologies on substrates with striped surface domains. *J. Appl. Phys.*, 92(8), 2002.
- [137] D.E. Packham. Work of adhesion: contact angles and contact mechanics. *Int. J. Adhes. Adhes.*, 16(2):121–128, may 1996.
- [138] Ankit Mahajan, Woo Jin Hyun, S Brett Walker, Geoffrey A Rojas, Jae-Hong Choi, Jennifer A Lewis, Lorraine F Francis, and C Daniel Frisbie. A Self-Aligned Strategy for Printed Electronics: Exploiting Capillary Flow on Microstructured Plastic Surfaces. *Adv. Electron. Mater.*, 1(9):n/a–n/a, 2015.
- [139] Tse Nga Ng, William S. Wong, Michael L. Chabinyc, Sanjiv Sambandan, and Robert a. Street. Flexible image sensor array with bulk heterojunction organic photodiode. *Appl. Phys. Lett.*, 92(2008):2013–2016, 2008.
- [140] Steven D Sprules, John P Hart, Robin Pittson, and Stephen A Wring. Evaluation of a new disposable screen-printed sensor strip for the measurement of NADH and its modification to produce a lactate biosensor employing microliter volumes. *Electroanalysis*, 8(6):539–543, 1996.
- [141] G Gustafsson, Y Cao, G M Treacy, F Klavetter, N Colaneri, and A J Heeger. Flexible light-emitting diodes made from soluble conducting polymers. *Nature*, 357(6378):477–479, jun 1992.
- [142] Milan Alt, Malte Jesper, Janusz Schinke, Sabina Hillebrandt, Patrick Reiser, Tobias Rödlmeier, Iva Angelova, Kaja Deing, Tobias Glaser, Eric Mankel, Wolfram Jaegermann, Annemarie Pucci, Uli Lemmer, U H F Bunz, W Kowalsky, G Hernandez-Sosa, R Lovrincic, and M Hamburger. The Swiss-Army-Knife Self-Assembled Monolayer: Improving Electron Injection, Stability, and Wettability of Metal Electrodes with a One-Minute Proces. *Adv. Funct. Mater.*, feb 2016.
- [143] He Yan, Zhihua Chen, Yan Zheng, Christopher Newman, Jordan R Quinn, Florian Dotz, Marcel Kastler, and Antonio Facchetti. A high-mobility electron-transporting polymer for printed transistors. *Nature*, 457(7230):679–686, feb 2009.

## BIBLIOGRAPHY

- [144] Stefan Hengen, Milan Alt, Gerardo Hernandez-Sosa, Jürgen Giehl, Uli Lemmer, and Norman Mechau. Modelling and simulation of gate leakage currents of solution-processed OTFT. *Org. Electron.*, 15(3):829–834, mar 2014.
- [145] Jui-Mei Hsu, Loren Rieth, Richard A Normann, Prashant Tathireddy, and Florian Solzbacher. Encapsulation of an integrated neural interface device with Parylene C. *IEEE Trans. Biomed. Eng.*, 56(1):23–29, 2009.
- [146] A. Asadpoordarvish, A. Sandström, and L. Edman. A Flexible Encapsulation Structure for Ambient-Air Operation of Light-Emitting Electrochemical Cells. *Adv. Eng. Mater.*, 18(1):105–110, jan 2016.
- [147] D Pozar. Considerations for millimeter wave printed antennas, 1983.

# Acknowledgments

I like to carry on the tradition to give credits to my partners, co-workers, supervisor and family.

First of all, I would like to thank Prof. Uli Lemmer the opportunity of having this great time at the InnovationLab. And to mention in particular, a special thanks for his great effort in organizing the solar excursion to California in 2010 where all started and which turned out to impact my further scientific career tremendously. I'd also like to thank Prof. Wolfgang Kowalsky for being the co-referee of my thesis.

A very special thank deserves my supervisor and dear friend Dr. Gerardo Hernandez Sosa for his faith, his respect, and his unlimited support in scientific and personal matters. I can look back to many fruitful discussions and helpful advices, as well as good times in the office and the long hours in the laboratories. Furthermore, thanks for proof-reading this thesis.

I'd like to thank all my colleagues from the LTI and the InnovationLab for being such an outstanding community and for your endless support. Besides, many thanks for all the social activities and great time. Furthermore, I want to thank my former supervisor Dr. Norman Mechau for bringing me to the InnovationLab and for the (still ongoing) support. Thanks to Tobias R. for the unique entertainment in the clean room and his superior knowledge about solvents. To Milan, Arno, Tobias B., Sebastian S., Serpil, with whom I treated the "KIT-group-at-InnovationLab-path" from the beginning and clearly contributed to the success of this group. Also many thanks to my master student Jan for his excellent work on modeling of organic solar cells. And of course to the whole KIT-group with Anthony, Stefan, Noah, Johannes, Nils, Florian, and Marta.

I kindly thank the InnovationLab management and organization team for all the colloquies, and for keeping the iL running, improving and advancing. Special thanks should be granted to Dr. Martin Raditsch and Prof. Wolfgang Kowalsky as the managing directors. Additionally, I want to thank Alaa, Holger, Stefan and Janusz for their great support in technical and scientific questions and not to forget to Janusz again for his never ending effort in organizing the weekly soccer sessions. Besides, I thank Thommy and Karsten for managing the clean room and laboratories. And to my ex-band member Martin G. for the perfect relief from work with our almost famous band and for the amicable support.

## *Acknowledgments*

For their special help with measurements I want to thank Christian M. (TU Braunschweig), Lars M. (TU Braunschweig), Tobias G. (University of Heidelberg), Sebastian H. (KIT), Konstantin G. (KIT), Torben A. and Manuel H. (University of Heidelberg). Also many thanks to Felix N. and Alexander C. (LTI. KIT) for the good and successful collaboration within the Delicious Project. Very special thanks deserves my Diploma-thesis supervisor Manuel R. for all the support, motivation and social events like Cannstatter Wasen, unique culinary events (pure beef!) and the canoe challenges.

Many thanks also to the secretary team Astrid Henne and Claudia Holeisen for their enormous help with the madness of bureaucracy.

Cordial thanks to the Karlsruhe School of Optics and Photonics (KSOP) for the financial support and the opportunity to get an insight into a broad spectrum of research areas, as well as business and soft-skill related courses and in particular to Denica Angelova-Jackstadt, Stefanie Peer, and Miriam Sonnenbichler for the great administration.

I want to acknowledge the Ministry of Education and Research (BMBF) for the financial support within the Delicious Project.

And last but not least: Muchas gracias a mi maraviosa esposa Claudia Fernanda Canales Aguila y mi hija querida Emilia Eckstein por todo el soporte, la fuerza, el esfuerzo y el amor. Les amo mucho. Ademas, agradezco mucho a mi familia querida en Chile. Muchas gracias a Myriam, Carlos, Carlos y Daniela por sus cariños y el soporte y por ser una familia tan afectuoso. Zudem danke ich von ganzem Herzen meinen Eltern Gabriele und Herbert, meinem Bruder Simon und seiner Familie, sowie auch dem Rest meiner Familie (Großeltern, Onkel,..) für die tolle Unterstützung in allen Belangen und den Zusammenhalt.